

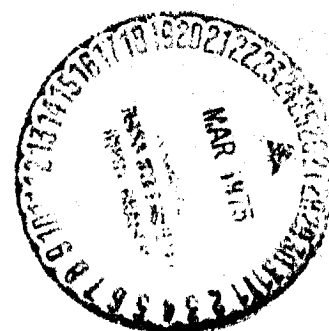
NASA CR

141651

APOLLO 14 VISIBILITY TESTS: VISIBILITY OF LUNAR
SURFACE FEATURES AND LUNAR LANDING

18 December 1972

20029-6018-RU-00



APOLLO 14 VISIBILITY TESTS: VISIBILITY OF LUNAR
SURFACE FEATURES AND LUNAR LANDING

18 December 1972

20029-6018-RU-00

Prepared by:


K. Ziedman

Approved by:


D. D. Cohen

Performed under NASA Contract NAS 9-12330, Subtask ASPO 88-C

CONTENTS

	<u>Page</u>
ACKNOWLEDGEMENTS.....	1
GUIDE TO THE REPORT.....	2
1. INTRODUCTION AND SUMMARY.....	3
1.1 Scope.....	3
1.2 Problem Statement.....	3
1.3 Lunar Visibility Analysis.....	4
1.4 Test Procedures.....	6
1.5 Results.....	6
1.6 Conclusions and Recommendations.....	7
2. PROBLEM STATEMENT.....	8
2.1 LM Descent and Visibility Requirements.....	8
2.2 LM Descent Trajectory and Viewing Geometry.....	9
2.3 Visibility and Viewing Geometry.....	10
2.4 Descent Visibility - Problem Statement.....	13
2.5 Operational and Mission Considerations.....	14
2.6 Overall Visibility Considerations.....	15
3. LUNAR VISIBILITY ANALYSIS.....	27
3.1 Lunar Photometric Function.....	27
3.1.1 Introduction.....	27
3.1.2 Geometry.....	28
3.1.3 Standard Photometric Functions.....	29
3.1.4 Lunar Surface Models.....	32
3.1.5 Discussion.....	32
3.2 Visibility Calculations for Lunar Features.....	33
3.2.1 Visibility Models.....	33
3.2.2 Contrast Models.....	36
3.3 Visibility Predictions.....	41
3.4 Limitations of Analytical Approach.....	44
4. TEST PROCEDURES.....	60
4.1 Approach.....	60
4.2 Selection of Target Areas and Observation Procedures.....	61
4.2.1 Orbital Pass Geometry.....	61
4.2.2 Target Location and Zero Phase Track....	62
4.2.3 Selection of Targets and Observational Sequence.....	62
4.3 Photographic Procedures.....	64
4.4 Training and Observation Procedures.....	65
4.5 Ground Support Activities.....	66

CONTENTS (Continued)

	<u>Page</u>
5. RESULTS.....	77
5.1 Data Quality.....	77
5.2 Data Analysis.....	78
5.2.1 CMP Observations.....	78
5.2.2 Timing Analysis.....	78
5.2.3 Measurement of Target Contrasts.....	79
5.2.4 Comparison With Analytical Predictions..	81
5.3 Summary of Results.....	81
5.3.1 Photographic Results.....	81
5.3.2 Visibility and Target/Background Characteristics.....	83
6. ANALYSIS.....	127
6.1 Comparison of Measured With Analytical Visibility Data.....	127
6.1.1 Albedo Determination.....	127
6.1.2 Subtended Angle Comparisons.....	130
6.1.3 Bright Side, Dark Side and Geometric Shadow.....	131
6.2 Fedoritz Function Compared to the LRM.....	132
6.3 Conical and Spherical Section Crater Model Comparison.....	133
6.4 Photometric Function Analysis.....	138
6.4.1 Contrast Measurements and the Photometric Function.....	138
6.4.2 Quantification of Modified Photometric Function.....	139
6.4.3 Evaluation.....	143
7. DISCUSSION.....	155
7.1 Visibility Models and Mission Planning.....	155
7.2 Generality of Results.....	156
7.3 Lunar Surface Visibility and the Apollo Program.....	158
REFERENCES.....	159
APPENDIX A. Photographic Processing and Calibration	163
APPENDIX B. Microdensitometry and Error Sources....	166
APPENDIX C. Observational Results For Each Target Area.....	173

CONTENTS (Continued)

	<u>Page</u>
APPENDIX D. Calculation of Equivalent Subtended Angles from Number of Scan Points.....	178
APPENDIX E. Hapke Model.....	180
APPENDIX F. Definition of Terms in Tables 5-1 Through 5-3.....	183

ILLUSTRATIONS

	<u>Page</u>
2-1 LM Descent Sequence.....	17
2-2 Altitude-Time Profile for Apollo 15.....	18
2-3 Geometrical Framework for Visibility Analysis.....	19
2-4 View Elevation Angle (VEA) at the Landing Point Versus Altitude.....	20
2-5 Down-Sun View of the Lunar Surface.....	21
2-6 Up-Sun View of the Lunar Surface.....	22
2-7 Cross-Sun View of the Lunar Surface.....	23
2-8 Viewing Geometry of Figure 1-5.....	24
2-9 Orbital View of the Lunar Surface.....	25
2-10 Effect of SRA on Shadow Visibility.....	26
3-1 Alpha Angle Definition and Sign Convention.....	45
3-2 Alpha Angle Definition in Astronomical Framework..	46
3-3 Lunar Reflectivity Model	47
3-4 Effect of Slope Variation on Value of Reflectance Factor.....	48
3-5 Fedoritz Function Developed by JPL.....	49
3-6 Surface Structure and Light Scattering.....	50
3-7 Typical Detection Results for Repeated Presentation of Visual Signals	51
3-8 Illustration of Subtended Angle Versus Threshold Contrast Function.....	51
3-9 Threshold Contrast Versus Angular Diameter Data from Blackwell.....	52
3-10 Threshold Contrast Versus Angular Diameter Data from Taylor.....	53

ILLUSTRATIONS (Continued)

	<u>Page</u>
3-11 Illustration of Geometric Shadow, Dark Side (Photometric Shadow), and Bright Side Regions.....	54
3-12 Input Example for Crater Contrast Program.....	55
3-13 Output Example for Crater Contrast Program.....	55
3-14 Typical Presentation of Visibility Predictions, SEA = 25°.....	56
3-15 Typical Presentation of Visibility Predictions, SEA = 10°.....	57
3-16 Effect of Approach Azimuth on Location of Washout Boundary.....	58
3-17 Simulation of Apollo 15 Site Appearance During Descent.....	59
4-1 Viewing Geometry for Frontside and Backside.....	71
4-2 Observation Sequences for Backside and Frontside Passes for Each Pass.....	72
4-3 CSM Ground Track and Zero Phase Track for Pass 16F (Areas 3 and 4).....	73
4-4a CSM Ground Track and Zero Phase Track for Pass 16B (Areas 1 and 2).....	74
4-4b CSM Ground Track and Zero Phase Track for Pass 30B (Areas 5 and 6).....	75
4-5 Sample Training Photograph.....	76
5-1 Example of Portion of THPRNT Output.....	105
5-2 Computer Reconstruction of Target 3B.....	106
5-3 Computer Reconstruction of Target 1C.....	107
5-4 Computer Reconstruction of Target 6B.....	108
5-5 Hasselblad 70mm Frames from 16B Pass (Areas 1 and 2).....	109
5-6 Hasselblad 70mm frames from 16F Pass (Areas 3 and 4).....	112

ILLUSTRATIONS (Continued)

	<u>Page</u>
5-7 Hasselblad 70mm Frames From 30B Pass (Areas 5 and 6).....	115
5-8 Targets 1A, 1B, and 1C.....	118
5-9 Targets 2A and 2B.....	119
5-10a Targets 3A and 3B.....	120
5-10b Targets 3A and 3B.....	121
5-11 Targets 4A and 4B.....	122
5-12a Targets 5A, 5B and 5C.....	123
5-12b Targets 5A, 5B and 5C.....	124
5-13 Targets 6B and 6C.....	125
5-14 Visibility Test Results.....	126
6-1 Visibility Results for the LRM, Spherical Section Craters.....	145
6-2 Visibility Results for the Fedoritz, Spherical Section Craters.....	146
6-3 Comparison of Visibility Model Results for Conical and Spherical Section Craters.....	147
6-4a Minimum Phase Contrast Minus Washout Contrast.....	148
6-4b Minimum Phase Contrast Versus Washout Contrast....	148
6-5 Graphical Illustration of Photometric Function Modification.....	149
6-6 Hapke Photometric Function.....	150
6-7 Retrodirective Function Versus Phase Angle.....	151
6-8 Visibility results for the Hapke Photometric Model	152
6-9 LRM Correction Term Versus Phase Angle.....	153
6-10 Visibility Results for the Modified LRM Photometric Function.....	154

TABLES

	<u>Page</u>
4-1. Apollo 14 Visibility Test Target Locations.....	68
4-2. Time Sequence for Each Observation Pass.....	69
4-3. Rating Scale used to Rank Target Visibility.....	70
5-1a. Trajectory and Solar Data for Rev. 16B.....	90
5-1b. Viewing and Illumination Conditions for 16B (Targets 1A, 1B, 1C).....	91
5-1c. Viewing and Illumination Conditions for 16B (Targets 2A, 2B).....	92
5-2a. Trajectory and Solar Data for Rev 16F.....	93
5-2b. Viewing and Illumination Conditions for 16F (Targets 3A, 3B).....	94
5-2c. Viewing and Illumination Conditions for 16F (Targets 4A, 4B).....	95
5-3a. Trajectory and Solar Data for Rev 30B.....	96
5-3b. Viewing and Illumination Conditions for 30B (Targets 5A, 5B, 5C).....	97
5-3c. Viewing and Illumination Conditions for 30B (Targets 6A, 6B, 6C).....	98
5-4. Targets and Frames Analyzed.....	99
5-5. Comparison of Actual and Photographic Minimum Phase.....	100
5-6a. Summary Result Table, Backside Passes, Visibility Data.....	101
5-6b. Summary Result Table, Frontside Passes, Visibility Data.....	102
5-7. Frequency Distribution of Target Characteristics...	103

TABLES (Continued)

	<u>Page</u>
5-8. Target Albedos Input to Visibility Program.....	104
6-1. Frequency Distribution of Alpha Angles.....	135
6-2 Comparison of Measured and Calculated Subtended Angle/Contrast Data.....	136-137

ACKNOWLEDGEMENTS

It is a pleasure to thank Lt. Col. Stu Roosa, who conducted the visual observations from lunar orbit and greatly contributed to the success of this program through his interest and suggestions. Personnel of NASA/MSC Flight Crew Support Division provided invaluable assistance in fitting these tests into the Apollo 14 time-line and in helping set-up the test procedures. Special mention should go to Lt. George Colton, Spencer Gardner, Elvin Pippert and Chuck Stough. Jack Sevier and Charles Glancy of NASA/MSC Apollo Program Office lent substantial support to the planning and integration of this work with the mission. Finally, my thanks to Wayne Moore, who jointly helped plan this program, and to Sam Rifman, who contributed to much of the data analysis.

GUIDE TO THE REPORT

The first section is a brief summary of the conclusions and recommendations and the main topics covered in the report. Section 2 presents background information for the Apollo 14 orbital tests, including a discussion of visibility considerations in lunar operations and a description of visibility in the lunar environment. A detailed discussion of the techniques developed for analyzing lunar visibility problems is given in Section 3. Topics included are lunar photometric functions, visual detection data, lunar visibility models, and typical applications. The rationale and test procedures employed in the Apollo 14 visibility tests are presented in Section 4. The test results and main conclusions are given in Section 5. Section 6 contains an in-depth discussion of the results and of the procedures used for their analysis. Concluding comments are given in Section 7.

The reader who is generally familiar with lunar visibility problems and is interested only in the main results of the Apollo 14 tests should read Sections 1, 5, and 7. For those not familiar with the impact of lunar visibility problems on Apollo operations and the lunar lighting environment, Sections 2 and 3 should be added to the above. Section 6 and the appendices are of interest primarily to those working on similar problems and for a critical evaluation of the conclusions.

Note that the figures and tables for any section are at the end of the corresponding section.

1.0 INTRODUCTION AND SUMMARY

1.1 Scope

This report describes an in-flight visibility test conducted on the Apollo 14 mission. The need for obtaining experimental data on lunar feature visibility arose from visibility problems associated with various aspects of the Apollo missions; and especially from anticipated difficulties of recognizing lunar surface features at the time of descent and landing under certain illumination conditions. Although visibility problems have influenced many other aspects of the Apollo mission, they have been particularly important for descent operations, due to the criticality of this mission phase and the crew's guidance and control role for landing site recognition and touchdown point selection. A series of analytical and photographic studies were conducted during the Apollo program (prior to as well as after the initial manned lunar operations) to delineate constraints imposed on landing operations by visibility limitations. The purpose of the visibility test conducted on Apollo 14 was to obtain data to reduce uncertainties and to extend the analytical models of visibility in the lunar environment.

Although this work was in support of Apollo program operations, the results are applicable to other lunar visibility problems, as well as to analysis of lunar photometric functions. In addition, the present report represents the culmination of an intensive program of visibility studies applied to a very complex mission and thus should be of interest to others working in similar areas.

1.2 Problem Statement

The critical aspect of lunar feature visibility results from a combination of the lunar surface reflectance properties and illumination by a collimated light source, the sun. Although visibility of the surface is good under most viewing/illumination conditions and not unlike viewing on the Earth, when looking down the sunline (sun in back of observer) a loss of shadowing and feature contrast occurs in a region in front of the observer. This area, termed the "washout" region is one of poor visibility

and in which many terrain features may not be seen. Because the Lunar Module (LM) descends in an East to West direction in the lunar morning (sun in the East at the crew's back), the washout region will be down-range of the LM and can cover the landing area itself if the sun elevation angle (SEA) is high enough. Further, surface operations need to be conducted in all directions with respect to the sun and the washout can present visibility problems on the surface.

Although surface feature visibility when looking down-sun is not the only visibility problem encountered in lunar operations, it has been a critical one for descent planning as it establishes a maximum limit on the SEA at the time of descent, and therefore has imposed limits on the Earth launch window. A mathematical model of visibility was developed early in the Apollo program to assist analysis of these problems. However, uncertainties in this model led to a decision to obtain observational data in the lunar environment with which to validate and extend the visibility prediction techniques.

1.3 Lunar Visibility Analysis

The model used to predict visibility of lunar features is based on two sets of data. The first is laboratory data of target detection by human observers that are standard results used in various visibility studies. The second set is the lunar photometric function, which specifies the reflectance properties of the lunar surface as a function of viewing and illumination vectors. The visibility data are summarized in a function which relates the luminance contrast needed to detect a target to the subtended angular size of that target. The lunar photometric function combined with geometrical models of lunar features allows the contrast of such features to be computed. The complete visibility model thus specifies the conditions under which idealized surface features can be visually detected as a function of viewing and illumination directions.

The results of such calculations have been applied in a variety of ways to predict lunar surface visibility in order to assist mission planners by specifying acceptable and unacceptable visibility conditions.

These calculations are a basic starting point in any study of lunar visibility but must be supplemented by considerations specific to a given site or surface region, such as availability of landmarks and adequacy of pre-mission photography.

As experience in the lunar environment was gained, it became clear that analytical predictions of visibility were not adequate to specify the limits of acceptable visibility. Optimal visibility conditions and conservative bounds on acceptable viewing (e.g., the equal albedo washout boundary) did correspond to qualitative judgements and observations obtained during the missions, but hard data was lacking on how far into the washout region (as defined above), if at all, one could obtain acceptable visibility for lunar descent. The limitations of the analyses were due to the use of simplified terrain models, uncertainty in the form of the photometric function, as well as to the inherent complexity of the descent situation in which visual information is only a part of a complex decision and control process required of the crew.

Although any test, short of an accurate display of surface appearance used in connection with the LM simulator would lack the complete set of elements needed to investigate the overall problem, it became obvious that some form of a quantitative test of lunar feature visibility, in the lunar environment, was necessary to make advancements in specification of acceptable visibility conditions. Such a test would provide threshold data obtained with realistic target and background configurations, and could also be used to study the validity of crater contrast predictions based on the photometric functions. Although many casual observations were available from Apollo crews concerning visibility, they could not be related to "ground truth," i.e., what could be seen was reported, but no record was available of what could not be seen. Thus, a test that provided independent verification of target contrast and size was required. On this basis, an appropriate visibility test was developed for the Apollo 14 mission.

1.4 Test Procedures

The Apollo 14 tests were designed to provide data on the two main aspects of the visibility models: the lunar photometric function and the threshold contrast necessary for target detection. The tests were conducted from lunar orbit by the command module pilot (CMP) who observed pre-selected target craters at specified times during the mission. The viewing and illumination conditions at the time of observation were selected so as to simulate the range of viewing conditions that occur during LM descent. The CMP made continuous comments on target visibility during each of three separate orbital passes over the target areas, which included 15 different visual targets.

In addition to the visual observations, a photographic record of the visual scene was obtained via an intervalometer-operated bracket mounted camera. The film record provided a means to measure target contrast and size and, thus, to relate the CMP's observations to target characteristics.

1.5 Results

The data analysis included three main tasks: (1) transcription of the CMP's comments and correlation with a time reference; (2) determination of the camera actuation time of each photographic frame; and (3) measurement of target contrasts and size from microdensitometer scans of the film record. The latter task was quite time-consuming and paced the overall analysis.

Comparisons of the obtained data with the visibility model predictions indicated generally good agreement with the visibility threshold criterion used in the model and strongly favored the Lunar Reflectivity Model, one of several lunar photometric functions employed in lunar visibility studies. The test results did indicate that visibility in the washout may be somewhat better than predicted and that the roughness of background terrain is an important factor in visibility. Further, comparisons of target detectability and overall scene appearance between the photographic and observational results indicated that lunar photography can produce a reasonable simulation of what is seen. Various analyses were performed to assist comparison of the predicted and obtained data.

These included: (1) Development of a rationale for determining target albedo from contrast measurements at small phase angles; (2) Comparisons of predictions based on the Lunar Reflectivity Model, Fedoritz Function, and Hapke photometric model; (3) Comparison of truncated cone and spherical section geometrical crater models; and (4) Examination of modifications to the lunar photometric functions to obtain a better fit between observed and predicted data.

1.6 Conclusions and Recommendations

It is concluded that the results from the Apollo 14 visibility tests support the present lunar visibility model with the LRM function and that such differences as were found are not large enough to justify quantitative revision of the model. However, many qualitative aspects of the test results increase understanding of lunar visibility problems and, further, quantitative corrections to calculations of crater contrasts are suggested that would be useful for special cases. For this reason, the test results should be understood by anyone attempting to apply or extend models of lunar feature visibility.

2.0 PROBLEM STATEMENT

The general nature of lunar visibility conditions and their relation to lunar descent operations are presented in this section.

2.1 LM Descent and Visibility Requirements

The Lunar Module (LM) starts its descent from a 50,000 altitude; at an altitude of about 7,000 feet (high-gate) the LM pitches up, allowing the crew to view the landing area. The LM descent path follows an approximately constant slope or flight path angle (FPA) from this point to about 600 feet altitude (low-gate). This descent sequence is diagrammed in Figure 2-1.

The initial task of the crew after obtaining visibility of the landing area following high-gate is to evaluate their position with respect to that of the nominal descent trajectory by observing the positions of terrain features relative to the LM. Following this initial evaluation, the location of the predicted landing point is estimated and tracked with the use of the Landing Point Designator (LPD)* system and compared to the desired target point. Corrective guidance actions may be made to move the predicted landing point closer to the desired target point or to avoid rough terrain. As the descent progresses, the crew's concern becomes directed towards selection of a safe landing point (rather than reaching a specific target); typically, final terrain evaluation and selection of a touch-down point is made after low-gate at altitudes of a few hundred feet or less. At low-gate the crew may assume manual control of the LM (several modes, including fully automatic landing, are available). A vertical descent is initiated at an altitude of about 200 feet or less, after this time the touchdown area itself cannot be seen because it is directly below the LM. During the final 80 to 100 feet of descent, dust from the LM exhaust will be present and may partially or completely obscure the surface.

*The LPD system consists of two components: a computer software and read-out capability which indicates angular coordinates of the predicted landing point in a LM centered coordinate system and a scale etched on the CDR's window which allows him to sight the surface point indicated by the readout coordinate. Corrective commands are input via a control lever.

Thus, a variety of visual tasks are required of the crew during descent. At the higher altitudes feature and pattern recognition and judgement of the relative position of the visual scene with respect to the visual framework provided by the LM window are most important. (Training in the Lunar Module Simulator using a TV infinity projected scene of the lunar surface has been extremely valuable in developing this ability). Use of the LPD system requires detailed attention to the predicted landing point, which decreases time available for an overall assessment of the visual scene. Selection of a touchdown point requires visual search for obstacle sized features (e.g., one-meter high boulders, craters deeper than a meter or two, slopes greater than 8° or 9°); in this case pre-mission photographic data and training can be relied on only to indicate areas in which a safe region is likely to be found, final selection depends on the crew. Finally, manual control of the LM after low-gate may require judgement of lateral motion between the LM and the surface.*

A limited amount of time is available in which to perform these and other tasks during descent. A typical altitude-time profile is shown in Figure 2-2. Note that about 120 sec. are available between high-gate and vertical descent, but that the time available at higher altitudes (above, say, 3,000 feet) where enough surface area can still be seen for overall visual assessment is less than 30 sec.

2.2 LM Descent Trajectory and Viewing Geometry

The geometrical framework commonly used to analyze lunar visibility is described here. This geometry is illustrated in Figure 2-3, which should be referred to in connection with the following discussion.

* Lateral and vertical motion readouts are provided as well as attitude hold and lateral motion hold modes.

The elevation angle of the line-of-sight from the local horizontal at a viewed point to the observer is termed the view elevation angle (VEA). Two other quantities of interest are the sun elevation angle (SEA), the elevation of the solar vector at the viewed point, and the sun relative azimuth angle (SRA). The SRA is the horizontal angle between the projections of the view and sun vectors on the lunar surface as shown in Figure 2-3. It is zero when the two vectors are in the same plane with the local vertical at the viewed point. A final quantity to be introduced here is the phase angle (g), the angle between the view and sun vectors to a given surface point. A zero phase angle (view and sun vectors parallel) has a particular significance to be described later in this section. A profile of VEA at the landing point versus altitude for Apollo 15 is shown in Figure 2-4. Note the nearly constant VEA of about 21° from 6,000 feet to about 1,000 feet altitude. This profile, typical for Apollo missions 15, 16 and 17, is a steeper descent than used on missions prior to 15 for which a FPA of about 16° was employed. The steeper descent trajectory provides a better visibility situation during descent, as discussed below.

The range of approach azimuths* has been within $\pm 15^\circ$ of true East-West for the different Apollo missions. Thus, because the time of landing occurs in the lunar morning (sun in the East), the crew descends with the sun more-or-less behind them.

2.3 Visibility and Viewing Geometry

An unusual or difficult visibility situation would not occur if the conditions described in Sections 2.1 and 2.2 were encountered by an aircraft landing on Earth on typical soils, grasslands, or runways. However, the visibility situation on the moon differs from that of the Earth because of three factors: 1) lack of an atmosphere, 2) presence of a collimated light source (the sun), and 3) unique reflectance properties of the lunar soil. On Earth, visual contrast between terrain features is usually due to hue as well as to luminance differences and is relatively independent.

*The approach azimuth (AA) is the angle between the LM ground track and north, measured clockwise from north at the landing point.

of the relative positions of the sun, observer and viewed object. On the moon, hue differences are not consistently related to topography and an observer must depend entirely on luminance differences (shades of gray) to distinguish features. Luminance differences are, in turn, strongly dependent on the viewing geometry and terrain slopes as well as on the albedo (reflectivity) of each surface area. Thus, a given lunar region viewed under different lighting conditions, or from different viewing directions, can change markedly in appearance.

These effects are best illustrated pictorially. Figures 2-5, 2-6, and 2-7 are reproduced from frames taken on the lunar surface and show, respectively, down-sun viewing (similar to the LM descent case), up-sun viewing (looking towards the sun), and cross-sun viewing (looking at a large SRA angle). The most dramatic difference is shown between down-sun viewing and the other two cases. The down-sun case (Figure 2-5) shows a marked decrease in feature contrast and shadowing in the region down-range of the astronaut's shadow, extending about $\pm 15^\circ$ to $\pm 20^\circ$ in azimuth from the down-sun direction.

In comparison, the cross-sun view (Figure 2-6) exhibits excellent contrast and shadowing over the entire scene as would the up-sun view (Figure 2-7), except for the glare due to scattering in the camera lens (a similar effect occurs in the astronaut's faceplate when working on the surface, and can present a difficult visibility situation).

The relationship of the viewing geometry defined previously to the down-sun scene in Figure 2-5 is depicted in Figure 2-8. Figure 2-8 diagrams the astronaut's position relative to the sun, the low contrast region referred to above, and two zero phase point locations. As mentioned in Section 2.2, a zero phase angle occurs when looking directly down-sun and the "zero phase point" is the surface point seen under this condition. For an observer standing on the surface, the zero phase point is where the shadow of his eyes would fall on the surface (point B in Figure 2-8) and for a photograph zero phase is at the shadow of the camera (point A in Figure 2-8). The SRA, of course, is zero when viewing the zero phase point. For comparison, the

view and sun lines are also indicated at a surface point that is not in the down-sun direction (point C in Figure 2-8). Although not evident from Figure 2-5 due to the presence of the astronaut's shadow, a luminance "surge" occurs at zero phase resulting in a very bright spot subtending an angle of 2° or 3° . This effect appears in an orbital frame reproduced in Figure 2-9; the bright zero phase point is easily seen as well as is the transition from the shadowed to non-shadowed regions. Orbital photography is a somewhat better simulation of what would be seen during descent than are surface views because the viewer's shadow does not interfere with the scene. The zero phase effect, which is considered in more detail in Section 3, is due to a strong retro-reflective characteristic of the lunar soil (i.e., light is maximally reflected back along the line of incidence).

The loss of surface detail that is apparent in Figures 2-5 and 2-9, and diagrammed in Figure 2-8, occurs in the region down-range of zero phase, or, roughly, when the VEA is less than the SEA (at least for phase angles smaller than 20° or 30°). This region of poor visibility, usually termed the "washout region," is a consequence of two effects: 1) shadowing geometry; and 2) the lunar photometric function. For small values of SRA, shadows in depressions will not be seen when the VEA is less than the SEA (as shown in Figure 2-10a). As the SRA increases (Figure 2-10b), shadows will begin to be seen; however, for typical lunar terrain very few shadows in depressions will be seen for SRAs less than 10° . (As the SEA increases, of course, all shadows except for those of rocks and very steep depressions will disappear.) Shadows are a prominent aspect of the lunar surface at low SEAs and provide good topographic cues; their absence increases the difficulty of visual evaluation.

The effect of the lunar photometric function on contrast and visibility is complex and only a simplified analysis is given here. The lunar photometric function specifies the luminance of a surface point given the viewing/illumination geometry and the albedo of the surface at that point. In terms of the geometry introduced above, if we specify the VEA, SEA, SRA, and the slope of the viewed point, we can determine its luminance from:

$$L = F(\text{VEA}, \text{SEA}, \text{SRA}, \text{slope}) \times \text{Solar Illuminance} \times \text{Albedo},$$

where F is the photometric function. The slope factor is critical for our purposes because it implies that two adjacent areas (such as a crater wall and the adjacent horizontal surface) can be of different luminances even if they have the same albedo and are viewed under the same conditions. Thus, contrasts or luminance differences between adjacent lunar areas can be due to a combination of slope and albedo variations. However, in the washout region described above, the photometric function is such that slope effects are minimal, that is, variation in slope results in only small or zero luminance differences. If the lunar soil in an area containing a crater is of uniform albedo, the crater will be of very low or zero contrast and will not be seen in the washout region. Conversely, features which have high albedos will be especially conspicuous in the washout region because of the typically bland appearance of this area.

2.4 Descent Visibility - Problem Statement

The principal visibility problem encountered during lunar descent follows from the above discussion: because the LM lands in a down-sun direction, the landing point and neighboring terrain will be in the washout area if the SEA is greater than the VEA at these regions. The VEA is fixed by the descent trajectory, which in turn is determined by various operational considerations. Thus, to ensure good visibility in the landing site area, a constraint would have to be placed on the maximum allowable SEA at the time of landing. The SEA increases with time due to lunar rotation (12° a day for a point near the equator) and, thus, a SEA constraint limits the size of the Earth launch window. For instance, consider a case for which the maximum acceptable SEA at a given site is 20° and assume the launch is planned for 10° (an optimal value). In the event of a slippage from the prime launch day, the SEA 24 hours later (next launch opportunity) is 22° , which exceeds the 20° limit. Thus, the launch must wait until the following month (one lunar day).

This qualitative statement of the visibility problem must be transformed into a more quantitative form to be useful for mission planning. Specifically, the boundaries of the washout region which delineate acceptable and unacceptable visibility conditions must be determined as a function of the SEA. For instance, for a given SEA and VEA, what SRA is necessary to ensure adequate visibility? This question applies to locomotion on the surface as well as to descent and landing. However, a less stringent criterion is applied to surface operations than landing, i.e., poor visibility during a surface traverse can be handled by slowing down and an unacceptable limit is reached only when speed becomes too low for conducting efficient exploration. Landing, on the other hand is time and fuel limited to a much greater degree than are surface operations.

The approach taken towards quantitative analysis of the visibility problem during the Apollo program is presented in detail in Section 3 for both the descent and surface conditions. Other aspects of the descent visibility problem and relationships between visibility and operational considerations are considered in the remainder of this section.

2.5 Operational and Mission Considerations

The above discussion should not be interpreted as indicating that difficult visibility situations are a common occurrence during lunar landing. Early analyses established an optimal range of the SEA and planning for the initial landing missions was based on this range. However, this optimal range was rather narrow and thus reduced the number of launch opportunities per month. As mission experience and operational flexibility developed, it became desirable to extend the limit of illumination conditions to one which, although not optimal, would still allow acceptable visibility.

Two changes in mission operations have significantly eased the problem of SEA restraints on the launch window. Initially, a free return trajectory was used which requires a constant Earth-moon transit time. Thus, if a launch slipped one day, the SEA at the landing site would have increased by 12° at the next launch opportunity, one day later. Even assuming the first launch was scheduled for the lowest acceptable SEA value

of 5° , the SEA 24 hours later would have increased to 17° . For the original Apollo trajectories using a 16° FPA, this would place the SEA equal to or greater than the VEA to the landing site, an undesirable situation. Thus, only one launch opportunity per month could be scheduled. As indicated previously, the FPA on recent missions has been increased to about 23° , allowing a somewhat higher SEA; in addition, a non-free return trajectory is now used which enables variation in the Earth-moon transit time by trajectory alterations. Thus, the SEA on a second launch day need not be 12° greater than on the first if the transit time is decreased. Recent mission configurations have, in fact, been based on two to three opportunities per month - due in part to increased knowledge of the visibility situation and in part to the increased flexibility of mission operations.

2.6 Overall Visibility Considerations

Visibility cannot be discussed independently of such factors as the use of visual information by the crew, time available to make decisions, adequacy of landmark patterns, consequences of a mis-identification, or, in other words, the overall systems considerations which lead one to a choice of descent strategies. It is appropriate to end this section with a brief listing of such factors. In the case of lunar landing, it has been found necessary to consider all of the following in judging the acceptability of visibility conditions at each Apollo site:

- 1) The surface regions covered by the washout area as a function of altitude for the particular combinations of descent trajectory, SEA and SRA considered for each mission and for each potential launch opportunity.
- 2) The excessive shadowing resulting from a too low SEA, requiring a lower limit on the sun elevation angle.
- 3) The effect of SEA on visibility through the dust plume (low SEAs on the order of 5° to 7° interact with the dust plume to severely degrade visibility).
- 4) The adequacy and locations of landmark patterns for each site.
- 5) The adequacy of pre-mission photography as well as the terrain model derived from the photography which is used in the descent simulator.

- 6) The ability to train the crew for anticipated visibility situations (simulator training and briefings).
- 7) Various operational tradeoffs which can be employed to obtain a better visibility situation (e.g., extra trans-lunar burns to arrive at the moon sooner and thus with a lower SEA at the time of landing).
- 8) Tradeoffs between factors such as a marginal visibility situation versus a missed launch opportunity if the SEA should increase too high due to a launch slippage.
- 9) Other operational problems related to SEA such as visibility requirements for landmark tracking at the site from the CSM prior to descent.
- 10) Interaction of planning for acceptable SEAs with the many other time-related mission requirements (consumables, communication coverage, etc.).

The main thrust of this report is directed at the first point - quantitative prediction of visibility in the washout region. However, the other factors which must be incorporated for a complete analysis should be kept in mind.

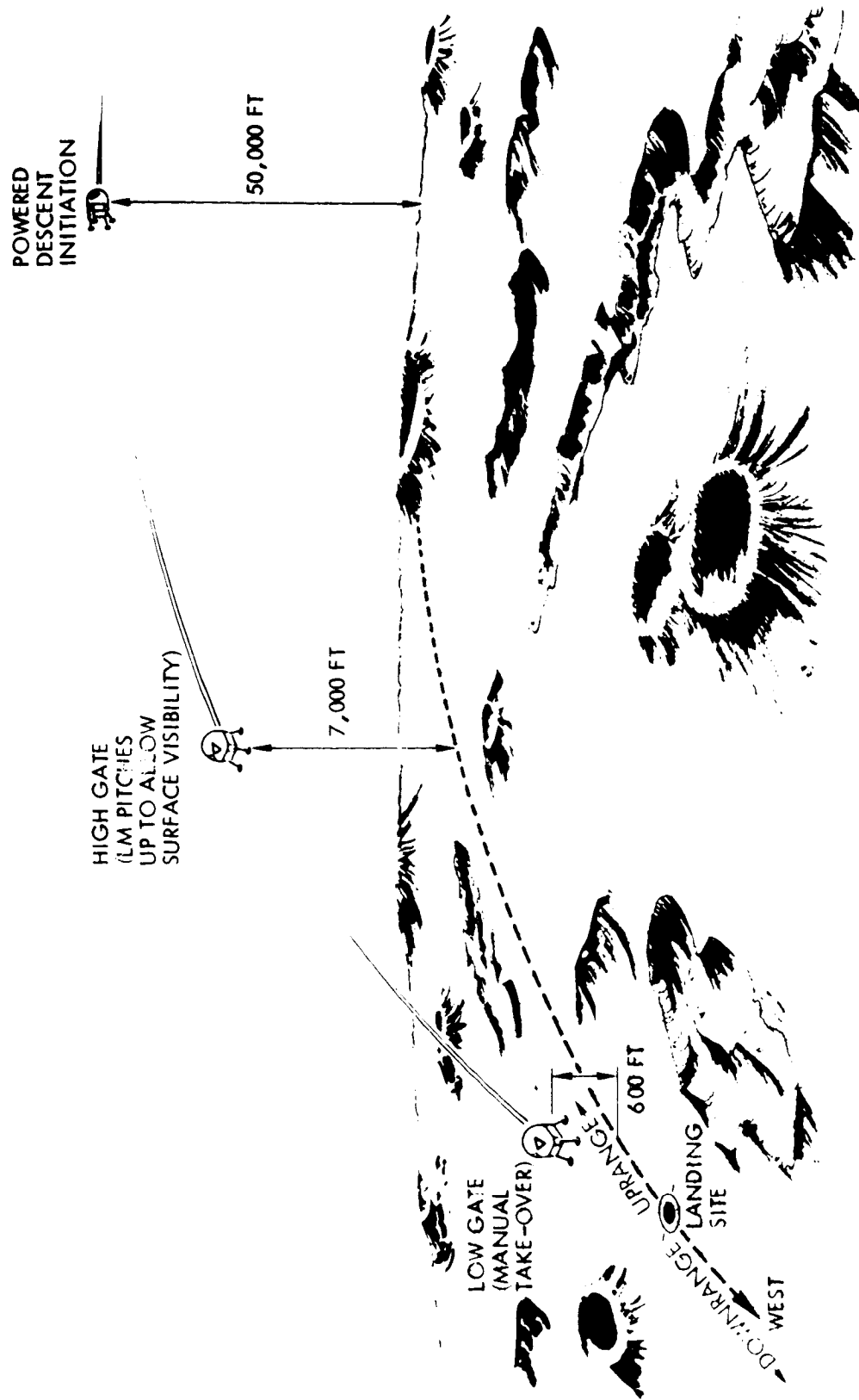


Figure 2-1. LM Descent Sequence

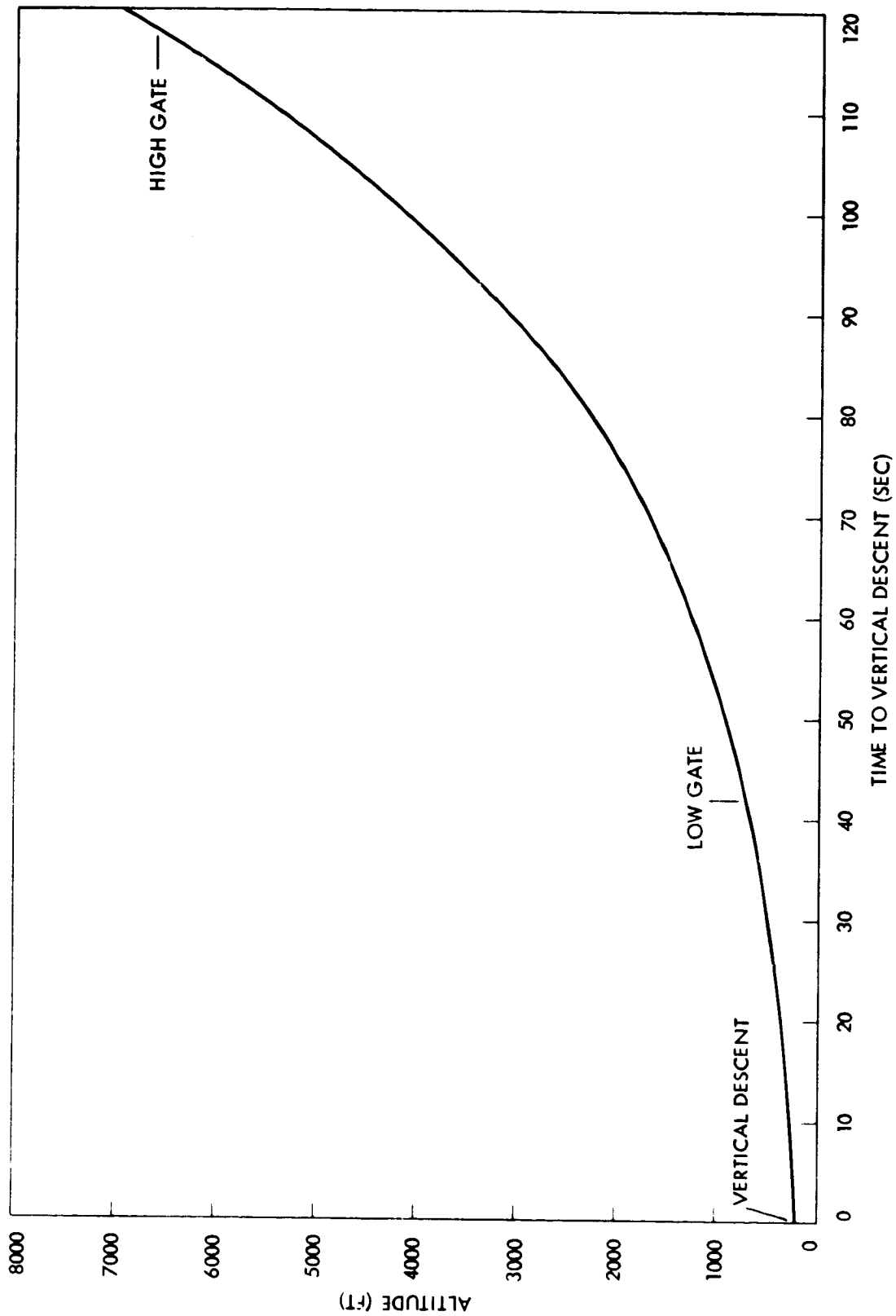


Figure 2-2. Altitude-Time Profile for Apollo 15, High Gate to Vertical Descent (Pre-Mission)

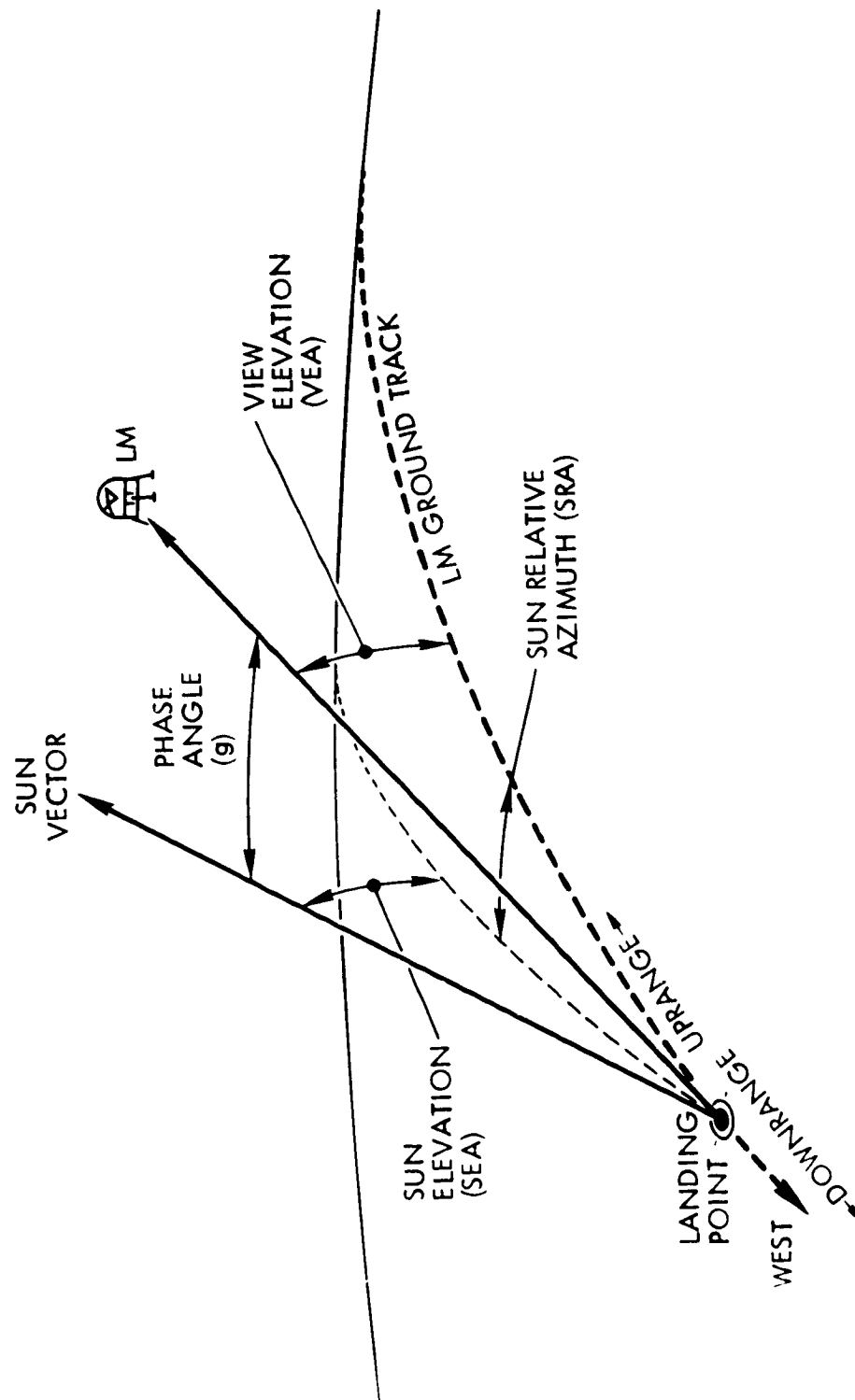


Figure 2-3. Geometrical Framework for Visibility Analysis (Elevation Angles are Measured from Local Horizontal at the Landing Point)

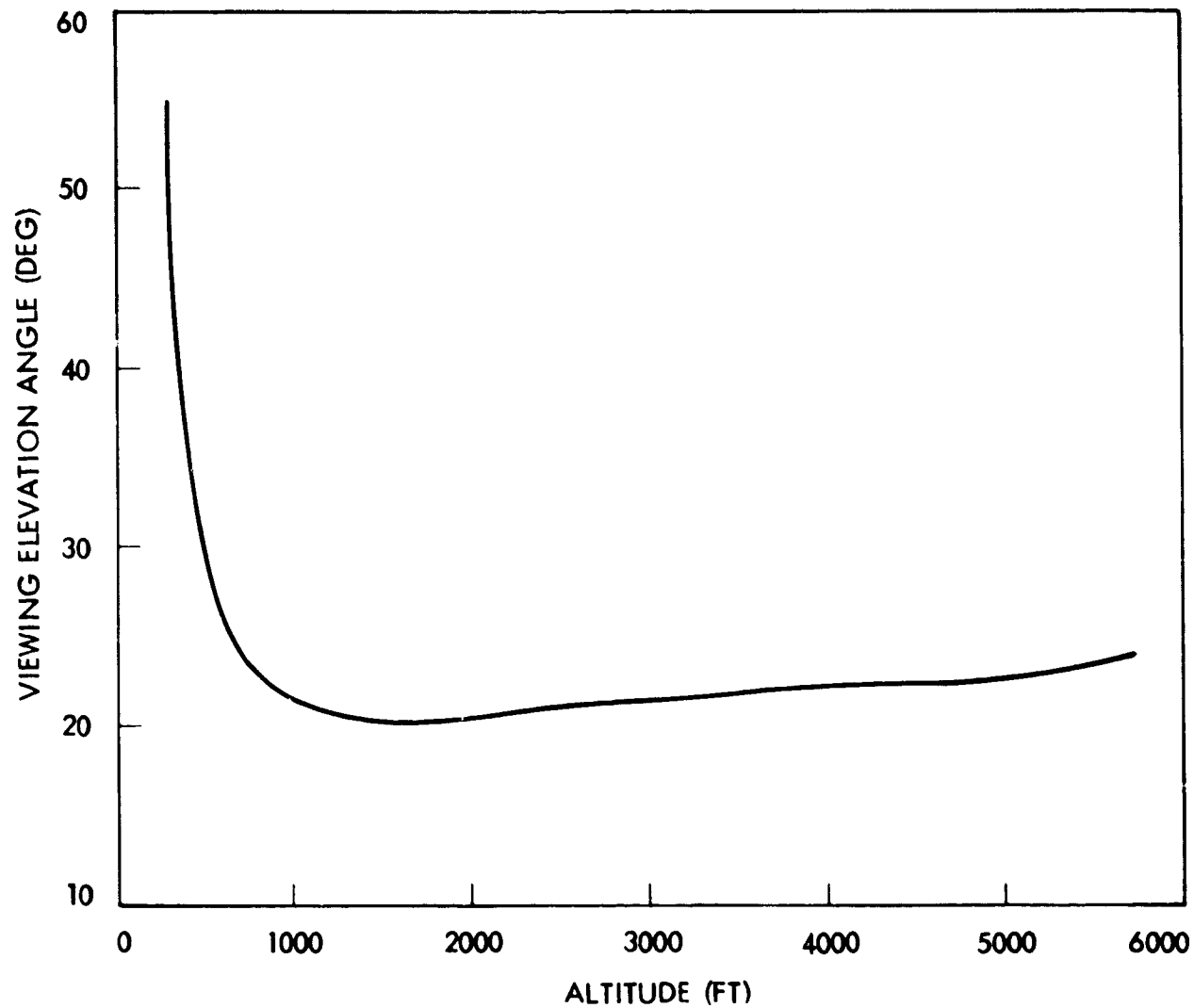


Figure 2-4. View Elevation Angle (VEA) at the Landing Point Versus Altitude During LM Descent for Apollo 15 (Pre-Mission)



Figure 2-5. Down-Sun View of the lunar surface
(Apollo 11, frame AS11-10-906)



Figure 2-6. Up-Sun View of the Lunar Surface
(Apollo 14, Frame AS14-108-15)

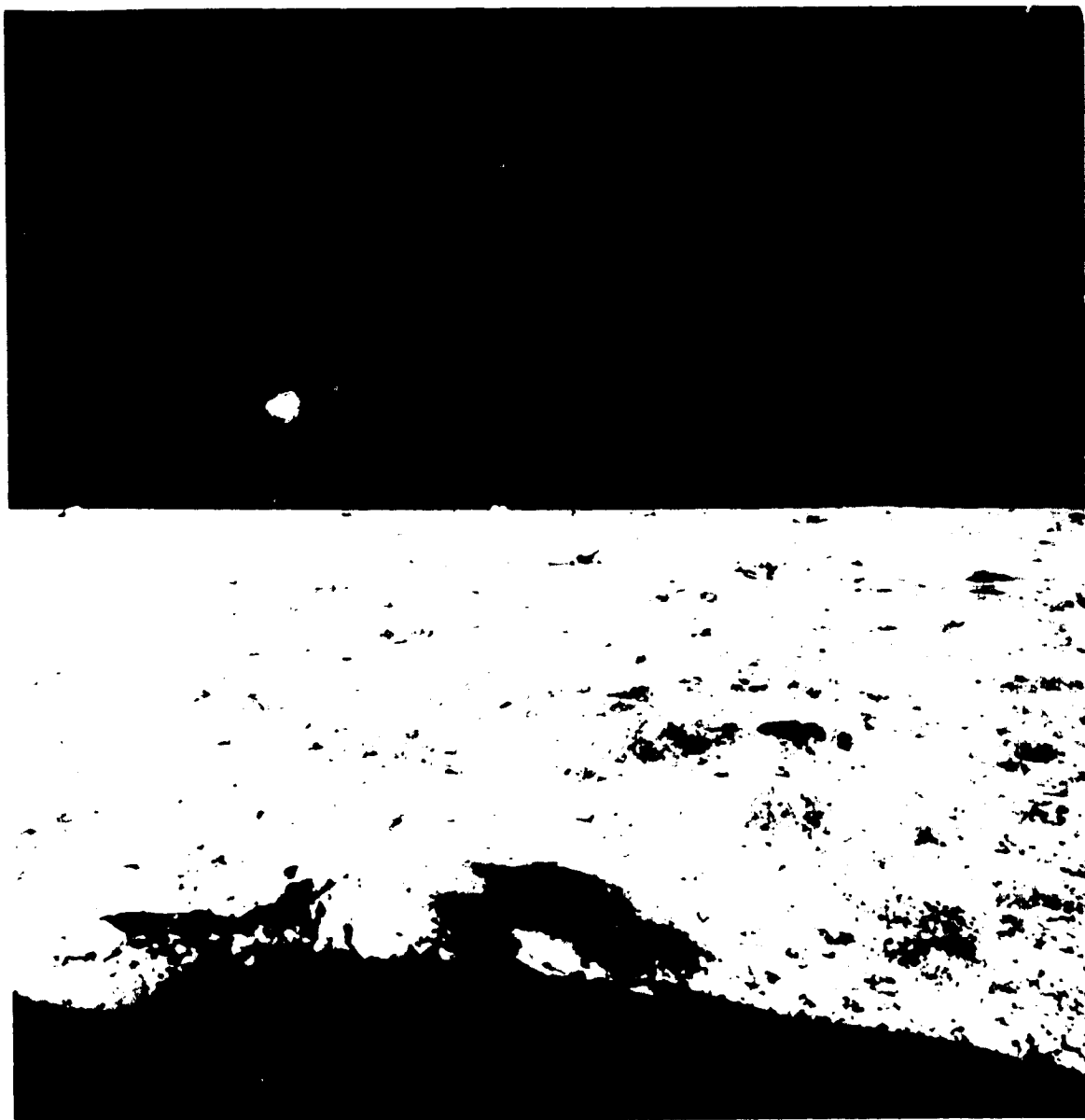


Figure 2-7. Cross-Sun View of the Lunar Surface
(Apollo 11, Frame AS11-10-1574)

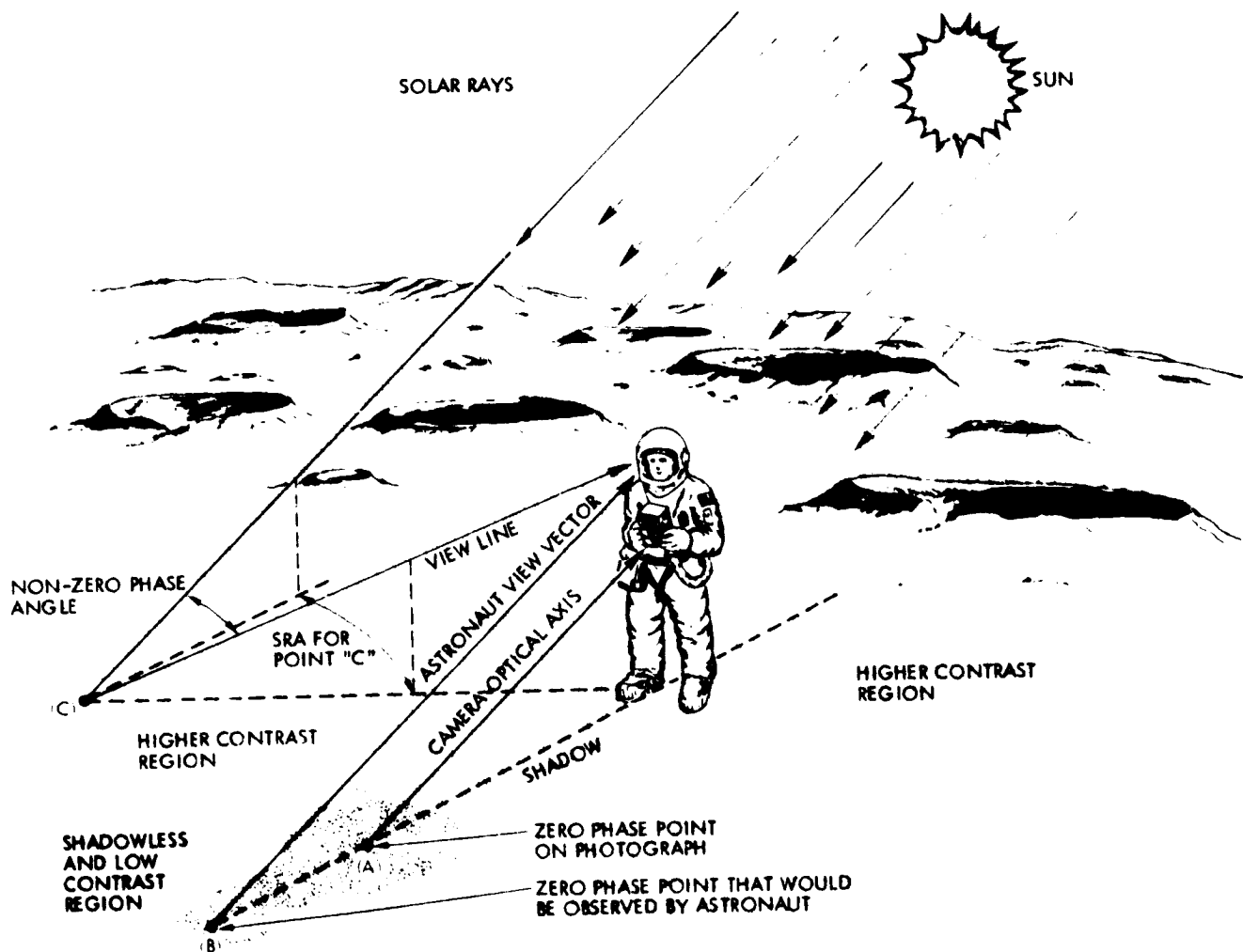


Figure 2-8. Viewing Geometry of Figure 1-5 Showing Zero Phase Points and Low Contrast Region

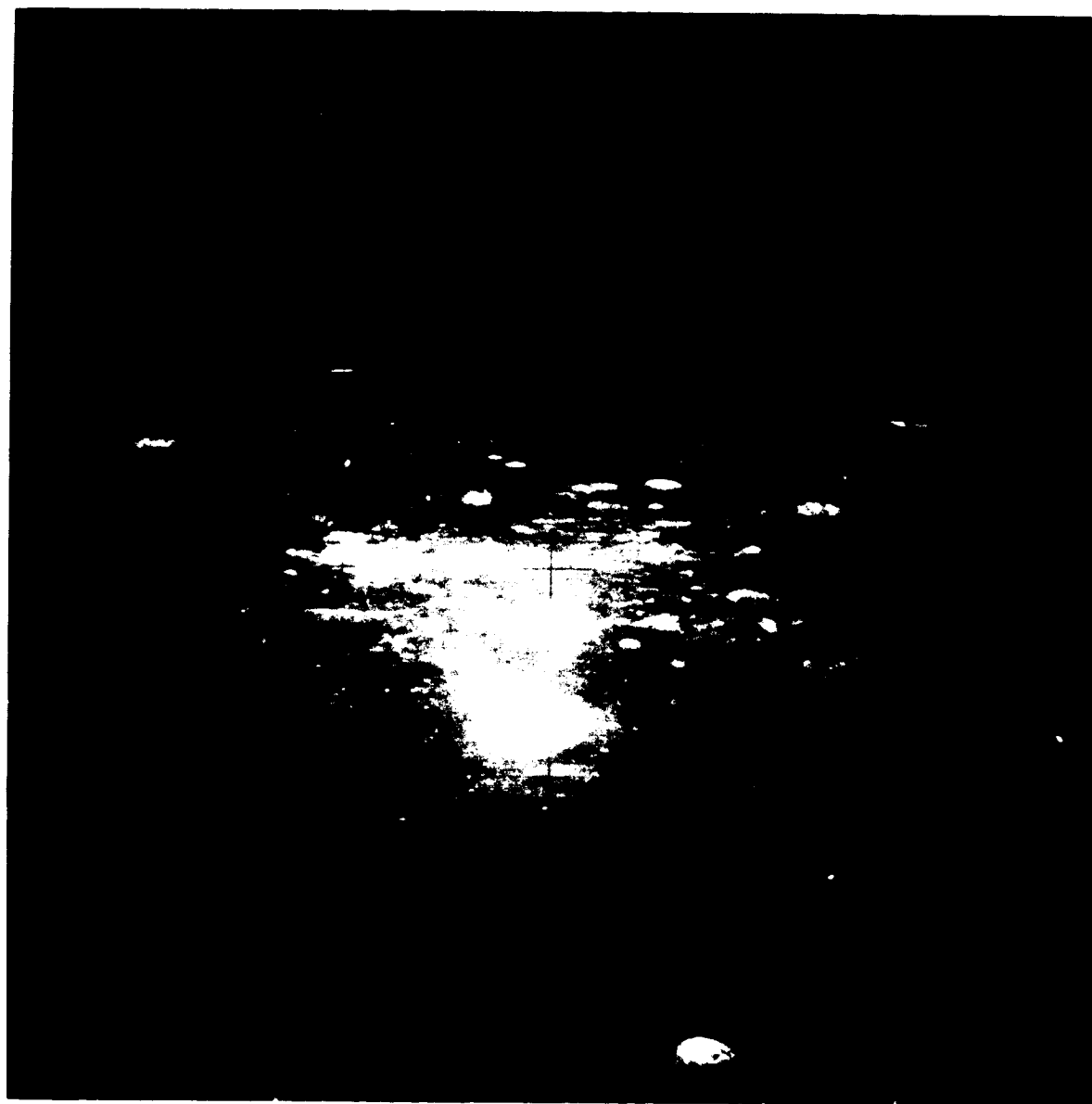


Figure 2-9. Orbital View of the Lunar Surface With Zero Phase Luminance Surge Visible at Center of Image Area (Apollo 14, Frame AS14-75-10257)

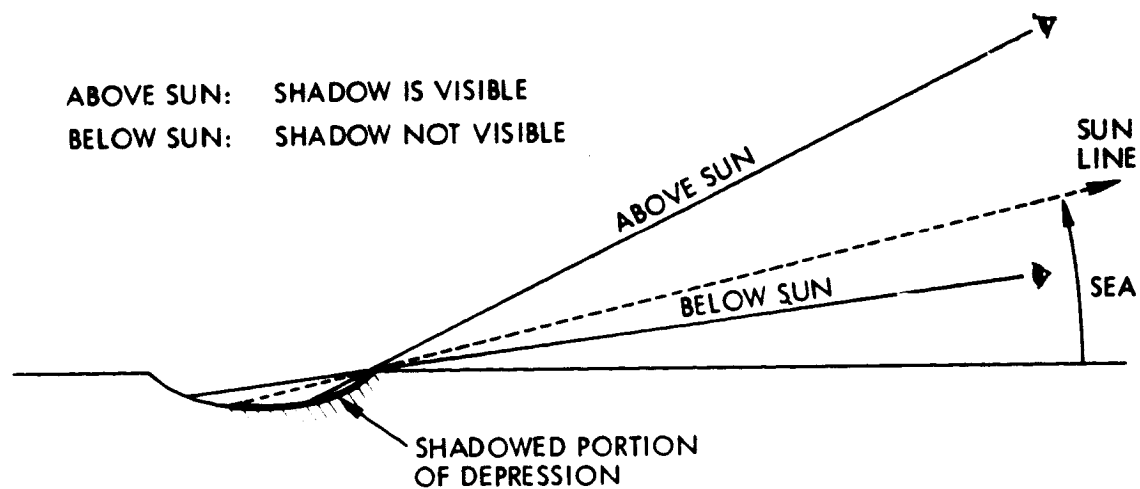


Figure 2-10a. Shadow Visibility Looking Downsun

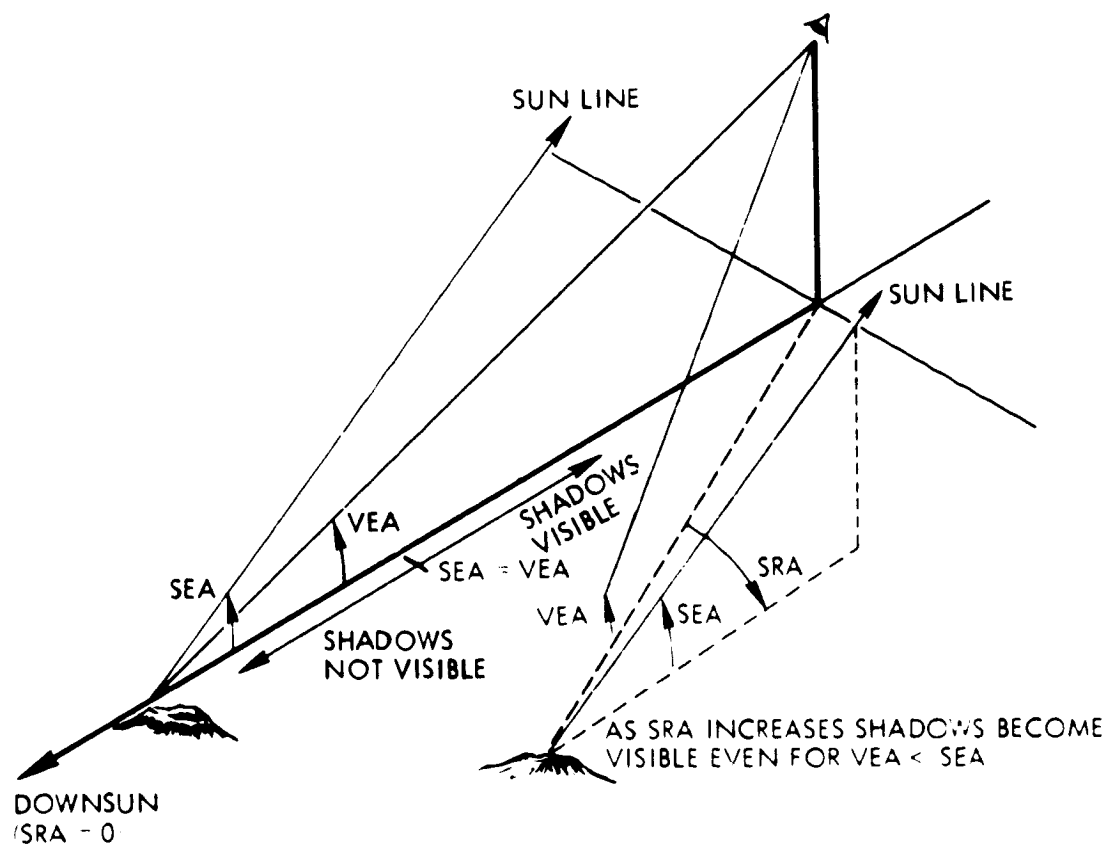


Figure 2-10b. Effect of SRA on Shadow Visibility

3.0 LUNAR VISIBILITY ANALYSIS

A description of lunar photometric properties and visibility prediction techniques is given in this section to provide a background to the Apollo 14 visibility test rationale and results. Typical analytical results and applications of visibility predictions are discussed as well as their limitations which led to the Apollo 14 tests.

3.1 Lunar Photometric Function

3.1.1 Introduction

In Section 2.0 it was noted that the amount of light reflected from a point on the lunar surface is a function of the viewing and illumination vectors and surface slope. The lunar photometric function referred to in the previous section is considered in more detail in the present section.

"The remarkable manner in which the surface of the moon scatters light is well known. Barabashev (1922) and Markov (1924) discovered that the brightness of almost all areas on the moon peaks sharply at full moon, when the sun is directly behind the observer. This is in contrast to most terrestrial materials, which reflect light more or less in accordance with Lambert's law. Opik (1924) found that the shape of the photometric function is similar for all types of formations. Further, for the same type of formation the maximum of the photometric curve at full moon is independent of position on the lunar disk. These results have been amply confirmed by the measurements of Bennett (1938), Fedoretz (1952), van Diggelen (1959), and others. van Diggelen confirmed Tschunko's assertion that the shape of the scattering law with phase angle is nearly independent of lunar latitude and depends primarily on the lunar longitude. These observations are reviewed by Minnaert (1961) and by Fessenkov (1962)."

Quoted from the Journal of Geophysical Research, Vol. 68, No. 15, August, 1963, "A Theoretical Photometric Function for the Lunar Surface," pages 4571 - 4586, by Bruce W. Hapke.

The reflectance properties of the moon summarized in the quotation from Hapke have been of interest to astronomers because they provide information as to the structure and composition of the lunar surface. Photometric functions derived from astronomical data by different investigators show the same general characteristics, but differ in some important

details. Because such functions were obtained from Earth-based telescopic measurements, they represent averages over fairly large lunar regions (on the order of 100 Km^2). Data from lunar soil samples indicate that in terms of general characteristics the Earth-based data hold down to small surface regions (on the order of a few square centimeters or less). Thus, the lunar reflectance function primarily results from properties of the soil rather than from large scale topography. However, there is evidence indicating that the photometric functions of different lunar regions (mare, rays, highlands, etc.) are somewhat different although sufficient data do not exist to quantitatively specify such differences. Lunar rocks which have a much more compact surface compared to soil show a more diffuse reflectance function and higher albedos than soil and, therefore, must be treated separately (Reference 1).

Although a substantial amount of optical data have been obtained from lunar samples, Apollo photography and Surveyor data, insufficient measurements have been made to allow quantitative derivation of a new photometric function or functions. Therefore, photometric functions based on pre-Apollo telescopic data have been used throughout the Apollo program. The two most widely used Earth-based functions are described below along with a brief mention of more recent data and their implications for visibility studies.*

3.1.2 Geometry

The geometrical framework presented in Section 2, although useful for mission and visibility analyses, is redundant and awkward for a description of the lunar photometric function itself. Empirical and theoretical results have shown that the lunar function can be reduced to a two-variable form as shown in Figure 3-1a. One variable is the phase angle (θ) which was already introduced as the angle between the view and sun vectors. The other is usually termed the alpha angle (α) or, in astronomical usage, the luminance longitude. Alpha is measured on the plane formed by the sun and view vectors (phase plane) by projecting the surface normal at the viewed point onto the phase plane and then taking alpha as the angle between the normal projection and the view vector. If the view vector falls between

*Some results of the present study which bear on the lunar photometric function are presented in Sections 5 and 6.

the normal projection and the sun vector alpha is positive, otherwise alpha is negative as shown in Figure 3-1b. When observed from the Earth, the luminance of the lunar surface is approximately constant along a line of constant longitude but varies with latitude. A line of constant longitude is equivalent to a line of constant α angle, hence the name "luminance longitude." A representation of the alpha and phase angles in astronomical terms (moon viewed from Earth) is shown in Figure 3-2.

Note that alpha is dependent on surface slope, except in the special case where the slope direction is such that the normal projection on the phase plane does not change. This fact is the basis for the statement in Section 2 that lunar surface slope and luminance are related. Note also that the values of phase and alpha and, hence, the surface luminance are independent of an azimuthal rotation of the surface around the surface normal*. Finally, note that the phase angle and phase plane are independent of surface orientation.

3.1.3 Standard Photometric Functions

The lunar photometric function used in the present study was derived by JPL (Reference 2) from data obtained by Sytinskaya and Sharanov (Reference 3) and is graphed in Figure 3-3. This function, also termed the Lunar Reflectivity Model (LRM), expresses the relationship:

$$\phi = \phi(g, \alpha)$$

where -

ϕ is the reflectance factor
 g is the phase angle
 α is the alpha angle.

Note that ϕ is plotted as a function of α with g a parameter.

The value of ϕ is a normalized ratio of reflected to incident light that obtains for a given α and g and is normalized to 1.0 at $g = 0$ (zero phase). The actual luminance of the viewed point is found by:

*This implies that the fine structure of the lunar soil does not show regular differences as a function of the azimuthal angle.

$$L = \phi (g\alpha) \times E_S \times \rho_n$$

where -

L = luminance (lumens/unit area/unit solid angle)

E_S = solar illumination (lumens/unit area)

ρ_n = normal albedo of the lunar surface*

Several significant relationships can be seen from Figure 3-3.

Firstly, consider the luminance change due to a slope variation for two initial viewing conditions: 1) positive α angle; and 2) negative α angle. These effects are illustrated in Figure 3-4.

A 10° phase angle is shown and for simplicity in-plane viewing is assumed (normal, view and sun vectors in same plane). The SEA is taken as 30° , thus the VEA is 40° for the positive alpha case and 20° for the negative alpha case. Case A (positive alpha angle) shows that ϕ varies from 0.55 to 0.49 for a slope change of 0° to 10° ; Case B (negative alpha angle) shows that ϕ remains constant at 0.65 for the same slope change. Thus, the luminance differences between identically sloped areas can be strongly dependent on the sign of alpha. Further, an area viewed under a positive alpha becomes brighter as it is tilted towards the observer, whereas an area viewed under negative alpha becomes darker or remains unchanged (consider a 10° change in alpha for a phase angle of 100° as an example of surface darkening).

Secondly, note that negative alpha values correspond roughly to the case where the VEA is less than the SEA. This is exactly true for the in-plane case and is approximately so for out-of-plane angles. For small phase angles (less than 20° or 30°) the curves of ϕ versus α are nearly flat for a negative alpha angle. It is this portion of the phase-alpha space that more exactly defines the washout region introduced in Section 2.0, than

*Normal albedo is the ratio of actual surface luminance to that of a Lambertian surface with a total albedo of 1.0, when both are illuminated and viewed normally. Note that two surfaces can have equal normal albedos but different total albedos (ratio of total reflected flux to total incident flux, often called Bond albedo, see Reference 4, page 306).

does the simpler criterion of VEA less than SEA.* Also note that at large phase angles slope contrasts are substantial even for a negative alpha angle and with the VEA less than the SEA (this is illustrated by the down-sun view in Figure 2-7 for which the phase angles are large over the entire scene).

Finally, note that at zero phase the value of ϕ is maximum (unity) and is independent of alpha, i.e., alpha is undefined at zero phase. Thus, the luminance at a surface point is independent of the viewing direction if the point is seen at zero phase:

$$\begin{aligned} L &= \phi(g, \alpha) \times E_S \times \rho_n \\ &= 1.0 \times E_S \times \rho_n \end{aligned}$$

Thus, not only does the lunar surface exhibit strong retro-reflective properties (reflection is maximum at zero phase when view and sun vectors are parallel), but the amount of light reflected under such conditions is constant, regardless of the viewing angle. The fact that the lunar disk appears equally bright over its entire surface at full moon when close to zero phase (no decrease at the edges as would be the case for a diffuse reflecting surface) is a consequence of this phenomenon. That is, at full moon the phase angle is about 1.5° for all points on the surface, whereas the alpha angle varies from 0° (near the center) to -90° (at the edges).

The photometric function presented above is the one presently used by most investigators for estimating luminance levels of the lunar surface (camera exposure, visibility calculations, etc.). A function based on data obtained by Fedoritz (Reference 5) which was also curve-fitted by JPL (Ref. 6) has been a main alternative to the LRM and shown in Figure 3-5. It is different from the LRM in that the curves of ϕ versus α have much larger slopes in the small phase angle-negative alpha regions. Thus, the Fedoritz function would predict larger contrasts (due to slopes) in the washout region and, hence, better visibility of surface features. Other photometric functions and analytical formula describing such functions have been proposed (see References 4, 7, & 8).

*The best definition of the washout region, of course, is in terms of what can actually be seen when viewing down-sun.

3.1.4 Lunar Surface Models

A theoretical model was developed by Hapke to explain lunar optical properties (References 9 and 10). This model, based on laboratory data, as well as theory, was advanced prior to the opportunity for direct examination of the surface and has been proven essentially correct. Hapke showed that the surface layer must be composed of small particles on the order of 10 μ m diameter or less (but larger than the wavelength of light), which are loosely piled on top of each other and adhere so as to form an intricate structure with many spaces and interstices. Under a microscope, this structure has a "dendritic growth" appearance to which the name "fairy castles" was given (see Figure 3-6). Such soil has a high porosity (ratio of empty space to soil). If the albedo of the individual particles is small, Hapke showed that the reflectance properties of such soils are similar to those of the moon (Reference 11). Examination of lunar samples has proven this model correct (Reference 12). The "fairy castle" structure can be seen in returned soil samples and in close-up stereo photography of the lunar surface, the lunar particle size distributions, indeed, show the majority of particles to be less than 10 μ m diameter, and the porosity is in the predicted range.*

3.1.5 Discussion

The significance of the lunar photometric functions for the present study, is that one or more such functions had to be selected for calculations of visibility predictions as well as for planning and interpretation of the Apollo 14 tests. In spite of the fact that all proposed functions have the same general form, their differences result in quite different visibility estimates; predictions based on the LRM, Fedoritz and Hapke functions will be compared with the results of the present study in Section 6.0. As indicated above, studies on lunar samples have confirmed prior models of lunar reflectance properties, but have not supplied enough data to warrant revision of the telescopic-derived results.

* A Boeing study (Reference 12) determined values of the Hapke parameters for many lunar areas based on photo-electric telescopic measurements. See, also, Section 6.4 and Appendix E of the present report.

3.2 Visibility Calculations for Lunar Features

This section describes the procedures used to calculate the visibility of lunar surface features. The definition of visibility terms and the basic data and relationships used to determine visibility are given in 3.2.1. Geometrical models of lunar features used to calculate feature contrasts are presented in 3.2.2.

3.2.1 Visibility Models

The visibility of any object is a function of its angular size (solid angle subtended by the object at the observer's eye) and its luminance contrast. Contrast is a basic parameter in studies of visual performance and is defined as:*

$$C = \frac{L_T - L_B}{L_B} = \frac{L_T}{L_B} - 1.0$$

where -

L_T = target luminance

L_B = background luminance

Visibility data are obtained, for instance, by exposing a target of fixed angular size to a subject for a pre-determined time and asking the subject to indicate whether he saw it. Target contrast is varied by the experimenter over a range from undetectable to detectable for a large number of such exposures and the results are expressed as a function of the percentage of correct responses obtained at each contrast level as illustrated in Figure 3-7. The contrast associated with a particular percentage value (usually 50%) is called the contrast threshold (C_T).

If such data are collected for a range of target angular sizes a function relating C_T to target size is obtained as illustrated in Figure 3-8. This type of function is the basic relationship used for visibility predictions to divide the contrast-size space into regions of "visible" and "not-visible."

*Two other common contrast measures are contrast ratio $C_R = L_T / L_B$, and modulation ratio, $C_M = L_T - L_B / L_T + L_B$.

Many factors other than size and contrast affect target visibility. Some of these factors relate to input variables such as target shape, extent of contrast homogeneity of the target and of the background, wavelength of light used, overall light level to which the eye is adapted, and exposure time. Other factors relate to subject effects such as training, knowledge of the locations and/or times at which the signal will occur, state of alertness and attention, and decision criteria (how obvious the signal must be before he or she says yes).

Constraints placed on the observer's response mode also will affect the experimental outcome. For instance, if the observer is allowed to give a "yes or no" response, he or she will establish a perceived signal level criterion which must be exceeded on any given trial before responding "yes." If he or she is forced to choose between two alternatives (e.g., signal appearing in one of two possible locations), he or she must then make a "forced choice" and, because what seems to the observer as "random guesses" are in fact correct at a higher than chance level, he or she will be correct more often than when responding in a typical "yes-no" situation, resulting in a lower apparent threshold.* Finally, if a reward-cost schedule is applied to the observer's responses (rewarding "hits," punishing "false alarms," for instance), the observer will modify his or her response probabilities accordingly.

The point of the above discussion is to emphasize problems encountered in the interpretation of visibility data. The particular set of threshold data used for predictions must be applicable to the actual situation. For example, in the case of landmark recognition, the crew has been thoroughly trained with photographs and simulator runs on recognition of a limited number of possible targets and, therefore, one would expect them to make correct judgements with less information required than if they were asked to detect targets in an entirely new situation. Data obtained, for instance, under conditions of unknown target location might not be applicable to landmark recognition, but would apply to obstacle detection, as the locations

* The concepts embodied in statistical decision theory which separate system sensitivity from decision criterion have been applied to analyze this situation in human performance (Reference 13).

of small features are not known pre-flight, whereas the shapes and locations of major landmarks are known.*

In practice, visibility estimations are typically based on well controlled laboratory data obtained with relatively simple input configurations (e.g., uniform circular targets). Corrections or transformations of these data to field conditions are then made using results of other experiments comparing field and laboratory situations or data from experiments investigating such factors as knowledge of target position, training, payoffs, etc. Exceptions to this procedure would be the case where the visual appearance of the target can be realistically simulated with modelling and/or photographic techniques and visibility data can be obtained directly in experiments using such simulations of the real scene.**

Several choices of laboratory data sets are available for use in visibility predictions. The most well-known set were obtained by Blackwell at the Tiffany Foundation (Reference 16) in 1944 - 46. Experimental conditions included both "yes-no" and "forced-choice" methods, circular uniformly illuminated targets (0.6 to 360 arc min. diameter range), and a background luminance range from 0 to 1000 ft.-L. Over 300,000 observations were obtained. Typical results given as plots of threshold contrast versus angular size for several background luminances are given in Figure 3-9. Although these data still represent the most extensive series of measurements available, another set of measurements by Taylor (Reference 17) was used for the present work. The Blackwell data were obtained with target exposure times of six seconds (forced-choice) and 13 seconds (yes-no), thus introducing the possibility of a visual search factor into the results. Although additional work by Blackwell and others (Reference 18) examined the influence of exposure time, it was felt best to use Taylor's data, which were for a short exposure time, and then to modify them in order to account for additional search time, if desired.

* That a situation assumed to be well learned can be altered into a "new" one, was illustrated on the Apollo 15 mission, where false information as to position of the ground-track prior to high-gate led to inappropriate guidance actions on the part of the CDR, which in turn led to a discrepancy between the actual and expected visual scene. This disparity, coupled with a lower distinctiveness of landmark patterns than expected, resulted in an inability to positively recognize some terrain features during descent (Reference 14).

**A more complete discussion of visibility procedures can be found in Ref. 15.

The Taylor data were obtained for a 0.33 sec. exposure time and a forced-choice situation. This duration was chosen because the average eye fixation time for visual search is about 1/3 second; thus, it was assumed by Taylor that a target exposure time of 1/3 second when the eye is more-or-less continuously fixated at the target point is equivalent (in terms of contrast threshold) to the free search case where the target is continuously present and the eye fixates on it for 1/3 second. Although this assumption is unproven experimentally, these data seemed a better base than did the Blackwell data for analysis of the lunar problem.

Two transformations were applied to the Taylor data to relate them to the lunar landing case. These transform the 50% contrast threshold level reported by Taylor to a 99% level (near certainty of detection) and the forced-choice response to the higher threshold expected for a yes-no response (more applicable to an operational situation). Each transformation multiplies the threshold contrast by a factor of two, giving a total factor of four.* That is, the threshold contrast value, C_T' , used for the visibility calculations is related to the original 50% probability, forced choice data, C_T , by:

$$C_T' = 4 C_T$$

Curves of C_T and C_T' versus angular size are given in Figure 3-10, which also shows the equation that was curve-fitted to the C_T' - angular subtense relationship for computer use. The use of the C_T' - angular size curve in connection with models of lunar feature contrast is discussed in the next section.

3.2.2 Contrast Models

An important consequence of the slope dependence of the lunar photometric function is that it can be used to compute contrasts of lunar features. Given a geometrical model or an actual topographical description, a surface feature can be divided into a matrix of small areas, the

* For a discussion of these "field factors," see References 15 and 19.

luminance of each area computed from its slope for given values of VEA and SEA from the photometric function and, finally, an average contrast is computed for the feature as a whole by summing and averaging the contrasts of each small area.

Several computer programs of this type were developed using various geometrical models of craters and protuberances. An early study of conical and spherically shaped protuberances using several simplifying assumptions concerning the photometric function was provided by Cole (Reference 20). Hughes Aircraft Company extended their protuberance and crater models developed for Surveyor landing analyses to visibility studies.* Their models (Reference 21) consisted of eight-sided craters and protuberances (eight plane triangles approximating a spherical section). A program developed at NASA/MSC using a spherical section crater was modified by TRW and has been used extensively in contrast predictions (References 22 and 23). Additional work on this problem has been conducted by others, including a Bellcomm (now Bell Labs) program (Reference 24) which accepts lunar topographic data as input and can, therefore, compute contrast data for specific lunar features, whereas all of the other programs mentioned only consider simple geometrical forms. A recent TRW program was developed which uses a truncated cone model, in which separate albedos can be input for the wall and floor, a convenient model for simulating relatively flat-bottomed craters, especially in the case where a crater wall is of higher albedo than its floor (Reference 25).

All of these models, however, follow a similar logic: given a specified feature geometry, the luminances of a matrix of points covering the feature are determined, and these luminances are then averaged to determine a contrast value with respect to a background of some arbitrary slope (usually assumed to be horizontal). Various luminance averaging

*This study by HAC also reports on the only laboratory experimental visibility tests conducted to examine lunar feature visibility. Copper oxide dust was used to simulate lunar soil reflectance properties. However, the maximum SEA used was 15° , so that comparison with the results of the Apollo test (where the SEA ranged from 20° to 30° for most targets) could not be made.

techniques have been employed. In addition, the visible shadow region (if any) produced by the feature is calculated. The areas of the shadowed region and the non-shadowed region are then calculated in terms of the solid angle subtended at the observer's position. Finally, the calculated angular sizes and contrasts are compared to the visibility criteria discussed above to determine if the feature is visible for the given viewing and illumination conditions. Some questions and problems in the use of this technique are considered.

Lunar features, including the spherical and conical geometrical models, are not of uniform contrast, whereas nearly all of the available experimental work have used uniform targets viewed against uniform backgrounds (as did, for example, both Blackwell and Taylor). Very few data are available which are based on non-uniform targets and backgrounds and which can be used to quantify such effects. An illustration of the luminance pattern in a typical lunar crater will clarify this point. Figure 3-11 illustrates the luminance patterns observed in a crater seen under fairly low SEA conditions. Note the three distinct areas: 1) the geometric shadow (GS) is that area blocked from the sun which does not receive any illumination; 2) the bright side (BS) is that area where the average luminance is greater than that of the average background, and 3) the dark side (DS) is that area darker than the average background. The BS and DS are photometric function effects, that is the slopes of these areas are such as to make them brighter or darker than the background.* As the viewing and illumination conditions change, of course, the relative proportion of each of these regions changes.

Within the BS and DS areas, a range of luminances may be encountered from nearly equal to the background to less or greater than the background. Further, the frequency distribution of luminances will change as viewing/illumination conditions change. Thus, two problems are posed for the prediction of lunar feature visibility:

*The dark side has also been termed the photometric shadow, as its darkness is due to photometric effects rather than to blockage of illumination.

- 1) Should a weighting function be applied when averaging luminances for given area (for instance, should a point of high luminance be weighted more than a point just slightly higher than the background luminance)?
- 2) How should one compute visibility estimates for a target involving bright/dark contiguous areas (i.e., dark shadow next to a bright region)?

As stated, very few data relevant to these topics were available at the time this work was originally formulated. One experiment dealing with contiguous light/dark areas did indicate that such areas could be treated independently* (Reference 26). Although some data did exist pertaining to contrast weighting over a non-uniform target, it was not deemed sufficient to allow a choice of a weighting function (Reference 27).** Therefore, a simple luminance average was used, but the BS, DS, and GS areas were treated as individual targets.

If the GS were a true shadow ($L_T = 0$), it would have a contrast of -1.0:

$$C_S = \frac{L_T - L_B}{L_B} = \frac{-L_B}{L_B} = -1.0$$

However, illuminated lunar regions in the vicinity of the shadow scatter light into the shadowed region. An estimate was made of the shadow luminance based on Apollo 8 observations (Reference 28), and this value was used to estimate shadow contrast, which was found to be $C_S = -0.96$. In practice, this is a negligible distinction, as this value is very high compared to typical BS and DS values (which are on the order of 0.1, or less) and, therefore, shadows tend to dominate visibility, if they exist at all.

* For independent treatment to be valid, however, the angle subtended by each region must be large enough to allow that region to be independently resolved by the eye. Otherwise, the bright and dark regions must be averaged (i.e., a black and white checkerboard will be seen as a grey square if the individual cells cannot be resolved).

** See, however, the HAC study (Reference 21) in which a weighting function was used.

A final problem to be discussed here concerns target shape and angular size. As mentioned, the size variable related to visibility is the solid angle subtended by the target.* Within an aspect ratio range of 1:1 to 1:7 it has been found that shape is a relatively unimportant variable; that is, a square $1^{\circ} \times 1^{\circ}$ will have about the same contrast threshold as a $0.1^{\circ} \times 10^{\circ}$ rectangle. As the aspect ratios of most lunar features fall below the 1:7 criterion (an exception might be the case of a long, thin shadow arc) shape was ignored. As noted in Section 3.2.1, the visibility data used for this study are expressed in terms of the angular subtense of the diameter of a circular target, rather than the solid angle itself. The fact that threshold contrast is relatively independent of shape and depends only on the subtended angle, allows one to compute an equivalent circular area for an irregularly shaped target and then to compare the angular subtense of the equivalent circular area with the visibility curves. That is, the area of the target is computed (taking the viewing geometry into account) and then the diameter of a circle of equal area to the target is found, and the angular subtense of this diameter is compared to the visibility threshold curves.

The above description applies to the logic used in developing the crater visibility program employed by TRW. The crater geometries available are either a spherical section or a truncated cone (rims are not considered); any combination of albedo, VEA and SEA can be employed and that the output consists of separate visibility data for each crater region (BS, DS, GS) as well as for an overall average of all BS and DS points. A typical input and output is shown in Figures 3-12 and 3-13. Inputs include the SEA, VEA, SRA, observer altitude, crater diameter-to-depth ratio, crater albedo and background albedo. Crater wall slope, wall albedo and floor albedo must also be input for the conical crater model. Outputs consist of the viewing/illumination geometry inputs for documentation, the value of $\phi(\alpha, g)$ for the horizontal background, background luminance, and the crater visibility data. The latter include the proportions of total viewed area occupied by each GS, DS, and BS sub-area, the contrast calculated for each sub-area, and the

*Some investigators have held that perimeter is a more useful variable than is total area, i.e., visibility is dependent on an edge detection process. See Reference 29.

diameter of the smallest detectible crater which results in that sub-area being visible for the given altitude. In addition, cross-range and down-range distances from the observer's nadir to the viewed point are provided; if a target diameter is input, then the program also calculates the angular subtended areas for the given crater size. The use of this program for visibility predictions is discussed in the next section.

3.3 Visibility Predictions

Typical predictions generated by the crater visibility model are presented in this section. Such predictions have been made for many viewing situations including surface and orbital as well as for the descent case. Only a few examples are presented here to indicate the general form of the results and their interpretation.

Figure 3-14 gives visibility predictions for a landing case for a 5,000 foot altitude and a 25° SEA. The LRM was used for these calculations. Shown in the figure are the LM nadir, a scale of range in feet from the landing point, a sun-relative azimuth scale and contours of minimum visible crater diameters. The albedo input to the program was set equal to that of the background (that is, luminance differences between the crater and background are due entirely to geometric shadow or photometric/slope effects). All data are for spherical section craters of an 8:1 diameter:depth ratio.* Note the shaded region, in which the equal albedo craters assumed for the calculations are predicted as not visible, regardless of their diameter.** This region corresponds to the negative alpha, low phase angle area mentioned in Section 3.1.1 and is the analytical description of the washout region depicted in Figures 2-5 and 2-9. Not only will equal albedo craters be difficult or impossible to see in this area, but so will any other feature whose albedo is low or equal to that of its background. Thus, the crater visibility model provides a means of separating good and poor visibility regions. Note also that the landing point (which is seen at a 23° view elevation angle) is within the washout region and that the washout boundary is at a SRA of about 40° .

* Steeper craters will in general be of higher detectibility, shallower craters will be of lower detectibility.

** "Equal albedo craters" is used to refer to the case where the soil covering the crater and its background area have the same albedo.

The effect of an albedo difference between a crater and its background is also shown in Figure 3-14. The numerals in the shaded washout area indicate minimum visible diameters for craters whose albedos are 10% greater than that of the background. As will be shown later, even a few percent albedo difference tends to make a crater easily visible in the washout. Such conclusions have been borne out by observational experience, in that higher albedo features stand out clearly in the washout region, the more so as this area takes on a rather flattened, homogeneous appearance and any bright objects tend to be especially conspicuous.

For comparison, the results of similar calculation for a 10° SEA descent case are shown in Figure 3-15. The greatly improved visibility situation is obvious.

The use of washout boundary plots for examining the effect of SRA, is illustrated in Figure 3-16, using points taken from Figure 3-14. This figure shows the consequences of different approach azimuths on the locations of the washout with respect to a typical landing dispersion ellipse for a 25° SEA. The sun azimuth is assumed to be 90° , and washout boundaries for approach azimuths from 90° to 70° are illustrated. As the approach azimuth moves to the north, so does the washout (the washout is symmetrical with the sun-line, which is east-west in this example). A sufficiently large SRA will move the washout away from the site area.

A more pictorial example than the above which shows results of visibility predictions superimposed on a lunar scene, is given in Figure 3-17. This is an orbital view exhibiting zero phase in the large crater Ptolemaeus, which has a mare-like floor with similar reflectance properties to many of the Apollo landing sites. Two types of calculated visibility data are superimposed on this photograph. The first are washout boundaries for steep (6:1 diameter:depth) and shallow (12:1 diameter:depth) craters computed for the viewing/illumination conditions of this frame. As can be seen, a fairly wide area is covered between the two boundaries, this included area corresponds fairly well to the transition region between the shadowed, good visibility area and the shadowless, poor visibility area as determined from the photograph itself. The zero phase point is distinctly visible, as are regions of high albedo down-range of the washout boundary.

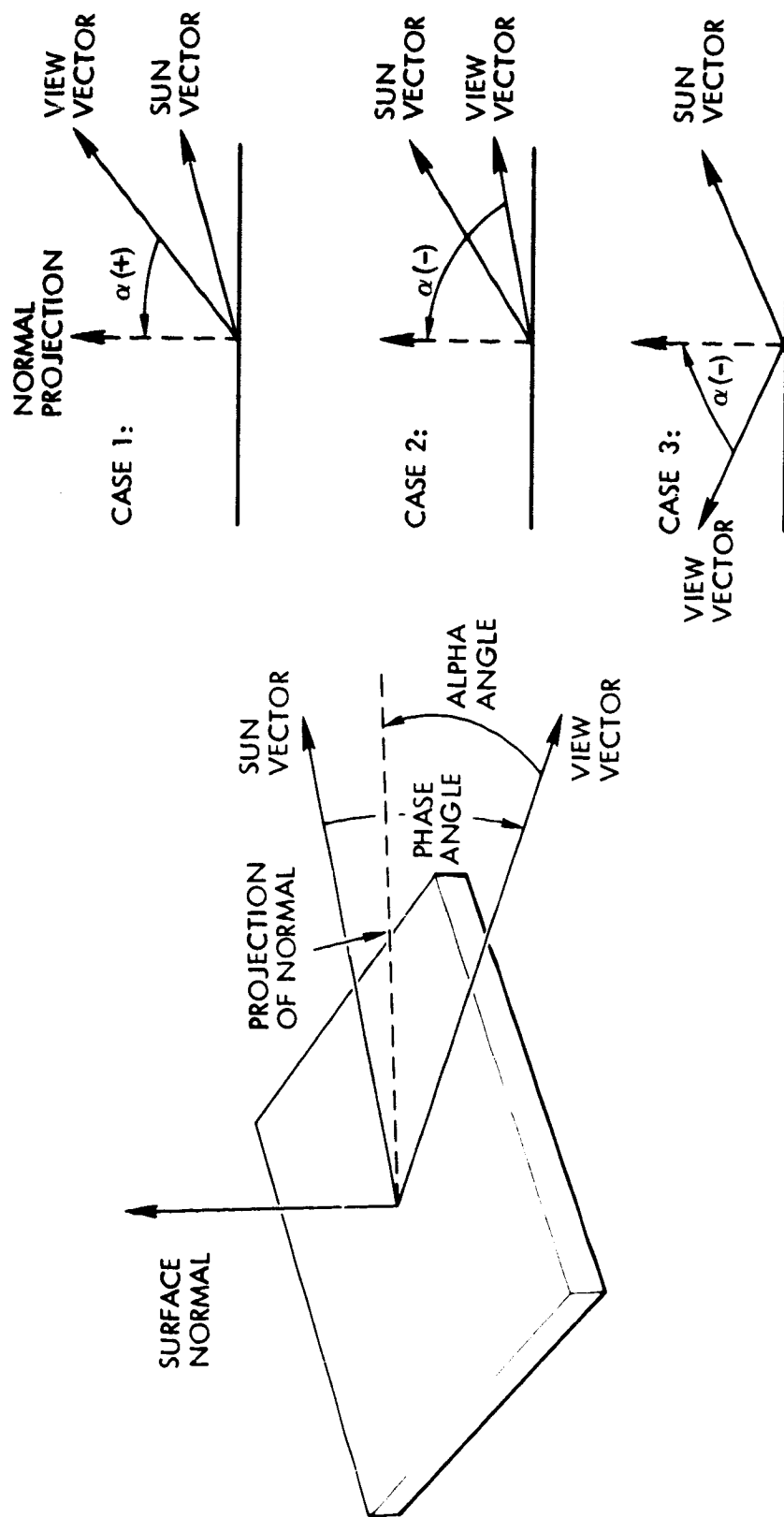
The second type of data included on the overlay relate to areas showing equivalent visibility to that predicted for various surface points viewed during descent on the Apollo 15 mission. The predictions are shown for an SEA of 23° and an SRA at the target point of 12.7° . The frame in Figure 3-17 was used to simulate surface appearance for selected points at the Apollo 15 site by first computing crater contrasts at these points as they would be viewed during descent, and then by finding those points in the photograph which have corresponding contrasts. If this is done for several altitudes, a locus of points on the photograph is determined which simulate the visibility situation at the corresponding point during descent. Such a match cannot be done exactly, of course, and its validity also depends on a general similarity between the terrain at the site and in the photograph, but it does provide a useful pictorial illustration of the results of visibility predictions. Two such loci are shown: 1) points in the photograph corresponding to visibility at the landing point (straight line marked landing point); and, 2) points in the photograph corresponding to visibility at a point north of the ground track (curved line marked point 1). The landing point line is at a constant SRA of 12.7° (as the landing point lies on the ground track, its SRA remains constant during descent). It is obvious from the figure that the zero phase region itself is not a critical factor due to the large SRA at the landing point; however, visibility at the landing point can be seen to change from a situation in which shadows are generally present at 5,727 feet altitude to a moderately "washed out" condition at lower altitudes (3,121 feet to 1,034 feet) with marked improvement below 1,000 feet (503 feet). This variation is due to the variation in the VEA during descent.

The visibility situation at Point 1 is much worse than at the landing point, as can be seen from the second line, which indicates this surface region is close to zero phase for part of the descent and remains in the washout region for altitudes below about 4,000 feet.

In analyzing the visibility situation at a given site the particulars of that site and mission are also considered (as discussed above in Section 2.7) as well as are the results of the type of analysis described in this section. However, the material presented here should provide a general picture of some of the uses of the analytical visibility models.

3.4 Limitations of Analytical Approach

The analytical approaches presented above depend on simplifying assumptions concerning terrain models, photometric functions and visual performance. The visibility tests described in the following section were designed to obtain data in the lunar environment which could be used to validate and extend the mathematical models.



3-1a. ALPHA ANGLE DEFINITION

3-1b. ALPHA SIGN CONVENTION

Figure 3-1. Alpha Angle Definition and Sign Convention. Note that if the Normal, Sun and View Vectors are Nearly Coplanar than Cases 1 and 2 in Figure 3-1b Correspond to Potential LM Landing Situations, i.e., Sun Behind the Observer.

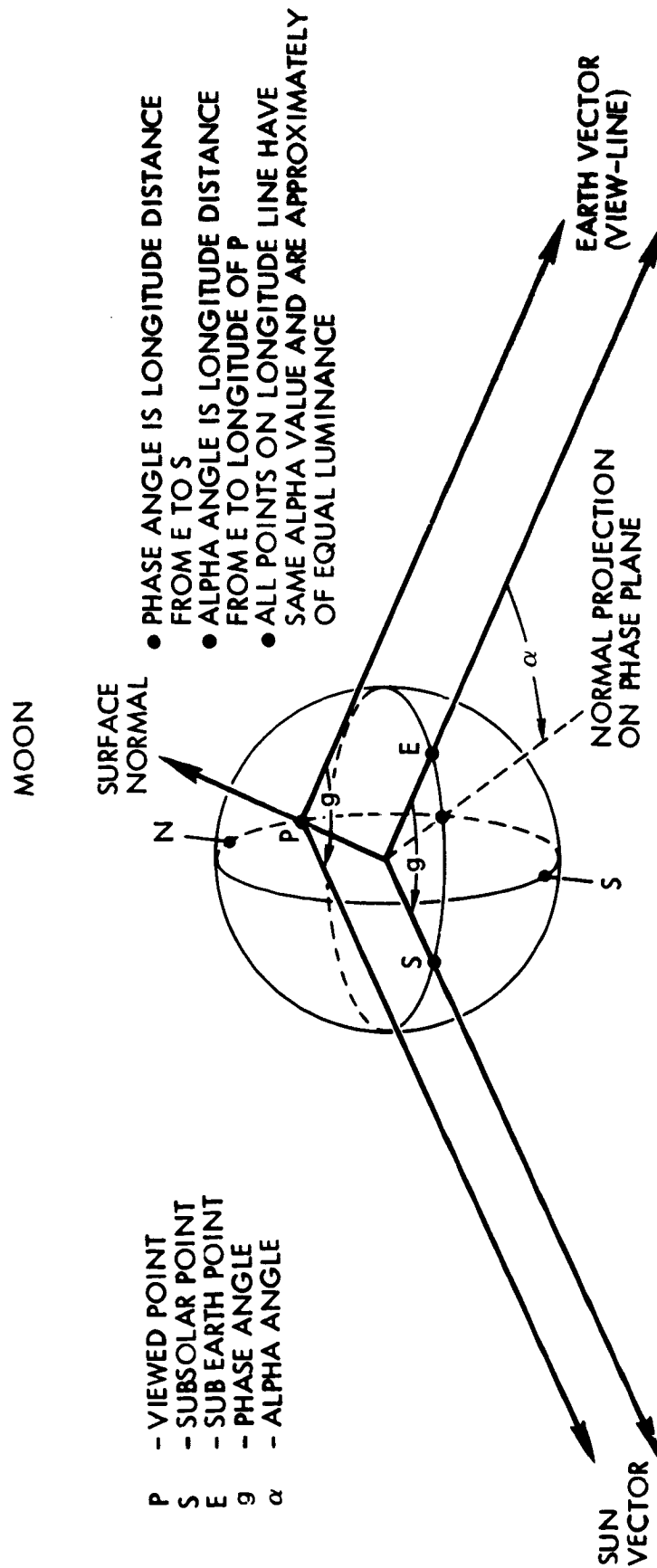


Figure 3-2. Alpha Angle Definition in Astronomical Framework

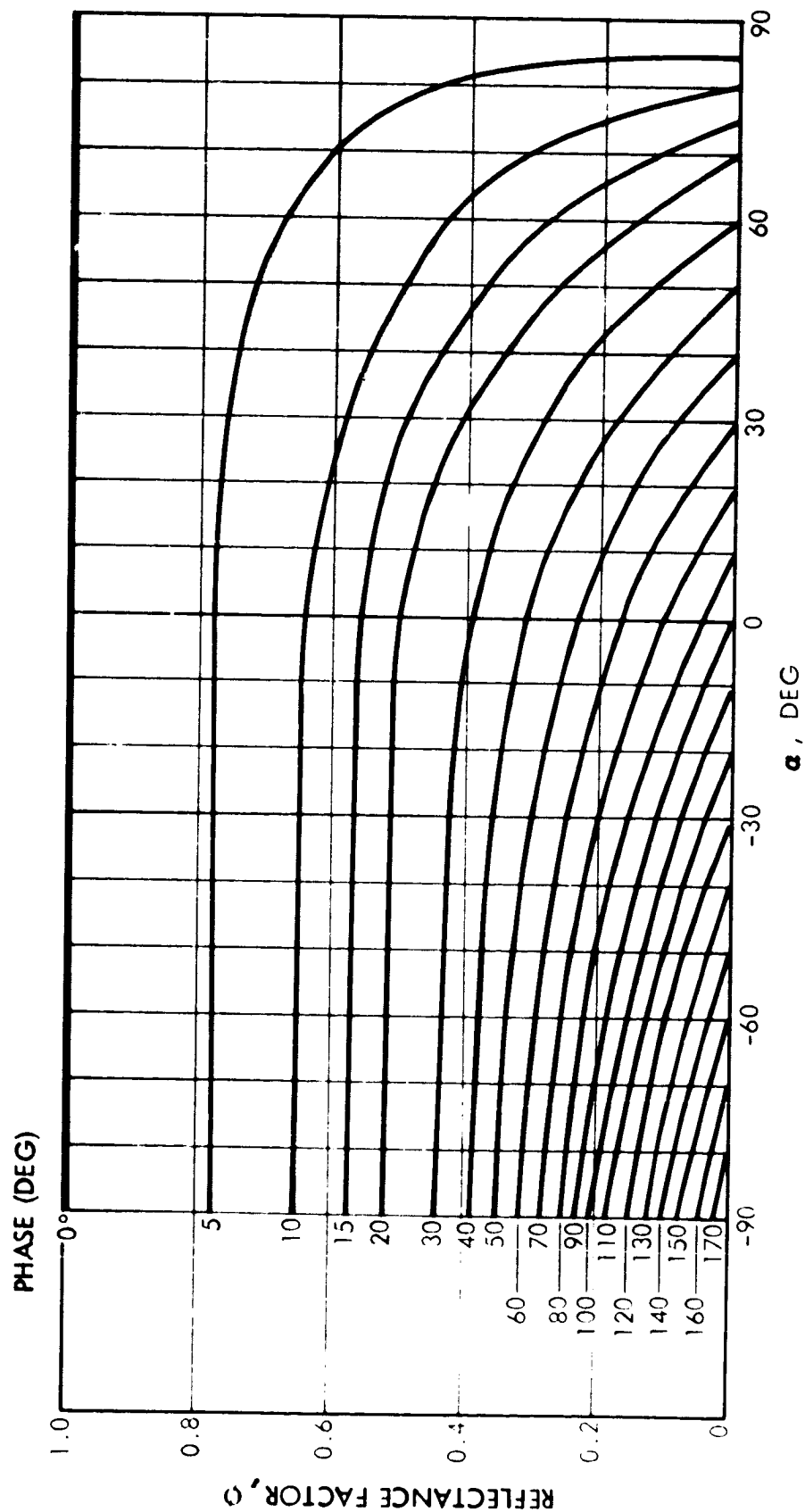


Figure 3-3. Lunar Reflectivity Model Developed by JPL Based on Data of Sytinskaya and Sharanov

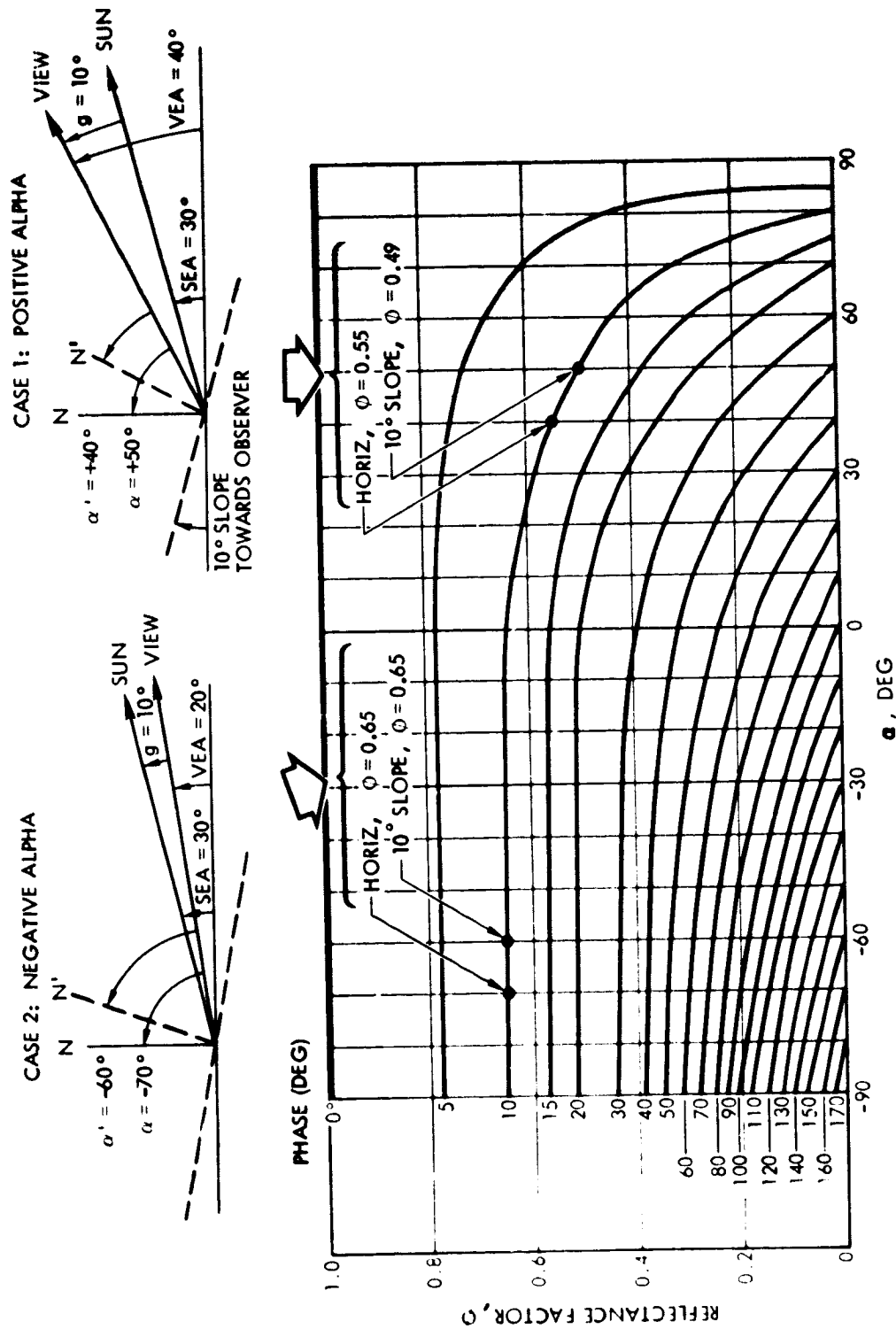


Figure 3-4. Effect of Slope Variation on Value of Reflectance Factor for Negative and Positive Alpha Values

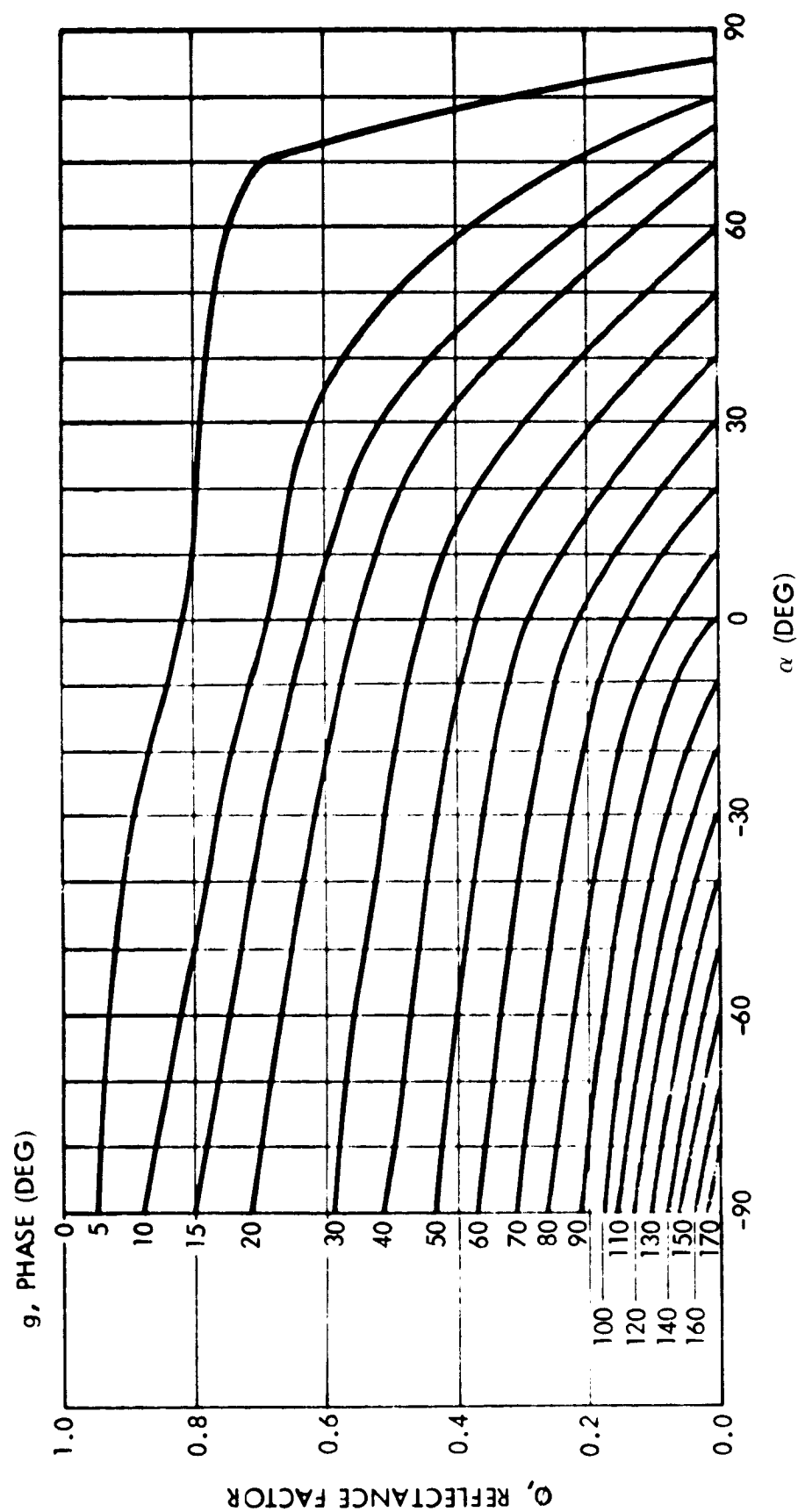


Figure 3-5. Fedoritz Function Developed by JPL

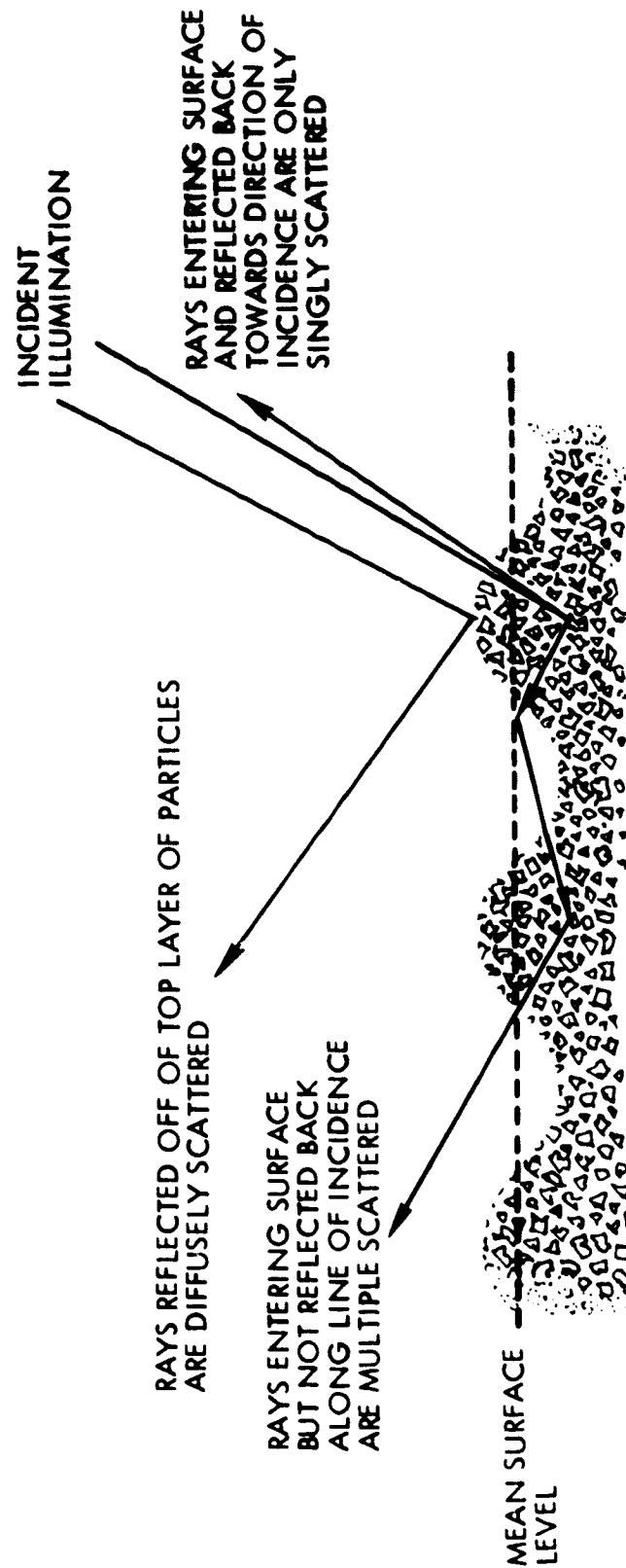


Figure 3-6. Lunar Surface Soil Structure and Light Scattering

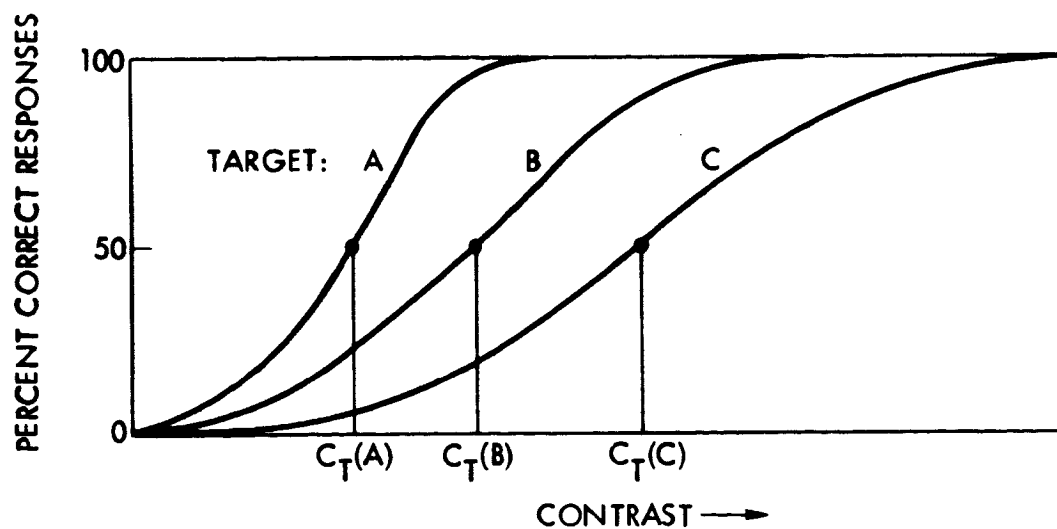


Figure 3-7. Typical Detection Results for Repeated Presentation of Visual Signals of Different Contrasts for Three Target Angular Sizes, $A > B > C$. $C_T(i)$ Indicates Threshold Contrast Taken as the 50% Correct Point for Each Angular Size.

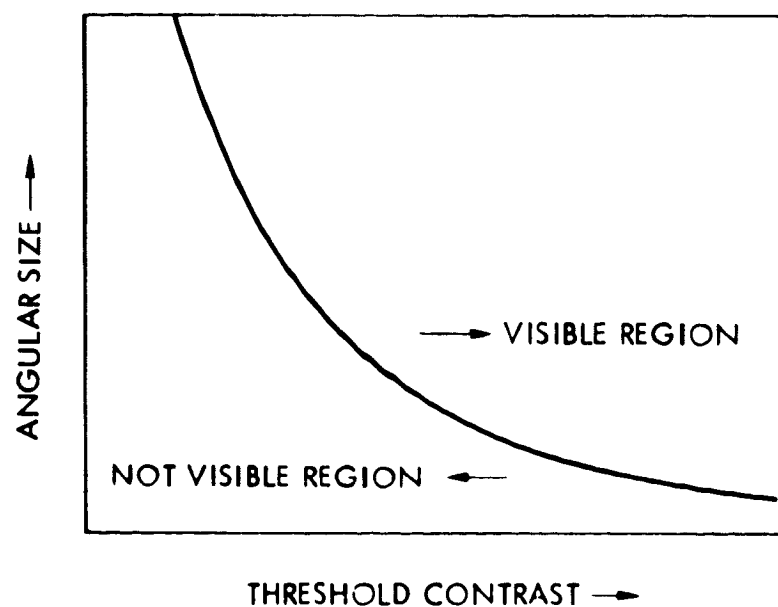


Figure 3-8. Illustration of Subtended Angle Versus Threshold Contrast Function

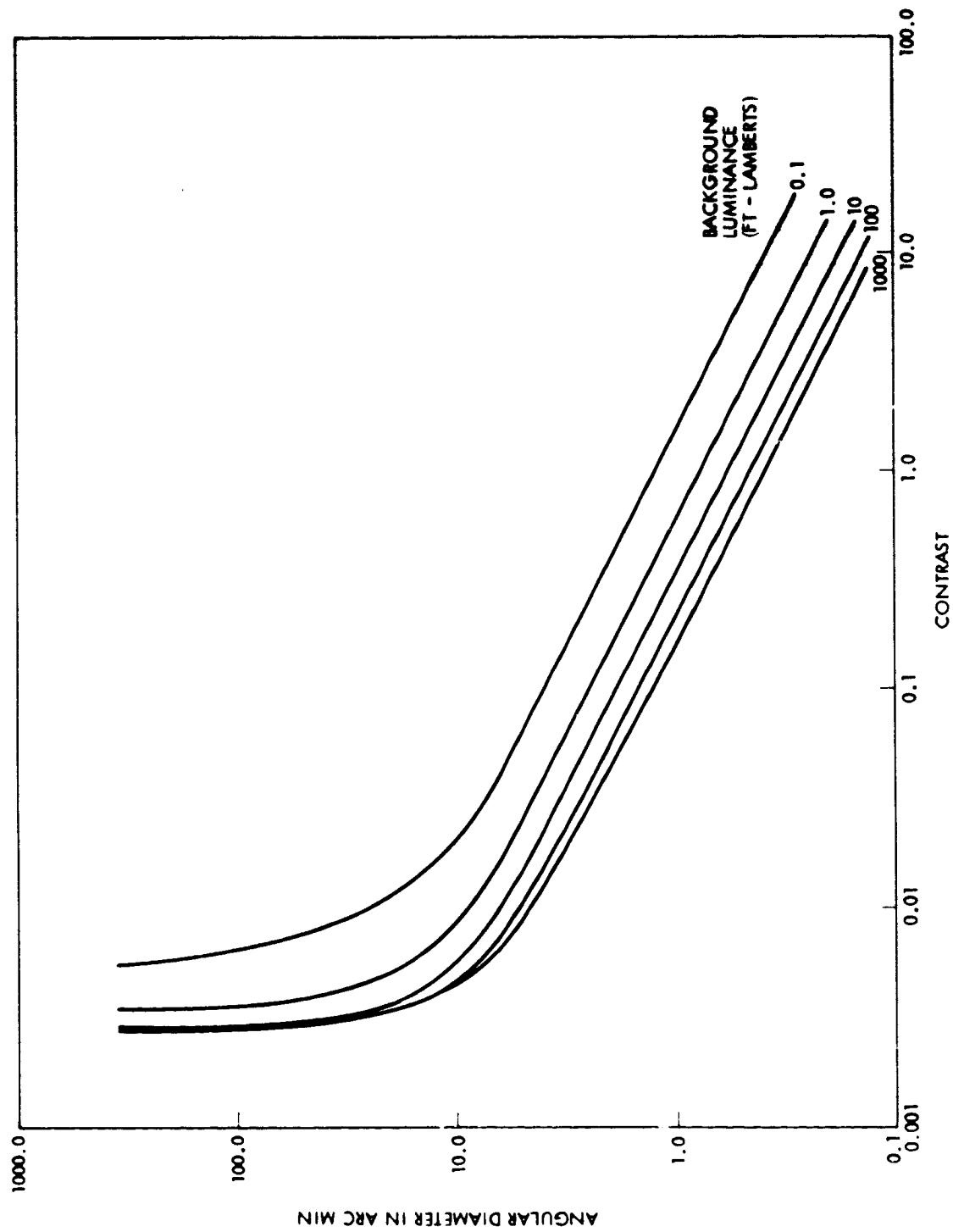


Figure 3-9. Threshold Contrast versus Angular Diameter Data from Blackwell (Reference 16) Probability of Detection = 50%

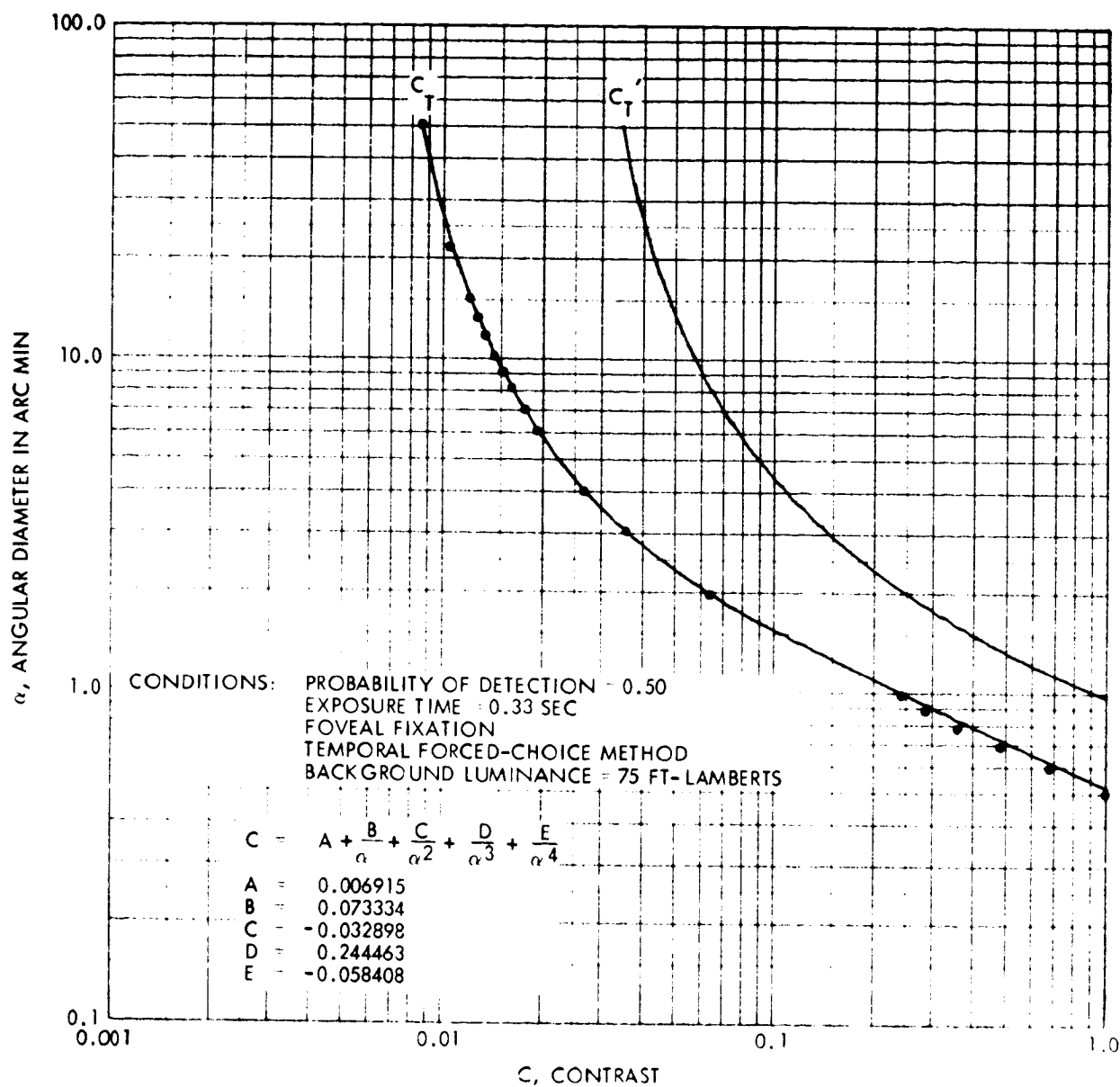


Figure 3-10. Threshold Contrast Versus Angular Diameter Data from Taylor (Reference 17). The C_T Curve is Taylor's Data for 50% Probability of Detection, the C_T' Curve Includes Transformation for Forced-Choice to Yes-No and 50% to 99% Detection Probability. Points are Taylor's Data, Curves are Least Squares Fit From the Equation Given Above.

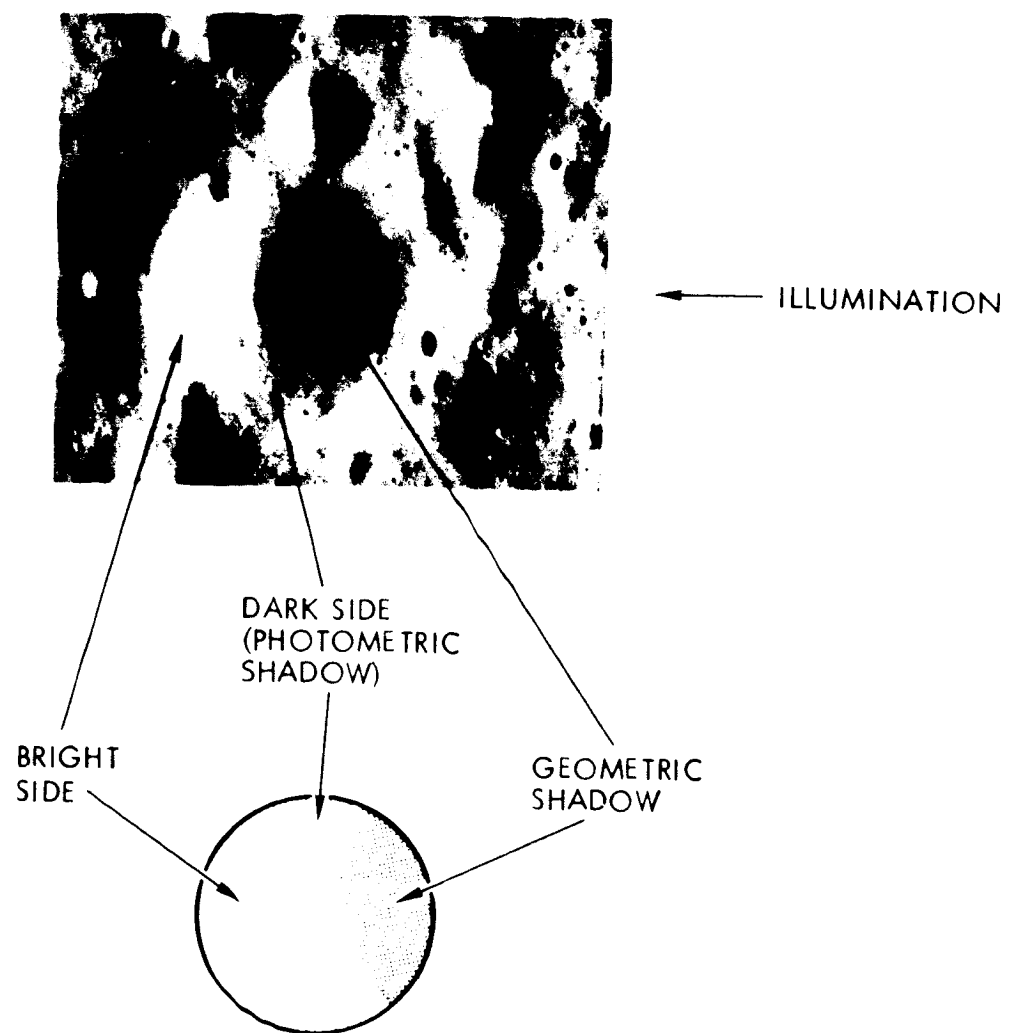


Figure 3-11. Photograph of Lunar Crater Illustrating Geometric Shadow, Dark Side (Photometric Shadow), and Bright Side Regions

```

1
  SCRATER
? NS=1
? SELV=30.98 _____ SUN ELEVATION ANGLE
? DIAM=6.1 _____ DIAMETER TO DEPTH RATIO
? DIA=11074 _____ DIAMETER IN FEET
? VELV=33.01 _____ VIEW ELEVATION ANGLE
? RAZI=4.76 _____ SUN RELATIVE AZIMUTH ANGLE
? ALT=349703 _____ ALTITUDE IN FEET
? ALBC=.1047 _____ CRATER ALBEDO
? ALBB=.10 _____ BACKGROUND ALBEDO
? OPTI0N=1 _____ PRINTS SUBTENDED ANGLES
? S

```

Figure 3-12. Input Example for Crater Contrast Program.

```

PH= 4.518 ALPH= 33.454 REF= .780
SEL=30.98 VEL=33.01 AZ= 4.76 DTD= 6.1 BLM= 970

ALB=.105 AGS= .0020 APS= .1613 ABS= .8367 APB= .9980
CGS= -.9581 CPS= -.0625 CBS= .0550 CPB= .0360
DGS= 5231 DPS= 4948 DBS= 2750 DPB= 8267

SGS= 2.09 SPS= 18.71 SBS= 42.62 SPB= 46.55

ALT= 349703 CRS= 39540 DWN= 475404

```

PH,ALPH,REF,BLM = phase angle, alpha angle, reflectance value, and luminance of horizontal surface at viewed point.

SEL,VEL,AZ,DTD,ALB = input data.

AGS,APS,ABS,APB = relative crater areas of geometric shadow, photometric shadow, bright side, and combined bright side and photometric shadow.

CGS,CPS,CBS,CPB = contrasts of relative crater areas as above.

DGS,DPS,DBS,DPB = minimum visible crater diameter required for visibility of each crater area as above.

SGS,SPS,SBS,SPB = equivalent subtended angle of each crater area for input diameter.

CRS,DWN = cross-range and down-range in feet of viewed point from observer nadir.

Figure 3-13. Output Example for Crater Contrast Program.

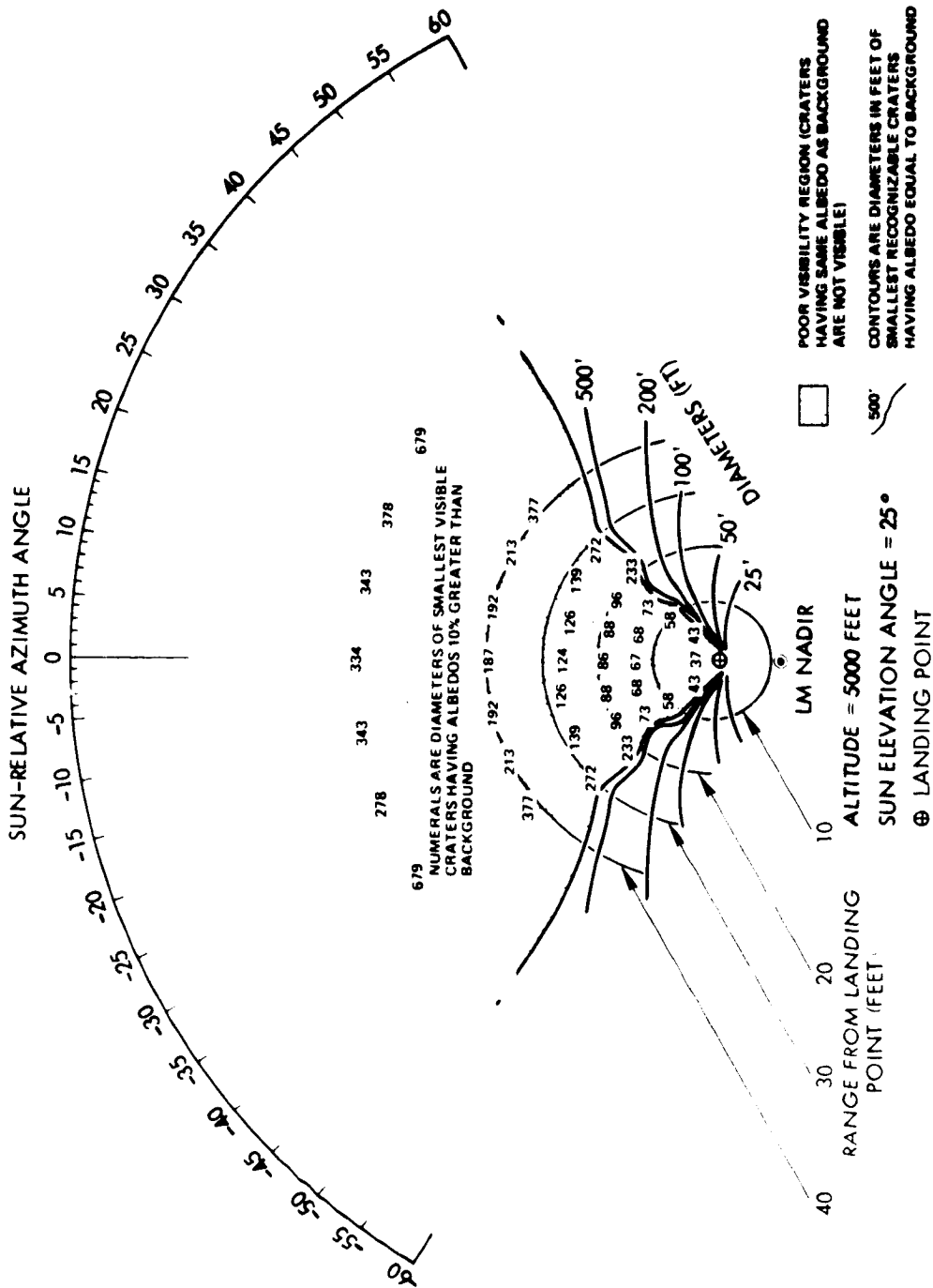


Figure 3-14. Typical Presentation of Visibility Predictions. Sun Elevation Angle = 25°. Observer should be visualized at a scaled height of 5,000 feet above the LM nadir point. Contour lines give smallest diameter craters (with an 8:1 diameter:depth ratio) that are visible as a function of range from the landing point. Dotted region corresponds to washout area.

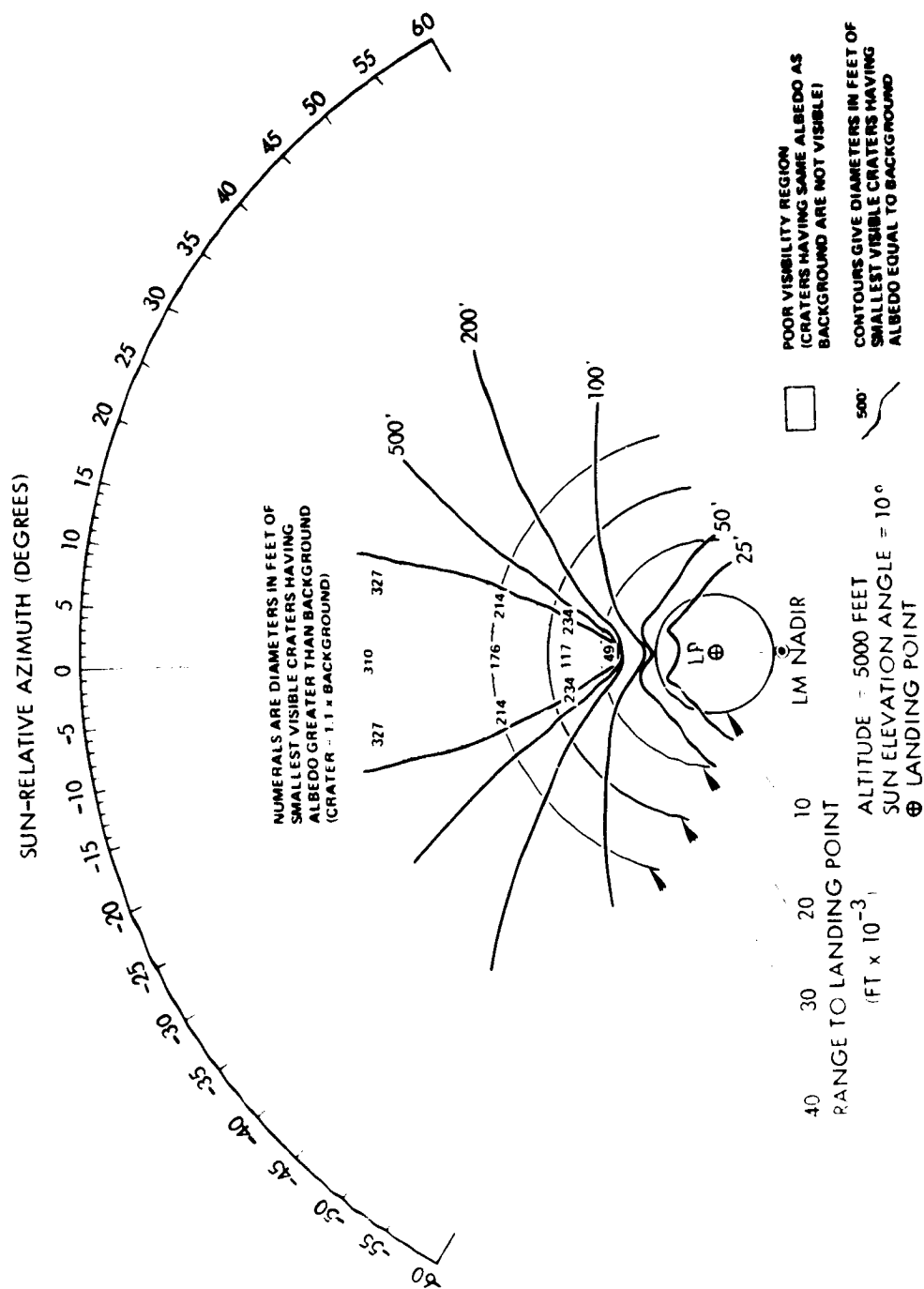


Figure 3-15. Typical Presentation of Visibility Predictions. Sun Elevation Angle = 10° . Observer should be visualized at a scaled height of 5,000 feet above the LM nadir point. Contour lines give smallest diameter craters (with an 8:1 diameter:depth ratio) that are visible as a function of range from the landing point. Dotted region corresponds to washout region.

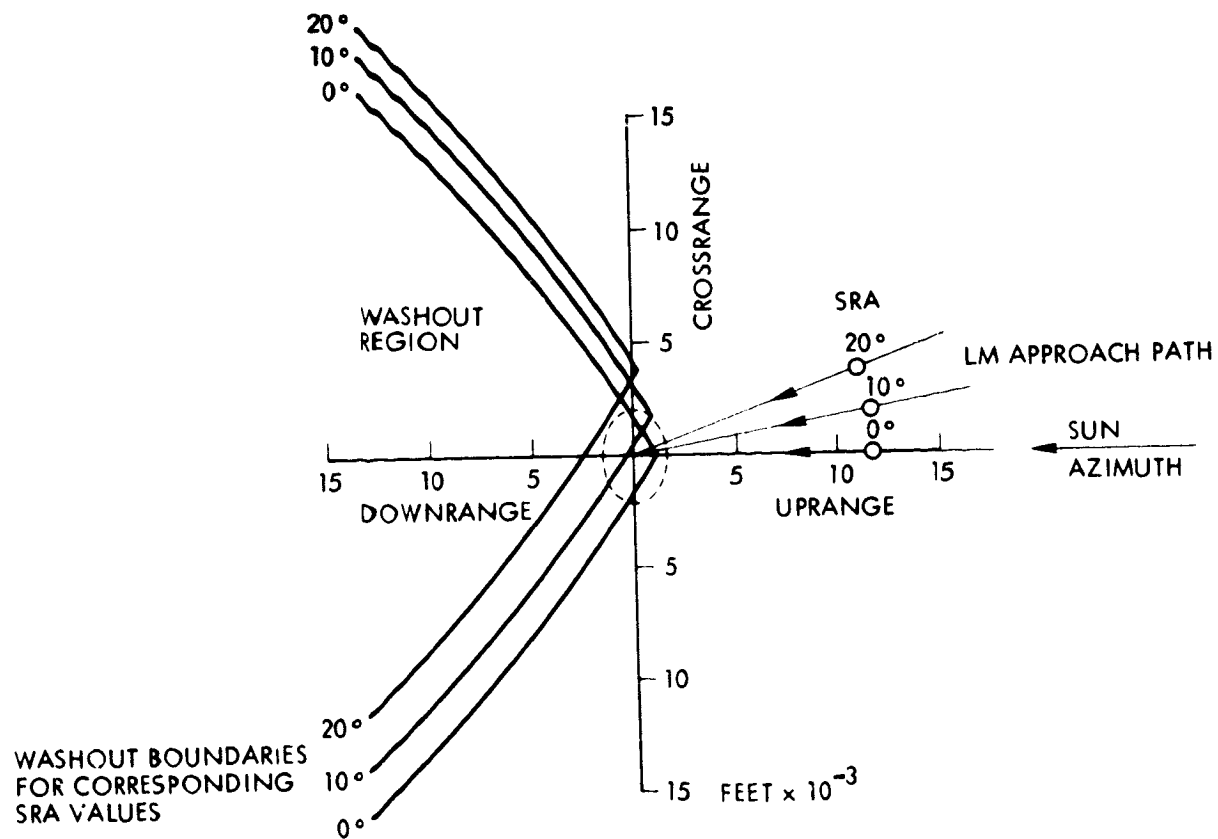


Figure 3-16. Effect of Approach Azimuth on Location of Washout Boundary with Respect to Landing Site (Ellipse). Data shown for a 5000 Foot Altitude, 25° SEA (O = LM Nadir)

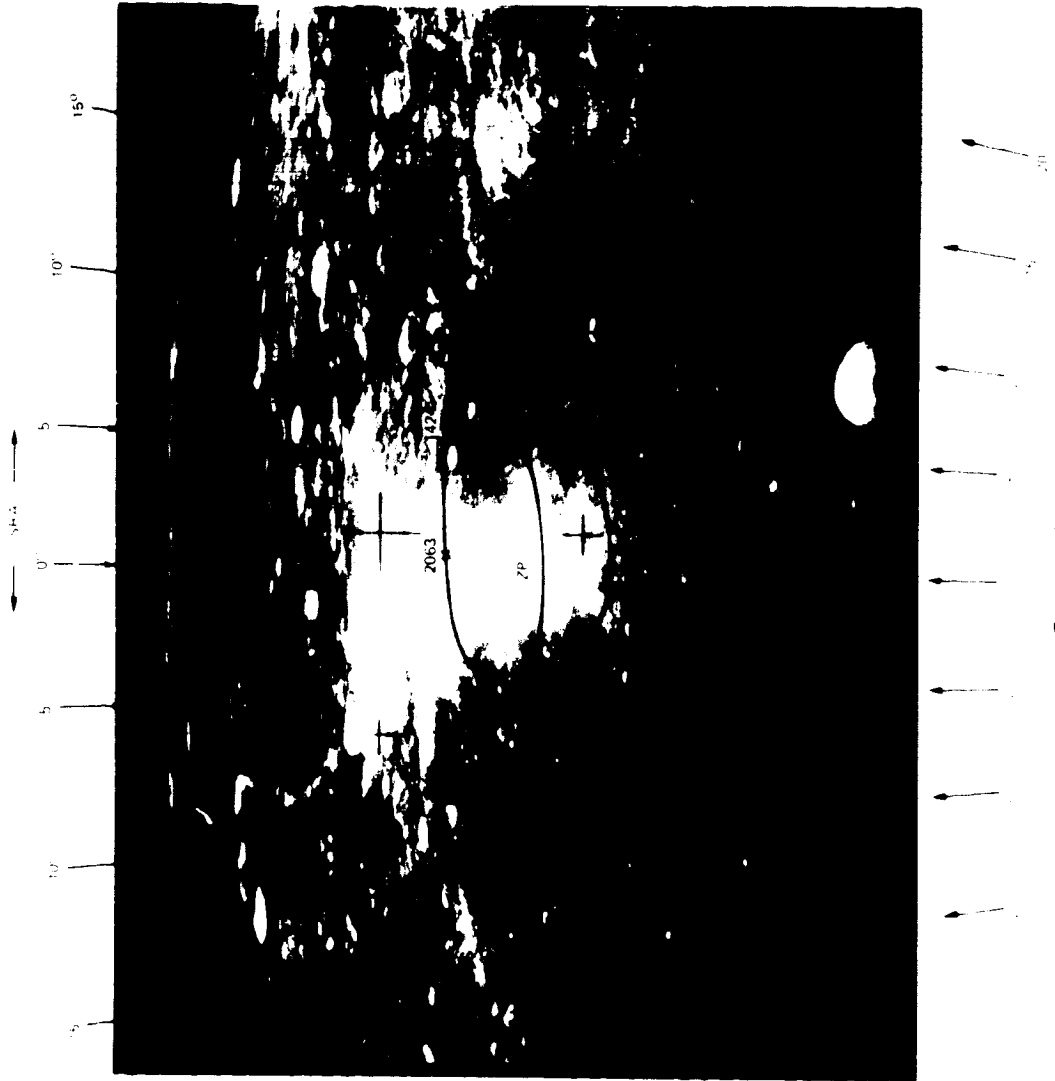


Figure 1-10. Simulation of Apollo 15 Site Appearance During Descent for a 23° Sun Elevation Angle. Points shown on the photograph (Apollo 14, Frame 10257) were calculated as representing equivalent crater contrasts to two surface points at the Apollo 15 site: (1) Landing point (straight line shown to the left of the frame), and (2) A point directly North of the landing point (curved line marked point 1). Numerals on each curve are altitudes in feet and indicate points of equivalent contrast at the corresponding altitudes. Wavelength of light is given for steep and shallow craters are calculated for the viewing conditions of the photograph. Zero phase point. SEA = Sun Relative Azimuth.

4.0 TEST PROCEDURES

4.1 Approach

Consideration of mission time-lines, observation time requirements and test flexibility led to the lunar orbital period as the only feasible mission phase for test conduct. As the crew is heavily occupied with pre-descent operations prior to descent and with scientific observations and trans-Earth insertion preparation after LM rendezvous, the observations were scheduled to be conducted by the CMP during the LM surface stay period.

In planning the visibility tests, it was assumed that the descent visibility situation was the most critical and that the observation conditions from orbit should be chosen to closely simulate the descent case. However, the results would also be applicable to surface operations, as the basic area of interest for either case is the washout region.

Simulation studies were conducted to determine the errors in simulating the descent viewing conditions by use of orbital observations. A complete time history of viewing conditions during descent to a given point in the site cannot be simulated with orbital measurements; however, segments of the descent viewing conditions can be matched approximately with segments of orbital viewing conditions. Furthermore, a point-by-point comparison is possible, in which an orbital viewing condition at a given time is found which is equivalent to a given descent viewing condition. On this basis, it was determined that useful data could be obtained from orbit.

As mentioned previously, a limitation in observational reports of visibility obtained from prior Apollo missions was the lack of "ground truth" information. Characteristics of detectable features, such as contrast and size, were unknown. Further, even if some features in a given region were detected, it was not known if others in the same area were not detected. In the design of the Apollo 14 visual tests, these problems were minimized by choosing targets prior to the mission and by photographic documentation during the observation periods. Target features were selected from available Apollo and Orbiter photography and included craters of various sizes, albedos, and in various terrain backgrounds. Thus, a range of

observational difficulty and terrain conditions were considered in addition to target size and shape.

Photographic coverage of the target features during the visual observations was provided by an intervalometer-operated camera. The film record provided a critical link in the analysis of results, as it is the only means whereby actual target contrasts and angular sizes can be measured. With this information, target visibility can be correlated with target data in order to test the analytical models. In addition, it is possible to compare actual target contrasts with those predicted from lunar photometric functions. Procedures were established by which it was possible to determine the actuation time of each frame, the CSM position in space, and the camera pointing direction.

Finally, the crew received extensive training with various visual aids to familiarize them with the targets and test procedures. Continuous verbal comments were requested during the observations so that target visibility could be placed on a time-line and later correlated with viewing conditions and photographic results. At the conclusion of each observation pass, a short debriefing was recorded which contained a rating of target visibility on a four point scale.

4.2 Selection of Target Areas and Observation Procedures

4.2.1 Orbital Pass Geometry

The viewing geometry for an orbital observation pass is shown in Figure 4-1. Two types of observation passes were included. As shown in Figure 4-1, a given sun elevation angle occurs on two portions of the ground track, one each on the frontside and the backside of each orbit. For a frontside pass as the S/C approaches the target, the zero phase point moves forward from near the S/C nadir to down-range of the target during the approach. The observer sees the target move from the horizon towards the S/C, disappearing at the lower edge of his window. During this time, the observer is looking forward in the direction of S/C motion. For a backside pass, he must look backwards from the direction of motion, and the target appears at the lower edge of his window and moves toward the horizon. In this case, the zero phase point moves from the horizon towards the S/C nadir.

Poor visibility occurs when the target is down-range of zero phase and in the washout region. This condition exists during the early portion of the frontside (forward-looking) pass and towards the late portion of the backside (backward-looking) pass. The frontside case is the more rigorous or revealing test, as the target must be acquired in poor visibility conditions with a consequent higher probability of tracking it through the poor visibility region.

4.2.2 Target Location and Zero Phase Track

The range of sun elevation angles of interest are those that would occur during descent for a launch 24 hours later than nominal: 18° to 25° . Thus, selection of ground targets for the orbital test was restricted to the narrow band of longitudes, on the frontside and backside respectively, which cover this sun elevation range (one degree in sun elevation angle was about one degree in longitude for the Apollo 14 orbit). A further restriction on target location arose from the position of the zero phase track on the lunar surface. Given an opportunity for a large number of observations, it would be advantageous to select targets at various displacements (sun relative azimuth) from zero phase. Because the number of observations was limited, target locations were selected which represented the worst case: zero phase passing over the target.* Furthermore, data for targets displaced from zero phase could be obtained when the feature was uprange or downrange of zero phase. Generally, it was not possible to locate targets directly at zero phase, but in all cases the closest acceptable targets were chosen.

4.2.3 Selection of Targets and Observational Sequence

Four observation periods during the mission were provided by mission planners for the visibility tests. These were on Revs 16 and 30, for both the frontside and backside opportunities. The four passes were denoted 16B, 16F, 30B and 30F, with F and B standing for frontside and backside passes, respectively.

*If a target at a given range could be seen under this condition, it could be seen under nearly all other conditions at the same range.

A goal of about 20 separate targets had been determined based on mission constraints and on requirements for a range of target sizes, albedos, and other characteristics. To meet this goal an average of five targets per pass should have been selected for each of the four observation passes. However, it was not thought likely that the CMP could simultaneously report changing visibility conditions for five targets in sufficient detail at the same time.

Rather than reduce the total number of targets, an expanded sun elevation angle range was decided upon and two target regions were selected for each pass, with two or three targets chosen for each region. Thus, on a given pass the CMP would comment on the first group of targets until a pre-set time, and then switch his attention to the second set of targets. This necessitated spacing the two regions at least 6° to 7° apart in longitude, thereby compromising the sun elevation criterion slightly, i.e., the first region of a frontside pass might be at a sun elevation angle 30° , with the second at 23° . The observation sequence, based on this scheme, is shown schematically in Figure 4-2. The target regions were numbered 1 through 8 in order of observation, i.e., target regions 1 and 2 on 16B; 3 and 4 on 16F; 5 and 6 on 30B; 7 and 8 on 30F.

For the target areas selected, the zero phase ground track was computed from the pre-flight trajectory and plotted on lunar maps and photographs.* Lunar photography was examined to determine likely targets on or near the zero phase track. The quality and relevance of the pre-mission photography varied considerably - in all cases, target selection was a compromise between factors such as size, shape, minimum phase angle during the pass, spacing between the two target regions and albedo. Albedo was particularly difficult to estimate, as appropriate photography was generally not available (low phase angles or high sun angles are necessary to distinguish bright from subdued craters).

* Only craters were selected. The reasons were that craters provided a simpler test of the analytical models used for visibility predictions and that with the relatively few observation opportunities, it was best not to include another uncontrolled factor (i.e., target type).

Twenty-one targets were finally selected. Target identifications and location data are given in Table 4-1. The locations of the targets are shown pictorially on lunar photomaps in Figures 4-3 (16F), 4-4a (16B), and 4-4b (30B).^{*} These figures also show the CSM ground-track, the zero phase ground-track and time marks showing corresponding locations of zero phase and the CSM nadir during each pass. The line-of-sight from the CSM to each target area is shown at the time zero phase is closest to the target area. Additional documentation of target characteristics is given in the Results section.

The times allotted to the observation sequences are given in Table 4-2. The difference in elapsed time between the first and second target areas for passes is due to the availability and locations of acceptable targets in each lunar area. Also, note that the backside passes permitted less time between the first and second areas (and between initial target acquisition and passage through zero phase) than did the frontside passes.

4.3 Photographic Procedures

The Hasselblad Electric Data Camera (HEDC) was used with an 80 mm lens. The 80 mm lens provided adequate resolution and covered a sufficient field of view to keep the targets in the frame over the desired time period. The HEDC camera is equipped with a glass plate with inscribed reseau marks mounted at the film plane. The plate keeps the film flatter than in the normal Hasselblad and the reseau marks provide a geometrical reference on the film. The camera was mounted on a bracket on the hatch window and was actuated by an intervalometer set for a 20 second interval during the observation passes. An orbit rate attitude mode was used which maintained a nearly constant spacecraft attitude with respect to the local orbital coordinate system.

Use of the camera system presented two data reduction problems:

- 1) determination of the actual times at which frames were taken; and
- 2) determination of the actual camera pointing angles. Telemetry or on-board recording of actuation times was not feasible, so the CMP was asked to give a verbal time mark at the first and last intervalometer actuations; the other frame times were derived from these data by the techniques described

^{*} 30F is not shown because this pass was deleted during the mission.

in Reference 30. The camera pointing angles could not be determined to better than $\pm 3^\circ$ prior to the mission because of uncertainties in hatch position introduced by the hatch seal. This variability was taken into account in the pre-flight specification of the vehicle attitude; camera position was determined more accurately post-mission by methods described in the above reference.

Type S0-349 black and white film was used to take advantage of its high resolution. Pre-flight calculations indicated that a single exposure setting was adequate for all lunar areas covered (1/125 sec. at f5.6). Photographic processing details and calibration are described in Appendix A.

4.4 Training and Observation Procedures

A major reason for using pre-selected targets was the ability to train the crew on target recognition. For purposes of the visibility tests detection of a given target should depend on intrinsic visibility of the target rather than on the difficulty or ease of search and acquisition. That is, it was desired to measure visibility independently of visual search. Several sessions were held with the crew to discuss test procedures and practice target identification. In addition, various visual aids were supplied to the crew for independent review. The visual aids included:

- 1) Books containing nearly all Apollo photography of the targets and target areas with overlays for many of the photographs identifying targets, lead-in features, ground track, zero phase track, etc. A sample of one such photograph with overlay is shown in Figure 4-5.
- 2) A composite movie film of all Apollo 16 mm sequence footage that covered the target areas which also included strips showing the relative motion of zero phase for forward and backward passes.
- 3) Lunar photomaps with overlays showing the ground track, zero phase track, time marks and other pertinent information (see Figures 4-3 and 4-4).
- 4) A computer generated movie showing a simulated pass over areas 3 and 4 which was used to portray surface motion and relative position of features during the pass. Craters were drawn as simple outlines.

All of the visual aids except the last were felt to be definitely useful by the crew. The computer generated movie lacked realism because of the simplified terrain representation, and its intended use as an aid to develop a sense of timing for the pass was judged of insufficient importance to justify production costs for the remaining passes.

A set of on-board maps and photographs similar to those used for training were developed and included as a section in the CSM on-board map book. These were used for review and target identification prior to and, if needed, during the observation passes.

A rating scale was developed to provide rank ordering of target detection difficulty. Because the visibility of each target was expected to vary considerably during the pass, the rating scale was applied to the visibility of the targets at closest approach to zero phase. The scale and definitions of each level are given in Table 4-3.

Many of the procedures described in previous sections were worked out or refined during the crew briefing sessions with the help of the crew. In general, the visibility tests were felt to be as complex, if not more so, than any of the other orbital activities due to the large number of targets which had to be learned, the requirement for accurate timing as well as simultaneous photographic and verbal reports, and air-to-ground coordination.

4.5 Ground Support Activities

Three factors necessitated real-time mission support of the visibility tests: 1) the tests would be useful only insofar as the zero phase track fell close to the targets; 2) a requirement that the targets be photographed as close as possible to zero phase so that albedo could be measured photometrically; and 3) the need to modify pre-mission camera pointing angles in the event of a ground track displacement from the nominal. Lateral dispersion in the ground track would shift the zero phase track north or south of its nominal pre-flight position. If these dispersions were too large, or if observations had to be conducted on a different Rev due to mission contingencies, zero phase might lie too far from the target for useful results. In that event, it would be necessary to cancel the observations.

The reason for the second requirement is that feature albedo can be measured directly from photography only when the feature is photographed at or very close to zero phase. The nominal camera start time was planned to obtain photography at minimum phase angles for all targets in a given pass, within the limitations of the 20 sec. intervalometer period. The camera start time had to be related to the actual time at which the CSM was a given distance from the targets, thereby requiring an update for the start time during the mission. The optimal camera pointing angles similarly depended on the CSM ground track and also had to be updated.

The TRW CDC 6500 Timeshare System at Redondo Beach was used to provide real-time support through a remote terminal located at NASA/MSC. Trajectory data were supplied as available by MSC and used to compute the necessary updates. In addition, a set of contingency plans were developed to provide actions for drastically off-nominal events, and a set of simplified computation procedures were developed to be used in the event of computer unavailability.

TABLE 4-1
APOLLO 14 VISIBILITY TEST TARGET LOCATIONS

TARGET AREA	TARGET NAME	REVISION	TARGET LOCATION	
			LATITUDE	LONGITUDE
1	1A	16B	-6.69	126.79
	1B		-7.375	128.0
	1C		-6.53	128.56
2	2A		-8.21	119.95
	2B		-8.13	120.63
3	3A	16F	-9.416	- 3.458
	3B		-8.92	- 4.08
4	4A		-7.71	- 14.77
	4B		-7.36	- 14.64
5	5A	30B	-8.677	113.45
	5B		-8.865	113.33
	5C		-9.02	113.36
6	6A		-9.687	104.854
	6B		-9.92	104.85
	6C		-9.81	105.15
7	7A	30F	-4.65	- 18.63
	7B		-4.75	- 19.05
	7C		-4.64	- 18.90
8	8A		-4.333	- 24.677
	8B		-4.17	- 24.375
	8C		-3.98	- 24.271

+ LATITUDE IS NORTH

+ LONGITUDE IS EAST

TABLE 4-2

TIME SEQUENCE FOR EACH OBSERVATION PASS (MIN:SEC)

E V E N T	PASS			
	16B	16F	30B	30F
Start Observations and Camera	0:0	0:0	0:0	0:0
Zero Phase (First Area)	1:40	3:40	1:40	3:40
Switch Areas	3:24	4:32	3:06	4:00
Zero Phase (Second Area)	3:54	6:16	3:46	4:56
End Observations (Start Debrief)	6:54	7:02	6:48	5:38
End Debrief	7:24	7:32	7:18	6:08

TABLE 4-3

RATING SCALE USED TO RANK TARGET VISIBILITY

Acquisition Level	Definition
ZERO	No acquisition.
LOW	Target possibly acquired but with large uncertainty, e.g., a bright spot is seen in the target area but identification as the actual target crater is not possible.
MEDIUM	Target acquired but based on surrounding terrain features rather than unique features of target, e.g., a feature visible as an undistinguished blob is fairly definitely identified as the target crater by using its location relative to surrounding features. For this criterion to apply, <u>something</u> must be visible at the expected target location.
HIGH	Target is positively acquired based on unique aspects of its features as well as its surroundings.

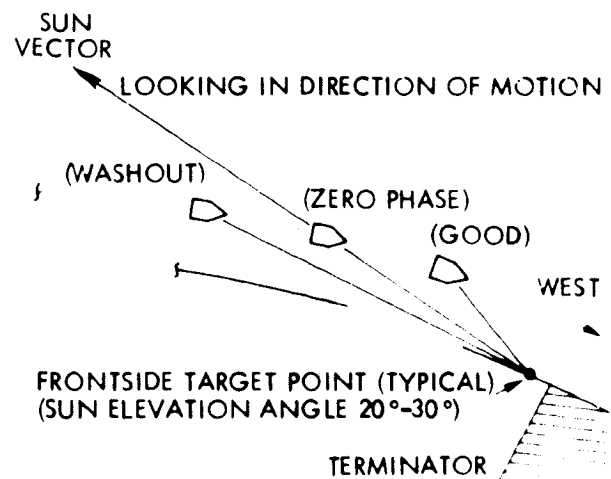
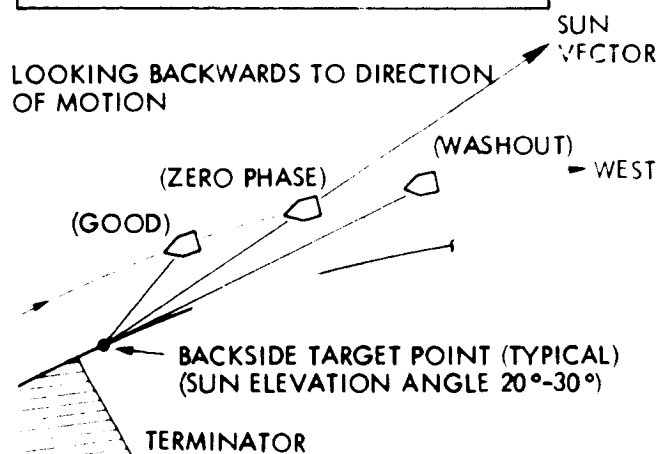
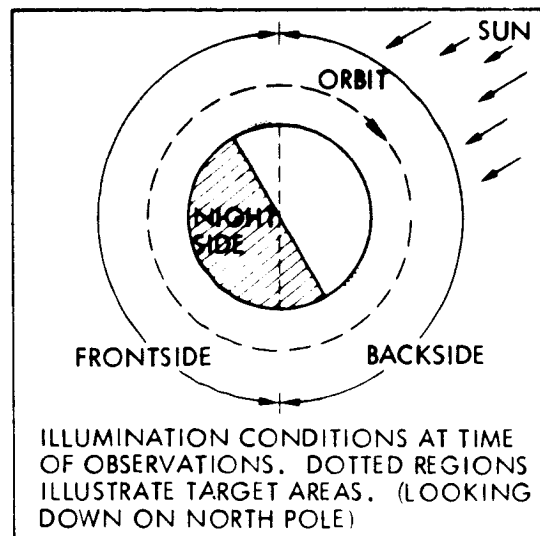


Figure 4-1. Viewing Geometry for Frontside and Backside Observation Passes. On backside Target Area Changes from Good Visibility to Zero Phase to Washout Region as View Elevation Angle Changes from Larger to Smaller than Sun Elevation Angle. Opposite Sequence Occurs on Frontside Pass.

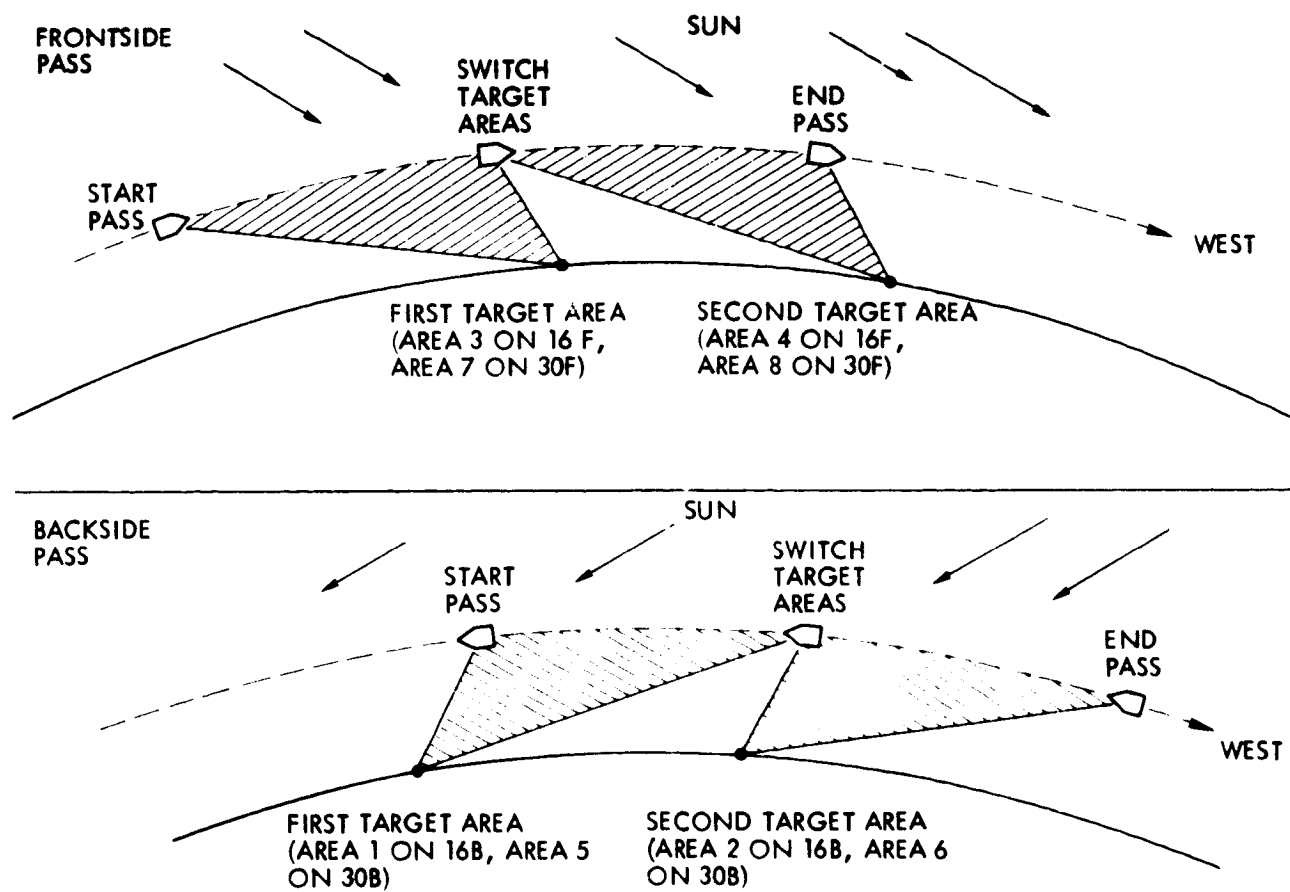
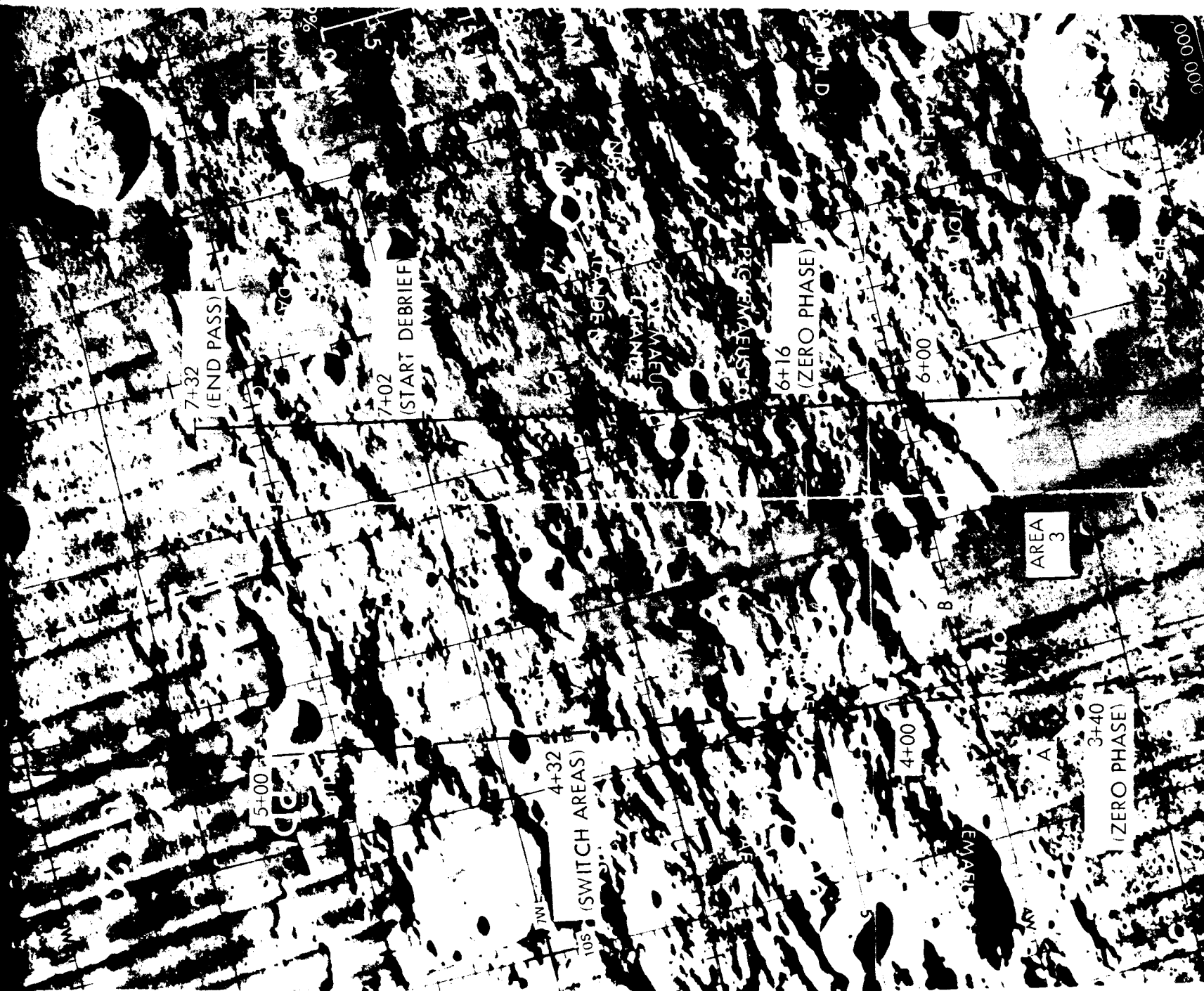


Figure 4-2. Observation Sequences for Backside and Frontside Passes for Each Pass. Two Target Areas Were Defined, the CMP Observed the First Area Until a Preset Time When he Switched Attention to the Second. (Looking Down From North Pole, Not to Scale)



FOLDOUT FRAME



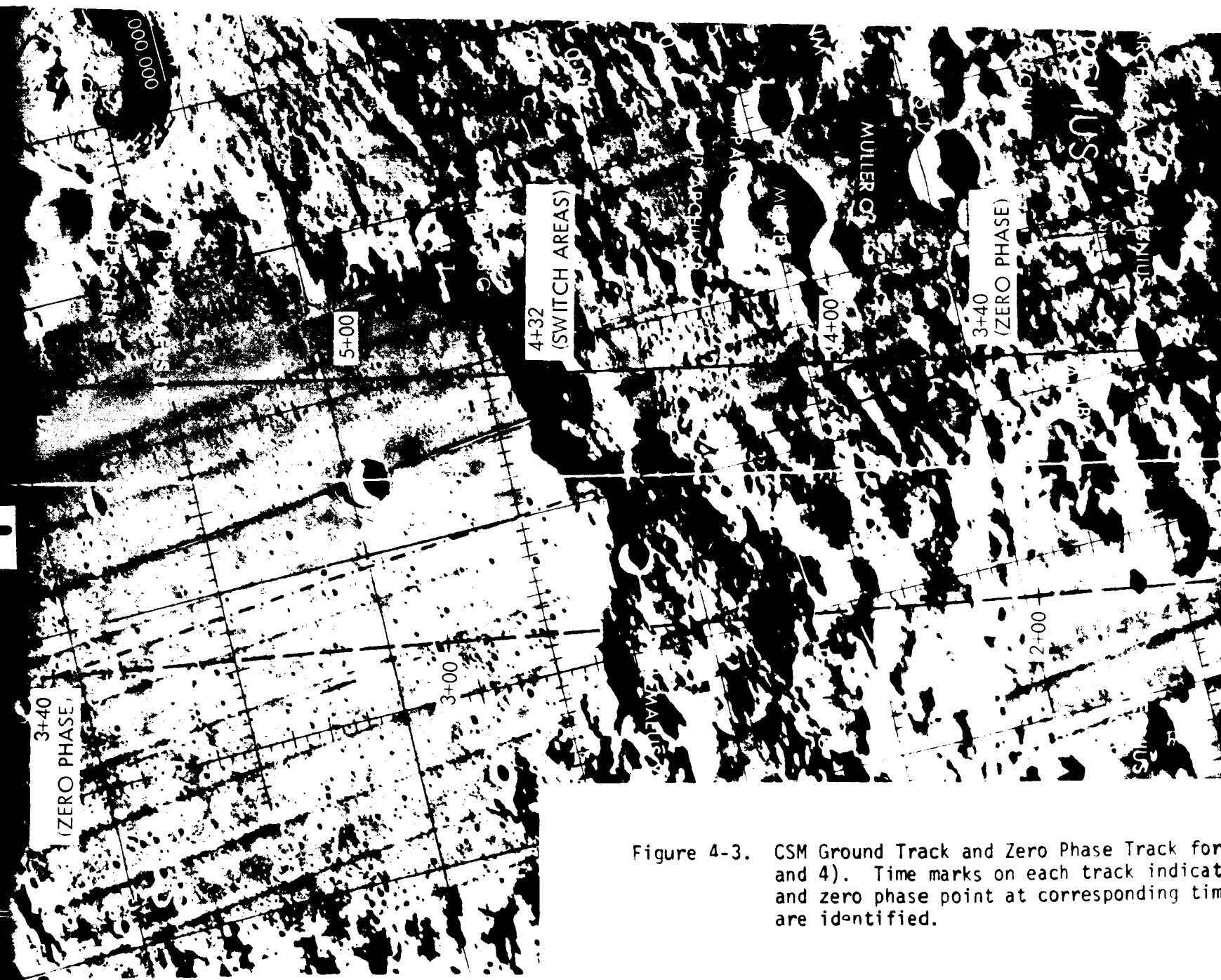


Figure 4-3. CSM Ground Track and Zero Phase Track for (3 and 4). Time marks on each track indicate ground track and zero phase point at corresponding time are identified.

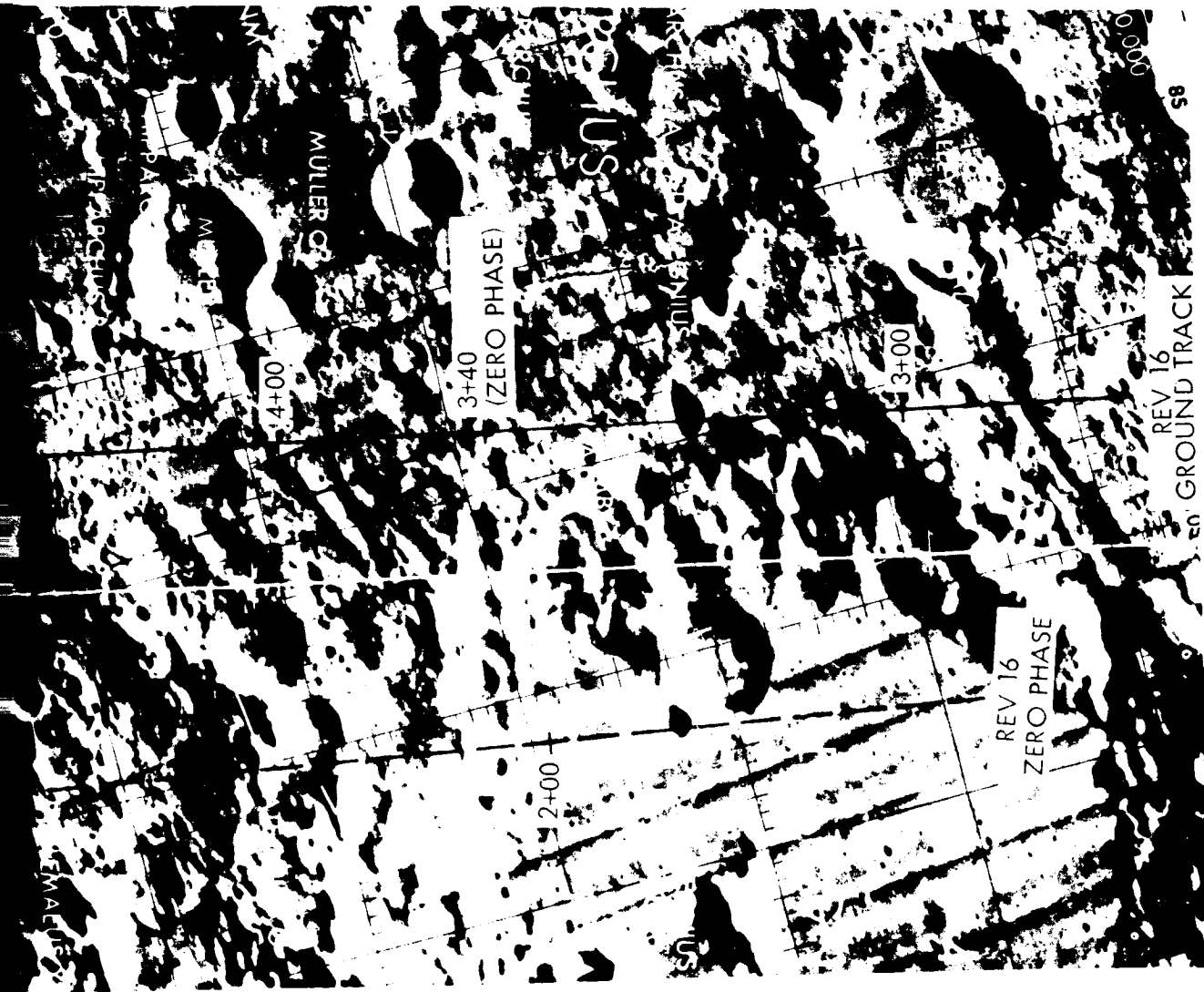
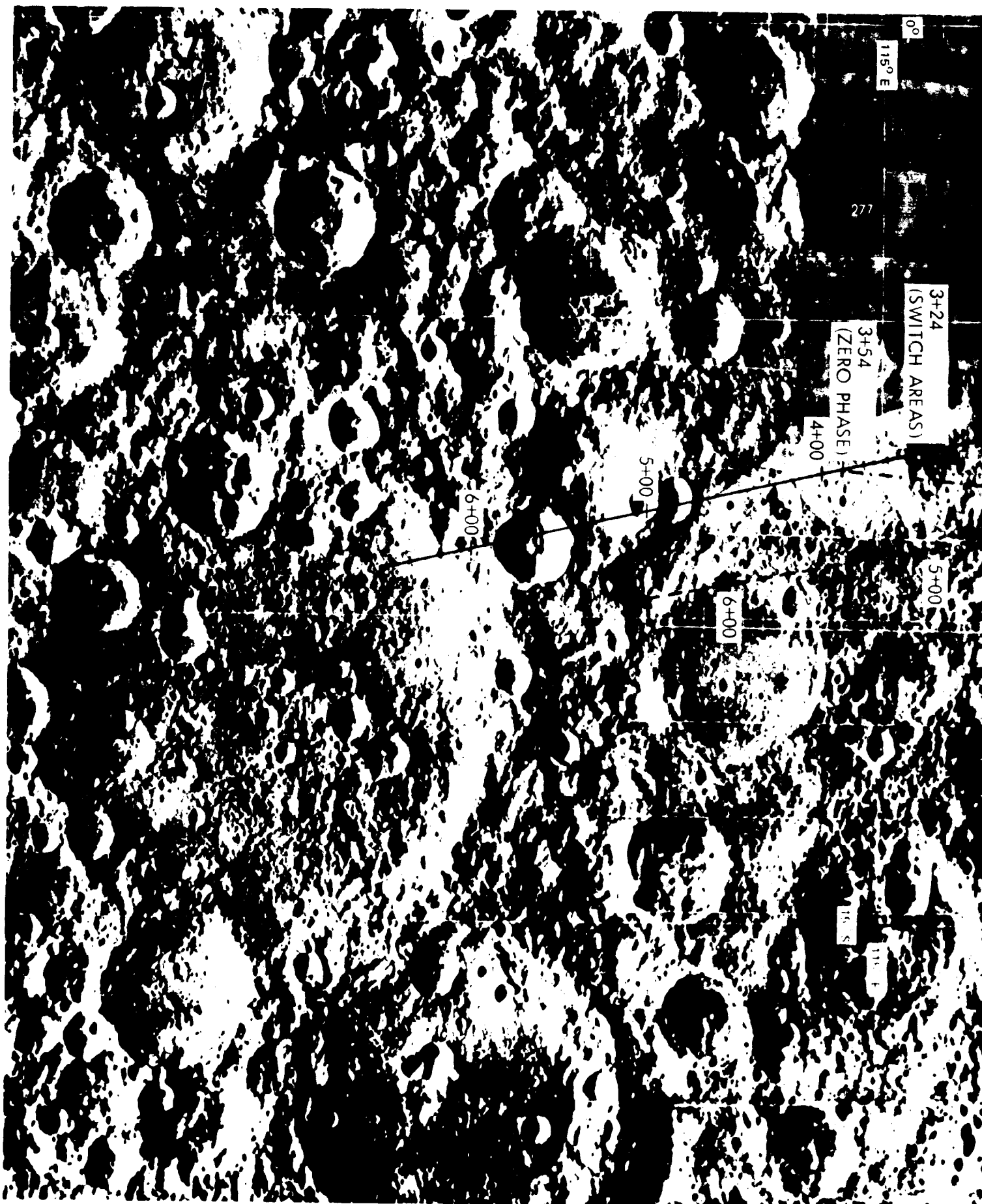


Figure 4-3. CSM Ground Track and Zero Phase Track for Pass 16F (Areas 3 and 4). Time marks on each track indicate positions of CSM and zero phase point at corresponding times. Target craters are identified.

ORIGINAL PAGE IS
OF POOR QUALITY

FOLDOUT FRAME



FOLDOUT FRAME

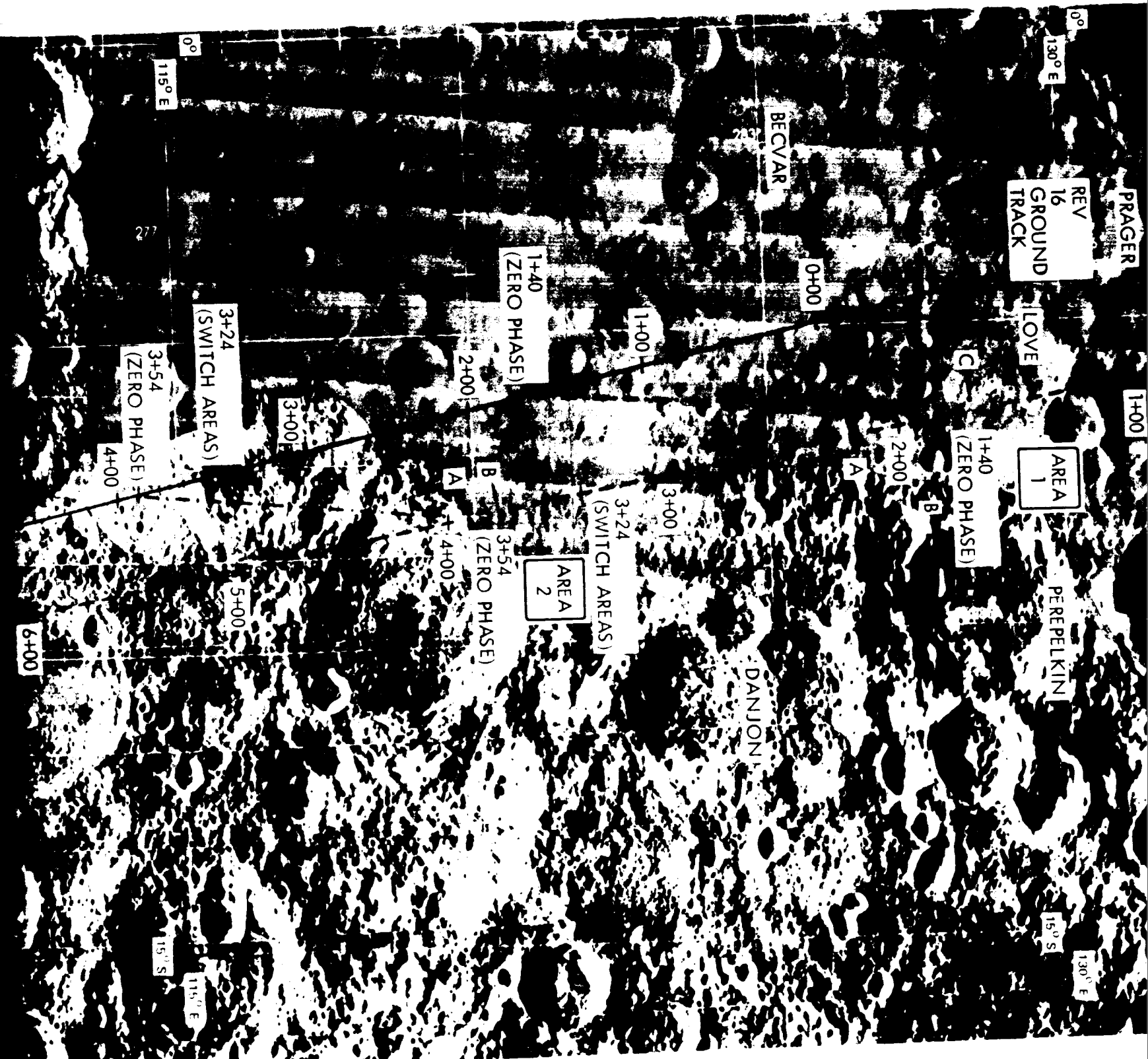


Figure 4-4a. CSM Ground Track and Zero Phase Track for Pass 1 and 2). Time marks on each track indicate position and zero phase point at corresponding times. Tracks are identified.

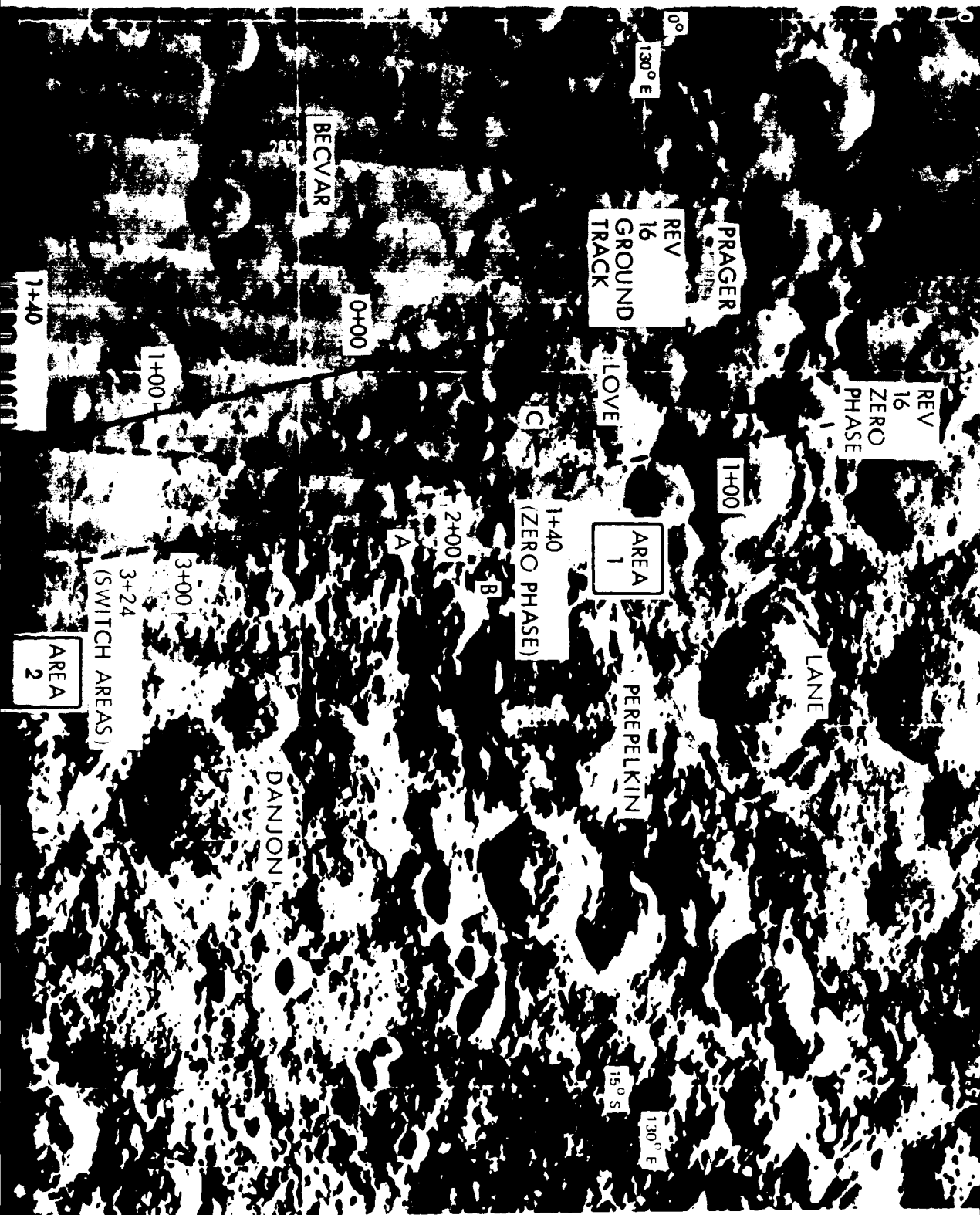
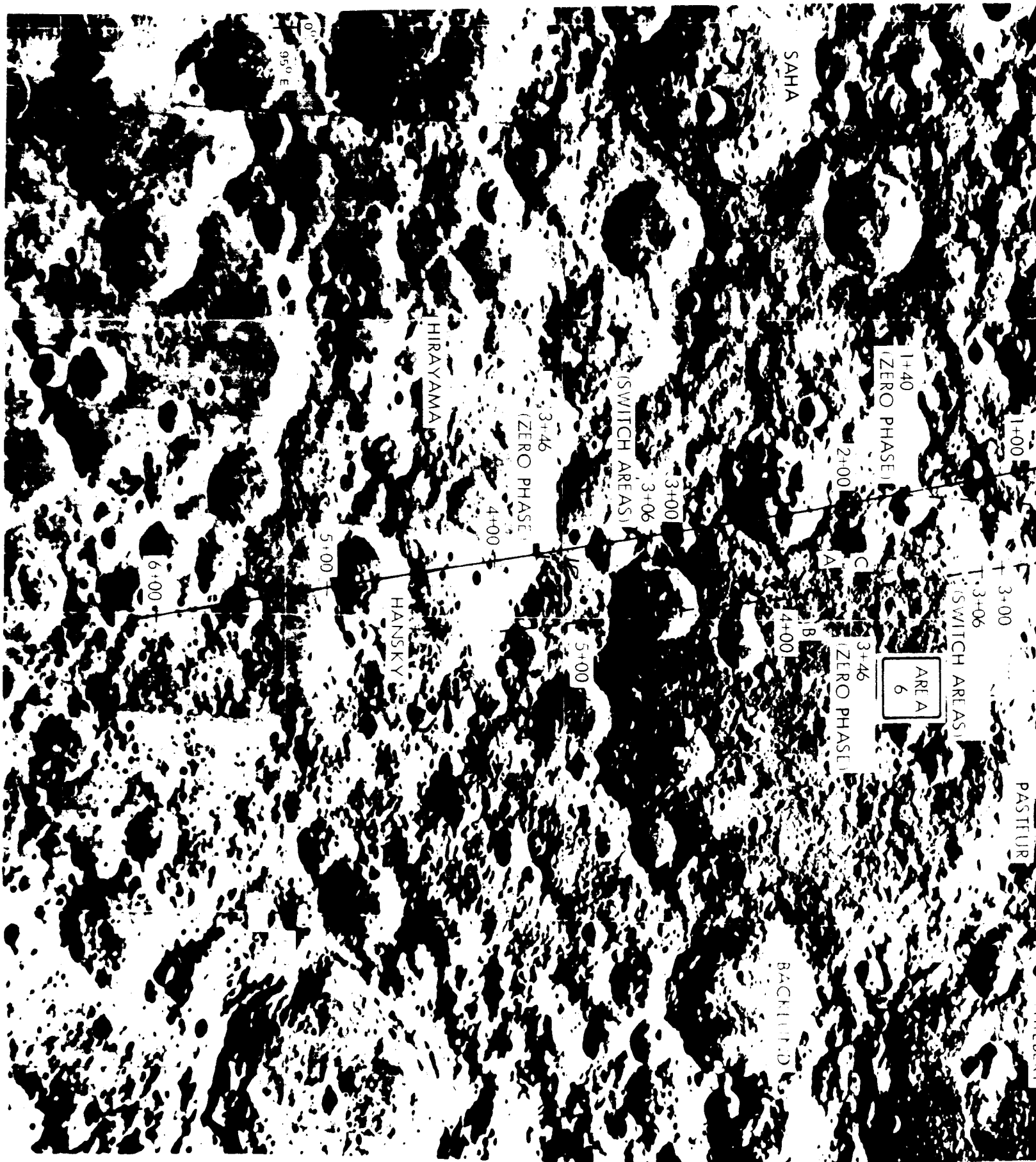


Figure 4-4a. CSM Ground Track and Zero Phase Track for Pass 16B (Areas 1 and 2). Time marks on each track indicate positions of CSM and zero phase point at corresponding times. Target craters are identified.

FOLDOUT FRAME

ORIGINAL PAGE IS
OF POOR QUALITY



FOLDOUT FRAME

ORIGINAL PAGE IS
OF POOR QUALITY

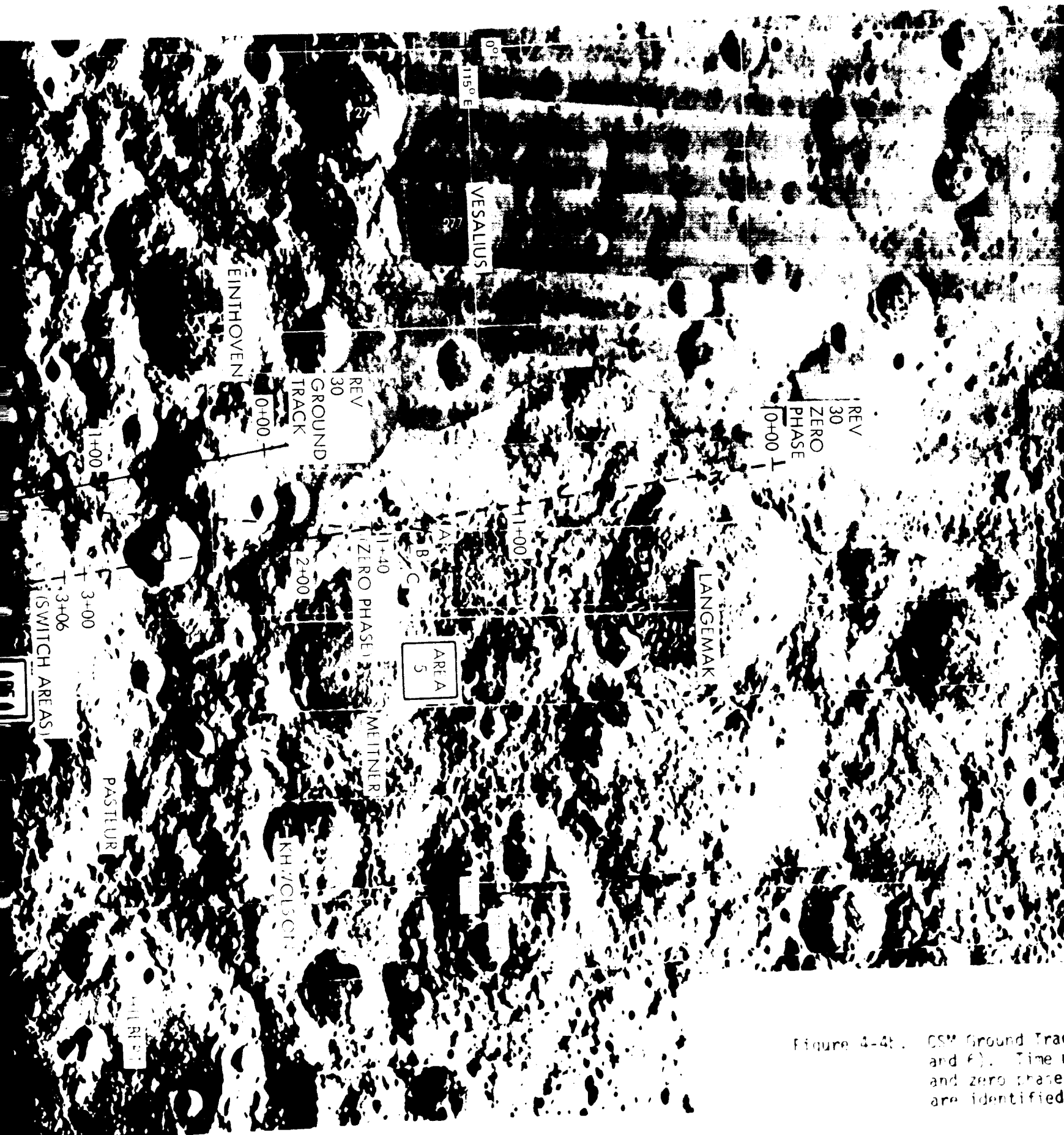
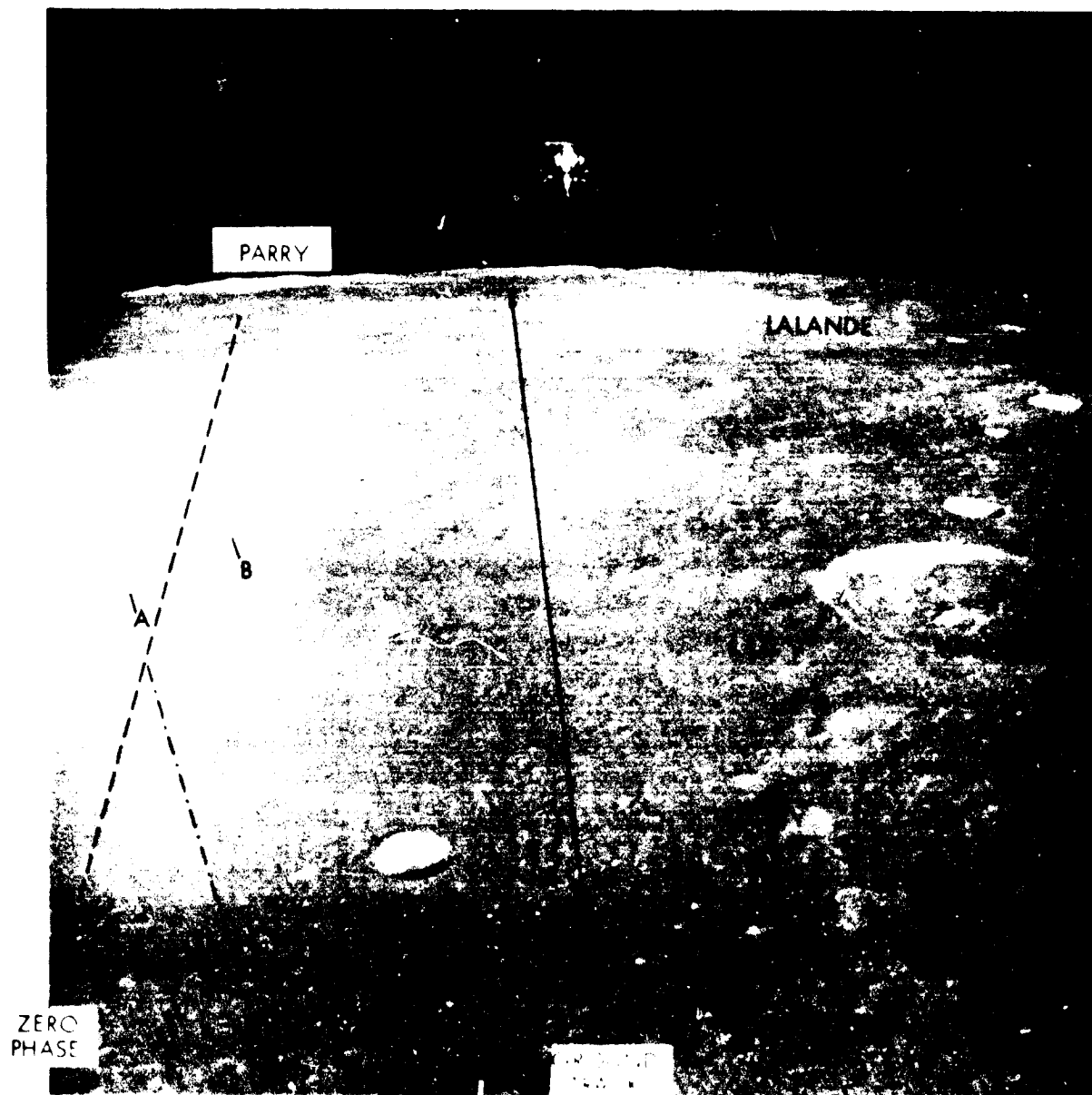


Figure 4-4b. CSM Ground Track and F). Time 1 and zero phase are identified



Figure 4-4b. CSM Ground Track and Zero Phase Track for Pass 300 (Areas E and F). Time marks on each track indicate positions of CSM and zero phase point at corresponding time. Target craters are identified.



AREA
3,4
REV
16
FORWARD

VIEWING
DISTANCE
10 IN

VIEWED
ELEVATION
21°

HERSCHEL

5.0 RESULTS

The discussion of results is divided into three main parts. The first summarizes the quality of the observational and photographic data compared to that expected; the second summarizes the sequence of data analysis steps; the third presents the outcome of the tests and conclusions. Further analysis of the results is given in Section 6. Additional details on the microdensitometric and data reduction procedures used for determination of target contrasts are given in Appendix B, and on a target-by-target breakdown of the CMP's observations in Appendix C.

5.1 Data Quality

Due to malfunctioning of the Hycon camera which was intended for high resolution photography of the Descartes area, the 30F visibility pass (areas 7 and 8) was cancelled in order to obtain additional 70 mm (HEC) photography of Descartes. For the remaining 15 targets in areas 1 through 6, the tests proceeded as planned and good quality photographic and observational data were obtained, except for an unforeseen tape dump that occurred during the 30B pass at the time the CMP was recording his observations. The CMP noticed the dump and rewound the DSE recorder in time for his debriefing comments, but his real-time comments were lost. In addition, the CMP was not able to attend closely to the backside targets after they passed down-range of zero phase (into the washout) because he had to switch attention to the next target as it approached zero phase. Thus, data on visibility in the washout were less precise than desired for the backside targets. Finally, it should be noted that late camera start times of 60 seconds and 40 seconds occurred for Revs 16B and 30B respectively; however, frames prior to zero phase were obtained for all targets so that no relevant data were lost.

The above problems are considered relatively minor in view of the difficulty of the observations and the complexities of planning, crew training and real-time support activities.

Most of the photographic frames were of good quality; each target was photographed under conditions of shadowing and washout and frames were obtained near minimum phase for each target.* A total of 74 frames were obtained which exhibit zero phase over a wide variety of terrain types resulting in a film record which should be useful for lunar photometric studies, in addition to its use in the present study.

5.2 Data Analysis

5.2.1 CMP Observations

The CMP's observations were recorded in the form of voice tapes with accompanying time tracks. Transcriptions were made of the tapes from each of the three passes and times were correlated with his comments. Ratings of zero phase visibility during the inflight debriefing period were obtained for all targets according to the scale described in Section 4.0. Additional information was obtained from the CMP at the post-mission Photographic Debriefing Session (Reference 31). Finally, the CMP was asked to compare a series of prints made with different contrast ranges to his memory of the actual lunar scene (Reference 32).

5.2.2 Timing Analysis

Values of viewing parameters (VEA, SEA, phase, α , etc.) during each pass were determined and placed on a common time-line with the CMP's comments and the actuation time of each photographic frame. The time-line was derived from an analysis of post-flight trajectory data, knowledge of the intervalometer period, and the start and stop camera voice marks supplied by the CMP (Reference 30). Although a certain amount of iteration and approximation was required due to incomplete or ambiguous data, the final times are believed accurate to 1 or 2 seconds. The obtained viewing parameter time histories are very close to those predicted pre-mission.

* As zero phase did not actually pass directly over the targets, the expression "minimum phase" is used to indicate the time and corresponding value of phase angle at which the smallest phase angle occurred for a given target during a pass.

Tables 5-1a, b, c through 5-3a, b, c, are reproduced from Reference 30 and present trajectory and viewing parameter data corresponding to each photographic frame for all passes and targets. Table 5-1 is for 16B, 5-2 is for 16F, and 5-3 is for 30B. The first table (A) of each group of three, presents vehicle location and sub-solar point location at the time of each frame. The second two tables (B, C) give SEA, VEA, g , α , look angles, etc., for each target for each frame for the first and second target areas of the pass.

5.2.3 Measurement of Target Contrasts

The measurement of target crater contrasts from the film record was an essential aspect of the visibility tests. This proved to be an extremely time-consuming task and one which slowed the progress of the entire data reduction effort. The procedure followed was:

- 1) A sub-set of targets was selected from the fifteen that were observed; at least three frames were selected per target such that each was included under conditions of outside the washout region, at photographic minimum phase,* and in the washout region (for some targets two frames in the washout were selected).

Dual considerations of economy and appropriateness resulted in the selection of seven of the fifteen observed targets for microdensitometric analysis. Three targets (1A, 2B, 6A) that were not acquired or whose acquisition was questionable, were rejected for analysis. Targets 4A and 4B proved to be of very high albedo and were observed at a low 15° SEA, so that their inclusion would not have added much information. Targets 2A and 1B were scanned, but they were left out of the analysis; due, in part, to a lack of time and, in part, because it was felt their analysis would be especially difficult due to shape (1B) or background (2A). Target 5C was scanned, but was dropped because it became obscured by a hill after moving into the washout region. The targets and frames that were analyzed are indicated in Table 5-4.

* As the intervalometer could not be set to actuate at the actual minimum phase point for all targets, the smallest phase angles on the photography are somewhat greater than the actual minimum phase.

- 2) A rectangular region on each frame which included the target crater was scanned by a vendor,* using a microdensitometer with a $16\mu\text{m}$ scan spacing and a circular aperture with a $16\mu\text{m}$ diameter. The resulting digital numbers (DN's) representing the sampled photographic density values over a possible range from 0 to 4, were recorded on magnetic tape. A typical scan area size for a single target was $2.4\text{ mm} \times 3.2\text{ mm}$ corresponding to 150×200 or 3.0×10^4 sample points.
- 3) The magnetic tapes provided by the vendor were recoded to a format compatible with the TRW computer system.
- 4) A sequence of data processing steps were conducted to arrive at a contrast value of each target crater, using computer programs written for this purpose:
 - a) A numerical x-y listing (THPRNT) of each of the sampled areas was generated to determine the density range for that target area and to check for data anomalies (see Figure 5-1).
 - b) A Calcomp x-y plot (APPLOT) was made in which four or five exposure levels were coded by symbols of different densities to reconstruct the original image. Because each plotted point could be related to its position in the scan matrix, the target crater boundaries could be related to the scan coordinate system. The target contours were then approximated by ellipses of arbitrary orientations and aspects (for regularly shaped target patterns) or by polygons (for irregularly shaped target patterns). A representative sample of APPLOT outputs and contour approximations is given in Figures 5-2, 5-3, and 5-4. A discussion of the probable errors in this process is given in Appendix B.
 - c) The target contour coordinates were input into a third program (ALTARG) which computed contrasts and sizes of the various target regions (bright side, dark side, and geometric shadow) against a defined background region (backgrounds were annuli of the same shape, but larger than the target). Contrasts and target regions were defined in the same manner as for the analytical models discussed in Section 3.0, allowing a direct comparison between analytical predictions and observational results. Equivalent circular subtended angles were determined for each target area from knowledge of the number of sample points in each area, camera parameters, and viewing geometry (see Appendix D).

* Photometric Data Systems, Inc., Webster, New York.

- d) Several sets of target and background area boundary delineations were made for each target on each scan in order to determine sensitivity of the results to errors in target outline determination. Finally, estimates were made of the total S/N present in the data due to noise introduced by the microdensitometer system.
- e) Densitometric calibration of the film was accomplished by scanning pre- and post-flight calibration gray scales exposed with known luminance levels with the same aperture and microdensitometer used for the target scans. The resulting density values were plotted against the gray step exposure values supplied by NASA and a polynomial was fitted to this curve for use in the computer programs. That is, contrast values of the targets were determined in terms of exposure rather than density. More detailed information on calibration procedures and error estimates is given in Appendix B.

The final results of these procedures were values of contrasts and subtended angles associated with each target in each frame that was scanned.

5.2.4 Comparison With Analytical Predictions

The final stage of the analysis was to generate analytical predictions of target contrast and visibility by using the visibility models described in Section 3.0 for the viewing/illumination conditions corresponding to the frames for which target contrast values had been obtained. Thus, predictions of visibility based on analytical models could be compared to actual test results.

5.3 Summary of Results

5.3.1 Photographic Results

Reproductions of all 74 visibility test frames from Mag R are given in Figures 5-5 (16B), 5-6 (16F) and 5-7 (30B). The half-tone reproductions in these figures are poor approximations of contrast levels in the actual lunar view, but they do provide a good simulation of the sequence of events and changing visual scene during the passes. The target craters are identified for each pass on the first frame showing the targets in good visibility which either precedes (backward pass) or follows (forward pass) the minimum

phase frame. In addition, the times of each frame are given relative to the first frame.* A set of full-tone prints is also given for selected frames in order to provide a more accurate visual display of target appearance. In this sequence, the target craters are shown under conditions of shadowing or "good" visibility, at minimum phase, and in the washout region. All of the frames used for the contrast analysis are included. Target areas 1 and 2 are shown in Figures 5-8 and 5-9, respectively; areas 3 and 4 in Figures 5-10a,b and 5-11; and areas 5 and 6 in Figures 5-12 and 5-13. Values of VEA, SEA, phase angle and alpha angle (corresponding to a horizontal surface) are given for each target for each frame. These data were taken from Tables 5-1 to 5-3.

The reader should examine these figures carefully, especially the full-tone prints, in order to appreciate the viewing situation encountered by the CMP and so that the ensuing discussion of target visibility can be related to a visual impression of target characteristics and related visibility parameters. Note the substantial differences in surface appearance between the frontside and backside views (areas 1, 2, 5, and 6, compared to areas 3 and 4). The frontside targets are located in relatively level areas and are seen against fairly homogeneous backgrounds, whereas the backside targets are generally in much more heterogeneous, hillier areas and in some cases are in heavily rayed regions (e.g., targets 2A and 2B in Figure 5-9, compared to 3A and 3B in Figure 5-10). Note, also that the targets themselves vary in appearance as to shape and apparent contrast. For instance, as shown in Figure 5-10 for 16F, target 3B is quite bright and well defined, whereas 3A is seen (in the washout) mostly by virtue of its bright rim. Similarly, Figure 5-13 shows that for 30B, target 6C is well defined, but 6B is a much shallower crater with its rim appearing only slightly brighter than its floor.

The frames for which the smallest phase angles occurred in the negative alpha regions are also indicated in Figures 5-8 through 5-13. Table 5-5 compares the actual minimum phase values observed by the CMP with the smallest values on the film. The largest difference is 0.96° , indicating that the photographs provide a satisfactory record of visibility conditions at the actual value of minimum phase.

*The nominal inter-frame interval was 20 sec.; but some double actuations occurred, resulting in a few 1 sec. intervals.

5.3.2 Visibility and Target/Background Characteristics

An overall summary of visibility results and target/background characteristics is given in Table 5-6. The table is divided into two sections corresponding to target areas 1,2 and 5,6 observed on the backside passes 16B and 30B, respectively (Table 5-6a); and areas 3,4 observed on the frontside pass 16F (Table 5-6b). (As discussed previously, backside targets were seen in a "good" visibility region up-range of zero phase at the beginning of the pass and then were seen down-range of zero phase in a "poor" visibility region as the pass progressed. The opposite sequence occurred for the frontside targets.) Three blocks of data are presented for each case: 1) target data such as crater diameter, diameter/depth ratio, contrast, etc.; 2) visibility data including general comments on acquisition difficulty and the CMP's ratings at minimum phase; and 3) characteristics of the terrain in the target vicinity.

Target Characteristics: Consider first the target data. Target diameters varied from about 5,000 feet (4B) to 44,000 feet (1B). These diameters correspond to equivalent subtended angles of 8 min. to 94 min. measured at the time of minimum phase. Diameter to depth ratios varied from very steep ($D/D = 1.9:1$ for 3A) to extremely shallow ($D/D = 47:1$ for 6A). The SEA at the targets at the time of observation varied from a low of about 15° (4A and 4B) to a high of 31° (6A, 6B, and 6C). Three target areas had SEAs in the range of direct interest to the LM descent (area 1 at 23° , area 5 at 23° , area 3 at 25°).

Contrast data are presented in two forms: 1) for all targets a ranking of contrasts into four categories based on visual inspection of the photography; and 2) measured contrasts for the eight targets that were subjected to analysis. All contrast data are referred to the minimum phase photographic frames. Measured contrast values range from a low of 0.037 (5B) to a high of 0.143 (3B). Note that the two highest contrasts of those analyzed occurred on the frontside and that the visual ratings correspond fairly well to the measured values, although some anomalies are apparent (e.g., 6C and 5C). When taken individually, a wide range of the various target characteristics was included in the set of targets, but not all combinations of values occurred; i.e., the

variables characterizing the targets are not independent. This is clearly shown in Table 5-7, in which the frequency distribution of target characteristics is given for four parameters: diameter/depth ratio, diameter, apparent contrast and SEA. Note that eight targets were in the low contrast category and that these were concentrated in the shallow and medium D/D categories, and that a correlation between steepness and brightness is apparent from the table.

Visibility Results: Examination of the visibility data columns in Table 5-6 indicates that of the fifteen targets observed, twelve were positively acquired, one was apparently misidentified (1A), another was not seen at all (6A), and a third was possibly acquired, but at a very low confidence level (2B).^{*} A marked difference in visibility was encountered between the backside and frontside targets. On the frontside, all targets were acquired at long ranges and low elevation angles down-range of zero phase (in the washout) and successfully tracked through minimum phase into the good visibility region. On the backside, although initial acquisition occurred under good visibility conditions, all targets became difficult to follow after they had passed down-range of zero phase (into the washout area) and some were completely lost at minimum phase; of the three targets which were either not acquired or were misidentified, all were on the backside.

The minimum phase visibility ratings also show backside-frontside differences; the only "high" ratings occurred on the frontside targets. The ratings also show a good correlation with the contrast data except for 5C and 6C, which do not seem to have been rated consistently with their minimum phase contrast values.

Frontside-Backside Differences: The terrain data column should be examined in relation to the photography of the target areas in Figures 5-8 through 5-13. The terrain descriptions give a relative measure of the roughness of each target area as well as a comparison to the Apollo 15 landing site (Hadley). Taken together, the terrain data, contrast values, and inspection

^{*}See Appendix C and Reference 30 for a discussion of 1A.

of the photography make obvious the reasons for the frontside-backside differences: the frontside targets were all of high contrast, had relatively homogeneous, non-cluttered backgrounds, and were easily locatable by virtue of good lead-in features. Conversely, the backside targets were of low contrast and were imbedded in a much more cluttered background. Given equal contrasts, it is well known that targets are less visible when viewed against a cluttered background. Further, the zero phase effect (size and brightness of the luminance surge) is apparently greater in rougher terrain than in smooth terrain (Reference 33) and the high albedo ray patterns encountered in some of the backside areas could further degrade visual recognition.

This happenstance combination of differences between frontside and backside is unfortunate because the frontside viewing situation would have been a more conservative test than was the backside viewing case, given equivalent target contrasts and backgrounds. The reason for this is that the frontside targets are seen first in the washout region when acquisition in the washout is tested, which is not tested in the backside viewing regions. Further, the floor of Ptolemaeus (Area 3) is more like the typical surface of Apollo landing sites than is any other test area. The fact that 3A and 3B were of high contrast and, thus, detectable at extremely long ranges, makes the observations on this pass less useful than if they had been of lower contrast.*

Visual/Photographic Detection Comparison: One of the problems encountered in analyzing lunar feature visibility has been the interpretation and use of lunar photography. That is, quantitative comparisons of feature visibility on photography, with their visibility in the lunar environment, were not available so that it was difficult to evaluate the realism of a given photograph, i.e., whether it provided more or less information than the actual lunar scene. An examination of second generation positive transparencies of the visibility was made to compare detectability on the film with observational results (see Appendix C). The results indicated that target detectability on the film for areas 3 and 4 was very similar to that

* It is especially unfortunate that area 7 was deleted, as it would have provided a frontside test of low albedo craters in rough terrain.

obtained by the CMP. Further, examination of paper prints made to different contrast levels of the target areas by the CMP (Reference 32), indicates that reasonable simulations of the dynamic range of the scene brightness can be achieved; although, in general, even low contrast prints tend to over-emphasize the brightness range between zero phase and the surrounding darker areas. However, this conclusion does not mean that all photography provides a good simulation, but that with proper exposure and printing, a reasonable simulation can be obtained. The case of target 3A is a case in point, as the pre-mission photography apparently under-estimated the contrast of this crater.

Correlation With Visibility Model: A convenient format for presenting the visibility test results is to plot the measured subtended angle/contrast data for the targets on the same graph and scale for which the threshold visibility curves were plotted (Figure 3-10). Such a plot is shown in Figure 5-14, which reproduces the threshold contrast versus subtended angle curve used in the visibility prediction model and includes the results for the seven target craters that were analyzed. (For the present, ignore the overlay on the Figure.) The bright side contrasts and subtended angles for the seven targets for each frame on which contrast was measured are shown. The points are coded according to the photometric region in which the target was located (\square = "good" visibility outside washout; Δ = minimum phase frame; 0 = washout region frame, or frames) and also according to the reported visibility of the target at the time that frame was taken (open symbol = visible; closed symbol = not visible; half-filled symbol = probably not visible, but data ambiguous). The CMP's visibility rating at actual minimum phase for each target is shown next to the minimum phase symbol (Δ). Finally, the time sequence of observations is indicated by an arrow associated with each set of target points. This figure should be examined in relation to the reproductions in Figures 5-8 to 5-12, which show the targets and viewing parameters corresponding to each point in Figure 5-14.

As an example, the point for target 3B (Frame 10250) indicates a contrast of about 0.2 with a subtended angle of about 10 arc min; the open circle indicates the target was in the washout area and was visible at that time. Reference to Figure 5-10a indicates that the VEA at 3B for Frame 10250 was 6.7° . As the pass progressed, the subtended angle increased, but the contrast decreased to about 0.16 by the time the target moved out of the washout (Frame 10258, Figure 5-10b) and, as all the symbols are open, visibility was maintained throughout the pass. For target 1C, the data show it was visible at the first point (Frame 10224, Figure 5-8) with contrast and subtended angle values of about 0.066 and 25 arc min, respectively. It was not visible at minimum phase (contrast = 0.046, subtended angle = 17.5) and was possibly visible after minimum phase in the washout region (contrast = 0.05 and subtended angle = 12.5 arc min).

Inspection of Figure 5-14 indicates that the threshold visibility curve used in the analytical models is a reasonable match to the observational data. The data for targets 1C and 5B show a visible/not visible transition very close to the threshold curve and the points for targets 5A, 6B, and 6C made a transition somewhat to the right of the curve (higher contrast values). Targets 3A and 3B, which were highly conspicuous, lie far to the right of the curve. If only these data were to be considered, the threshold curve might be moved to the right about 0.05 log units, resulting in higher threshold contrasts, i.e., the present threshold data are somewhat optimistic compared to such an altered curve.

Some anomalies are evident in Figure 5-14 and appear to be, in part, due to difficulties in relating observational data to the specific times the photographs were taken. For instance, the CMP reported that target 1C disappeared at minimum phase, reappeared in the washout, and then became undetectable further down-range. However, the minimum phase photograph was not taken at actual minimum phase, and his comment about the final disappearance in the washout was a general one and could not be related to the time-line. Similar ambiguities existed for targets 5A and 6C. However, no targets which fell to the left of the threshold curve were ever visible, and it is not unexpected that with so few observations some ambiguity occurred.

Another significant fact to be observed from Figure 5-14 is that there is a trend for target contrasts to increase after the minimum phase point. The significance of this result lies in that the analytical visibility model predicts constant values in the washout region. As discussed previously with the LRM, contrast is determined entirely by albedo in the washout due to the horizontal slopes of the photometric function - thus, equal albedo craters are rendered invisible. However, the test results indicate that contrast may increase in the washout when the target moves away from zero phase, resulting in better visibility than predicted. The implications of this finding for the form of the photometric function and visibility predictions are discussed in Section 6.

Visibility predictions for the target craters are shown in the overlay to Figure 5-14. The predictions of visibility were generated using the observation and illumination conditions determined for each pass as contained in Tables 5-1 to 5-3, and the LRM photometric function. Two factors need comment relative to these results. The first, is that the albedo values input into the computer program (given in Table 5-8) were taken to be the contrast values obtained for each target at photographic minimum phase. This results in a match of observed and predicted minimum phase contrast values, since the analytical contrast value in the washout is determined entirely by albedo.* Secondly, the set of predictions shown in the overlay were adjusted so that the predicted subtended angles at minimum phase matched the measured values. Thus, the predicted and observed results were matched at the photographic minimum phase point.** Finally, the calculation results are shown for bright side points, as are the experimental points in Figure 5-14.

The predicted values of contrast and subtended angle follow the general trend shown by the measured values: for the low contrast backside targets, both the actual and predicted curves show a drop in contrast from the good visibility points (\square) to the minimum phase point (\triangle). However,

* This only holds for the LRM.

** The rationale for this procedure and comparisons with the "raw" predictions are presented in Section 6.

the model shows a smaller change in contrast between these two points than was measured from the photography. Also, the magnitude of the change in visual angle from good visibility to minimum phase is different between the model and the measurements; however, the direction of this difference is not consistent. For the high albedo frontside targets, the model also generally follows the observed data, except that the discrepancies in the washout region are fairly large, especially for target 3A. Note, however, that the model does distinguish between the general shape of the frontside and backside results. As mentioned previously, the model predicts constant values of contrast in the washout region, especially for the lower albedo targets, whereas the test results show a trend towards increased contrast. This effect can be explained by assuming the photometric function shape depends somewhat on the albedo of the surface layer. If true, this finding would provide a basis for modification of the photometric function and possible improvement of visibility prediction techniques.

Similar predictions to the above were made using the Fedoritz function rather than the LRM. The Fedoritz results were generally quite different from the observed results. In some cases, for reasonable input target albedo values negative contrast values were obtained, contrary to the positive values observed.

It is concluded that the Apollo 14 visibility tests show that prior visibility models are sufficiently accurate for use in tradeoff studies involving visual tasks in the lunar environment and that the LRM is definitely preferred to the Fedoritz function. Further, the data suggest modifications of the photometric function to improve visibility predictions in the washout area.

Additional discussion and analysis of the results are presented in the next section

Frame No.	Time			Vehicle Position			Sub-Solar Point		Vehicle Attitude		
	hr	Min	Sec (AET)	Lat (°)	Lon (°)	Alt (ft)	Lat (°)	Lon (°)	Roll (°)	Yaw (°)	Pitch (°)
AS14-75-10223	111	25	43	-5.848	122.713	375900.8	-1.1923	60.6870	-163.270	-3.325	-87.843
224	111	26	3	-6.077	121.797	376007.1	-1.1923	60.6842	-163.955	-3.235	-87.867
225	111	26	23	-6.301	120.730	376100.3	-1.1923	60.6814	-163.972	-3.280	-87.847
226	111	26	43	6.526	119.749	376133.6	-1.1923	60.6786	-163.768	-3.306	-87.827
227	111	26	44	-6.537	119.730	376146.2	-1.1923	60.6785	-163.757	-3.308	-87.827
228	111	27	4	-6.760	118.711	376286.1	-1.1923	60.6756	-163.547	3.331	-87.811
229	111	27	5	-6.771	118.661	376289.9	-1.1923	60.6755	-163.537	-3.332	-87.810
230	111	27	25	-6.989	117.676	376365.4	-1.1923	60.6727	-163.319	-3.344	-87.784
231	111	27	45	-7.208	116.679	376440.8	-1.1923	60.6698	-163.535	-3.345	-87.768
232	111	28	5	-7.424	115.687	376510.0	-1.1923	60.6670	-164.060	-3.346	-87.772
233	111	28	25	-7.636	114.693	376567.6	-1.1923	60.6642	-163.923	-3.378	-88.100
234	111	28	45	-7.849	113.699	376625.2	-1.1923	60.6614	-163.760	-3.434	-88.511
235	111	29	5	-8.058	112.704	376676.4	-1.1923	60.6586	-163.597	-3.460	-88.736
236	111	29	25	-8.263	111.707	376716.0	-1.1923	60.6558	-163.412	-3.408	-88.574
237	111	29	45	-8.468	110.711	376755.5	-1.1922	60.6529	-163.215	-3.342	-88.416
238	111	30	5	-8.670	109.713	376788.7	-1.1922	60.6501	-164.021	-3.277	-88.257
239	111	30	25	-8.867	108.713	376810.2	-1.1922	60.6473	-163.996	-3.403	-88.090
240	111	30	45	-9.064	107.713	376831.7	-1.1922	60.6445	-163.810	-3.648	-87.908
241	111	31	5	-9.258	106.712	376846.9	-1.1922	60.6417	-163.625	-3.920	-87.835
242	111	31	25	-9.447	105.708	376850.4	-1.1922	60.6389	-163.450	-4.198	-88.003
243	111	31	45	-9.636	104.705	376853.9	-1.1922	60.6361	-163.275	-4.190	-88.205
244	111	32	5	-9.822	103.701	376851.1	-1.1922	60.6333	-163.863	-4.169	-88.388
245	111	32	13	-9.834	103.298	376845.3	-1.1922	60.6322	-164.059	-4.153	-88.461

See Appendix F for definition of terms.

TABLE 5-1a. TRAJECTORY AND SOLAR DATA FOR REV 16B

Frame No.	Target Name	Time Hr Min Sec (AET)	Viewing Elevation (°)	Surface Range (n.m.)	Relative Azimuth (°)	Sun Elevation (°)	Alpha Angle (°)	Phase Angle (°)	Equivalent Angular Subtense (minutes)	Look Elevation (°)	Look Azimuth (°)
AS14-75-10223	1A	111 25 43	39.22	68.14	8.39	23.73	47.49	17.05	149.42	43.38	115.34
	1B		30.54	90.73	13.08	22.45	41.74	14.26	158.62	35.18	150.35
	1C		28.93	96.26	4.09	21.98	57.74	7.87	36.30	34.80	159.74
224	1A	111 26 03	33.12	83.42	3.64	23.72	55.28	9.93	122.72	38.21	160.07
	1B		36.37	105.40	8.62	22.45	40.19	8.77	132.85	32.81	154.77
	1C		24.72	111.90	1.14	21.97	63.73	2.94	30.16	31.55	162.66
225	1A	111 26 23	28.11	99.11	.39	23.72	61.82	4.40	101.07	34.16	163.31
	1B		22.72	120.55	5.27	22.45	5.42	4.88	111.58	30.08	158.11
	1C		21.19	127.78	1.06	21.97	-58.01	1.25	25.23	28.99	164.85
226	1A	111 26 43	23.98	115.04	1.99	23.72	17.37	1.84	83.85	27.90	165.67
	1B		19.60	135.97	2.66	22.45	-64.84	3.78	94.20	26.98	160.69
	1C		18.21	143.73	2.79	21.97	-68.27	4.58	21.25	26.98	166.56
227	1A	111 26 44	23.80	115.81	2.09	23.72	4.60	1.91	83.09	30.87	165.77
	1B		19.45	136.78	2.55	22.45	-65.83	3.82	93.42	27.80	160.80
	1C		18.07	144.54	2.87	21.97	-68.48	4.74	21.08	26.89	166.64
228	1A	111 27 04	20.39	131.85	3.86	23.71	-61.68	4.89	69.51	28.44	167.52
	1B		16.77	152.45	.49	22.44	-73.18	5.68	79.29	26.08	162.82
	1C		15.51	160.68	4.24	21.97	-72.01	7.60	17.87	25.32	167.99
229	1A	111 27 05	20.23	132.68	3.94	23.71	-62.20	5.05	68.91	28.33	167.60
	1B		16.65	153.21	.40	22.44	-73.32	5.80	78.65	26.00	162.91
	1C		15.40	161.43	4.30	21.97	-72.16	7.73	17.72	25.25	168.05
230	1A	111 27 25	17.36	148.83	5.30	23.71	-68.60	8.06	58.08	26.44	168.95
	1B		14.32	169.06	1.24	22.44	-75.55	8.20	67.03	24.64	164.54
	1C		13.18	177.62	5.40	21.97	-74.93	10.18	15.09	24.02	169.14
231	1A	111 27 45	14.88	165.08	6.41	23.71	-72.34	10.70	49.25	24.96	170.04
	1B		12.26	185.00	2.62	22.44	-77.41	10.48	57.30	23.55	165.89
	1C		11.21	193.91	6.33	21.97	-77.27	12.34	12.88	23.05	170.05
232	1A	111 28 05	2.71	181.38	7.32	23.70	-75.22	13.00	41.94	23.79	170.93
	1B		10.41	201.10	3.78	22.43	-79.16	12.55	49.03	22.69	167.02
	1C		9.45	210.18	7.12	21.96	-79.34	14.25	10.99	22.28	170.81
233	1A	111 28 25	10.79	197.68	8.07	23.70	-77.62	15.03	35.77	22.86	171.68
	1B		8.74	217.25	4.76	22.43	-80.82	14.42	41.88	22.01	167.98
	1C		7.86	226.42	7.79	21.96	-81.18	15.97	9.36	21.68	171.47
234	1A	111 28 45	9.06	214.06	8.72	23.70	-79.70	16.84	30.51	22.13	172.31
	1B		7.22	231.42	5.61	22.43	-82.36	16.13	35.64	21.47	168.81
	1C		6.40	242.75	8.38	21.96	-82.85	17.53	7.92	21.22	172.03
235	1A	111 29 05	7.50	230.35	9.28	23.70	-81.54	18.48	25.93	21.56	172.85
	1B		5.83	249.52	6.36	22.42	-83.82	17.69	30.06	21.06	169.53
	1C		5.05	259.12	8.89	21.95	-84.38	18.97	6.62	20.87	172.53
236	1A	111 29 25	6.06	246.78	9.76	23.70	-83.20	19.97	21.88	21.13	173.31
	1B		4.53	265.77	7.01	22.42	-85.18	19.13	24.98	20.75	170.16
	1C		3.79	275.56	9.34	21.95	-85.79	20.29	5.42	20.61	172.96
237	1A	111 29 45	4.23	263.21	10.19	23.70	-84.72	21.35	18.21	20.80	173.72
	1B		3.31	282.14	7.59	22.42	-86.46	20.47	20.21	20.54	170.72
	1C		2.62	291.87	9.75	21.95	-87.10	21.52	4.26	20.44	173.35
238	1A	111 30 05	3.50	279.53	10.57	23.69	-86.11	22.62	14.78	20.57	174.08
	1B		2.17	298.43	8.12	22.41	-87.68	21.72	15.52	20.39	171.21
	1C		1.51	308.30	10.11	21.94	-88.33	22.67	3.07	20.33	173.69

See Appendix F for definition of terms.

TABLE 5-1b. VIEWING AND ILLUMINATION CONDITIONS FOR 16B (TARGETS 1A, 1B, 1C)

Frame No.	Target Time	Hr.	Min.	Sec.	Viewing Elevation (°)	Surface Range (n.mi.)	Relative Azimuth (°)	Sun Elevation (°)	Alpha Angle (°)	Phase Angle (°)	Equivalent Angular Subtense (minutes)	Look Elevation (°)	Look Azimuth (°)
14-75-1013	13*	111	27	25	48.35	40.19	11.71	29.96	29.85	25.11	32.95	51.98	140.86
14-75-1014	13*	111	27	26	45.25	38.58	11.71	29.53	32.78	21.54	65.54	48.67	143.80
14-75-1015	13*	111	27	45	41.59	33.14	12.10	29.44	39.09	15.20	27.50	45.45	150.37
14-75-1016	13*	111	27	46	38.46	31.35	11.64	29.53	40.19	12.56	54.60	42.73	151.80
14-75-1017	13*	111	28	05	35.20	27.11	11.17	29.95	44.60	7.35	22.78	39.96	156.37
14-75-1018	13*	111	28	06	32.65	24.55	6.39	29.57	40.14	5.58	45.10	37.63	157.07
14-75-1019	13*	111	28	23	29.98	23.27	2.07	29.95	-4.45	1.75	18.78	35.58	160.42
14-75-1020	13*	111	28	24	27.81	20.27	1.72	29.50	-55.02	2.28	37.30	33.93	160.75
14-75-1021	13*	111	28	45	25.49	18.45	0.71	29.95	-64.17	4.52	15.56	32.14	163.33
14-75-1022	13*	111	29	03	23.79	16.46	0.36	29.52	-65.98	5.79	31.04	30.87	163.41
14-75-1023	13*	111	29	04	21.03	14.84	0.19	29.94	-67.13	8.57	12.99	29.45	165.49
14-75-1024	13*	111	29	05	20.41	13.96	0.14	29.51	-68.82	9.51	26.02	28.46	165.45
14-75-1025	13*	111	29	25	16.72	10.11	4.77	29.34	-70.12	12.01	10.93	27.33	167.16
14-75-1026	13*	111	29	45	15.53	147.91	4.55	29.51	-71.56	12.71	21.96	26.56	167.04
14-75-1027	13*	111	30	03	16.08	157.04	1.12	29.94	-72.84	14.94	9.25	25.67	168.49
14-75-1028	13*	111	30	04	15.05	163.34	5.35	29.51	-74.06	15.46	18.63	25.06	168.33
14-75-1029	13*	111	30	25	13.72	173.13	7.22	29.93	-75.26	17.43	7.86	24.35	169.57
14-75-1030	13*	111	30	26	12.87	180.29	7.02	29.50	-76.31	17.86	15.87	23.87	169.38
14-75-1031	13*	111	30	45	11.74	189.45	5.12	29.93	-77.42	19.69	6.71	23.31	170.46
14-75-1032	13*	111	30	46	10.34	196.42	7.91	29.55	-78.34	19.97	13.55	22.93	170.25
14-75-1033	13*	111	30	46	9.32	205.29	10.90	29.93	-79.37	21.66	5.72	22.48	171.21
14-75-1034	13*	111	30	46	9.20	212.75	10.67	29.53	-80.18	21.86	11.57	22.19	170.99
14-75-1035	13*	111	31	05	8.26	220.02	9.56	29.92	-81.12	23.42	4.88	21.84	171.85
14-75-1036	13*	111	31	05	7.18	229.51	9.33	29.49	-81.86	23.56	9.84	21.61	171.63
14-75-1037	13*	111	31	25	6.76	239.46	13.12	29.92	-82.74	25.02	4.13	21.34	172.40
14-75-1038	13*	111	31	25	6.16	245.41	9.69	29.49	-83.40	25.11	8.31	21.16	172.18
14-75-1039	13*	111	31	45	5.40	254.83	10.62	29.92	-84.22	26.48	3.47	20.96	172.88
14-75-1040	13*	111	31	45	4.85	261.72	10.39	29.49	-84.82	26.53	6.93	20.83	172.66
14-75-1041	13*	111	32	05	4.12	271.29	11.06	29.91	-85.59	27.83	2.86	20.68	173.31
14-75-1042	13*	111	32	05	3.61	278.05	10.84	29.49	-86.15	27.84	5.64	20.58	173.08
14-75-1043	13*	111	32	25	3.03	287.70	11.22	29.91	-86.11	28.34	2.62	20.59	173.46
14-75-1044	13*	111	32	25	3.13	294.68	11.00	29.49	-86.66	28.34	5.14	20.51	173.24

See Appendix F for definition of terms.

TABLE 5-1c. VIEWING AND ILLUMINATION CONDITIONS FOR 16B (TARGETS 2A, 2B)

ORIGINAL PAGE IS
OF POOR QUALITY

Frame No.	Time			Vehicle Position			Sub-Solar Point		S/C Attitude		
	Hr.	Min. (AET)	Sec.	Lat (°)	Lon (°)	Alt (ft)	Lat (°)	Lon (°)	Roll (°)	Yaw (°)	Pitch (°)
AS14-75-10246	112	00	59	-10.838	14.346	358469.4	-1.1916	60.3892	-15.306	-.528	-84.749
247	112	01	19	-10.667	13.330	358138.4	-1.1916	60.3863	-14.958	-.343	-84.723
248	112	01	39	-10.496	12.314	357807.4	-1.1916	60.3835	-15.431	-.174	-84.689
249	112	01	59	-10.324	11.297	357476.4	-1.1916	60.3807	-15.761	-.008	-84.645
250	112	02	19	-10.143	10.284	357145.5	-1.1916	60.3779	-15.305	.158	-84.590
251	112	02	39	-9.962	9.271	356814.6	-1.1916	60.3751	-14.972	.287	-84.544
252	112	02	59	-9.780	8.257	356483.7	-1.1916	60.3723	-15.443	.190	-84.581
253	112	03	19	-9.590	7.247	356153.8	-1.1916	60.3694	-15.745	.085	-84.616
254	112	03	39	-9.400	6.237	355823.9	-1.1916	60.3666	-15.350	-.017	-84.667
255	112	03	59	-9.210	5.227	355494.1	-1.1916	60.3638	-14.997	-.104	-84.717
256	112	04	19	-9.012	4.219	355166.1	-1.1916	60.3610	-15.363	-.183	-84.796
257	112	04	39	-8.813	3.211	354838.1	-1.1916	60.3582	-15.750	-.259	-84.894
258	112	04	59	-8.615	2.204	354510.2	-1.1916	60.3554	-15.391	-.345	-85.014
259	112	05	19	-8.409	1.199	354185.0	-1.1916	60.3526	-15.037	-.432	-85.144
260	112	05	39	-8.203	.195	353859.8	-1.1916	60.3498	-15.247	-.402	-85.218
261	112	05	59	-7.996	-.809	353534.8	-1.1916	60.3470	-15.764	-.240	-85.241
262	112	06	19	-7.783	-1.811	353213.4	-1.1916	60.3441	-15.473	-.085	-85.258
263	112	06	39	-7.570	-2.812	352891.9	-1.1916	60.3413	-15.148	.067	-85.275
264	112	06	59	-7.356	-3.814	352570.7	-1.1916	60.3385	-14.999	.211	-85.284
265	112	07	19	-7.136	-4.813	352253.8	-1.1916	60.3357	-15.645	.351	-85.271
266	112	07	39	-6.915	-5.813	351937.0	-1.1915	60.3329	-15.627	.502	-85.265
267	112	07	59	-6.695	-6.812	351620.4	-1.1916	60.3301	-15.371	.618	-85.249
268	112	08	19	-6.468	-7.808	351309.1	-1.1916	60.3272	-15.115	.401	-85.140
269	112	08	20	-6.457	-7.858	351293.6	-1.1916	60.3271	-15.103	.389	-85.128
270	112	08	40	-6.231	-8.855	350982.3	-1.1915	60.3242	-15.015	.164	-84.884
271	112	09	00	-6.004	-9.851	350671.6	-1.1915	60.3214	-15.653	-.044	-84.667
272	112	09	20	-5.772	-10.846	350366.8	-1.1915	60.3186	-15.646	-.203	-84.561

TABLE 5-2a. TRAJECTORY AND SOLAR DATA FOR REV 16F

See Appendix F for definition of terms.

Frame No.	Target Name	Time Hr. Min. Sec. (AET)	Viewing Elevation (°)	Surface Range (n.mi.)	Relative Azimuth (°)	Sun Elevation (°)	Alpha Angle (°)	Phase Angle (°)	Equivalent Angular Subtense (minutes)	Look Elevation (°)	Look Azimuth (°)
AS14-75-10246	3A	112 00 59	2.41	287.21	10.80	25.87	-87.39	25.66	4.01	19.94	6.16
	3B		1.68	297.99	12.00	25.32	-88.14	26.32	4.39	19.87	4.60
247	3A	112 01 19	3.57	270.80	10.40	25.87	-86.12	24.43	5.17	20.10	6.58
	3B		2.81	281.34	11.71	25.32	-86.89	25.18	5.99	19.99	4.91
248	3A	112 01 39	4.82	254.26	9.97	25.87	-84.75	23.12	6.38	20.34	6.98
	3B		4.00	264.88	11.40	25.32	-85.54	23.98	7.57	20.17	5.20
249	3A	112 01 59	6.16	237.81	9.50	25.88	-83.28	21.70	7.68	20.68	7.40
	3B		5.29	248.25	11.07	25.33	-84.08	22.68	9.25	20.45	5.49
250	3A	112 02 19	7.62	221.33	8.93	25.88	-81.68	20.14	9.13	21.13	7.98
	3B		6.67	231.80	10.66	25.33	-82.49	21.26	11.08	20.82	5.90
251	3A	112 02 39	9.22	204.88	8.28	25.88	-79.91	18.43	10.78	21.73	8.61
	3B		8.18	215.30	10.20	25.33	-80.72	19.72	13.14	21.33	6.34
252	3A	112 02 59	10.99	188.47	7.54	25.89	-77.95	16.51	12.70	22.50	9.32
	3B		9.85	198.75	9.69	25.34	-78.72	18.02	15.51	21.98	6.83
253	3A	112 03 19	12.97	172.15	6.62	25.89	-75.76	14.34	14.96	23.48	10.23
	3B		11.70	182.31	9.05	25.34	-76.43	16.10	18.29	22.83	7.47
254	3A	112 03 39	15.23	155.79	5.54	25.89	-73.28	11.85	17.64	24.74	11.30
	3B		13.80	165.80	8.30	25.34	-73.71	13.94	21.59	23.92	8.20
255	3A	112 03 59	17.83	139.55	4.21	25.89	-70.44	8.96	21.02	26.35	12.59
	3B		16.20	149.37	7.41	25.35	-70.27	11.47	25.61	25.32	9.06
256	3A	112 04 19	20.88	123.38	2.51	25.89	-67.31	5.52	23.15	28.41	14.29
	3B		18.99	133.00	6.26	25.35	-65.42	8.60	31.57	27.11	10.21
257	3A	112 04 39	24.51	107.36	.32	25.89	-65.02	1.41	33.36	31.07	16.46
	3B		20.30	126.13	4.81	25.35	-54.88	5.36	36.79	29.43	11.64
258	3A	112 04 59	28.92	91.50	2.61	25.90	54.93	3.80	36.97	34.51	19.36
	3B		26.31	100.43	2.92	25.36	33.69	2.80	44.72	32.44	13.51
259	3A	112 05 19	34.30	76.03	6.79	25.90	49.59	10.24	45.30	38.94	23.54
	3B		31.23	84.38	.26	25.36	58.75	5.88	54.90	36.38	16.18
260	3A +	112 05 39	40.85	61.16	13.03	25.90	41.59	18.44	55.56	44.59	29.75
	3B		37.38	68.56	3.62	25.36	51.60	12.41	67.91	41.57	20.03

+ Target 3A not on frame.

See Appendix F for definition of terms.

TABLE 5-2b. VIEWING AND ILLUMINATION CONDITIONS FOR 16F (TARGETS 3A, 3B)

Case No.	Target Name	Time Hr. Min. Sec.	Viewing Elevation (°)	Surface Sample (meters)	Relative Elevation (m)	Sur. Elevation (°)	Altra Angle (°)	Prate Angle (°)	Equivalent Angular Subtense (minutes)	Look Elevation (°)	Look Azimuth (°)
A-14-75-1255	41	112 03 59	Over the horizon		0.21	14.33	-69.99	17.26	.12	19.73	6.91
	42		1.1	322.36	2.21	14.33	-69.99	15.67	2.11	19.74	8.42
	43	112 04 19	1.2	305.24	2.21	14.33	-69.99	16.12	1.16	19.74	7.29
	44		1.25	324.30	2.21	14.33	-69.99	14.50	3.27	19.81	8.88
	45	112 04 39	1.39	283.87	1.37	14.33	-67.75	14.50	1.75	19.82	7.69
	46		2.11	245.11	1.34	14.33	-67.53	15.04	4.32	19.94	9.38
	47		3.13	251.34	6.37	14.74	-66.46	13.25	2.29	19.96	8.12
	48	112 04 59	3.26	275.11	7.49	14.94	-66.16	13.82	5.39	20.14	9.98
	49		4.34	232.11	5.76	14.74	-65.09	11.90	2.85	20.18	8.64
	50	112 05 19	5.40	232.11	5.76	14.74	-64.69	12.50	6.54	20.44	10.64
A-14-75-1256	51		5.63	174.11	5.27	14.74	-63.62	10.43	3.45	20.49	9.22
	52	112 05 39	6.30	174.11	5.35	14.80	-63.03	8.84	7.80	20.85	11.38
	53		7.22	174.11	5.68	14.35	-61.18	9.53	4.11	20.91	9.87
	54	112 05 59	8.56	174.11	6.39	14.80	-60.35	7.07	9.22	21.38	12.27
	55		9.77	174.11	6.88	14.95	-59.54	7.81	4.86	21.46	10.65
	56	112 06 19	10.24	174.11	7.34	14.80	-58.60	5.10	10.85	22.07	13.30
	57		11.49	174.11	7.95	14.95	-57.34	5.90	5.73	22.18	11.56
	58	112 06 39	12.41	174.11	1.11	14.81	-56.99	2.90	12.77	22.96	14.50
	59		13.57	174.11	2.67	14.96	-56.07	3.78	6.75	23.11	12.61
	60	112 06 59	14.61	174.11	2.93	14.81	-55.32	7.0	15.04	24.08	15.97
A-14-75-1257	61		15.61	174.11	3.54	14.96	-54.77	1.54	17.78	24.28	13.92
	62	112 07 19	16.61	174.11	4.26	14.81	-54.18	2.77	9.44	25.50	17.76
	63		17.36	174.11	4.76	14.96	-53.94	2.03	21.12	25.78	15.51
	64	112 07 39	18.36	174.11	4.42	14.81	-53.14	6.22	11.27	27.31	19.96
	65		19.34	174.11	4.76	14.96	-52.65	5.34	25.24	27.69	17.48
	66	112 07 59	20.55	174.11	7.03	14.81	-52.43	10.40	13.53	29.59	22.80
	67		21.52	174.11	4.63	14.96	-52.43	9.44	25.47	30.12	20.06
	68	112 08 19	22.70	174.11	7.45	14.81	-52.21	10.63	13.66	29.71	22.97
	69		23.52	174.11	4.92	14.96	-52.21	9.67	30.53	30.26	26.21
	70	112 08 39	24.61	174.11	11.23	14.81	-52.21	15.77	16.52	32.62	26.72
A-14-75-1258	71		25.61	174.11	6.27	14.96	-52.21	14.78	36.95	33.41	23.65
	72	112 08 59	26.61	174.11	16.34	14.82	-48.89	22.12	20.09	36.25	31.80
	73		27.61	174.11	13.54	14.96	-51.36	21.17	44.40	37.40	28.40
	74	112 09 19	28.61	174.11	23.52	14.82	-49.91	30.03	24.39	40.62	38.96
	75		29.61	174.11	19.97	14.96	-49.02	29.23		42.33	36.30
	76	112 09 39	30.61	174.11							
	77		31.61	174.11							
	78	112 09 59	32.61	174.11							
	79		33.61	174.11							
	80	112 10 19	34.61	174.11							
	81		35.61	174.11							

TABLE 5-20. VIEWING AND ILLUMINATION CONDITIONS FOR 16F (TARGETS 4A, 4B)

Frame No.	Time		Variable Position				Sub-Solar Point		S/C Attitude		
	hr	min	sec	lat	lon	alt	lat	lon	Roll (°)	Yaw (°)	Pitch (°)
4014-75-10273	19		00	-7.532	159.321	35.437.4	-1.1596	36.6336	-164.365	.218	-93.277
"	19		01	-7.701	159.361	35.436.3	-1.1596	36.6439	-164.611	.020	-93.162
"	19		02	-7.863	159.399	35.435.1	-1.1597	36.6472	-164.616	-.221	-93.044
"	19		03	-8.026	159.436	35.433.3	-1.1597	36.6443	-164.365	-.486	-92.897
"	19		04	-8.189	159.473	35.431.3	-1.1597	36.6442	-164.361	-.499	-92.889
"	19		05	-8.352	159.510	35.429.3	-1.1596	36.6415	-164.366	-.692	-92.742
"	19		06	-8.515	159.547	35.427.4	-1.1596	36.6387	-164.235	-.640	-92.620
"	19		07	-8.678	159.584	35.425.4	-1.1596	36.6360	-164.371	-.590	-92.491
"	19		08	-8.841	159.621	35.423.4	-1.1596	36.6332	-164.354	-.546	-92.355
"	19		09	-9.004	159.658	35.421.4	-1.1596	36.6305	-164.633	-.405	-92.197
"	19		10	-9.167	159.695	35.419.4	-1.1596	36.6277	-164.712	-.486	-92.385
"	19		11	-9.330	159.732	35.417.4	-1.1596	36.6250	-164.813	-.467	-92.591
"	19		12	-9.493	159.769	35.415.4	-1.1596	36.6222	-164.942	-.437	-92.807
"	19		13	-9.656	159.806	35.413.4	-1.1596	36.6194	-164.577	-.395	-93.043
"	19		14	-9.819	159.843	35.411.4	-1.1596	36.6166	-164.160	-.332	-93.182
"	19		15	-9.982	159.880	35.409.4	-1.1596	36.6139	-164.369	-.241	-93.129
"	19		16	-10.145	159.917	35.407.4	-1.1596	36.6111	-164.600	-.132	-93.080
"	19		17	-10.308	159.954	35.405.4	-1.1596	36.6084	-164.363	-.021	-93.047
"	19		18	-10.471	159.991	35.403.4	-1.1596	36.6056	-164.639	.088	-92.985
"	19		19	-10.634	160.028	35.401.4	-1.1596	36.6029	-164.186	.185	-92.934
"	19		20	-10.797	160.065	35.399.4	-1.1596	36.6001	-164.438	.216	-92.863
"	19		21	-10.960	160.102	35.397.4	-1.1596	36.5974	-164.737	.015	-92.772
"	19		22	-11.123	160.139	35.395.4	-1.1596	36.5946	-164.363	-.228	-92.654
"	19		23	-11.286	160.176	35.393.4	-1.1596	36.5919	-164.278	-.470	-92.526
"	19		24	-11.449	160.213	35.391.4	-1.1596	36.5891	-164.335	-.665	-92.398

TABLE 5-34. TRAJECTORY AND SOLAR DATA FOR REV 30B

TIME DATA IS FOR ORBITATION OF 26 DAYS.

Frame No.	Target Name	Time	Viewing Elevation	Surface Range (n.mi.)	Relative Azimuth (°)	Sun Elevation (°)	Alpha Angle (°)	Phase Angle (°)	Equivalent Angular Subtense (minutes)	Look Elevation (°)	Look Azimuth (°)
4514-75-10273	5A	139 07 10	36.58	69.79	12.53	22.90	45.12	17.45	106.42	40.84	153.63
	5B		37.08	68.64	15.36	23.02	41.78	19.31	42.73	41.27	150.71
	5C		36.65	69.62	16.93	22.99	39.85	20.00	77.11	40.90	149.08
274	5A	139 07 30	30.73	85.02	7.54	22.90	51.15	10.32	86.62	35.92	158.61
	5B		31.23	83.57	9.77	23.02	47.29	11.95	34.90	36.33	156.29
	5C		30.36	84.35	11.11	22.99	44.56	12.70	67.19	36.11	154.89
275	5A	139 07 49	26.17	99.90	4.21	22.90	52.41	5.04	71.54	32.27	161.91
	5B		26.63	98.25	6.03	23.02	46.73	6.57	28.87	32.63	159.99
	5C		26.45	98.89	7.19	22.99	41.60	7.40	52.39	32.49	158.77
276	5A	139 08 09	22.20	115.85	1.65	22.89	45.58	1.67	58.95	29.27	164.46
	5B		22.61	114.04	3.17	23.01	19.05	2.94	23.81	29.58	162.85
	5C		22.49	114.56	4.17	22.98	18.73	3.88	43.27	29.49	161.78
277	5A	139 08 10	22.02	116.65	1.54	22.89	52.37	1.67	53.40	29.14	164.57
	5B		22.43	114.83	3.04	23.01	27.01	2.87	23.58	29.44	162.97
	5C		22.31	115.36	4.04	22.98	24.86	3.79	42.87	29.35	161.91
278	5A	139 08 29	18.99	131.99	1.29	22.89	71.07	4.00	48.99	26.95	166.38
	5B		19.26	130.03	1.00	23.01	70.21	3.86	19.79	27.20	165.00
	5C		19.18	130.46	1.88	22.98	69.09	4.19	36.02	27.14	164.05
279	5A	139 08 49	16.10	148.19	1.82	22.89	73.44	6.99	41.04	25.15	167.89
	5B		16.42	146.19	1.70	23.01	73.50	6.61	16.58	25.35	166.68
	5C		16.36	146.57	1.08	22.98	73.64	6.61	30.20	25.31	165.83
280	5A	139 09 08	13.81	163.66	2.99	22.88	75.60	9.50	34.87	23.80	169.04
	5B		14.10	161.58	2.00	23.00	75.61	9.10	14.08	23.96	167.96
	5C		14.05	161.93	1.30	22.97	75.83	9.01	25.67	23.94	167.19
281	5A	139 09 28	11.69	180.06	3.99	22.88	77.71	11.82	29.48	22.68	170.04
	5B		11.95	177.93	3.12	23.00	77.66	11.44	11.91	22.81	169.07
	5C		11.92	178.18	2.49	22.97	77.84	11.31	21.72	22.80	168.36
282	5A	139 09 47	9.91	195.61	4.81	22.88	79.54	13.76	25.19	21.85	170.83
	5B		10.14	193.50	4.02	23.00	79.45	13.41	10.18	21.96	169.94
	5C		10.12	193.68	3.44	22.97	79.58	13.27	18.56	21.94	169.29
283	5A	139 10 07	8.22	212.05	5.53	22.87	81.30	15.59	21.30	21.16	171.53
	5B		8.43	209.91	4.85	22.99	81.18	15.27	8.61	21.25	170.73
	5C		8.41	210.11	4.30	22.97	81.28	15.13	15.72	21.24	170.13
284	5A	139 10 26	6.76	227.71	6.12	22.87	82.84	17.16	18.08	20.66	172.11
	5B		6.96	225.48	5.47	22.99	82.70	16.87	7.32	20.73	171.36
	5C		6.94	225.70	4.99	22.97	82.78	16.73	13.36	20.72	170.80
285	5A	139 10 46	5.35	244.21	6.67	22.87	84.33	18.66	15.06	20.26	172.64
	5B		5.53	242.03	6.08	22.99	84.18	18.41	6.11	20.31	171.94
	5C		5.52	242.15	5.63	22.97	84.24	18.27	11.16	20.30	171.42
286	5A	139 11 06	4.04	260.83	7.14	22.86	85.71	20.05	12.32	19.96	173.09
	5B		4.22	258.47	6.60	22.98	85.56	19.82	5.02	20.00	172.45
	5C		4.21	258.60	6.19	22.96	85.60	19.68	9.16	20.00	171.96
287	5A	139 11 26	2.83	277.33	7.56	22.86	87.00	21.33	9.72	19.76	173.50
	5B		3.00	274.94	7.06	22.98	86.84	21.12	3.99	19.78	172.89
	5C		2.99	275.08	6.67	22.96	86.87	20.99	7.27	19.78	172.43

See Appendix F for definition of terms.

TABLE 5-3b. VIEWING AND ILLUMINATION CONDITIONS FOR 308 (TARGETS 5A, 5B, 5C)

Target No.	Target Name	Time	Altitude	Flowing Elevation	Surface Elevation	Relative Azimuth	True Elevation	Alpha Angle	True Angle	Equivalent Angular Subtense (minutes)	Look Elevation (°)	Look Azimuth (°)
1	100	30	3	42.43	57.45	3.75	31.31	41.32	13.12	76.46	45.94	156.35
2	101	30	3	41.43	56.45	3.75	31.31	37.30	14.14	92.45	45.05	152.72
3	102	30	3	39.57	53.13	3.54	31.31	35.36	11.79	57.59	43.43	155.11
4	103	30	3	35.17	73.33	3.47	31.31	49.25	4.83	63.72	39.63	161.60
5	104	30	3	34.54	74.56	3.39	31.31	36.16	4.25	74.90	39.09	158.59
6	105	30	3	33.51	75.51	4.76	31.31	33.43	4.52	46.59	37.80	160.22
7	106	30	3	30.63	53.33	3.33	31.31	-50.20	1.68	51.59	35.02	164.83
8	107	30	3	29.21	53.46	3.46	31.31	-50.26	3.04	51.38	34.67	162.27
9	108	30	3	27.95	93.58	11.49	31.31	-60.08	3.29	38.22	33.66	163.49
10	109	30	3	24.34	124.33	2.16	31.31	-64.13	6.64	42.03	31.31	167.22
11	110	30	3	24.63	135.46	1.14	31.23	-65.35	6.58	50.17	31.09	165.03
12	111	30	3	23.61	135.54	1.21	31.23	-65.24	7.41	31.30	30.30	165.96
13	112	30	3	21.12	125.61	3.34	31.31	-57.36	10.77	34.59	28.48	168.97
14	113	30	3	20.91	121.61	2.18	31.22	-66.78	10.50	41.39	28.33	167.05
15	114	30	3	20.34	125.66	2.96	31.22	-69.50	11.22	25.88	27.73	167.79
16	115	30	3	17.34	137.52	5.26	31.31	-71.13	14.16	28.74	26.31	170.29
17	116	30	3	17.76	137.93	3.72	31.22	-71.75	13.64	34.45	26.20	168.58
18	117	30	3	17.05	142.18	4.27	31.22	-72.40	14.44	25.58	25.73	169.20
19	118	30	3	15.22	155.12	6.26	31.31	-73.51	16.31	24.29	24.70	171.29
20	119	30	3	15.26	151.45	4.31	31.21	-74.24	16.56	29.14	24.62	169.75
21	120	30	3	14.52	153.51	5.36	31.21	-74.83	17.56	18.28	24.25	170.27
22	121	30	3	13.35	162.73	7.14	31.29	-76.25	19.39	20.46	23.37	172.14
23	122	30	3	12.95	162.31	5.91	31.21	-75.57	19.56	24.57	23.32	170.74
24	123	30	3	12.49	174.11	5.29	31.21	-77.15	19.45	15.43	23.03	171.19
25	124	30	3	11.10	154.55	7.61	31.21	-76.30	21.43	17.43	22.39	172.80
26	125	30	3	11.22	155.11	6.75	31.31	-76.54	21.12	20.95	22.35	171.51
27	126	30	3	10.53	153.60	7.02	31.31	-79.82	21.44	15.16	22.12	171.91
28	127	30	3	9.25	201.33	6.41	31.29	-80.23	23.35	14.75	21.57	173.38
29	128	30	3	9.41	202.51	7.41	31.31	-80.40	23.03	17.73	21.54	172.20
30	129	30	3	8.77	204.31	7.62	31.31	-85.84	23.31	11.13	21.37	172.55
31	130	30	3	7.72	217.55	5.91	31.23	-81.37	24.38	12.55	20.97	173.06
32	131	30	3	7.66	217.69	7.99	31.21	-82.01	24.69	15.10	20.95	172.76
33	132	30	3	7.26	271.39	5.22	30.95	-82.42	24.91	9.47	20.81	173.08
34	133	30	3	6.23	233.55	9.34	31.25	-83.45	26.53	10.52	20.49	174.29
35	134	30	3	6.16	234.15	6.49	31.21	-83.56	26.26	12.66	20.47	173.26
36	135	30	3	5.80	238.60	8.70	31.21	-83.93	26.44	7.92	20.37	173.55
37	136	30	3	4.92	249.33	9.71	31.26	-84.32	27.89	8.80	20.14	174.64
38	137	30	3	4.88	249.84	8.93	31.21	-84.91	27.63	10.58	20.13	173.68
39	138	30	3	4.53	254.27	9.11	30.95	-85.26	27.77	6.59	20.05	173.94
40	139	30	3	3.64	265.97	10.05	31.27	-86.17	29.20	7.12	19.88	174.97
41	140	30	3	3.60	266.51	9.34	31.21	-86.24	29.36	8.56	19.87	174.07
42	141	30	3	3.29	270.88	9.50	30.94	-86.57	29.57	5.28	19.82	174.30
43	142	30	3	2.51	281.75	10.33	31.27	-87.37	30.27	5.60	19.71	175.24
44	143	30	3	2.48	282.14	9.66	31.27	-87.42	30.13	6.72	19.70	174.39
45	144	30	3	2.17	296.64	9.81	30.94	-87.73	30.22	4.37	19.67	174.61
46	145	30	3	1.39	298.26	10.60	31.27	-88.54	31.51	3.95	19.60	175.50
47	146	30	3	1.36	298.74	9.98	31.20	-88.58	31.29	4.71	19.60	174.69
48	147	30	3	1.33	303.18	10.11	30.94	-88.88	31.36	2.71	19.58	174.89

See Appendix E for definition of terms.

TABLE 5-3c. VIEWING AND ILLUMINATION CONDITIONS FOR 308 (TA-415 6A, 6B, 6C)

Target	Frames
1C	10224, 10225, 10228
3A, 3B	10250, 10255, 10257, 10258
5A, 5B	10275, 10276, 10278, 10279
6B, 6C	10283, 10284, 10285

Table 5-4. Targets and Frames Analyzed

Table 5-5. Comparison of Actual and Photographic Minimum Phase

REV	Target	Frame No.	View Elevation Angle At Actual Minimum Phase	Actual Minimum Phase	Minimum Phase On Photography	Phase Angle Diff. (Photo-Actual)
16B	1A	10226	24.55°	1.74°	1.84°	0.1°
	1B	10226	20.19°	3.69°	3.78°	0.09°
	1C	10225	22.19°	0.48°	1.25°	0.86°
16F	2A	10233	29.17°	1.53°	1.75°	0.22°
	2B	10233	28.25°	2.19°	2.28°	0.09°
	3A	10257	25.75°	0.45°	1.41°	0.96°
	3B	10258	26.53°	2.78°	2.80°	0.02°
	4A	10265	14.44°	0.65°	0.70°	0.05°
30B	4B	10265	15.52°	1.06°	1.54°	0.49°
	5A	10277	22.02°	1.67°	1.67°	0°
	5B	10277	21.55°	2.70°	2.87°	0.17°
	5C	10277	21.10°	3.50°	3.79°	0.29°
	6A	10284	30.98°	0.89°	1.68°	0.79°
	6B	10284	29.72°	2.96°	3.04°	0.08°
	6C	10284	29.95°	2.56°	3.13°	0.57°

TABLE 5-6a. SUMMARY RESULT TABLE, BACKSIDE PASSES

Target	Target Data			Visibility Data			Terrain Data ⁴	
	Dia. (ft)	Diameter/Depth Ratio ¹	Contrast at Photo. Min. Phase ²	Sun Elevation (deg)	Initial Acquisition (Duration of Zero Phase in "Good" Visibility)	Minimum Phase Visibility ³	Acquisition Downrange of Zero Phase (in "Poor" Visibility)	
1A	31117	Medium	Medium	23.8	Apparently misidentified	(Low?)	Difficult for all Backside Targets	<u>Area 1</u> (near Low): non-descript fairly heavily cratered old rolling uplands (Imbrian or pre-Imbrian age); crossed by very bright diffuse rays.
1B	44084	Shallow	Low	22.7	Easily acquired	Med to Low		
1C	10798	Steep	3.1 (.046)Low	22.0	Easily acquired	Zero		
2A	5384	Very Steep	2.3 High	30.5	Easily acquired	Med. to Low		<u>Area 2</u> (near Langemak): hummocky ejecta of a fairly fresh (upper Imbrian) crater; small crater density is similar to or less than for Hadley mare. Hummocky topography possibly analogous to Apennine Mountain but on a very much finer scale. Area very bright from superposed rays.
2B	11044	Medium	1.9 Low	29.8	Not acquired, or acquired with low confidence	Low		
5A	22455	Medium	6.7 (.049)Low	23.0	Easily acquired	Medium		<u>Area 5</u> (near Weitzner): featureless hilly terra on rim of an old (upper pre-Imbrian) crater whose ejecta is no longer distinct.
5B	9875	Medium	8.6 (.037)Low	23.0	Easily acquired	Low		
5C	16234	Medium	6.7 (.067)Low	23.0	Easily acquired	Low		
6A	13940	Extremely Shallow	47 Low	31.3	Not acquired	-		<u>Area 6</u> (in Pasteur): heavily cratered old basin fill; possibly like Ptolemaeus but older, probably brighter, much more heavily cratered.
6B	16874	Very Shallow	18.8 (.040)Low	31.3	Easily acquired	Medium		
6C	11074	Medium	6.1 (.047)Med.	31.0	Easily acquired	High to Med.		

NOTES:

- 1 - From data supplied by Mapping Sciences Laboratory, NASA/MSC.
 2 - Numerals are contrasts measured from the photographic minimum phase frame; ratings are from visual inspection of Apollo 14 photography.
 3 - The CME rated target visibility at minimum phase on a four point scale (zero, low, medium, high).
 4 - Terrain data supplied by Dr. Keith Howard, USGS/Menlo Park.

TABLE 5-6b. SUMMARY RESULT TABLE, FRONTSIDE PASS

Target	Target Data				Visibility Data			Terrain Data ⁴	
	Dia. (ft)	Diameter/Depth Ratio	Contrast at Photo. Min. Phase	Sun Elevation (deg)	Initial Acquisition (Downrange of Zero Phase in "Poor" Visibility)	Minimum Phase Visibility ³	Acquisition Downrange of Zero Phase (in "Good" Visibility)		
3A	10417	Very Steep	1.9 (.077) Med.	25.8	Acquired about 3° VEA and confirmed about 5° VEA	High	All targets tracked through zero phase into good visibility region.	Area 3 (Ptolemaeus): a typical example of light plains (lower Imbrian age) known as "Cayley Formation"; flat like Hadley mts but a little older, more heavily cratered, brighter, and probably lacking many small very sharp craters.	
3B	14102	Steep	3.0 (.143) High	25.2	Acquired about 3° VEA and confirmed about 5° VEA	High			
4A	9443	Very Steep	1.7 Very High	14.7	Immediately acquired at switch time, 7° VEA	High		Area 4 (Parry): Imbrian ejecta; hillier than Hadley mare but less rugged than highlands near Hadley.	
4B	4376	Medium	8.6 High	14.9	Immediately acquired at switch time, 7° VEA	High			

NOTES:

- 1 - From data supplied by Mapping Sciences Laboratory, NASA/MSC.
- 2 - Numerals are contrasts measured from the photographic minimum phase frame; ratings are from visual inspection of Apollo 14 photography.
- 3 - The CDP rated target visibility at minimum phase on a four point scale (zero, low, medium, high).
- 4 - Terrain data supplied by Dr. Keith Howard, USGS/Menlo Park.

Table 5-7. Frequency Distribution of Target Characteristics (The number of targets falling in a given category of size, contrast, diameter/depth ratio, and SEA is indicated inside the SEA code symbol.)

APPARENT CONTRAST RELATIVE TO BACKGROUND

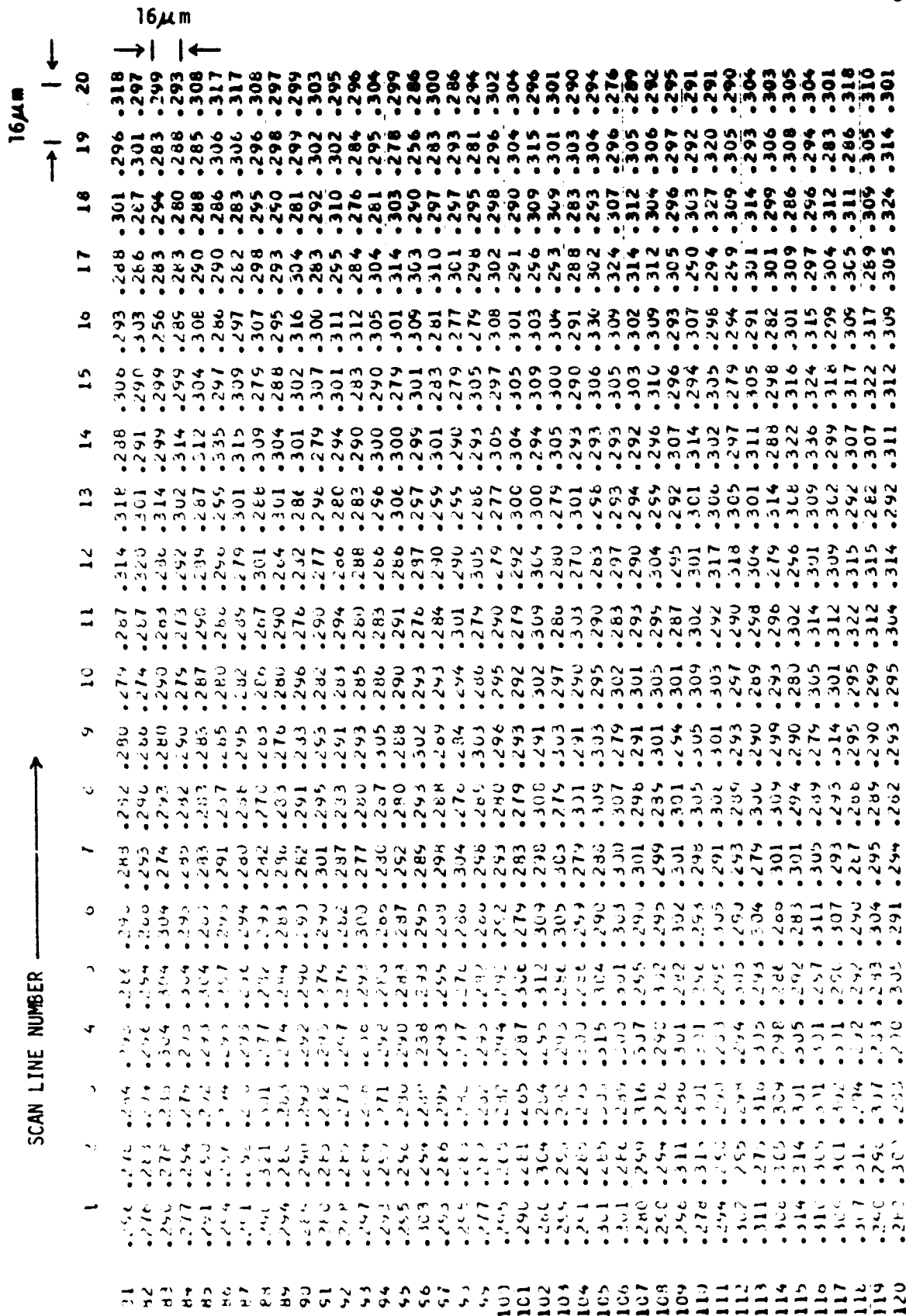
Size Range (Ft x 10 ⁻³)	Low				Medium				High				Very High			
	10	10-20	20	20	10	10-20	20	20	10	10-20	20	20	10	10-20	20	20
	10	10-20	20	20	10	10-20	20	20	10	10-20	20	20	10	10-20	20	20
Diameter/ Depth Ratio	Very Shallow															
	Shallow															
	Medium															
	Steep															
	Very Steep															

Sun elevation angle code:
 □ less than 20°
 ○ 20°-26°
 △ 29°-31°

Note. Apparent contrast judged from Apollo 14 photography

Target	Albedo for Spherical Section Model (relative to background)
1C	4.6%
3B	11.6%
5A	4.9%
5B	3.7%
6C	4.7%
3A	10.8% (for cone model floor albedo = 0%, wall albedo = 10.8%, wall angle from vertical = 40°)
6B	4.0% (for cone model floor albedo = 0%, wall albedo = 4.0%, wall angle from vertical = 70°)

Table 5-8. Target Albedos Input to Visibility Program



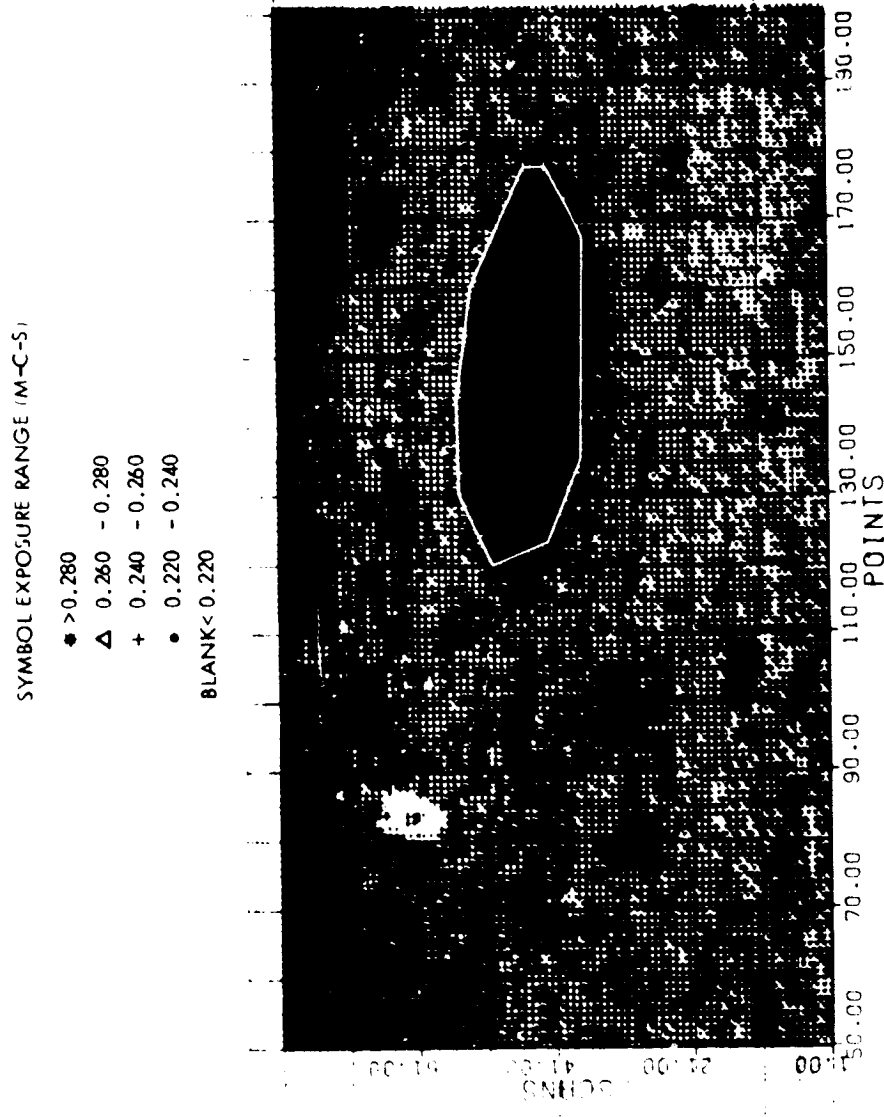


Figure 5-2. Computer generated reconstruction of target 38, Frame 10255. Polygon outlines area used to define crater boundary. Each plotted point is a sampled point from the original image; exposure category for each point is given in the table (denser points correspond to greater exposures).

SYMBOL EXPOSURE RANGE (M-C-5)

* > 0.450
 Δ 0.400 - 0.45
 + 0.350 - 0.40
 • 0.300 - 0.35
 BLANK < 0.300

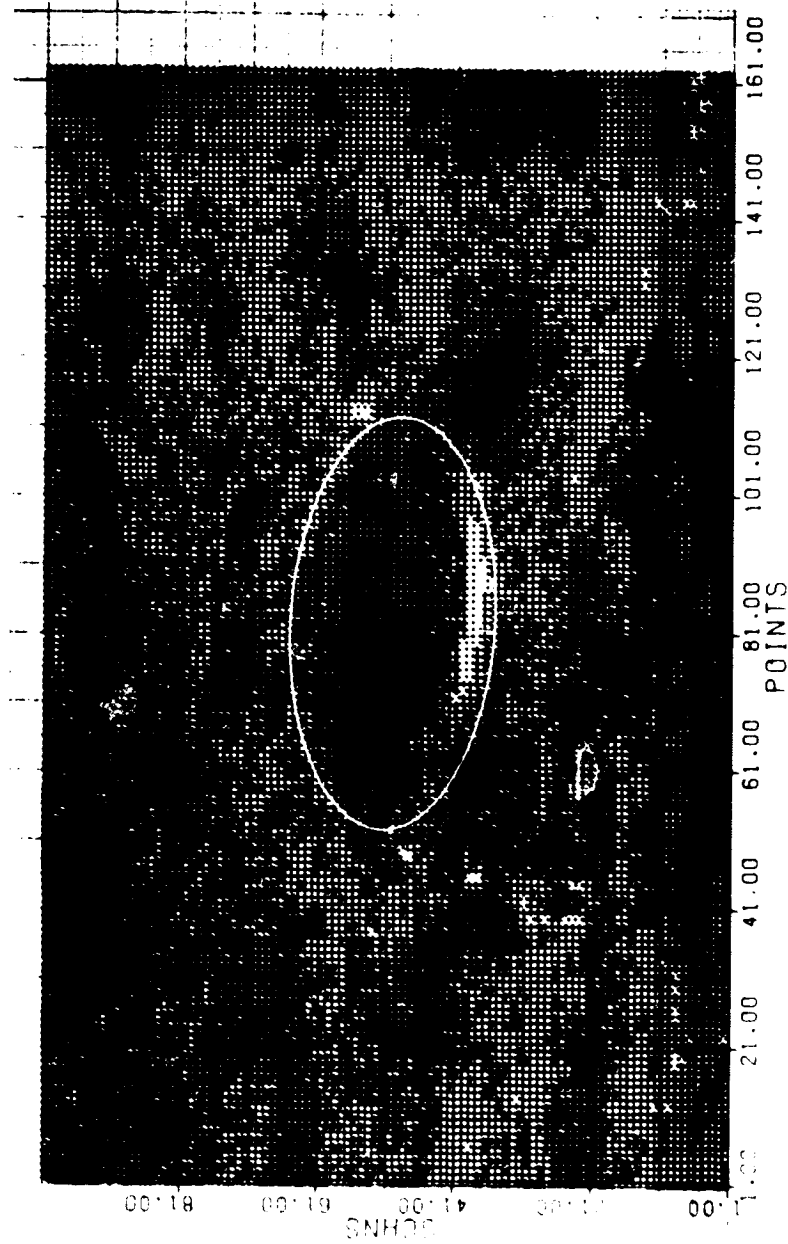


Figure 5-3. Computer generated reconstruction of target 1C, Frame 10224. Ellipse outlines area used to define crater boundary. Note shadow area (clear region) at lower edge of crater. Each plotted point is a sampled point from the original image; exposure category for each point is given in the table (denser points correspond to greater exposures).

SYMBOL EXPOSURE RANGE (M-C-S)

* >0.310

Δ 0.300 - 0.310

+ 0.290 - 0.300

• 0.280 - 0.290

BLANK <0.280

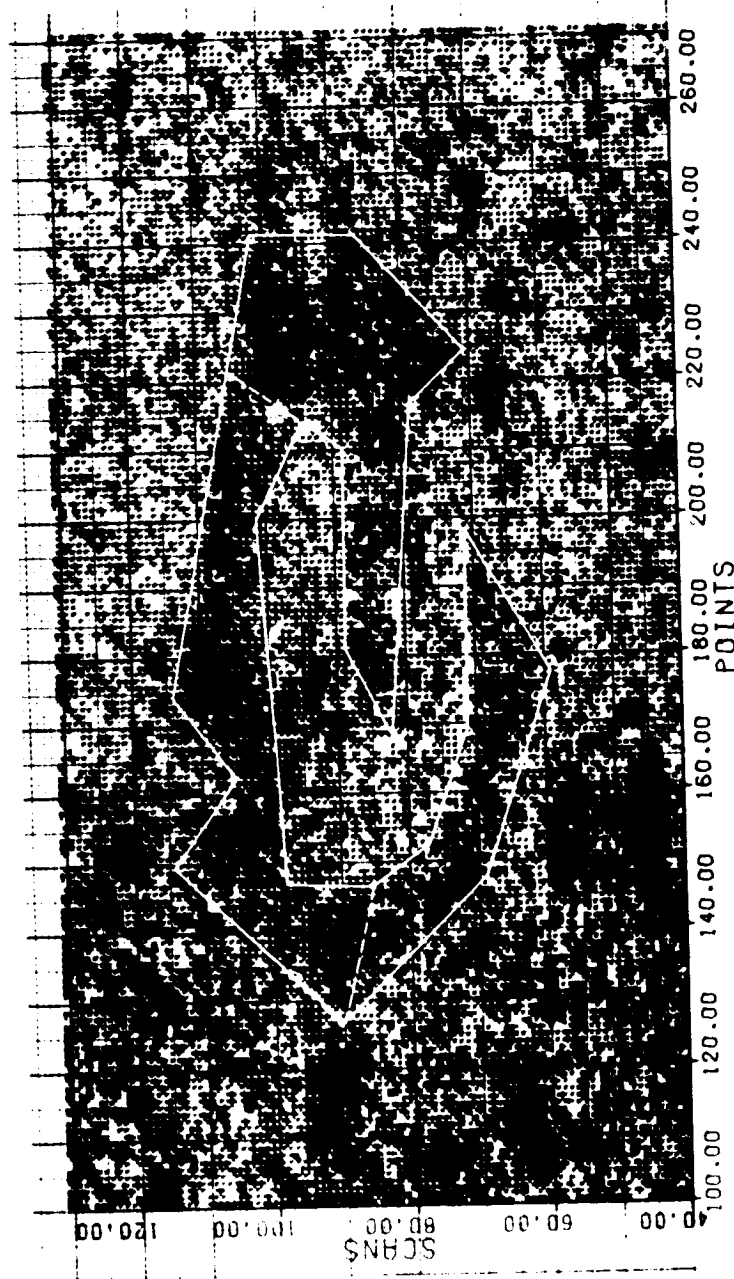
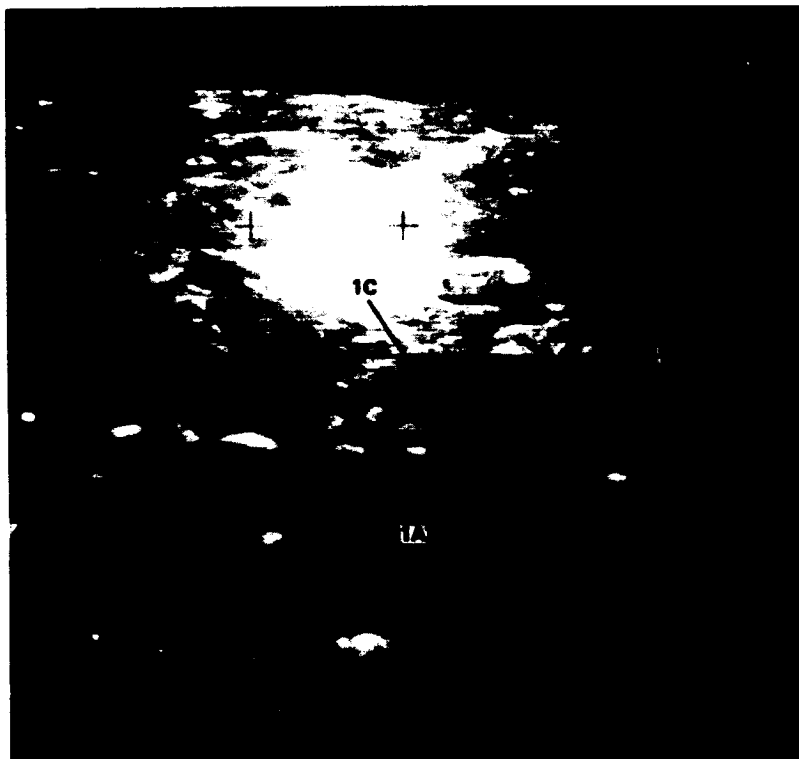


Figure 5-4. Computer generated reconstruction of target 6B, Frame 10285. Polygon outlines area used to define crater boundaries. Note that bright crater rim was taken as significant portion of this target. Dotted lines indicate subareas for which contrast was measured separately. Each plotted point is a sampled point from the original image; exposure category for each point is given in the table (denser points correspond to greater exposures).

→ AREA 1 PASS
10223

0 SEC

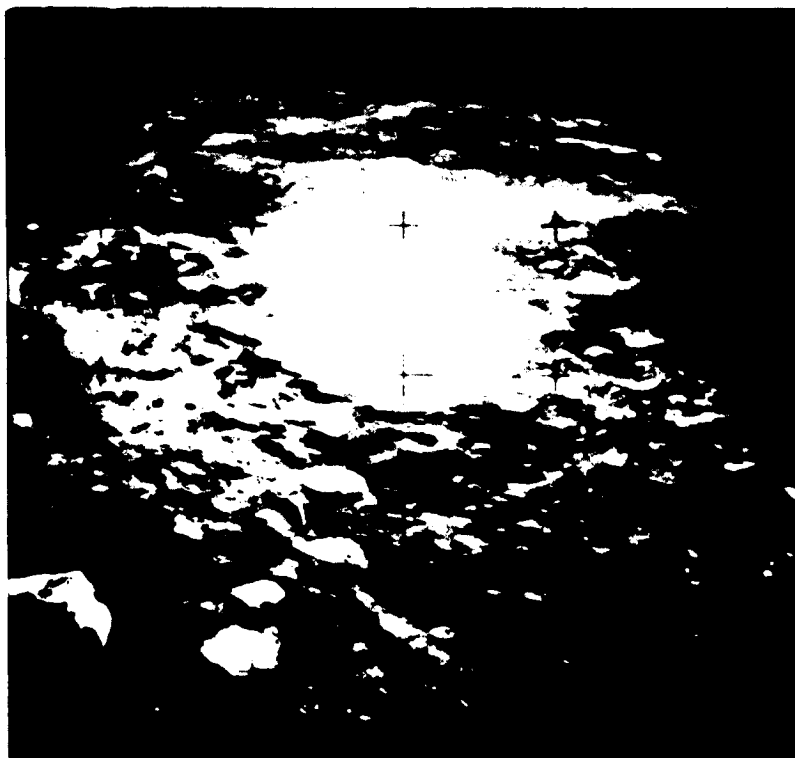


10224

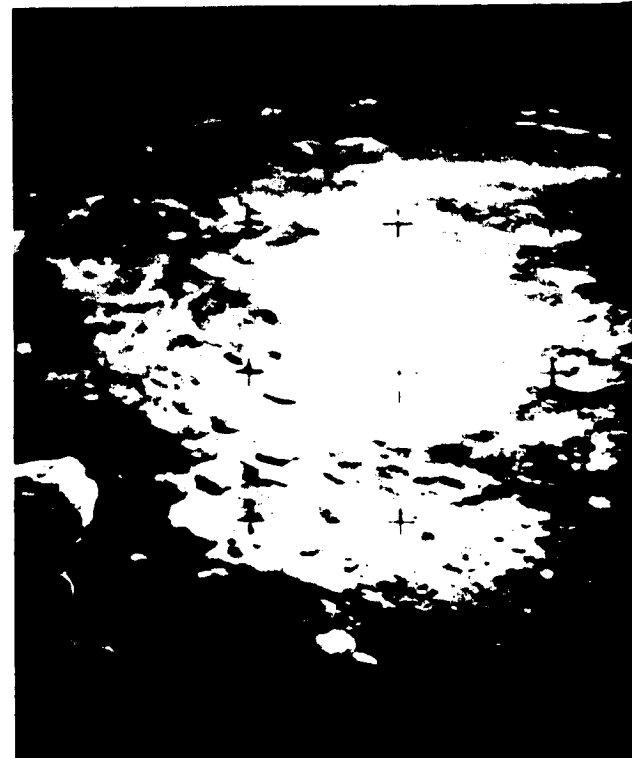


10227

61 SEC



10228



FOLDOUT FRAME

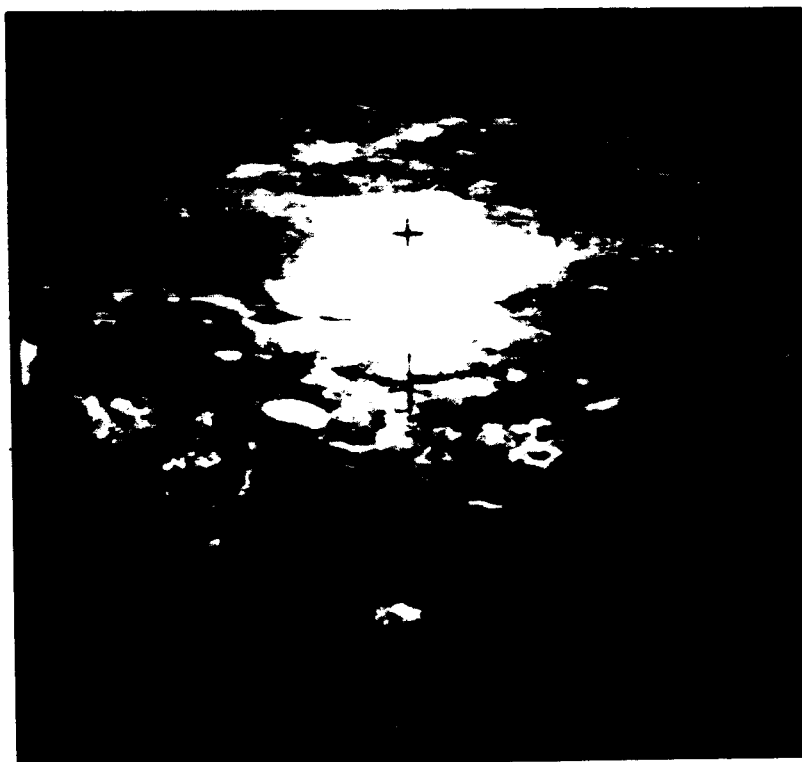
10223
10224
10227
10228

20 SEC

10225

40 SEC

10226



81 SEC

10229

82 SEC

10230

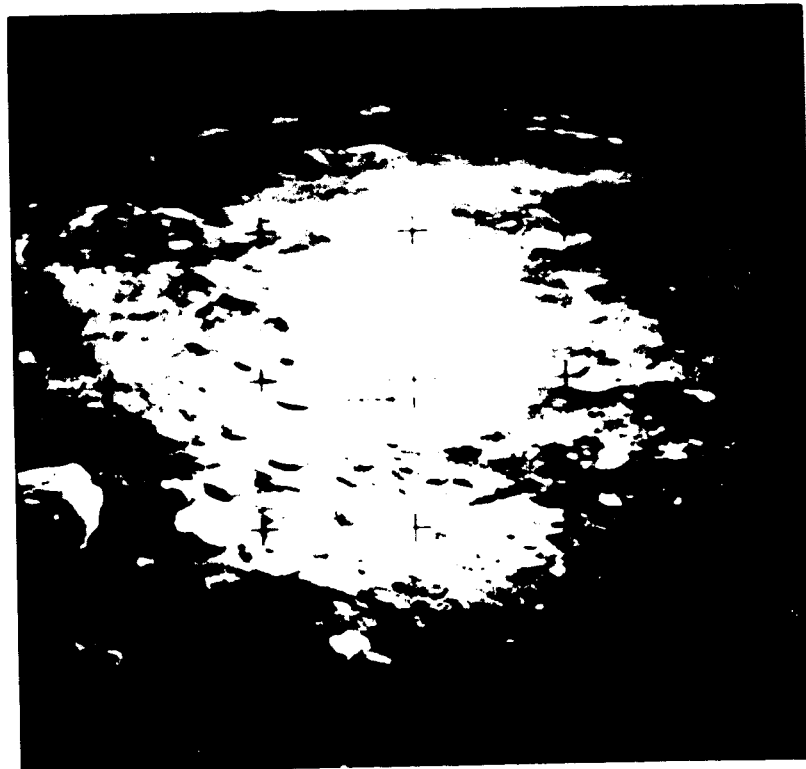


Figure 5-5.

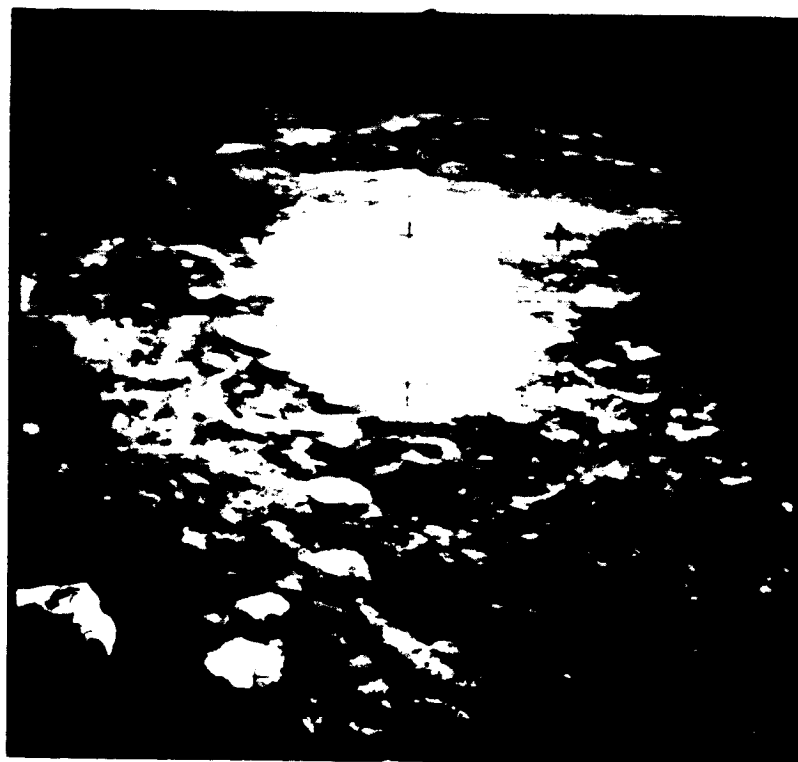
Hasselblad 70mm Frame
Relative Frame Times
are Identified on Frame
(Area 2). See Table
and Viewing Data.

OUT FRAM

40 SEC



10226

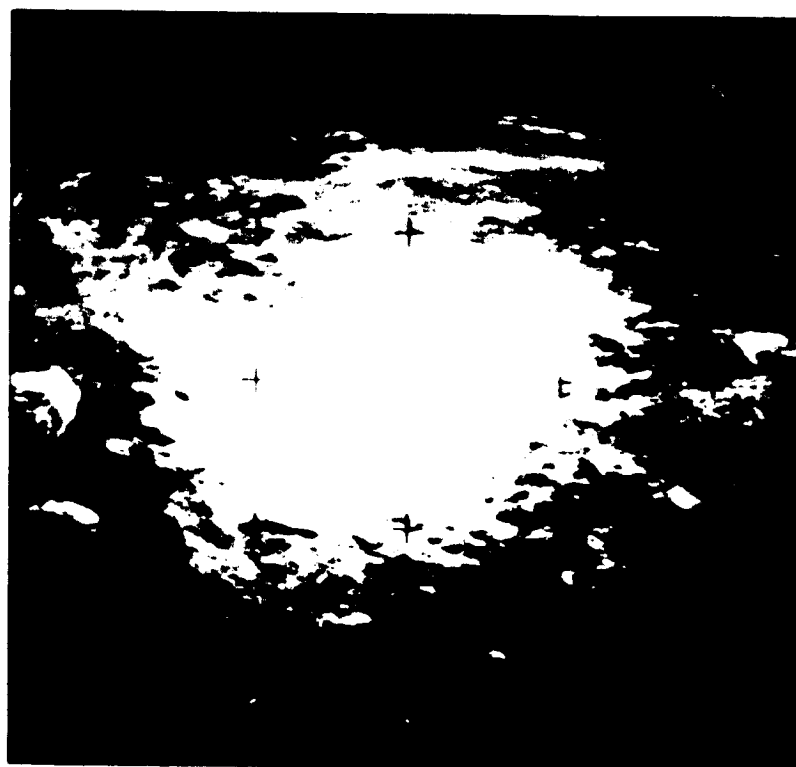


60 SEC

82 SEC



10230

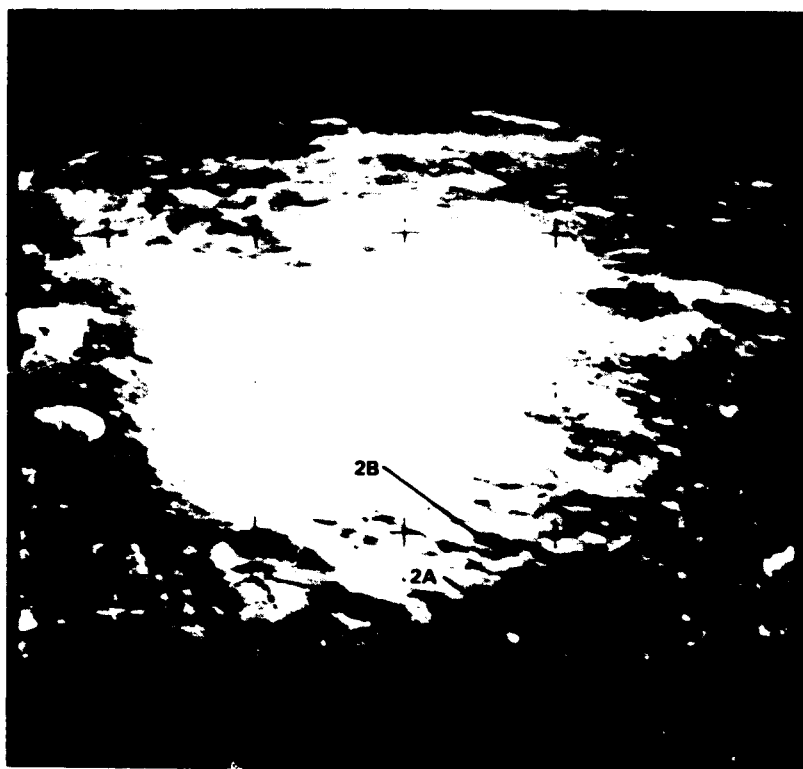


102 SEC

Figure 5-5. Hasselblad 70mm Frames from 16B Pass (Areas 1 and 2). Relative Frame Times are Given With Each Frame. Targets are Identified on Frames 10223 (Area 1) and 10231 (Area 2). See Table 5-1 for Corresponding Trajectory and Viewing Data.

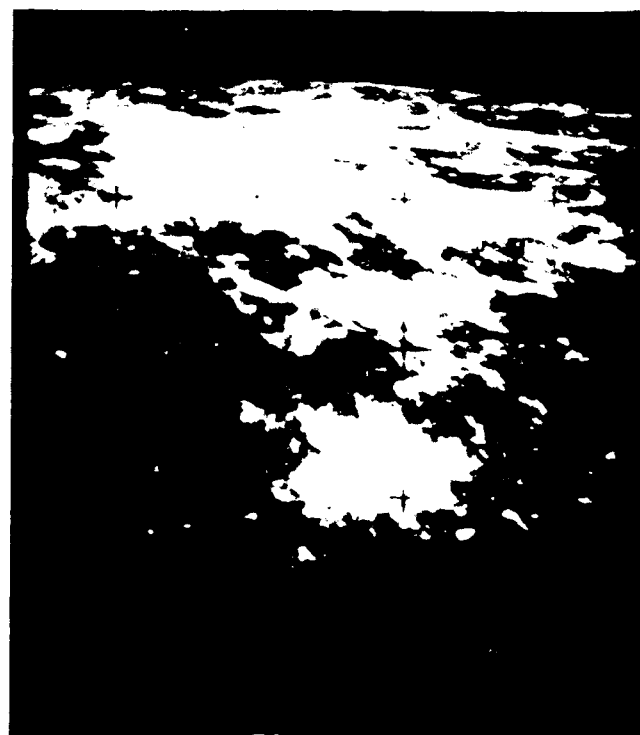
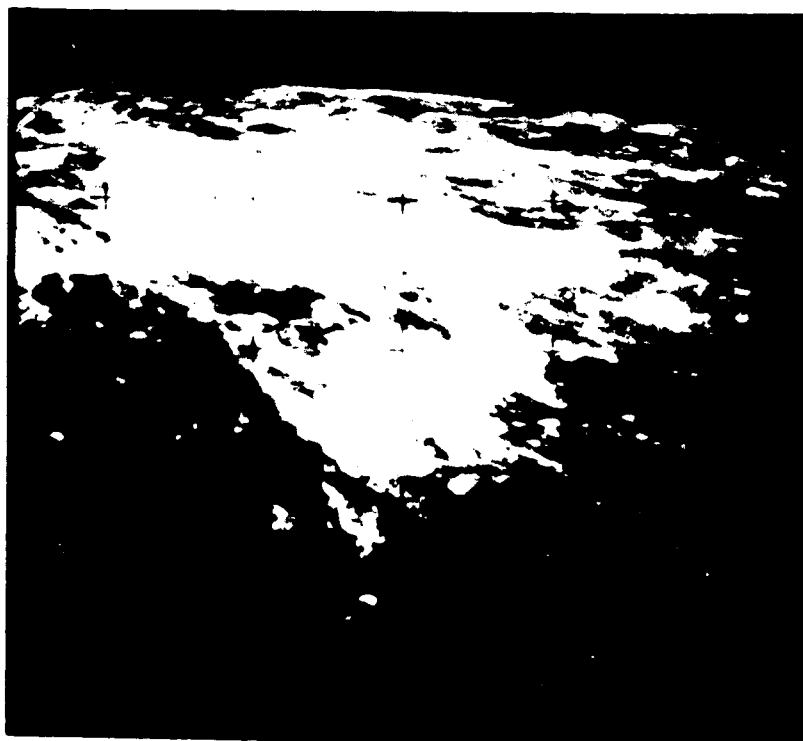
122 SEC

10232



202 SEC

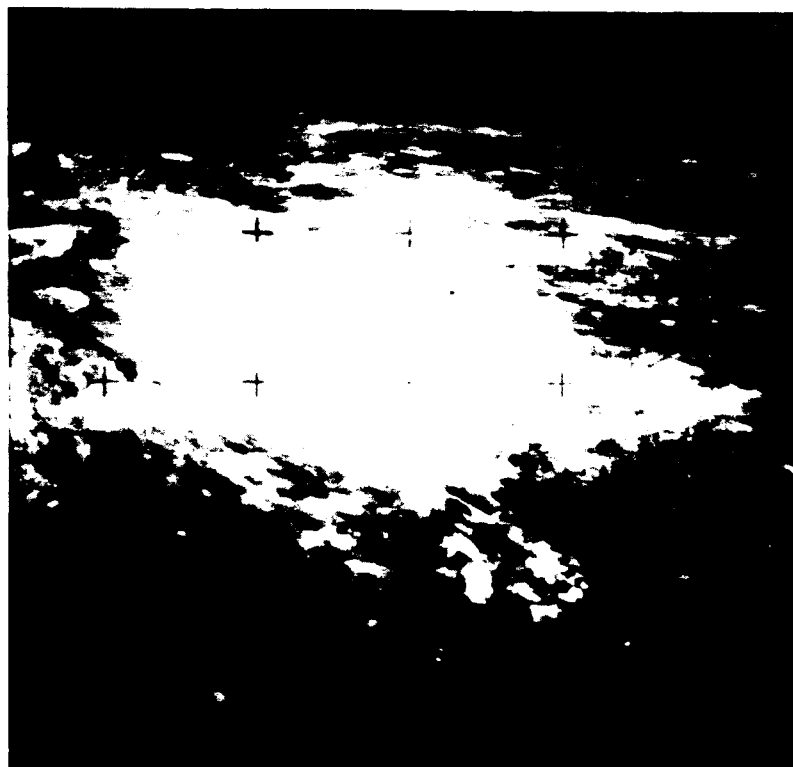
10236



142 SEC

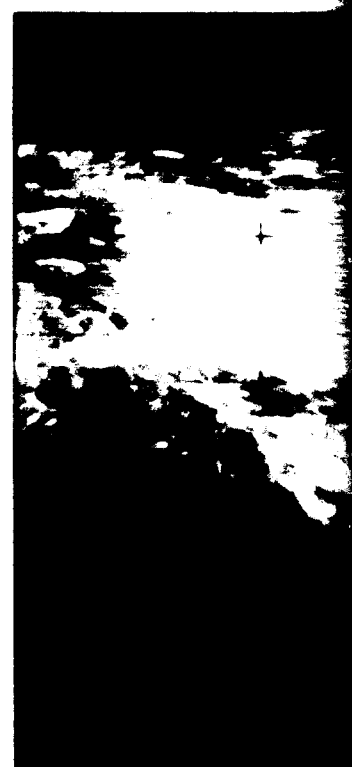


10233



162 SEC

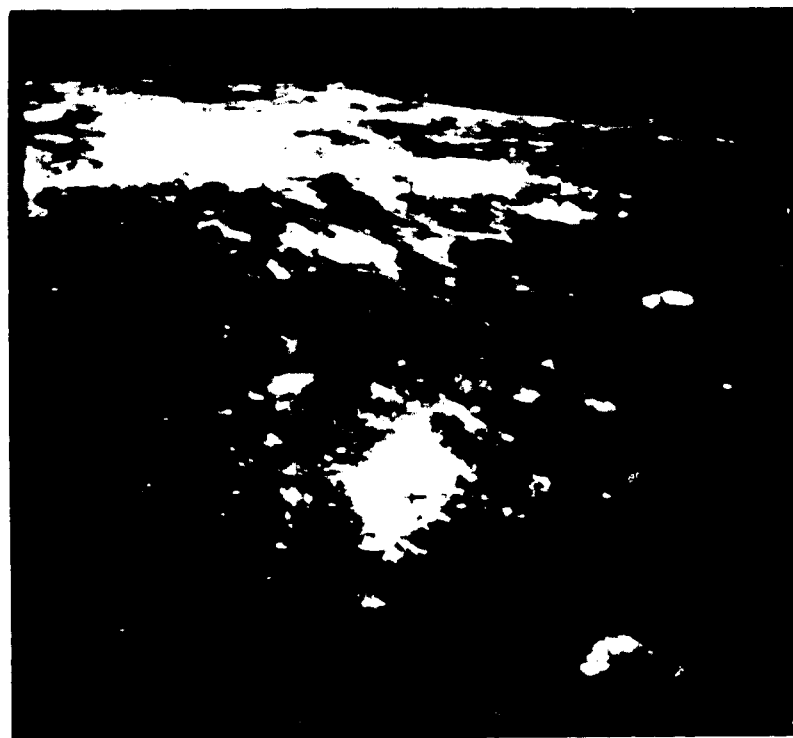
10234



222 SEC



10237



242 SEC

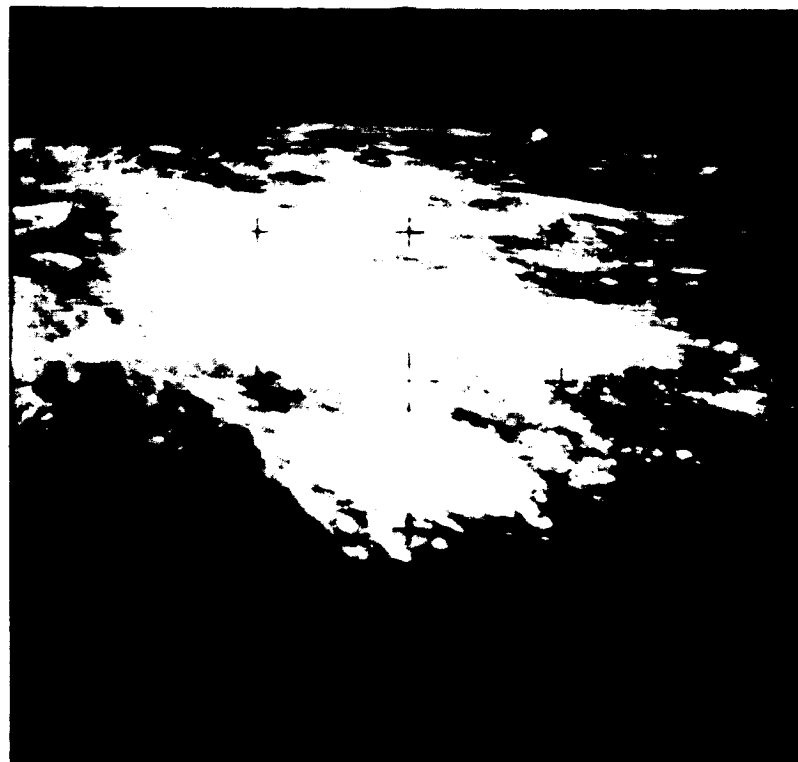
10238



162 SEC

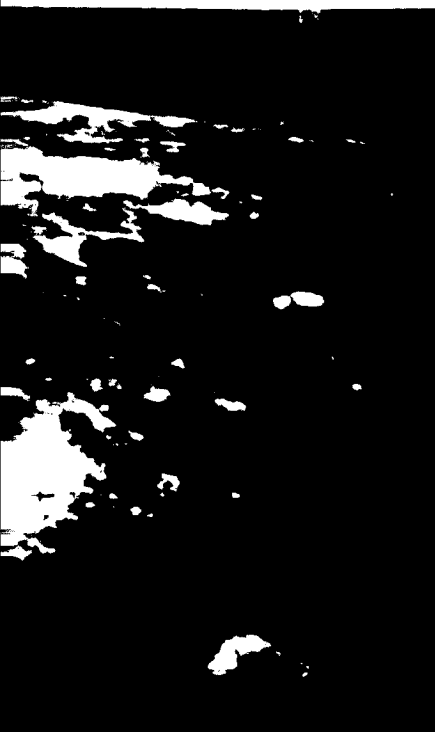


10234



182 SEC

242 SEC



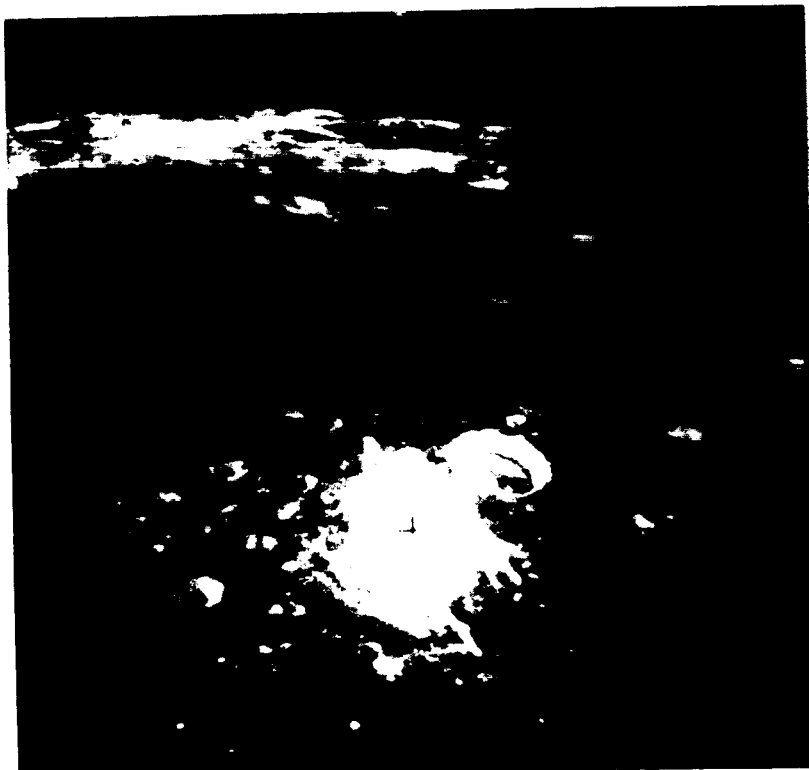
10238



262 SEC

10239

282 SEC



10240



10243

362 SEC



10244



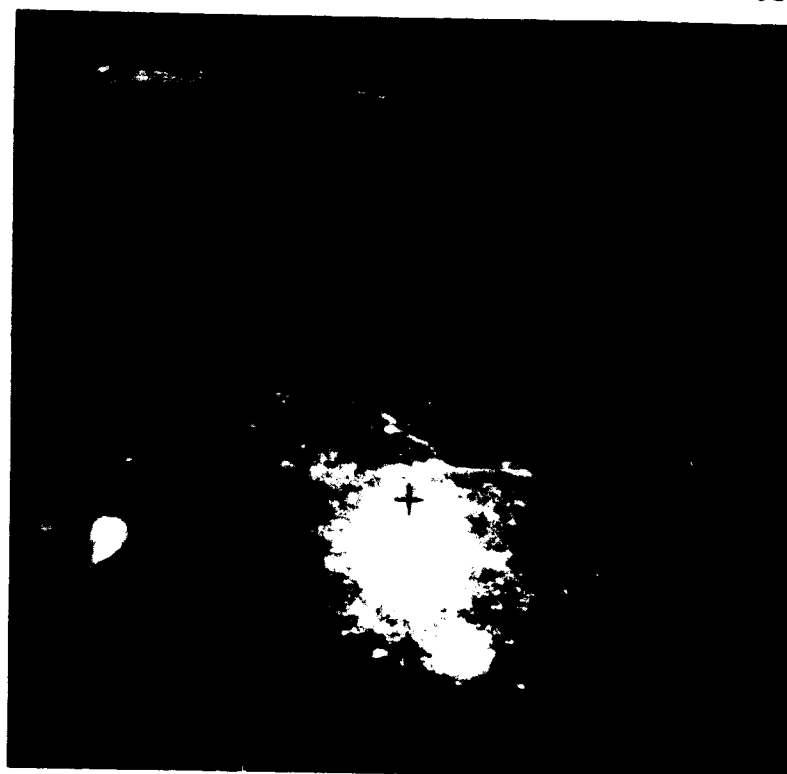
FOLDOUT FRAME

ORIGINAL PAGE IS
OF POOR QUALITY

302 SEC



10241



322 SEC

10242



382 SEC



10245



390 SEC

FOLDOUT FRAME

ORIGINAL PAGE IS
CONTAINED IN

322 SEC

10242

342 SEC



390 SEC



ORIGINAL PAGE IS
OF LOW QUALITY

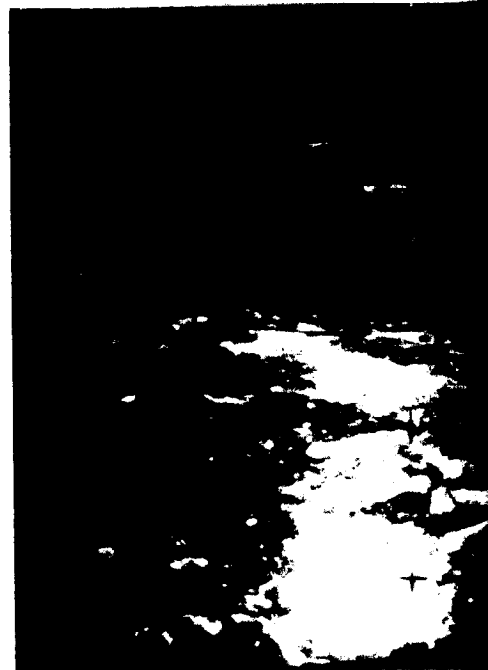
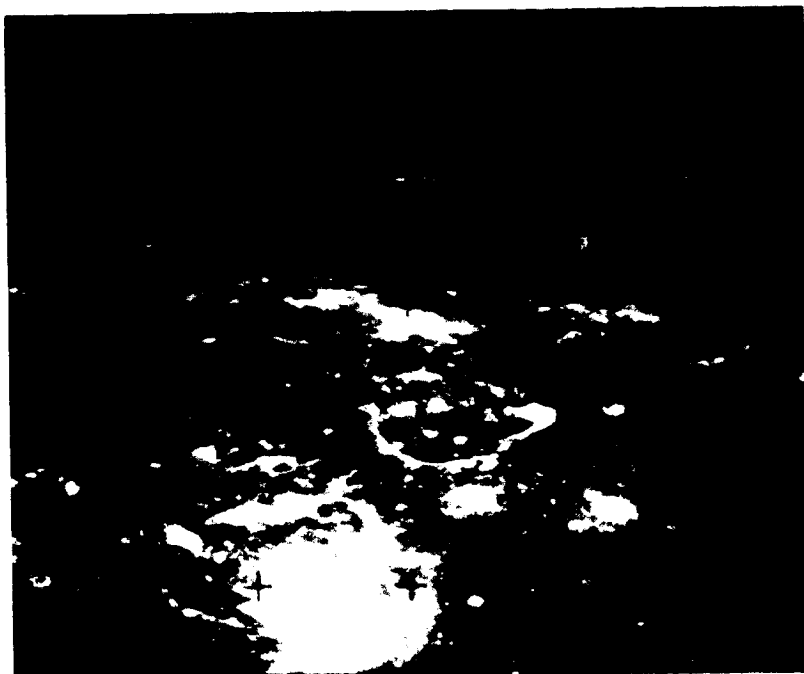
FOLDED: FRAM

→ AREA 3 PASS

10246

0 SEC

10247



10251

100 SEC

10252



RECEIVED 10/10/77

RECEIVED 10/10/77

20 SEC



10248

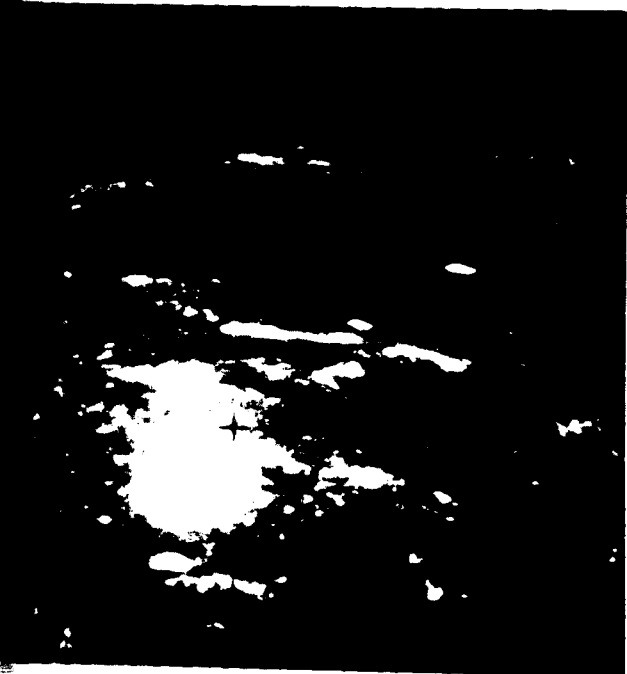


40 SEC

10249



120 SEC



10253



140 SEC

10254



40 SEC

10249

60 SEC

10250

140 SEC

10254

160 SEC

10255

Figure 5-6.

Hasselblad 70mm Frames from
Relative Frames Time are Given
Targets are Identified on Frame
10266 (Area 4). See Table 5-2
Trajectory and Viewing Data.

50 SEC

10250

80 SEC



160 SEC

10255

180 SEC

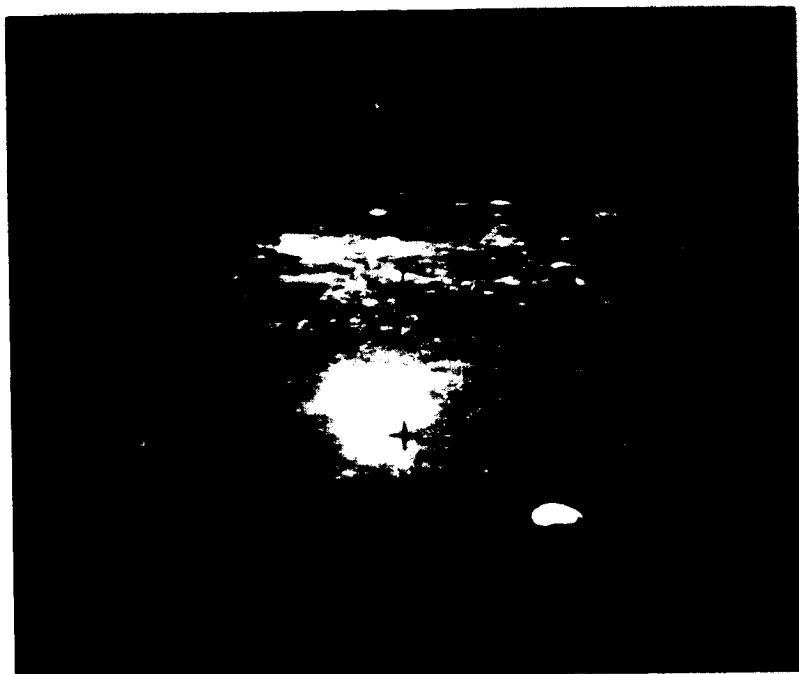


Figure 5-6. Hasselblad 70mm Frames from 16F Pass (Areas 3 and 4)
Relative Frames Time are Given With Each Frame.
Targets are Identified on Frames 10258 (Area 3) and
10266 (Area 4). See Table 5-2 for Corresponding
Trajectory and Viewing Data.

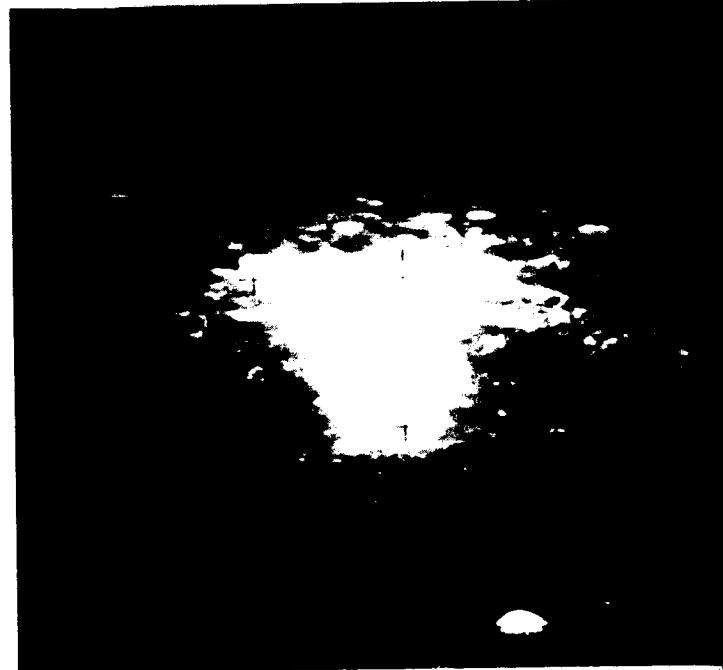
Area 3 Pass

10256

200 SEC



10257

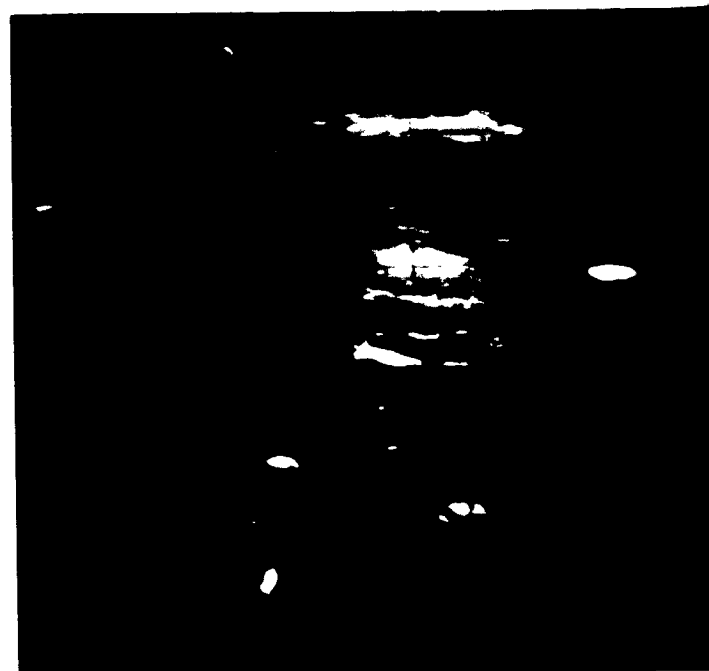


10261

300 SEC



10262



ORIGINAL PAGE IS
OF POOR QUALITY

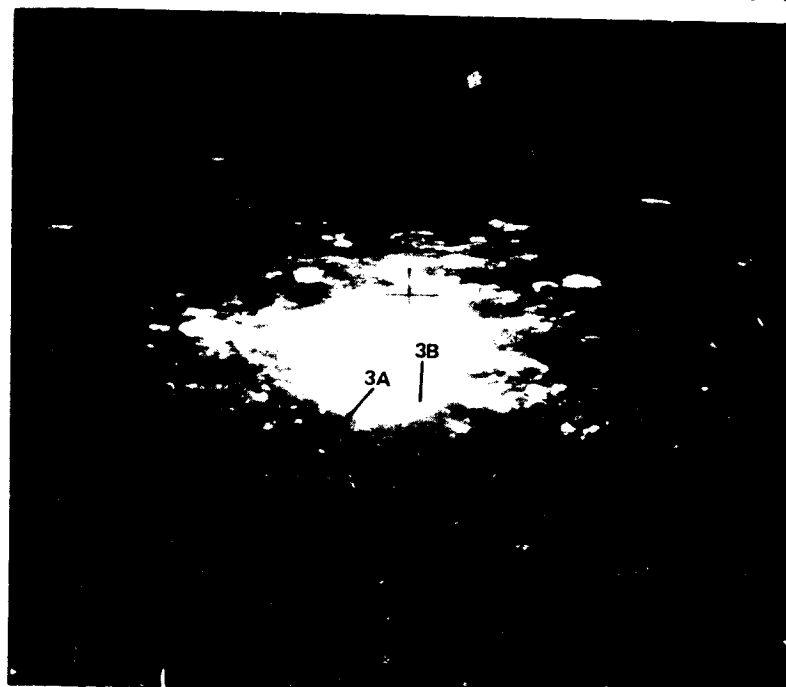
FOLDOUT FRAME

220 SEC

10258

240 SEC

10259

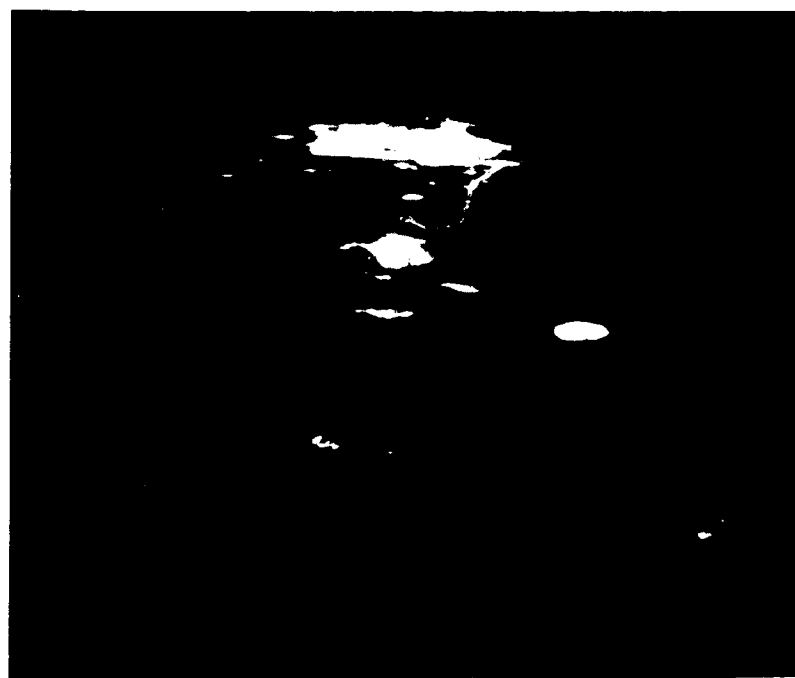
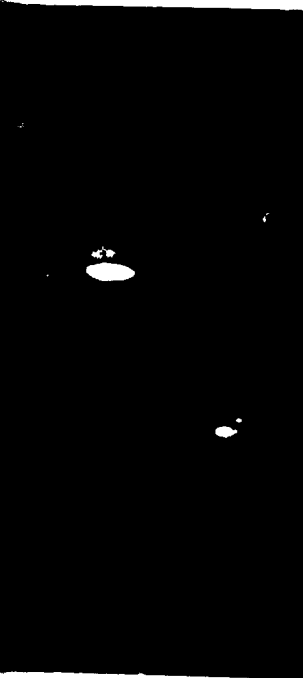


320 SEC

10263

340 SEC

10264



ORIGINAL PAGE IS
OF POOR QUALITY

SOLO DOUT FRAME

AREA 4 PASS

260 SEC

10260

280 SEC



360 SEC

10265

380 SEC

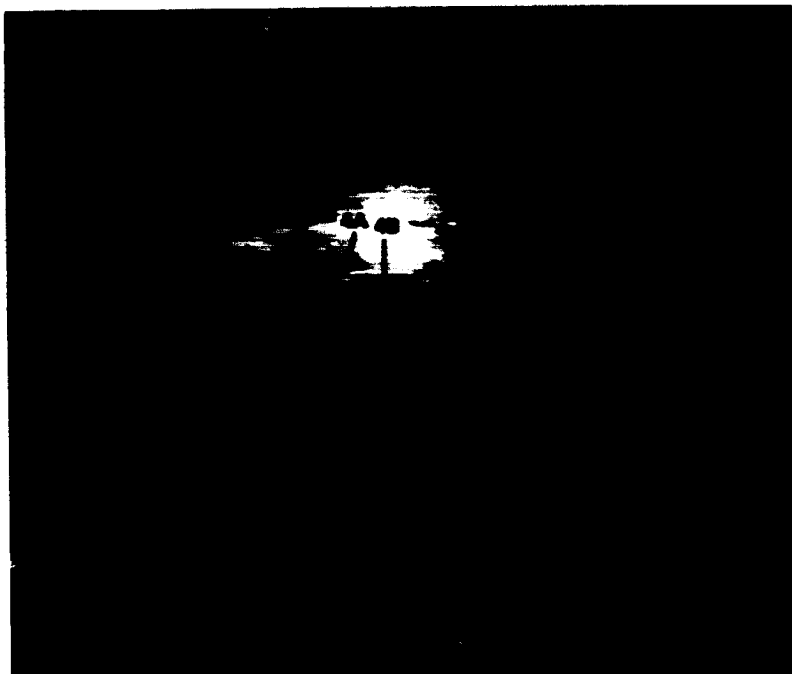


COPIES OF THIS PAGE TO
 BE FORN OFFICES
 FOR INFORMATION FRAME

Figure 5-6. Continued

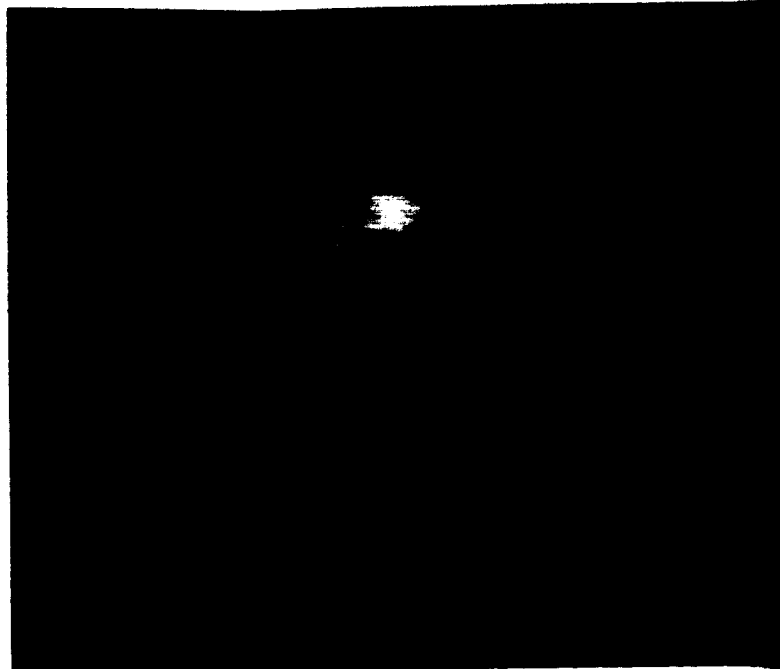
10266

400 SEC



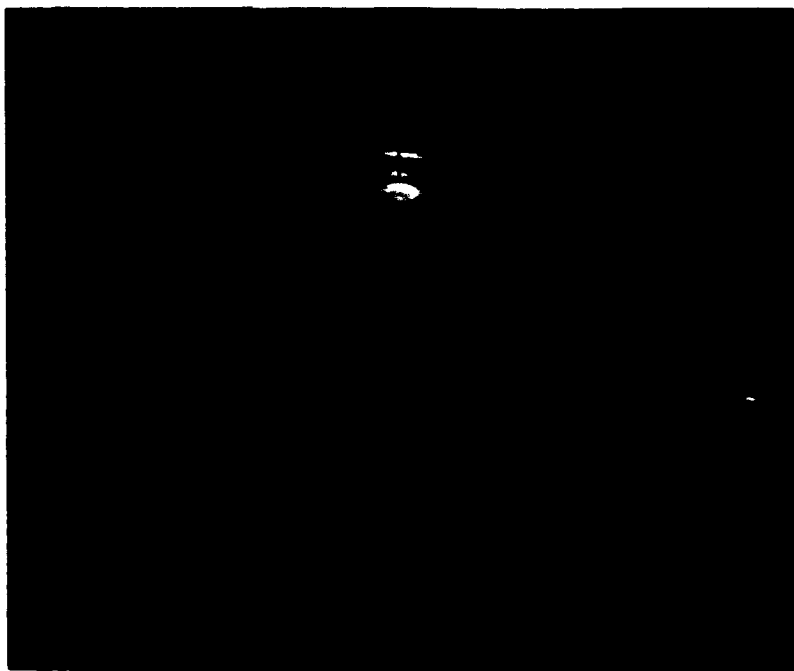
10267

420 S



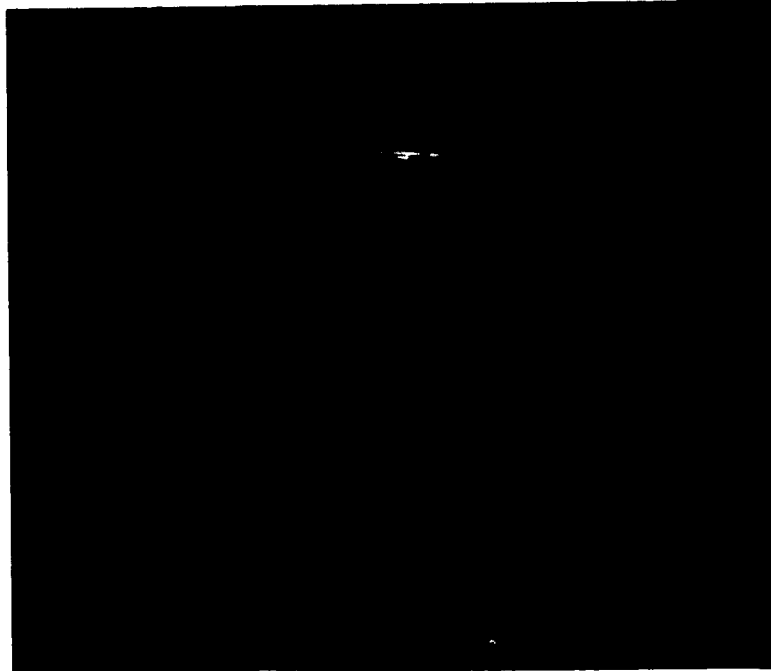
10270

461 SEC



10271

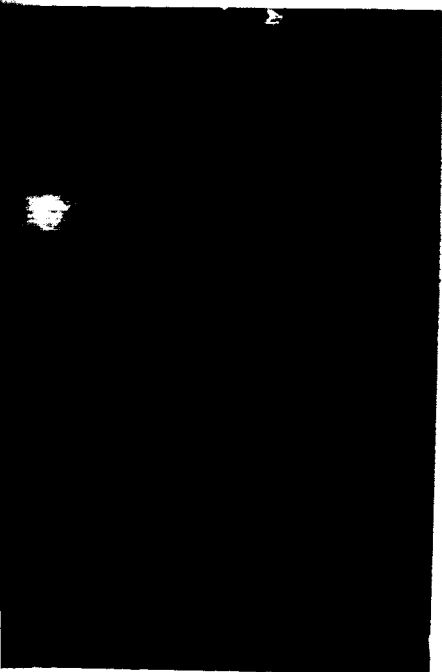
481 S



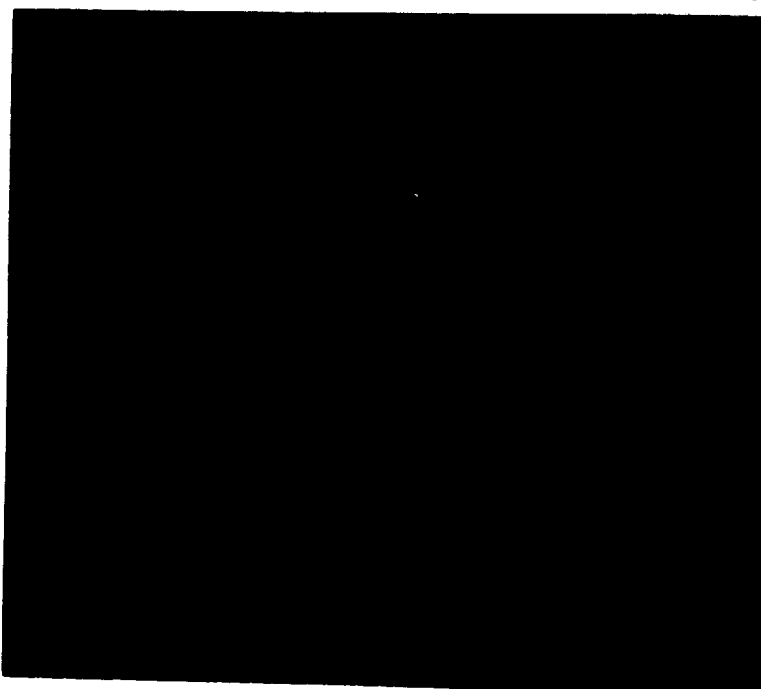
ORIGINAL PAGE IS
OF QUALITY

מחזור חורף

420 SEC

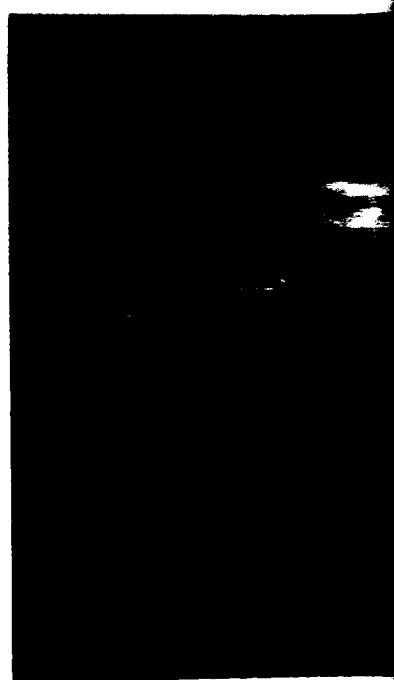


10268

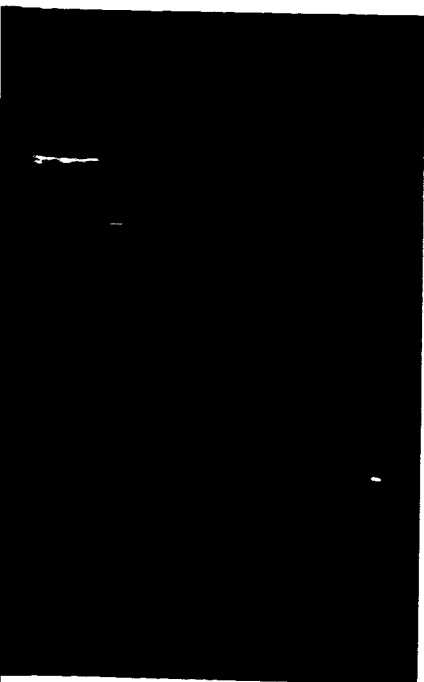


440 SEC

10269



481 SEC



10272



501 SEC

440 SEC

10269

441 SEC

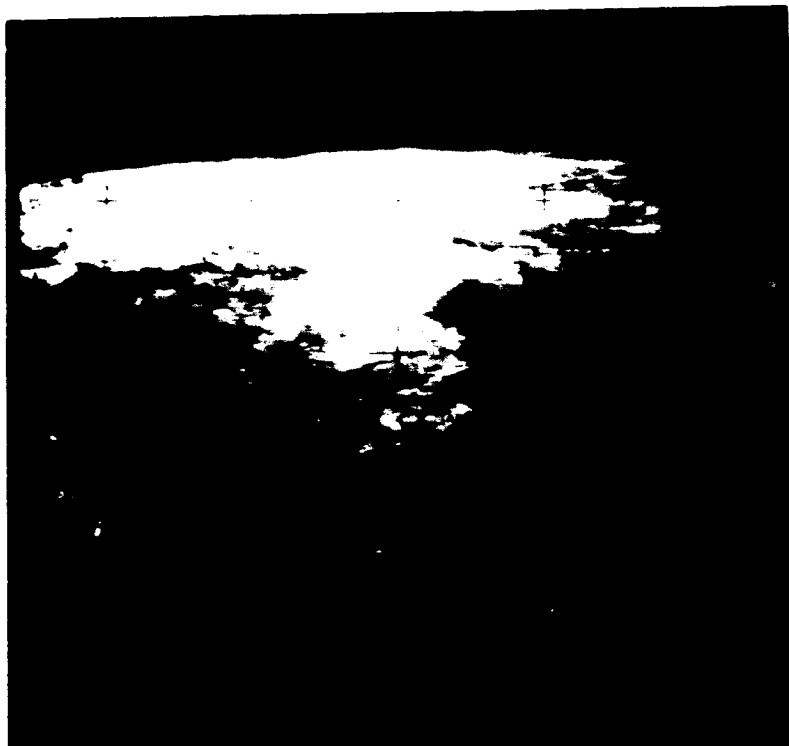
501 SEC

END OF FRAME

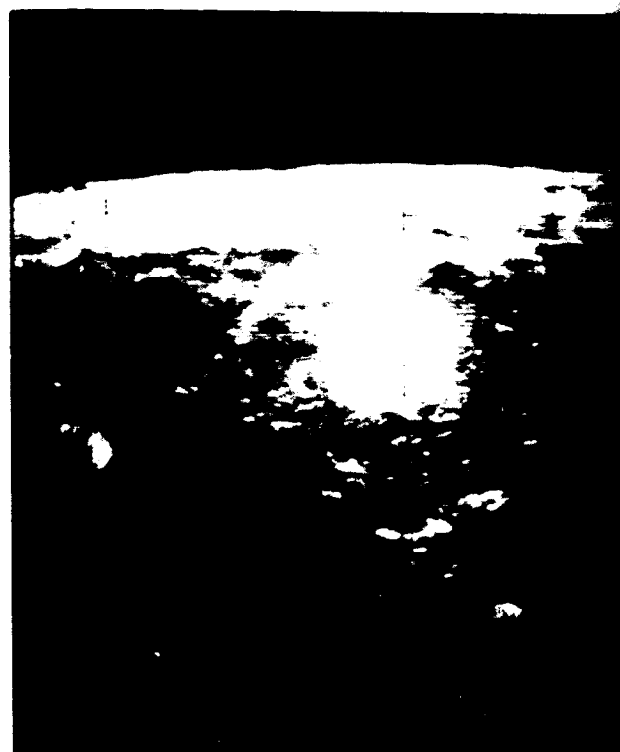
→ AREA 5 PASS

10273

0 SEC

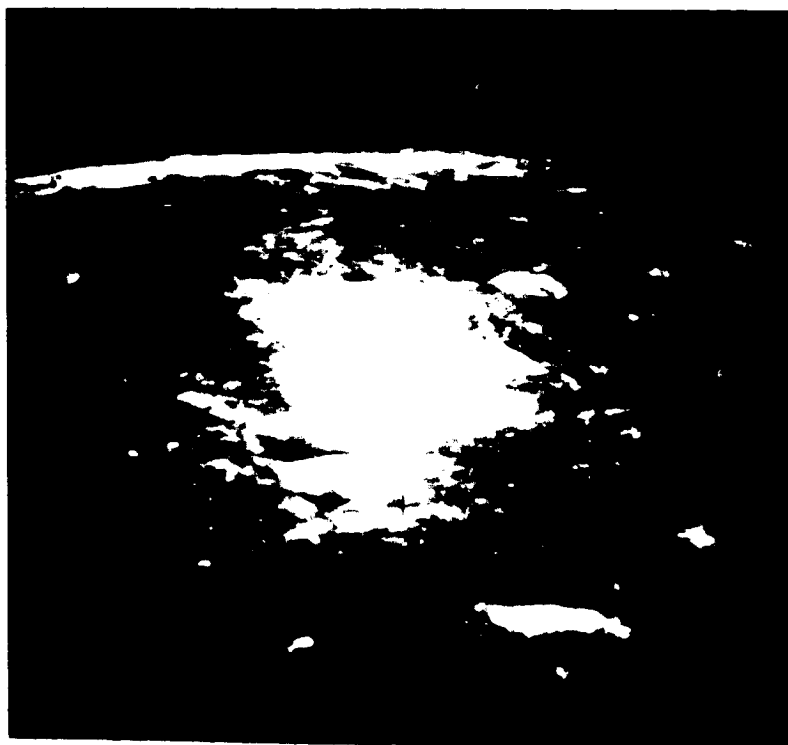


10274

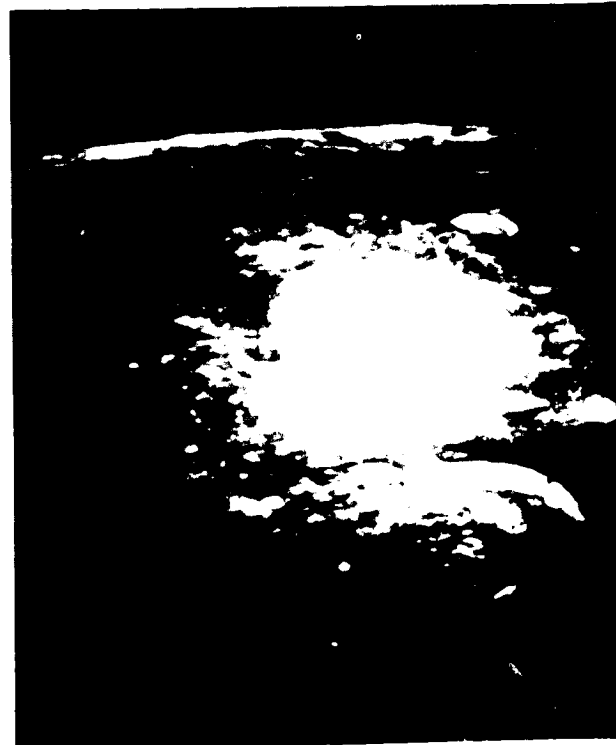


10278

79 SEC



10279

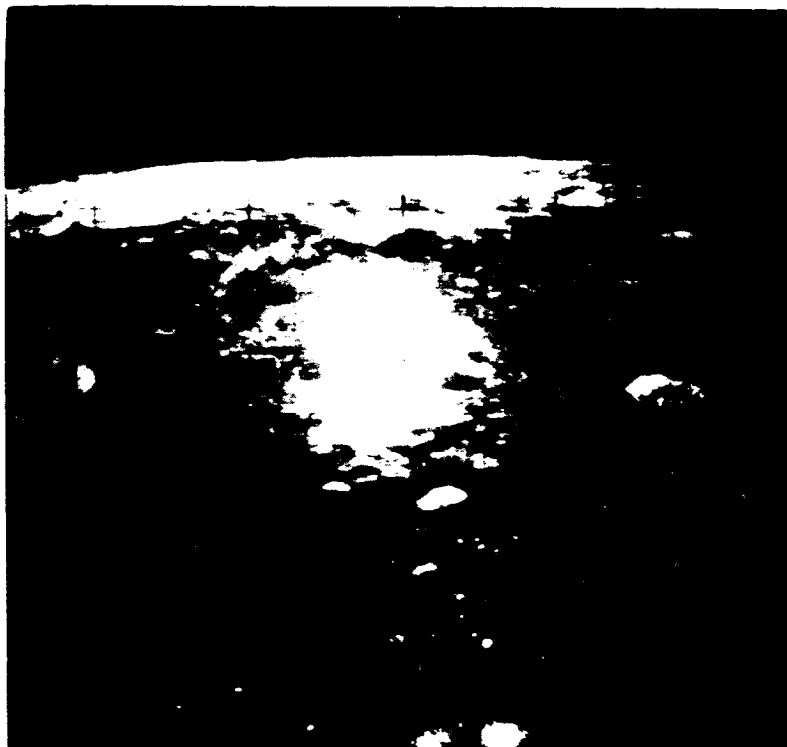
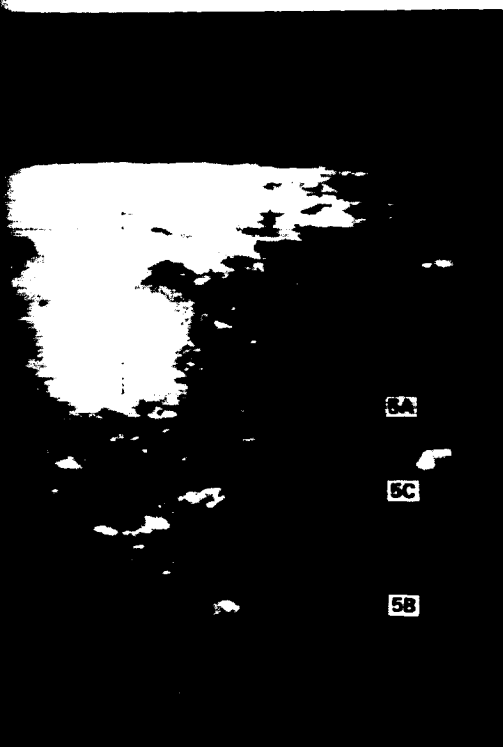


20 SEC

10275

39 SEC

10276

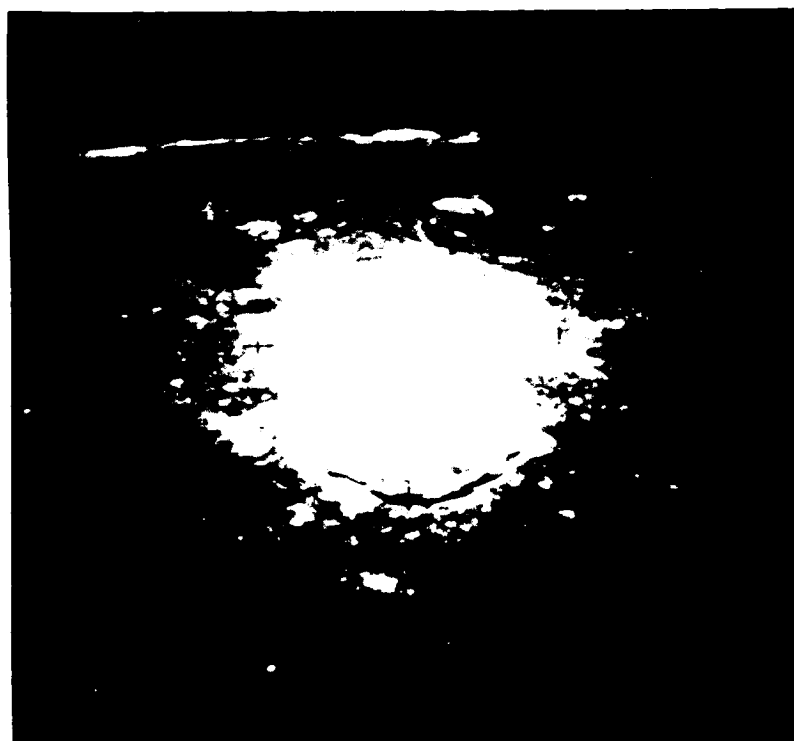


99 SEC

10280

118 SEC

10281

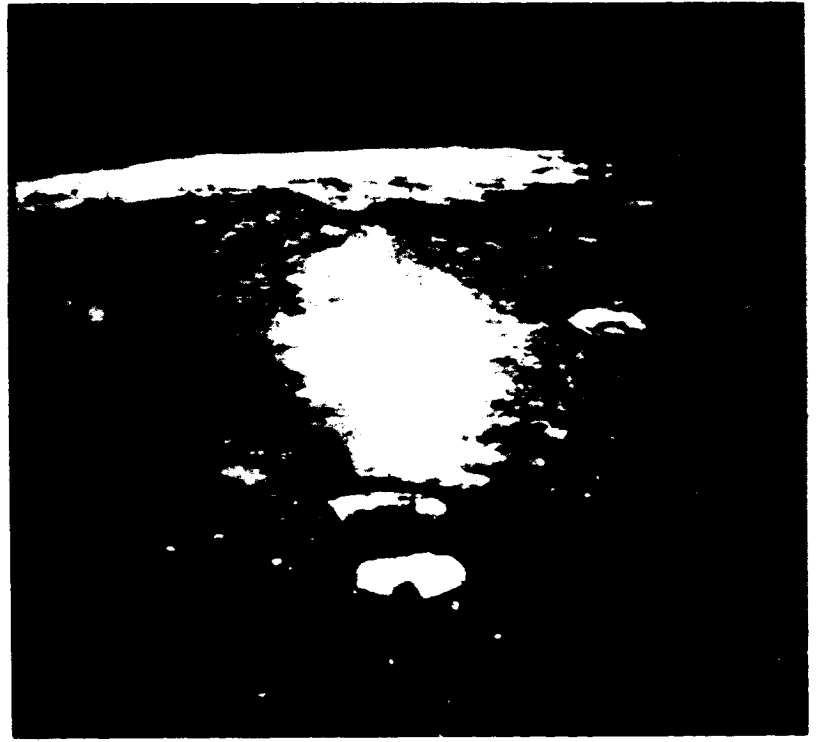


FOLDOUT FRAME

59 SEC

10277

60 SEC



138 SEC

10282

157 SEC



→ AREA 6 PASS

Figure 5-7.

Hasselblad 70mm Frames from 30B Pass (Areas 5 and 6). Relative Frame Times Are Given With Each Frame. Targets Are Identified on Frames 10274 (Area 5) and 10283 (Area 6). See Table 5-3 For Corresponding Trajectory And Viewing Data.

ORIGINAL PAGE IS
OF POOR QUALITY
FOLDOUT FRAME.

A high-contrast, black and white photograph of a dark, textured surface, possibly a rock or cave wall. The surface is covered in intricate, light-colored patterns and textures. A bright, circular light source is visible in the upper right quadrant, creating a strong contrast with the dark background. The overall composition is abstract and dramatic.

A high-contrast, black and white photograph of a dark, textured surface, possibly a book cover or a piece of fabric. A bright, glowing circular light source is visible in the lower center, surrounded by smaller, scattered light spots. The overall image is very dark, with the light source providing the primary illumination.

(continued from page 60)

the same time, it is important to note that the majority of the respondents were male, which may have influenced the results. Future research should include a more diverse sample of participants.

In conclusion, the findings of this study suggest that there are several factors that can influence the effectiveness of a training program. These factors include the type of training, the duration of the training, the quality of the training materials, and the support provided by the organization. By understanding these factors, organizations can design more effective training programs that will lead to improved performance and productivity.

[illegible]

ORIGINAL PAGE IS
OF LOWER QUALITY

236 SEC

10287

256 SEC



334 SEC

10292

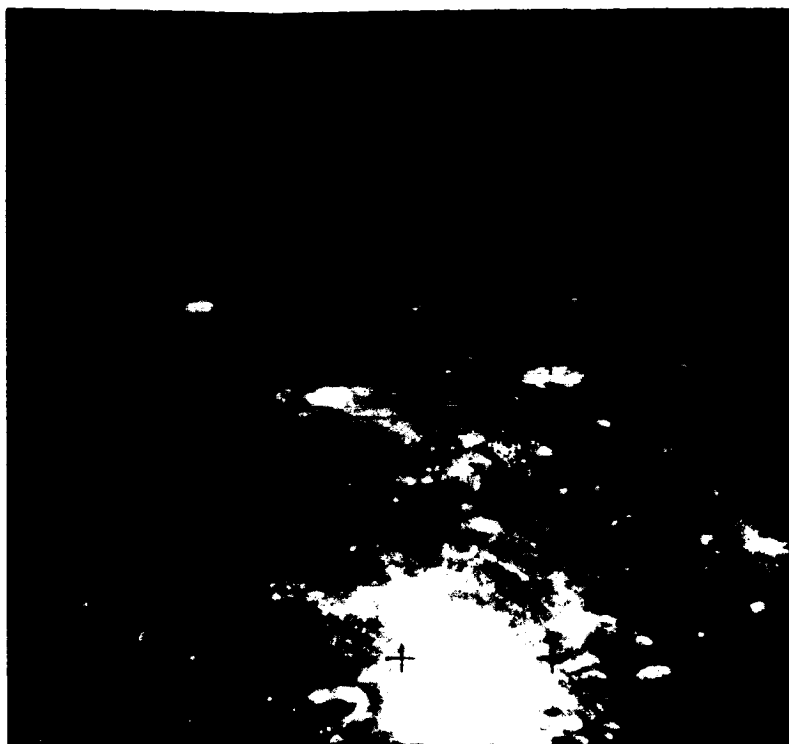
353 SEC



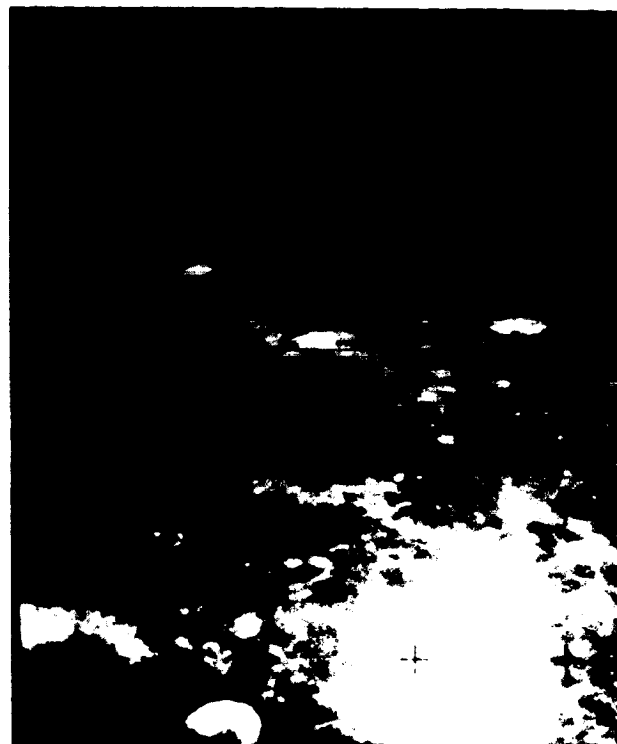
Figure 5-7. Continued

10293

373 SEC

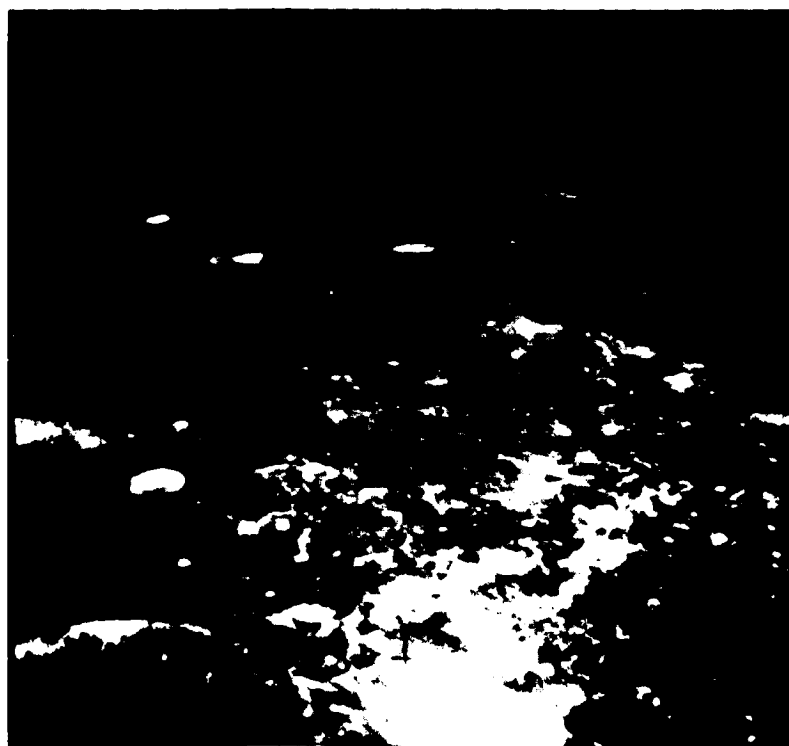


10294

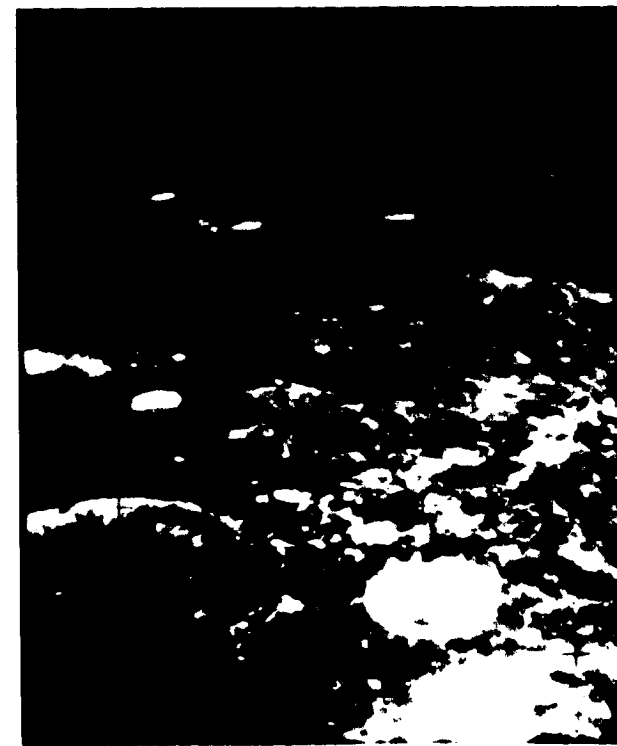


10296

431 SEC



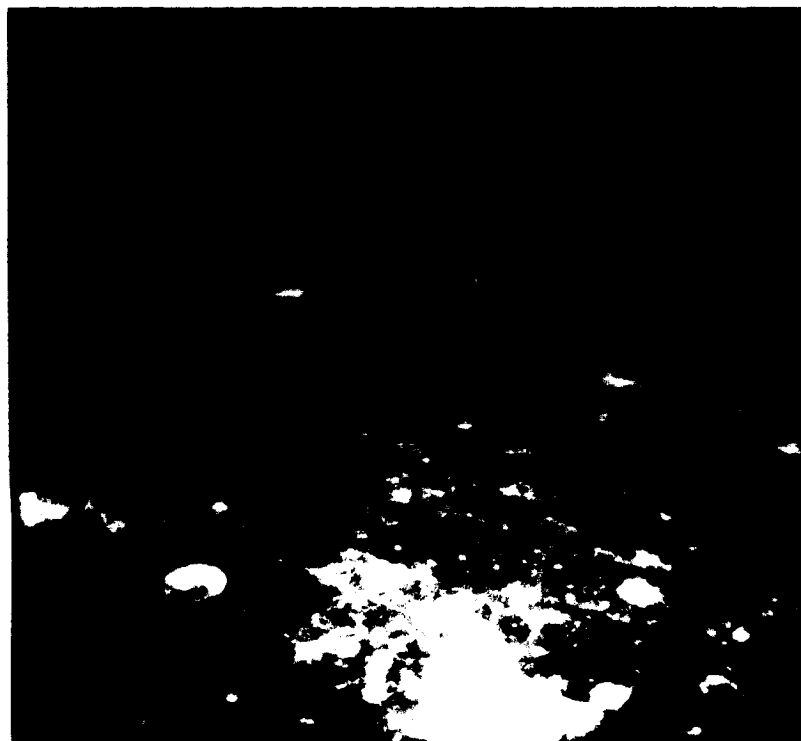
10297



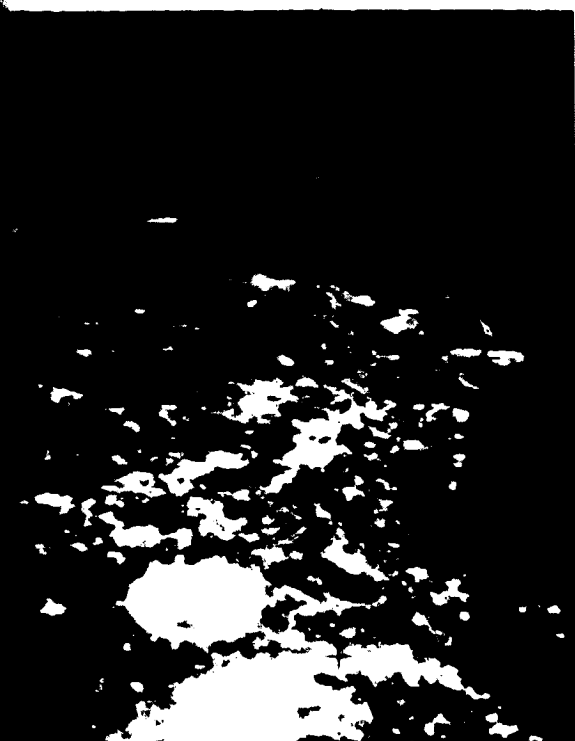
392 SEC

10295

412 SEC



451 SEC



451 SEC

ORIGINAL PAGE IS
OF POOR QUALITY

Figure 5-7. Continued

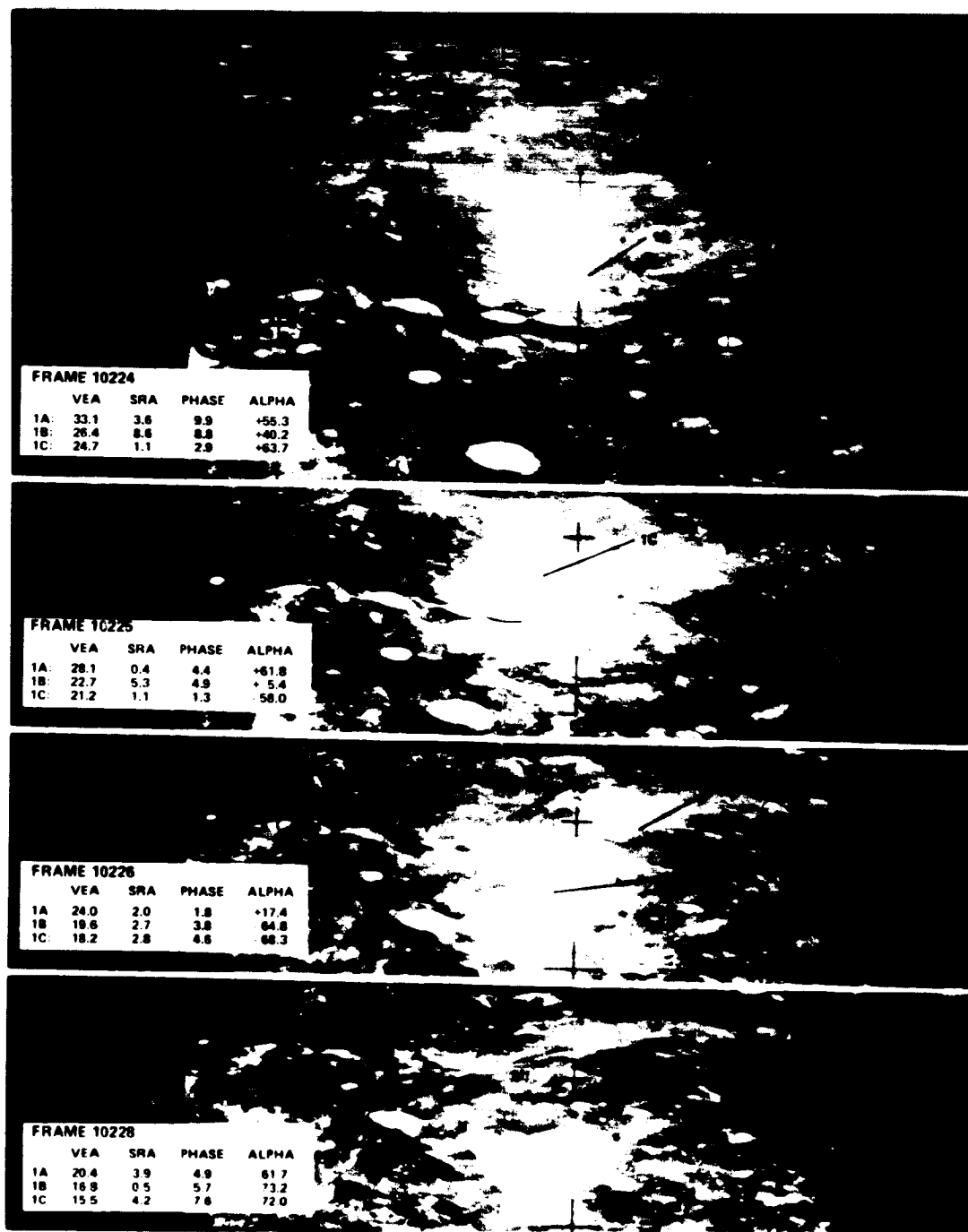


Figure 5-3. Targets 1A, 1B, and 1C. Frame 10224 shows all targets in "good" visibility region, Frame 10225 shows 1C at photographic minimum phase, Frame 10226 shows 1A and 1B at photographic minimum phase, Frame 10228 shows all targets in washout. SEA 23.7° at 1A, 22.5° at 1B, and 22.0° at 1C. (All angles are in degrees.)

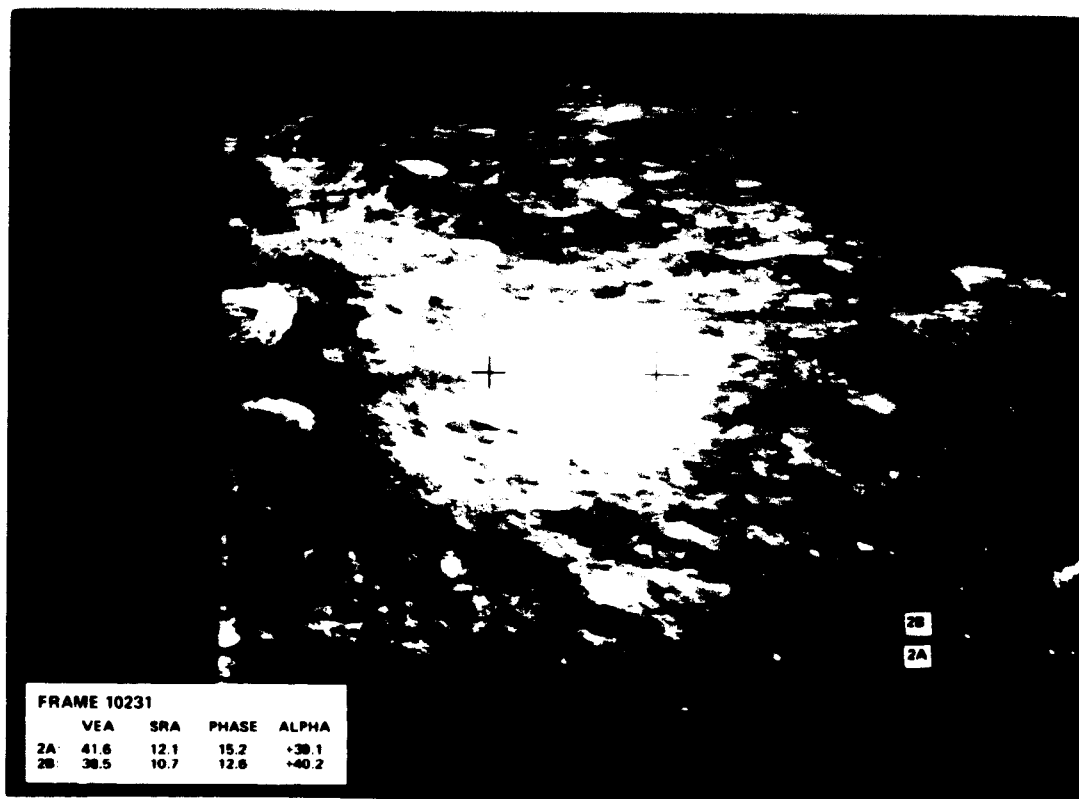


Figure 10-1. Targets 2A and 2B. Frame 10231 shows both targets in the good visibility region, frame 10233 at the transition to radar only, frame 10234 in the radar only region. SRA = 0.9 at 2A, 29.6 at 2B. (All angles in degrees.)

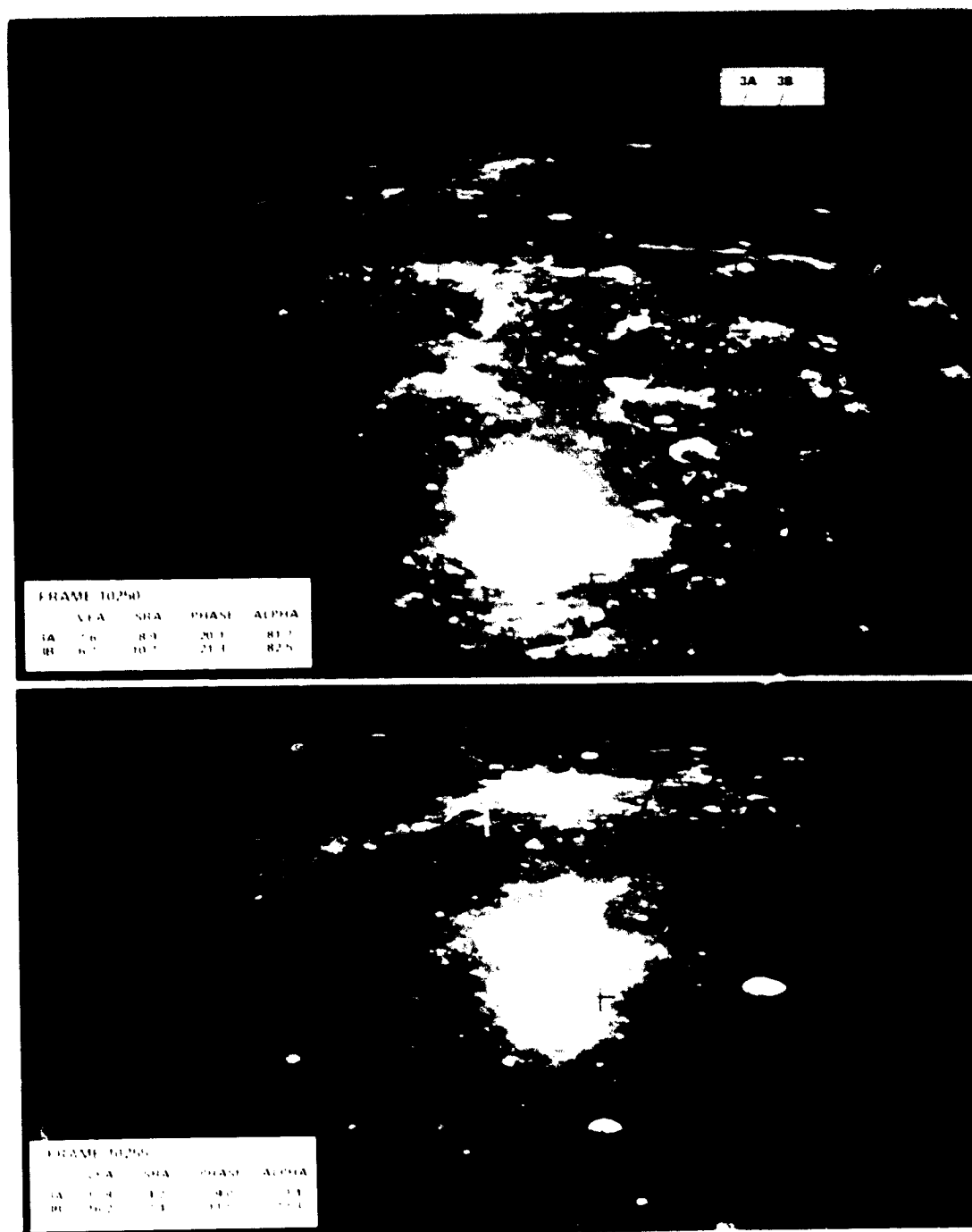


Figure 5-10a. Targets 3A and 3B. Both frames show targets in washout region. SEA 25.9° at 3A, 25.3° at 3B. (All angles in degrees.)

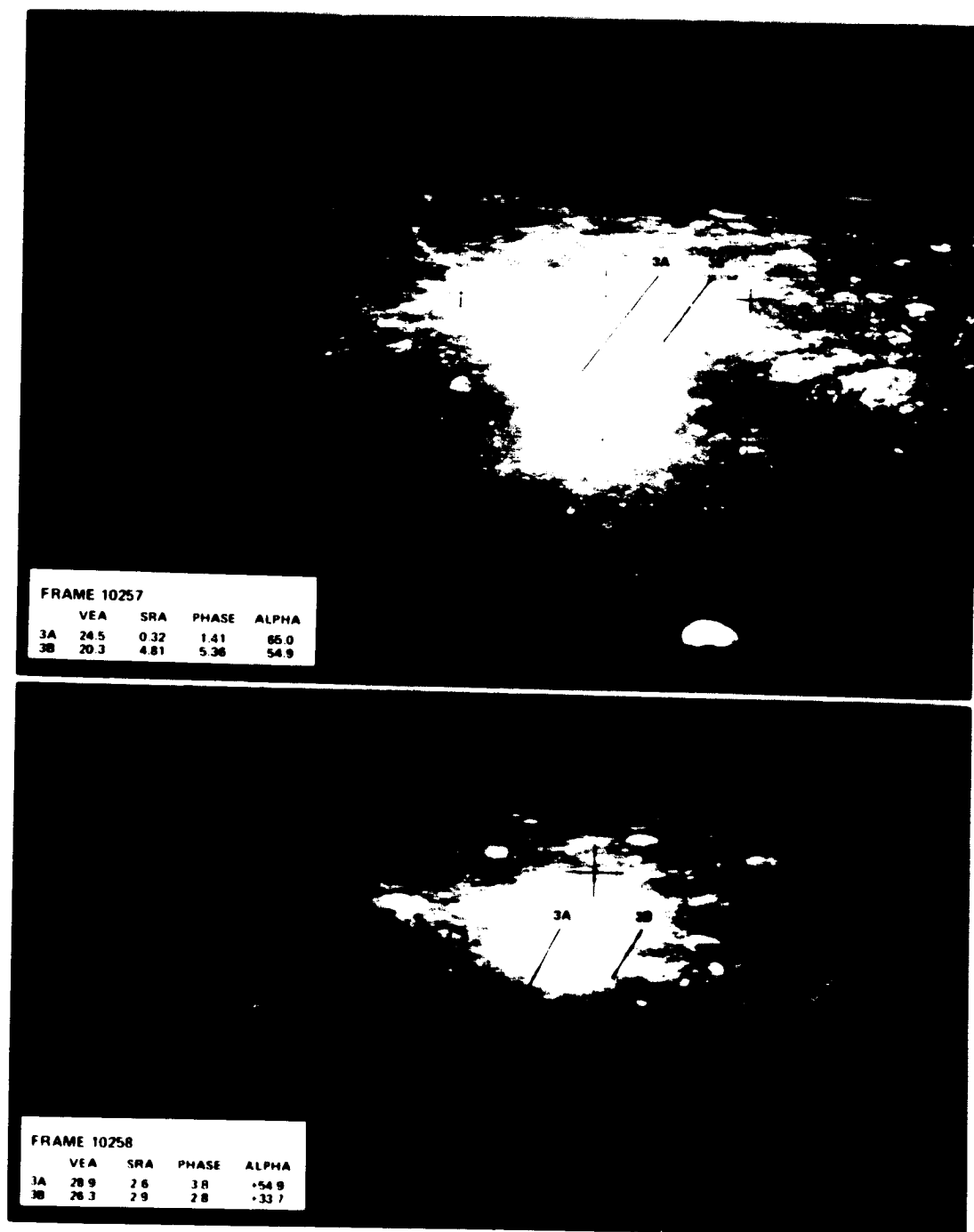
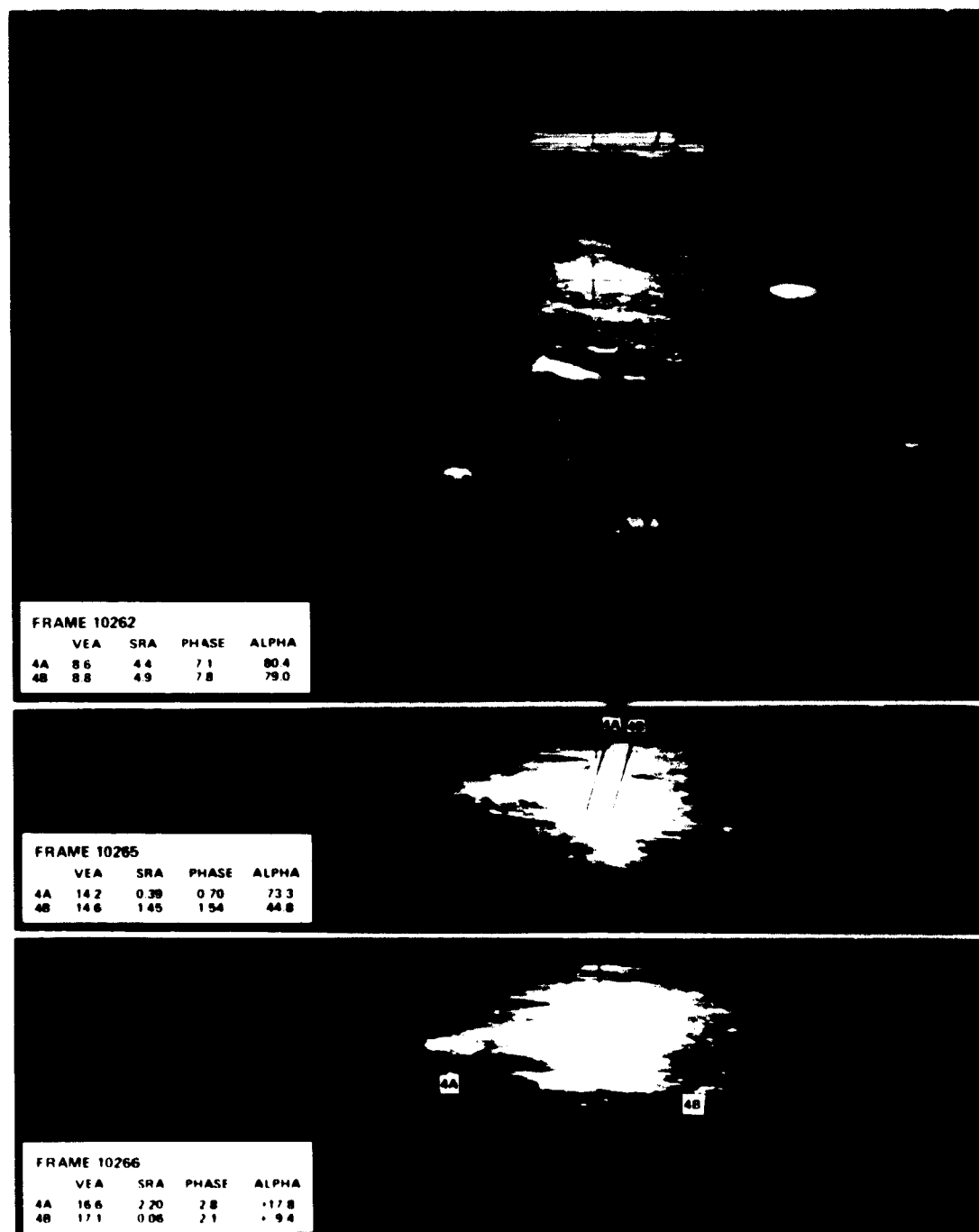


Figure 5-10b. Targets 3A and 3B. Frame 10257 shows targets at photomagnetic minimum phase. Frame 10258 in "good" visibility region.
SEA = 25.9° at 3A, 25.4° at 3B. (All angles in degrees.)



Frame 5-11. Target 4A and 4B. Frame 10262 shows targets in an "out" region, Frame 10265 at the transition minimum point, Frame 10266 in "good" visibility region. 4A = 14.1° at 4A, 14.6° at 4B. (All angles in degrees.)

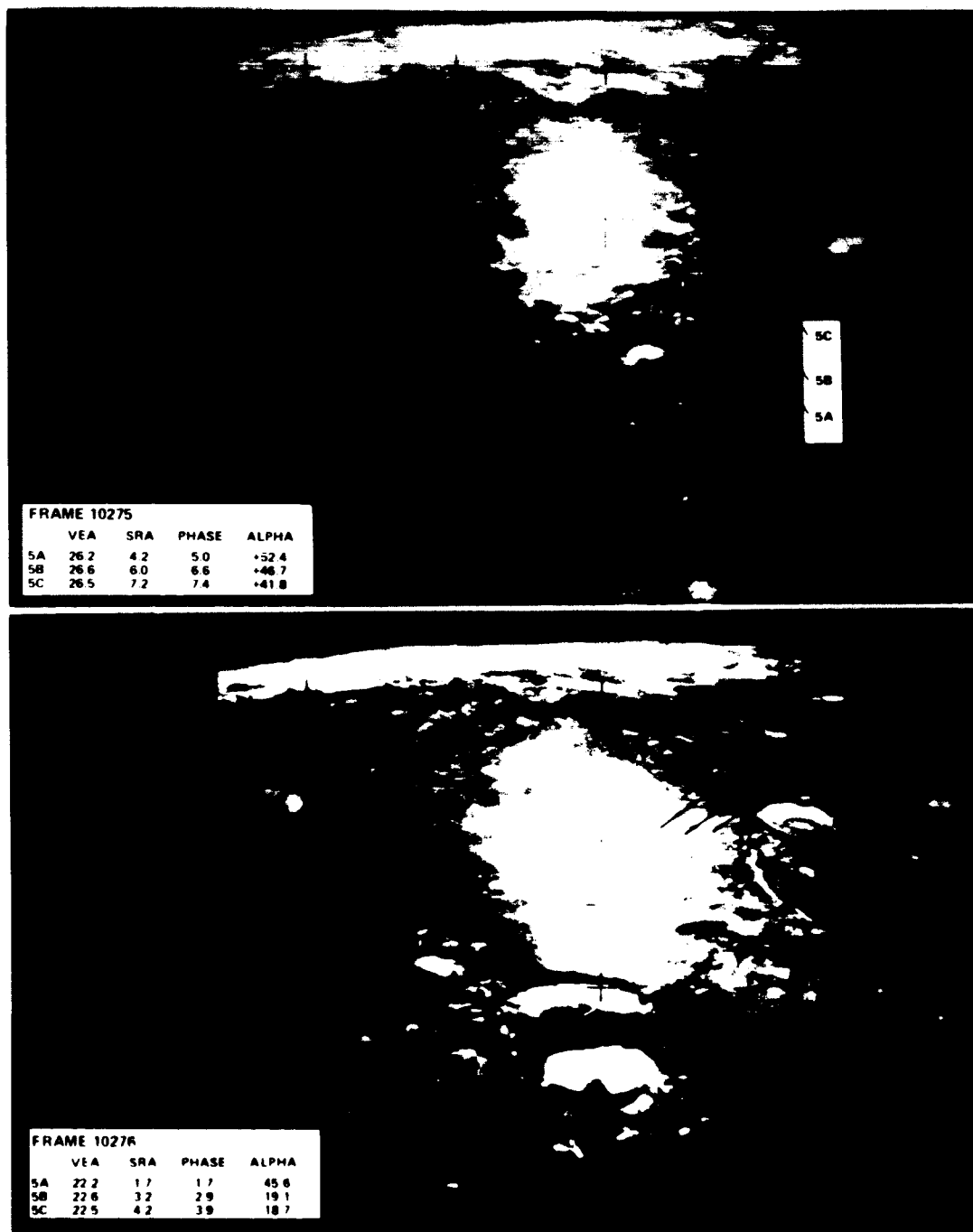


Figure 5-12a. Targets 5A, 5B, and 5C. Frame 10275 shows targets in visibility region. Frame 10276 at photographic minimum phase. SEA = 22.9° at 5A, 23.0° at 5B and 5C. (All angle in degrees.)

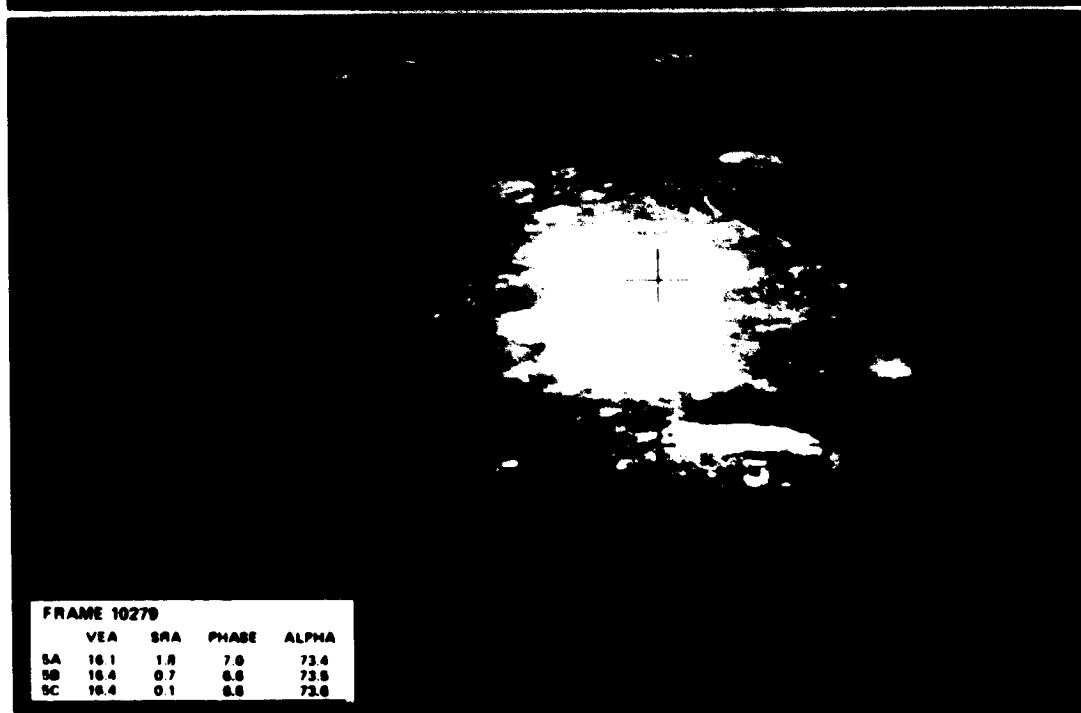
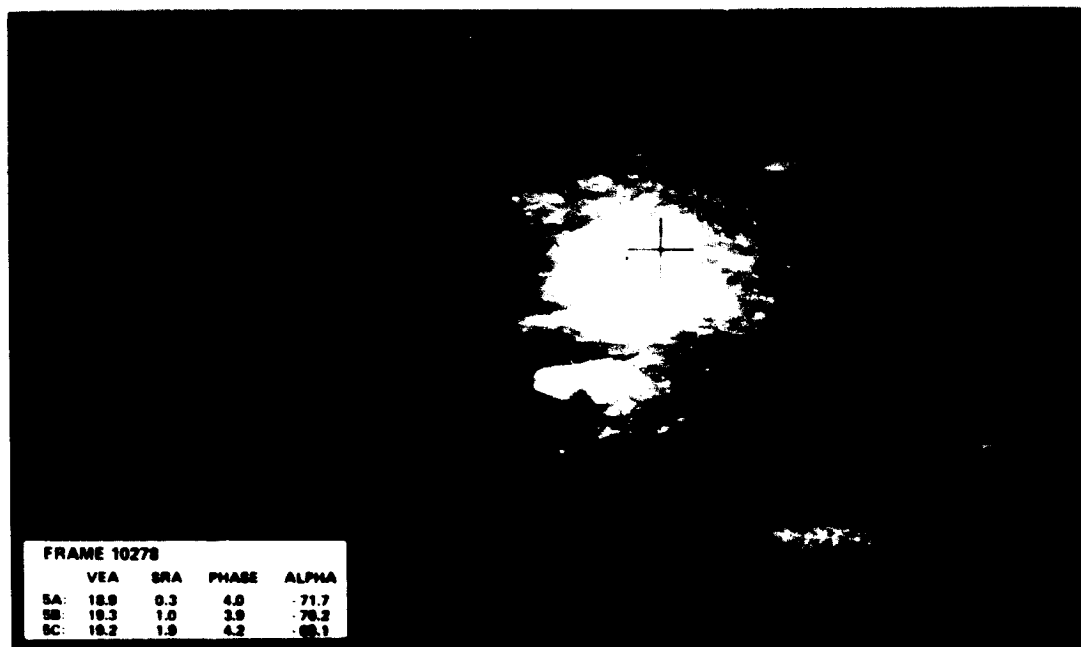


Figure 5-10b. Targets 5A, 5B, and 5C. Both frames show targets in washout region. SEA = 20.0° at 1A, 13.0° at 1B and (All angles in degrees.)

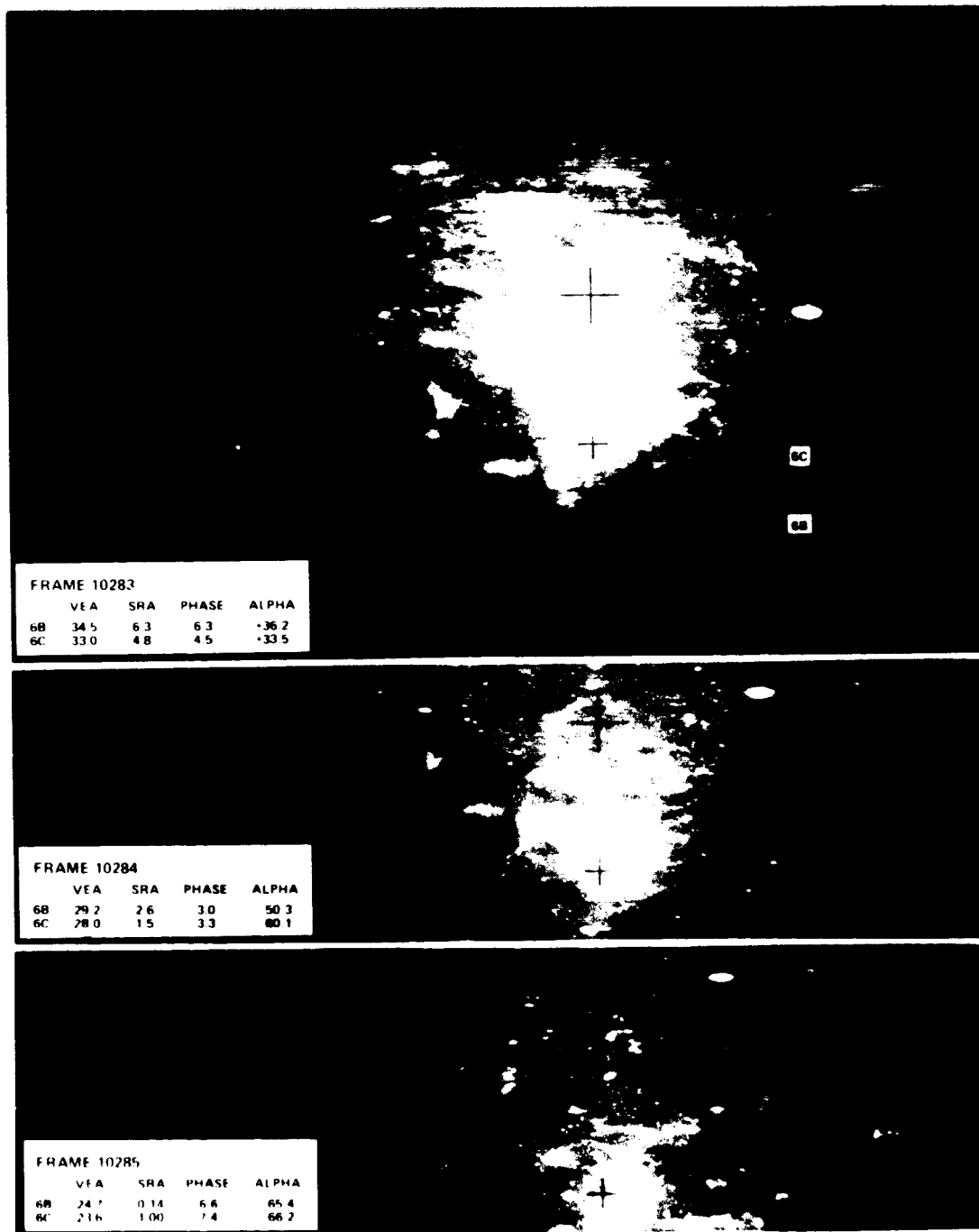


Figure 4-13. Targets 6B and 6C. Frame 10283 in visibility region, frame 10284 at photo match point, phase, frame 10285 in washout region. VEA = 31.0° at 6B and 31.0° at 6C. (All angles in degrees.)

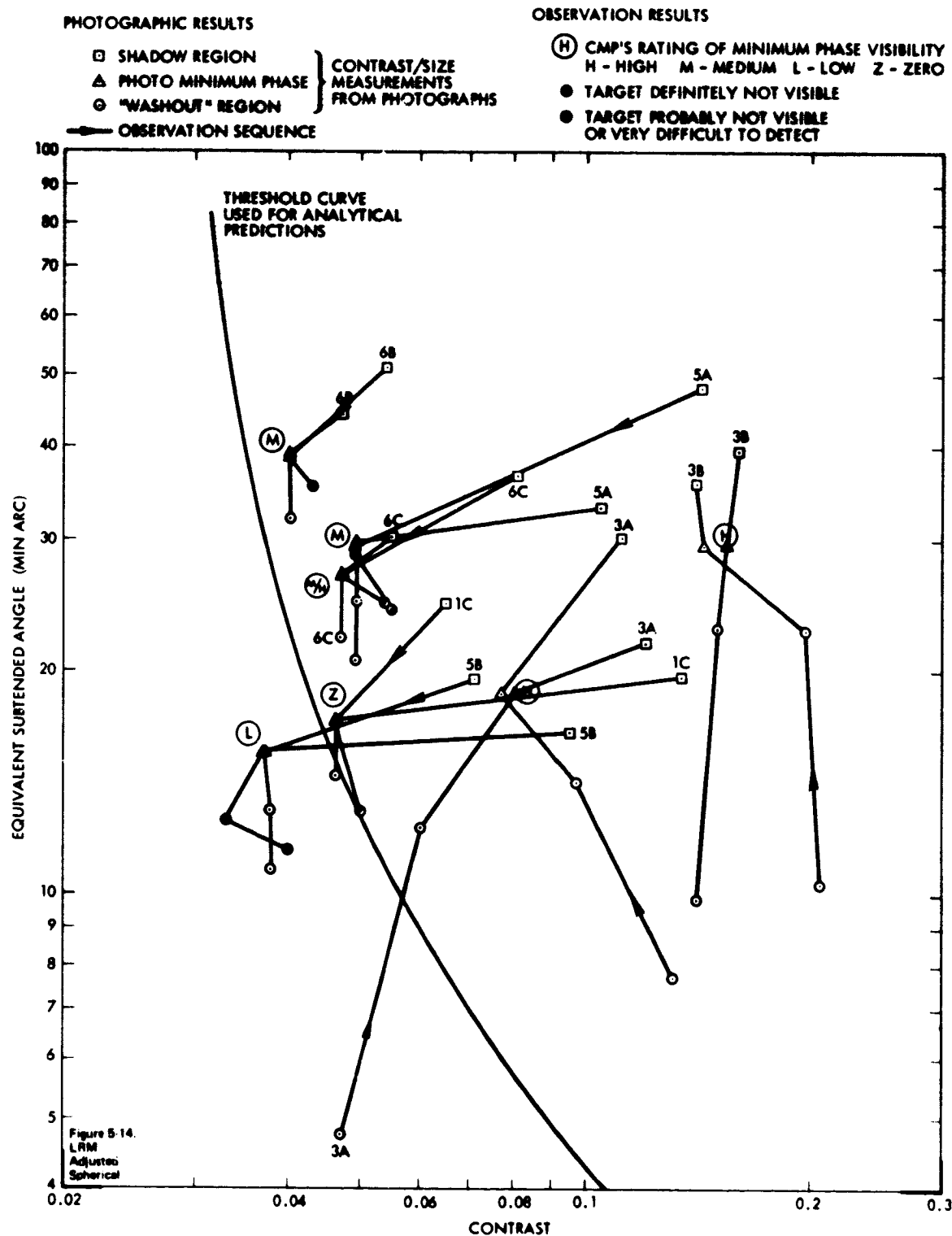


Figure 5-14. Visibility Test Results for Seven Target Craters (Printed Page). Overlay shows Visibility Model Results for the LRM, Spherical Section Craters, Adjusted for Subtended Angle.

6.0 ANALYSIS

The results presented in Section 5 are further analyzed below. Various forms of both the geometrical crater model and the photometric function are examined to determine if a better fit to the data can be obtained. Problems in the interpretation of the results are considered, especially as to differences between the idealized visibility and geometric models and the actual situation.

6.1 Comparison of Measured With Analytical Visibility Data

In the comparison of the analytical visibility calculations with observed data, it was indicated that certain adjustments had been performed on the analytical predictions. These adjustments are discussed here, as well as other assumptions made in the evaluation of the analytical calculations.

6.1.1 Albedo Determination

The logic used to select values of albedo for the analytical contrast calculations is presented in this section. As discussed in Section 3, the luminance of any point on a crater surface (actual crater or geometrical model) is found by determining the value of α and g for that point and using the expression:

$$(6.1) \quad L_i(\alpha, g) = \phi_i(\alpha, g) \cdot E_s \cdot \rho_n, \quad \text{where } \underline{L_i(\alpha, g)} \text{ is the luminance of the point } i$$

$\underline{\phi_i(\alpha, g)}$ is the value of the photometric function at i for the given α, g

$\underline{E_s}$ is the solar constant

$\underline{\rho_n}$ is the normal albedo.

For the target craters, of course, ϕ , E_s and p_n were not measured separately, as only the resultant value of $L_i(\alpha, g)$ was measured from the microdensitometric scans for each point. Further, α and g were unknown for each scanned point. For the analytical calculations α and g and, thus, ϕ could be calculated from the assumed forms of the crater model and photometric function. In either case, the set of values of $L(\alpha, g)$ are separated into those greater than the background luminance, L_B , and those less than L_B (bright side and dark side). Finally, each set is averaged and contrast ratios are calculated:

$$C_{BS} = \frac{\overline{L_{BS}} - L_B}{L_B} \quad \text{and} \quad C_{DS} = \frac{\overline{L_{DS}} - L_B}{L_B},$$

where the subscripts BS and DS refer to bright side and dark side, respectively.

In order to perform the analytical calculations and to compare the results to the contrast values measured from the photography, the normal albedos of the target and background materials (or the ratio p_{nT}/p_{nB}) must be specified. The albedos can be determined uniquely from the measured data if it is assumed:

- o The LRM photometric function is valid.
- o The photometric functions of the target and background areas only differ by the ratio of their normal albedos, p_{nT}/p_{nB} . That is, the slopes of the $\phi(\alpha, g)$ curves do not change for the two surface regions.
- o The crater points all fall in the low phase angle, negative alpha angle region of the photometric function.

Under these conditions, the contrast ratio between target and background at small phase angles is equal to the contrast ratio at zero phase, as shown in the following.

At zero phase, the slope contribution to contrast is zero, $\phi = 1.0$, and the luminance of any point equals:

$$(6.2) \quad L(g = 0) = 1.0 \cdot E_s \cdot \rho_n$$

Thus, at zero phase target luminance is $E_s \cdot \rho_n$ and background luminance is $E_s \cdot \rho_n$ and contrast at zero phase is:

$$(6.3) \quad C(g = 0) = \frac{L_T(g = 0) - L_B(g = 0)}{L_B(g = 0)} = \frac{\rho_{nT} - \rho_{nB}}{\rho_{nB}}$$

Hence, a contrast measurement at zero phase provides the ratio of normal albedos needed as input to the analytical calculations. This argument cannot be applied directly to the contrast measurements for the target craters, because they were obtained at non-zero phase angles (from 0.5° to 3.0°). However, under the conditions of near zero phase viewing used for the contrast measurements, all the crater points fall in the negative α , small phase angle region. Because the ϕ versus α curves for the LRM function are flat in this area (see Figure 3-3), slope effects are, thus, also negligible for small phase angles. In addition, because of the flatness of the curves, each crater point will have the same luminance and, thus, the ratio of average luminance at small phase angles to that at zero phase is a constant:

$$(6.4) \quad \begin{aligned} L_T(\text{small phase angles}) &= K \cdot L_T(g = 0) \cdot E_s \cdot \rho_n \\ &= K \cdot E_s \cdot \rho_n \end{aligned}$$

Furthermore, this ratio is the same for the background as it is for the target points, as both are observed at the same phase angle:

$$(6.5) \quad \begin{aligned} L_B(\text{small phase angle}) &= K \cdot L_B(g = 0) \cdot E_s \cdot \rho_n \\ &= K \cdot E_s \cdot \rho_n \end{aligned}$$

and their ratio is:

$$(6.6) \quad C(\text{small phase angle}) = \frac{\rho_{nT} - \rho_{nB}}{\rho_{nB}} = C(\text{zero phase})$$

Thus, under the assumptions given above, the measurement of target contrast at small phase angles is a valid measure of target/background albedo ratio.* Finally, use of the minimum phase contrast values for the target/background albedo ratio automatically results in a match between the calculated and measured contrast values, again because the LRM does not introduce slope effects for the low phase - negative alpha angle situation, and the contrast at minimum phase is equal to the albedo ratio.

The validity of the assumption that the target crater points all fall in the low phase angle, negative alpha region was examined by computing frequency distribution of the alpha angle for the spherical model and actual viewing conditions (results are shown in Table 6-1). This is not an exact test, because the frequency distribution of alpha angle computed from the spherical model will not correspond exactly to that of the actual crater. However, as shown in Table 6-1, most of the points do fall in the low phase angle, negative alpha angle region, which lends support to the assumption. The assumptions concerning the photometric functions can be verified only indirectly and will be considered later in this section.

6.1.2 Subtended Angle Comparisons

The match between calculated and observed contrast at minimum phase has a rational basis, as discussed above. A somewhat more arbitrary adjustment made to the data, that of matching subtended angles for the analytical calculations to the measured values at minimum phase, is based on the following:

The subtended angles generated by the analytical procedures assume a rimless spherical section crater. The actual target craters, of course, are not exactly spherical and, in fact, several are quite irregular and have definite rims. Thus, there is no reason to expect the analytical values of subtended angle to match the measured values exactly, although they should not be greatly disparate, as the actual crater diameters are used for the predictions. Figure 6-1, in which the calculated results

*Note that for target albedos greater than the background albedo, all target points will be of greater luminance than the background luminance under the assumed conditions.

(unadjusted for subtended angle) are compared with the measured data, verifies this expectation to be reasonable. The largest discrepancy in subtended angle is a factor of two (for target 5A). Therefore, because it was not feasible to use the actual crater topography for the contrast and subtended angle calculations, the subtended angles were equated between the predicted and measured data, but for the minimum phase point only. (This amounted to sliding each curve in Figure 6-1 vertically a distance appropriate to match the angular values for the minimum phase point, resulting in the curves shown in the Figure 5-14 overlay.)

This procedure, together with the rationale for albedo selection, effectively matched the calculated and observed curves at the minimum phase point and provides a convenient reference for use in evaluating the relationship of the calculated to obtained data for the other points.

6.1.3 Bright Side, Dark Side and Geometric Shadow

All of the data presented above have been for bright side areas for both the measured and calculated values of contrast. The basis for emphasis of the BS data is discussed below.

Because geometric shadow contrasts are large ($C = -1$), the existence of even a small shadow makes a crater very conspicuous and tends to override the effects of slope and albedo. Also, geometric shadows only depend on the topography of the crater (and the view/sun vectors) and, therefore, shadow measurements do not pertain to analysis of the photometric function. Finally, shadows for the target craters only appeared in the good visibility region which is less relevant to the present study than are the washout and minimum phase points.

With some exceptions, significant DS areas appeared for the target craters only in the good visibility region. In some cases, DS points were not due solely to slope effects (which result in distinctly different DS and BS areas), but to "mottling" of the crater surface, probably caused by albedo variations.

The values of equivalent subtended angle and contrasts obtained from the micro-densitometric measurements are shown in Table 6-2, for illustration of the above points. The corresponding calculated values obtained from the LRM and spherical crater model are shown for comparison. The data in Table 6-2, thus, correspond to the points shown in Figure 6-1 for the measured data (printed page) and unadjusted calculated data (overlay). In examining Table 6-2, first compare the relative magnitudes of the DS contrasts and subtended angles with those of the BS. For most of the targets, the only cases for which the DS values are of appreciable magnitudes compared to the BS is when the target is in the good visibility region. This is as expected, because the slope effects are strongest for this case. Targets 5A and 5B do not fit this pattern, as they show relatively large DS values for the minimum phase and washout points. Inspection of the photographs for these craters (Figure 5-12) indicated that this result is probably due to albedo variation over the crater surface. The analytical calculations show very low DS contributions for the minimum phase and washout cases as expected from the properties of the LRM function. In the good visibility region, the DS calculations do not seem to agree with the measured DS values as well as do the BS measured and calculated points.

The various discrepancies are most likely due to a combination of geometrical differences between the target craters and geometrical models as discussed in the previous section, non-uniformity of albedo over the target surface, and to differences between the LRM and the actual photometric function for the particular surface areas that were observed. Within these limitations, it is concluded that the BS predictions are the most useful for analysis of crater visibility.

6.2 Fedoritz Function Compared to the LRM

Contrast-subtended angle predictions made with the Fedoritz function are compared to the experimental results in Figure 6-2. The Fedoritz results are substantially different than the LRM predictions shown in Figure 6-1. The main differences show up in the washout region where two of the targets show a transition from positive to negative contrast values (1C, 3A) and where the others all show continuously decreasing

values of contrast. In comparison, the experimental results all show positive contrast values in the washout, and as discussed previously, slight increases in contrast after minimum phase are indicated. The LRM predictions, although not showing the contrast increase after minimum phase, do not show negative contrasts and are generally more regular than are the Fedoritz data (compare Figures 6-1 and 6-2).

The same albedo values were used for the Fedoritz calculations as for the LRM predictions. The difference in results between the two cases is attributed to the greater slopes of the Fedoritz curves in the negative alpha-small phase angle region of the photometric function (see Section 3.1.4 and Figures 3-3 and 3-5). These slopes result in negative contrasts which subtract from the positive contrasts generated by the input albedos. Unrealistically large albedo values would have to be used to raise the resultant low or negative contrasts to the values actually obtained. Further, both the LRM and the Fedoritz functions show about the same magnitudes of discrepancies between calculated and measured points corresponding to targets in the "good" visibility region ("□" symbol). Therefore, it is concluded that the LRM is a significantly more accurate model than the Fedoritz function.

6.3 Conical and Spherical Section Crater Model Comparison

The conical crater model was developed to take into account features such as albedo differences between crater floors and rims and craters with flat floors (such as older, filled-in craters). The crater is modelled as a truncated cone with provisions for separate albedo inputs for the floor and rim. The crater geometry is specified by its diameter-to-depth ratio and by the slope of the wall.

The conical and spherical models are compared for two target craters in Figure 6-3. Target 6B is a shallow crater with a bright rim and dark floor. Target 3A was a steep crater, but its rim was much brighter than its floor. Wall slopes were estimated from photographs and were taken as 70° for 6B and 40° for 3A (measured from vertical). Diameter-to-depth values and wall albedos were assumed to be the same as used for the spherical model, but floor albedos were set equal to the background. The

results in Figure 6-3 show some differences between the two models, especially for 3A, for which the washout points show a less marked drop-off in contrast for the conical model. However, a quantitative comparison is difficult, because both models could be more-or-less equally incorrect geometrically and because the wall slope parameter introduces additional uncertainty, as it is difficult to measure with high confidence. Additional comparisons made between the two models indicate that either model is adequate for a "normal" spherically-to-conically shaped crater, but that the conical model should be used in the case where the crater floor is flat and of a relatively large area compared to the crater wall.

Table 6-1. Frequency Distribution of Alpha Angles for Spherical Section Craters Under Viewing Conditions of Apollo 14 Visibility Tests. (Results are shown for three typical craters.)

TARGET	FRAME	ALPHA ANGLE RANGE																
1C	10224 ¹																	
	10225 ²	15	27	43	60	68	69	52	38	27	11	12	3	2	1			
	10228 ³	10	27	46	76	101	101	80	37	13	5							
3B	10258 ¹	5	13	19	28	42	45	55	53	56	50	44	34	23	10	6	1	
	10257 ²	11	27	43	59	78	81	73	49	33	18	8	3	1				
	10255 ³	10	24	41	70	89	90	85	46	26	9	4	1	1				
	10250 ³	9	18	37	72	111	128	85	22	5	2							
6C	10283 ¹					13	29	53	57	72	72	67	54	43	25	10		
	10284 ²	72	90	111	110	66												
	10285 ³	95	119	130														

1 = good visibility region

2 = minimum phase

3 = washout region

TABLE 6-2. COMPARISON OF MEASURED AND CALCULATED SUBTENDED ANGLE/CONTRAST
DATA FOR DARK SIDE (DS) AND BRIGHT SIDE (BS)

Target	Frame	Measured				Calculated (LRM/Spherical Model)				Region
		CBS	LBS	CDS	LDS	CBS	LBS	CDS	LDS	
1C	10224	0.065	24.6	-.066	15.7	0.134	28.9	0	0	Good Min Ph Washout
	10225	0.046	17.1	-.034	13.5	0.046	25.2	-.029	1.1	
	10228	0.050	12.9	-.031	8.6	0.043	17.8	0	0	
3A	10258	0.108	29.4	-.066	20.6	0.155	35.0	0	0	Good Min Ph Washout Washout
	10257	0.077	18.7	-.025	5.3	0.081	30.4	0	0	
	10255	0.097	14.2	-.009	2.7	0.056	19.9	-.067	6.7	
	10250	0.132	7.7	-.012	1.6	0.047	7.8	-.11	4.8	
3B	10258	0.140	35.3	-.107	8.9	0.160	44.3	-.26	2.0	Good Min Ph Washout Washout
	10257	0.143	29.3	-.018	3.6	0.154	33.0	0	0	
	10255	0.196	22.6	-.012	1.9	0.148	25.5	-.11	2.0	
	10250	0.211	10.3	0	0	0.140	11.05	-.07	0.71	
5A	10275	0.142	47.9	-.097	26.6	0.103	65.6	-.073	26.8	Good Min Ph Washout Washout
	10276	0.049	29.3	-.044	25.6	0.049	60.0	0	0	
	10278	0.049	29.0	-.040	19.1	0.049	49.0	0	0	
	10279	0.055	24.2	-.030	12.9	0.049	41.0	0	0	

(Continued)

TABLE 6-2. COMPARISON OF MEASURED AND CALCULATED SUBTENDED ANGLE/CONTRAST DATA FOR DARK SIDE (DS)
AND BRIGHT SIDE (BS)
(continued)

Target	Frame	Measured				Calculated (LRM/Spherical Model)				Region
		CBS	LBS	CDS	LDS	CBS	LBS	CDS	LDS	
5B	10275	0.071	19.5	-.094	18.9	0.093	25.2	-.11	14.1	Good Min Ph Washout Washout
	10276	0.037	15.5	-.040	15.1	0.037	23.8	-.020	1.5	
	10278	0.033	12.6	-.029	12.1	0.037	19.8	0	0	
	10279	0.040	11.5	-.031	10.7	0.037	16.6	0	0	
6B	10283	0.054	51.1	-.027	33.1	0.047	69.7	-.015	27.5	Good Min Ph Washout
	10284	0.040	38.7	-.025	22.8	0.040	61.4	0	0	
	10285	0.043	35.3	-.023	20.7	0.040	50.2	0	0	
6C	10283	0.081	36.7	-.044	40.7	0.055	42.6	-.063	18.7	Good Min Ph Washout
	10284	0.047	26.9	-.025	15.8	0.047	38.2	0	0	
	10285	0.054	24.6	-.028	12.5	0.047	31.3	0	0	

6.4 Photometric Function Analysis

Several comments have been made in the preceding sections indicating that the target crater contrast measurements suggest modifications of the lunar photometric function. The form of such modifications and various attempts at their implementation are discussed in this section. As will be seen, the present data are insufficient to allow precise specification of a new photometric function, but it is possible to apply corrections to the existing functions for the purpose of visibility calculations.

6.4.1 Contrast Measurements and the Photometric Function

From the considerations presented above, it was concluded that the main discrepancy between the contrast data obtained from the microdensitometric analysis and those calculated from the LRM was the increase in contrast that occurred in the washout relative to minimum phase. Although other discrepancies exist between the two sets of data, they can be more readily attributed to topographic and albedo factors than can the contrast change in the washout region. The following discussion indicates the form of a modification to the photometric function which can explain the measured data and discusses the problems in quantifying such modifications.

The present discussion will focus on the above mentioned increase in target contrast corresponding to the down-range displacement of the target from minimum phase. As the target moves down-range from minimum phase, its phase angle increases. As mentioned, the LRM does not generate a contrast increase under these conditions due to the flatness of the ρ versus α curves for the small phase angle-negative alpha angle region. A further observation is that the magnitude of contrast increase seems to be a function of crater albedo. These effects can be seen from the test results in Figure 6-1. However, the two relationships can be seen more clearly in Figure 6-4, which gives the following data for each crater on each of the frames:

- (1) $C_{\min} - C_w$ (difference between minimum phase contrast and washout contrast) versus $g_{\min} - g_w$ (phase angle difference corresponding to the frames on which C_{\min} and C_w were measured), and
- (2) Washout contrast (C_w) versus minimum phase contrast (C_{\min}).

The first plot tests whether contrast increases as phase angle increases (Figure 6-4a) and the second shows whether the magnitude of increase is related to crater albedo (Figure 6-4b). These data indicate that washout contrast does seem to depend on both phase angle and albedo (as measured by C_{\min}); although, it is possible that the results are biased by targets 3A and 3B (these points are labelled in Figure 6-4), which were measured at much larger phase angles than the other targets and which also had the largest albedos. The relationships illustrated in Figure 6-4 suggest that the drop-off in surface luminance that occurs as phase angle increases from zero to larger values is less steep for the target crater than for the surrounding soil. Further, the steepness of drop-off seems to be a function of crater albedo, higher albedo craters having a less steep drop-off than do lower albedo craters. This modification to the photometric function is illustrated graphically in Figure 6-5, in which ϕ is plotted versus g with α a parameter. An unmodified photometric function ϕ is shown with solid lines, a modified version ϕ' with dashed lines. As can be seen from Figure 6-5, the two functions generate the same reflectance factor value at $g = 0$, but as g increases, the modified function generates larger ϕ values than the other, and at still larger values of g the two functions are identical. Note that both are normalized to $\phi = 1.0$ at $g = 0$, and that both ϕ and ϕ' must be multiplied by appropriate normal albedos to obtain an actual reflective value for a given α and g and particular surface region. Further, note that even if the two functions ϕ and ϕ' were applied to two different soils having the same normal albedo, the total albedos will be different for the two soils, due to the greater reflectance of the ϕ' function at low phase angles.

6.4.2 Quantification of Modified Photometric Function

Two approaches were tried in order to derive a modified photometric function with which to fit the experimental data. A critical problem encountered is that either approach was, of necessity, an indirect one: rather than deriving a photometric function directly from lunar photometry, it was necessary to assume a functional form of the type given above and then to manipulate the parameters of the function such that crater contrast values calculated from the new function matched the measured values obtained from the Apollo 14 photography. This technique suffers from being more trial-and-

error than rational; in that, errors in the measured target crater contrasts could confuse the attempt at matching, and crater contrasts were measured for only a relatively small range of conditions. For instance, it would be desirable to obtain additional contrast measurements in the washout region to confirm the apparent increase in contrast on which the modifications to the photometric functions are based.

Hapke Function: The first approach used the Hapke photometric model described in References 9 and 10. The Hapke function is the only lunar photometric model based on theoretical considerations that reasonably fits observed data, and was used here because it seemed to provide a rational basis for relating physical lunar soil properties to modification of the photometric function. Further, it was of interest to compare contrast predictions generated with this model to those of the LRM and Fedoritz functions. The Hapke model is composed of three terms:

$$\phi(\alpha, g) = L(\alpha, g) \cdot \Sigma(g) \cdot B(g)$$

where - $\phi(\alpha, g)$ is the photometric function as defined previously

$L(\alpha, g)$ is a term which describes the luminance of a surface which is porous on a microscopic scale, but flat on a large scale.

$\Sigma(g)$ describes the average scattering function of a single soil particle.

$B(g)$ is the retro-directive function which describes back scattering due to effects of blocking and shadowing within the lunar soil ("fairy castle" effect)

The model has three parameters:

h , appears in the $B(g)$ term and is related to the porosity of the lunar surface.

γ , appears in the $L(\alpha, g)$ term and specifies the average slope of depressions in the lunar surface.

F , appears in the $L(\alpha, g)$ term and specifies the fraction of the surface covered by depressions.

A fourth parameter, normal albedo, must also be specified and has the same meaning as the normal albedo term defined previously. The Hapke function for $F = 0.9$, $\gamma = 45^\circ$ and $h = 0.4$, which Hapke found were reasonable values to represent the average moon photometric function, is shown in Figure 6-6.* Note that it tends to resemble the Fedoritz function more than LRM, in that the curves have negative slopes in the small phase angle-negative alpha angle region (compare to Figures 3-3 and 3-5).

The retro-directive term $B(g)$ provided a natural basis for examining modifications of the photometric function as the parameter h controls the steepness of the retroreflective peak. For larger values of h the drop-off of $\phi(\alpha, g)$ is less as g increases, as shown in Figure 6-7. Thus, the h parameter provides the desired variation in the photometric function. Crater contrast calculations were made in which h was varied between 0.4 and 0.6 for the crater, whereas it was maintained at a constant value of 0.4 for the background. Albedo values used in the calculation were the same as previously used. Typical results of the calculations are shown in Figure 6-8, in which the Hapke contrast values are shown overlayed on the Apollo 14 test results. Curves are shown for only $h = 0.5$, except for craters 6A and 6B, where data are also given for $h = 0.4$ (no change in function between background and crater). Note the general resemblance of the curves to those generated by the Fedoritz function, i.e., contrasts in the washout region tend to be driven towards low positive or negative values. In three cases, the desired increase in contrast in the washout is generated (6-B, 6-C, 5-A), but the other cases are dominated by the negative contrast effects. An additional complication in attempting to derive a modified photometric function is illustrated by the results for 6B, in which the entire curve is displaced to higher contrast values as the value of h increases. This occurs because, as mentioned previously, an increase in h increases the total albedo of the crater, even though the value input for normal albedo is held constant. Thus, a variation in the form of the photometric function between the background and crater is confounded with variation in albedo, and the simple

*The complete equation for the Hapke function and a listing of the computer program used to evaluate it, are given in Appendix E.

method of deriving a value of normal albedo for the analytical calculations from the contrast measurements (Section 6.2.1) is not applicable. Thus, an additional parameter (total albedo, as well as normal albedo) is introduced into a situation where there already exist too many parameters to be fitted uniquely.

Modified LRM Function: The failure of the Hapke function to fit the data prompted investigation of the LRM function with the addition of an empirical correction to the calculation of $\phi(\alpha, g)$. The correction added was:

$$(6.7) \quad \phi'(\alpha, g) = \phi(\alpha, g) + \left[e^{-A1 \cdot g} \cdot (1 - e^{-B1 \cdot g}) \right] SK$$

where -

$\phi'(\alpha, g)$ = corrected value of reflectance factor

$\phi(\alpha, g)$ = original value of reflectance factor from LRM

$A1, B1, SK$ = input constants

The first term in the brackets ($e^{-A1 \cdot g}$) equals one when $g = 0$, and decreases to zero as g increases. The second term ($1 - e^{-B1 \cdot g}$) is zero when $g = 0$, and increases to 1.0 at large phase angles. Thus, the combination of the two exponentials results in zero correction at $g = 0$ and at large phase angles. The SK term is used to adjust the overall magnitude of the correction term. A plot of the correction term magnitude versus g , is shown in Figure 6-9 for $A1 = 0.06$, $B1 = 0.14$ and $SK = 0.01$. These values were determined by trial and error to generate the desired magnitude of correction. Note that an explicit term relating magnitude of correction to target albedo was not included, but that albedo could be accounted for by variations of SK.

Contrast-subtended angle curves were generated using the modified LRM function and the values of normal albedo used previously. Values of SK from 0.01 to 0.1 were used with $A1 = 0.06$ and $B1 = 0.14$. As in the case of the Hapke function, larger values of the correction term (larger SK) move the entire curve to higher contrast values and tend to overly accentuate the contrast increase in the washout region. Results for spherical craters and for $SK = 0.01$ are shown superimposed on the Apollo 14 test results in Figure 6-10.

The curves were adjusted to match subtended angles at the minimum phase point only, but no adjustment was made along the contrast axis. Thus, Figure 6-10 should be compared to the overlay on Figure 5-14, which shows the adjusted LRM data without the correction term. Inspection of Figure 6-10 reveals that the desired contrast increase in the washout is generated for the lower albedo targets and that the amount of correction is of the right order of magnitude. Note, however, that the minimum phase contrast values no longer match the experimental data because of the additional reflectance term added by the correction factor, although the mismatch is relatively small for $SK = 0.01$. The curves for the high albedo targets (3A and 3B) are essentially unchanged by the correction for $SK = 0.01$, as would be expected because their normal albedo terms outweigh the contribution due to the correction term (compare to Figure 5-13). A curve for $SK = 0.075$ is shown for 3A and, although the detailed slope of the curve does not match the experimental curve any better than for $SK = 0.01$, the washout points are moved to higher contrast values providing a better overall match. (However, note that the same effect could be obtained by increasing the value of normal albedo for 3A. In general, 3A seems to be a somewhat anomalous case, possibly due to the fact that it is a very steep crater with a high rim and a bright layer of material on the rear wall and rim.)

6.4.3 Evaluation

The results for the modified LRM functions are encouraging in that the form suggested for the modified function does generate appropriate contrast - subtended angle curves. However, for purposes of practical visibility calculations some caution should be exercised in the use of the modified function:

- o The modification is an ad hoc term fitted to a fairly narrow range of data, rather than one obtained directly from lunar photometry.
- o The correction term is zero for equal albedo targets and, thus, visibility prediction for this case will be unchanged.

- o The question of how the correction term should vary for high albedo targets was not resolved. However, high albedo targets will generally be very conspicuous, so that exact predictions of their visibility are less important than for low albedo targets.
- o The most useful application of the correction factor would seem to be for targets whose albedos are slightly greater than that of the background (2% to 5% greater) when observed in the washout region. Even in this case, however, a few percent albedo difference is usually sufficient to make a crater visible in the washout and, thus, no practical differences would obtain between the two functions. It is concluded that the unmodified LRM function is generally sufficient for lunar visibility calculations, but that the modified LRM could be employed in well-defined situations requiring exact visibility predictions (for instance, where it is necessary to know the range at which a particular crater can be detected).

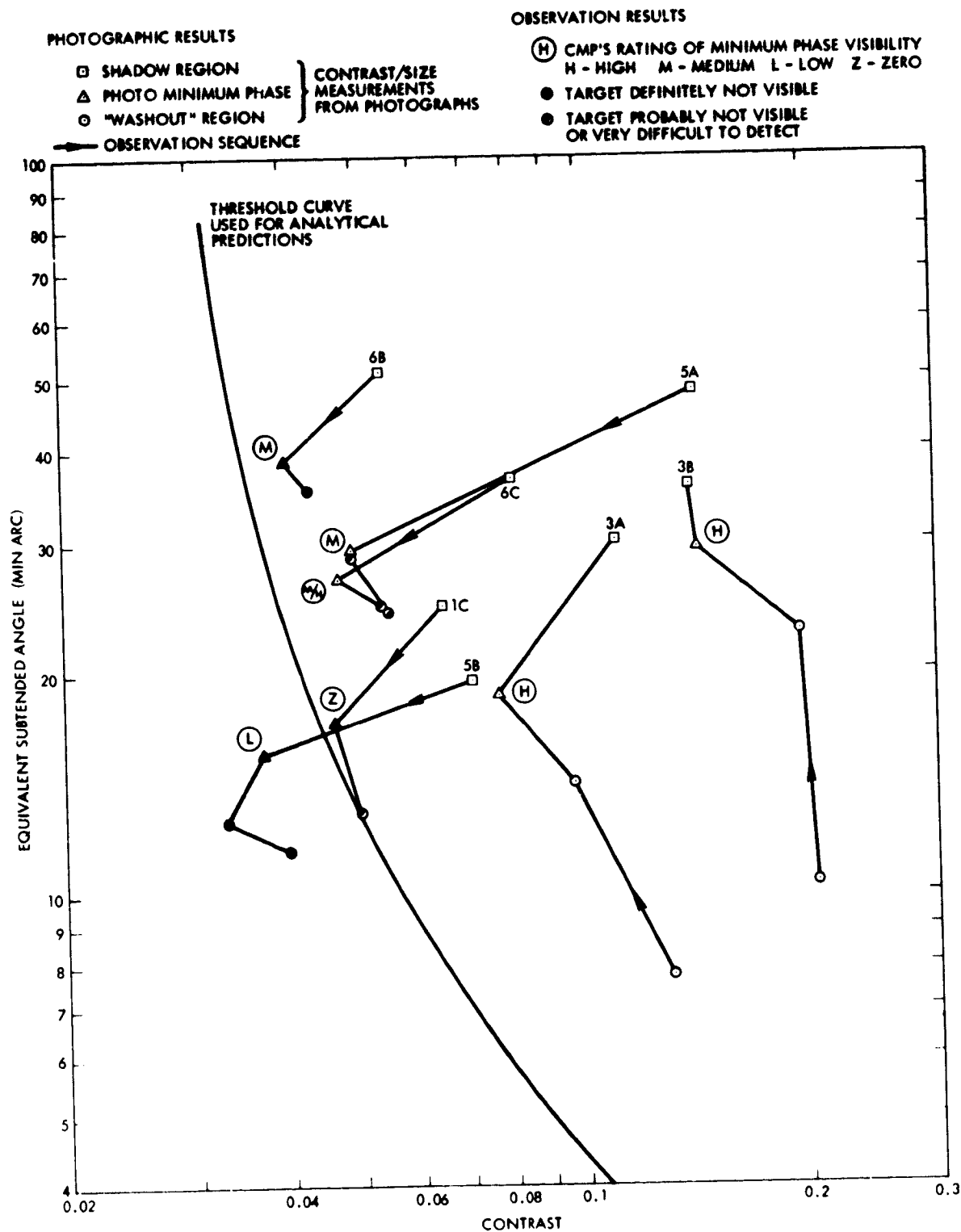


Figure 6-1. Overlay shows the Visibility Model Results for the LRM, Spherical-Section Craters Unadjusted for Subtended Angle. Printed Page shows the Apollo 14 Visibility Test Results. Compare to Figure 5-14.

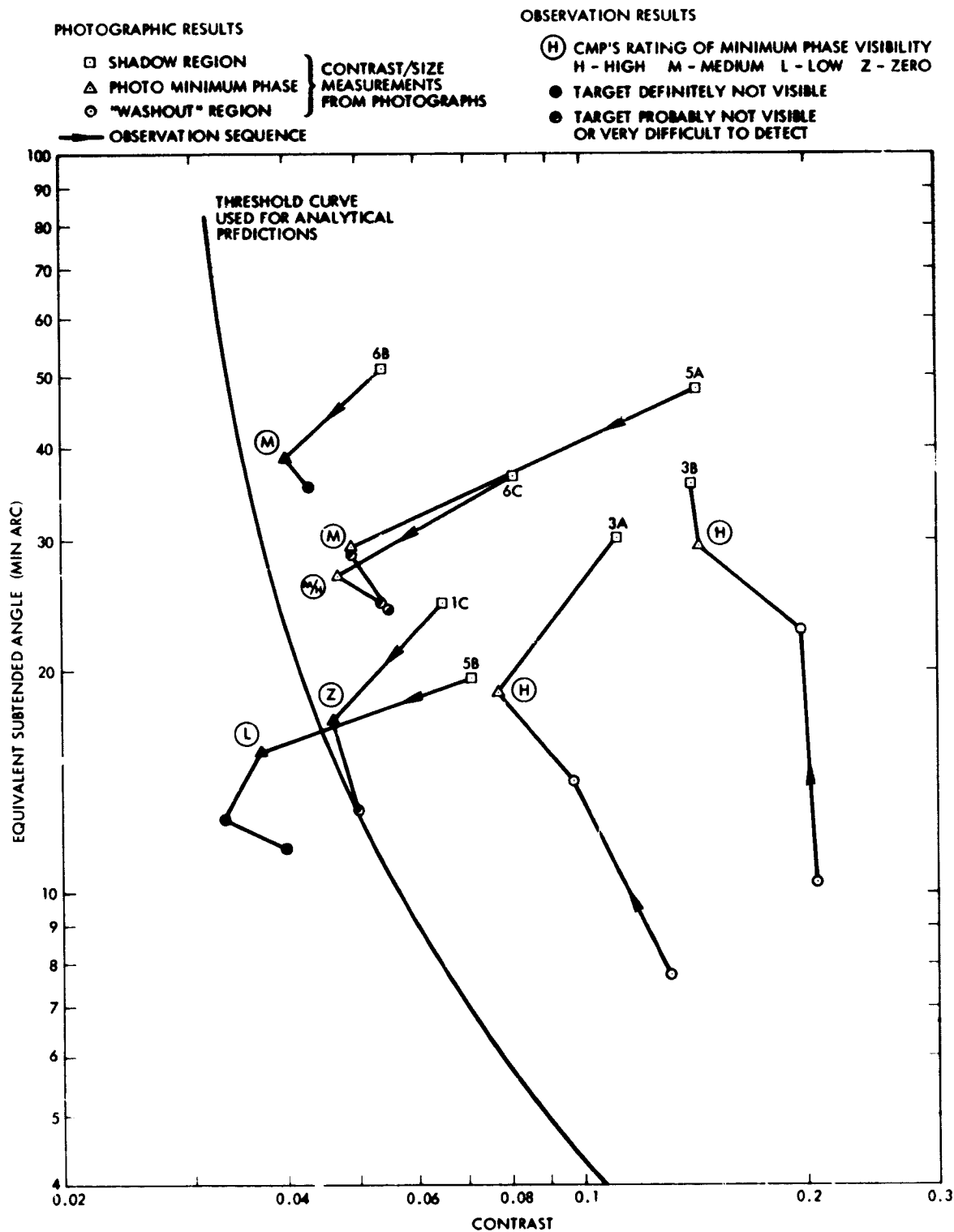


Figure 6-2. Overlay shows the Visibility Model Results for the Fedoritz Function, Spherical-Section Craters Unadjusted for Subtended Angle. Printed Page shows the Apollo 14 Visibility Test Results. Compare to LRM Model Results in Figure 6-1.

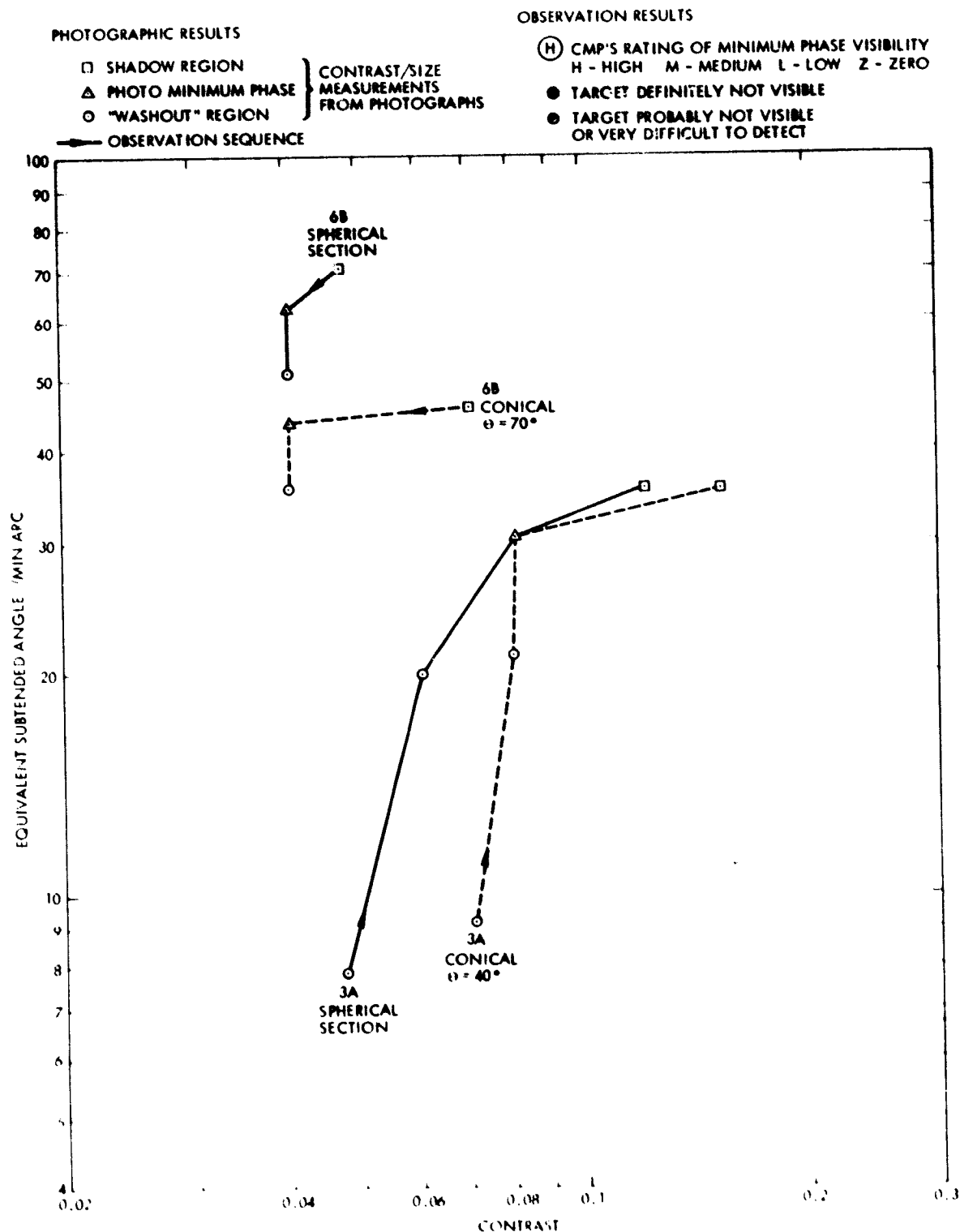


Figure 6-3. Comparison of Visibility Model Results for Conical (dashed lines) and Spherical Section (solid lines) Crater Geometries. Theta is Cone Half-Angle Measured from Vertical. LRM, Unadjusted for Subtended Angle. (Same diameter:depth ratios for conical and spherical section cases.)

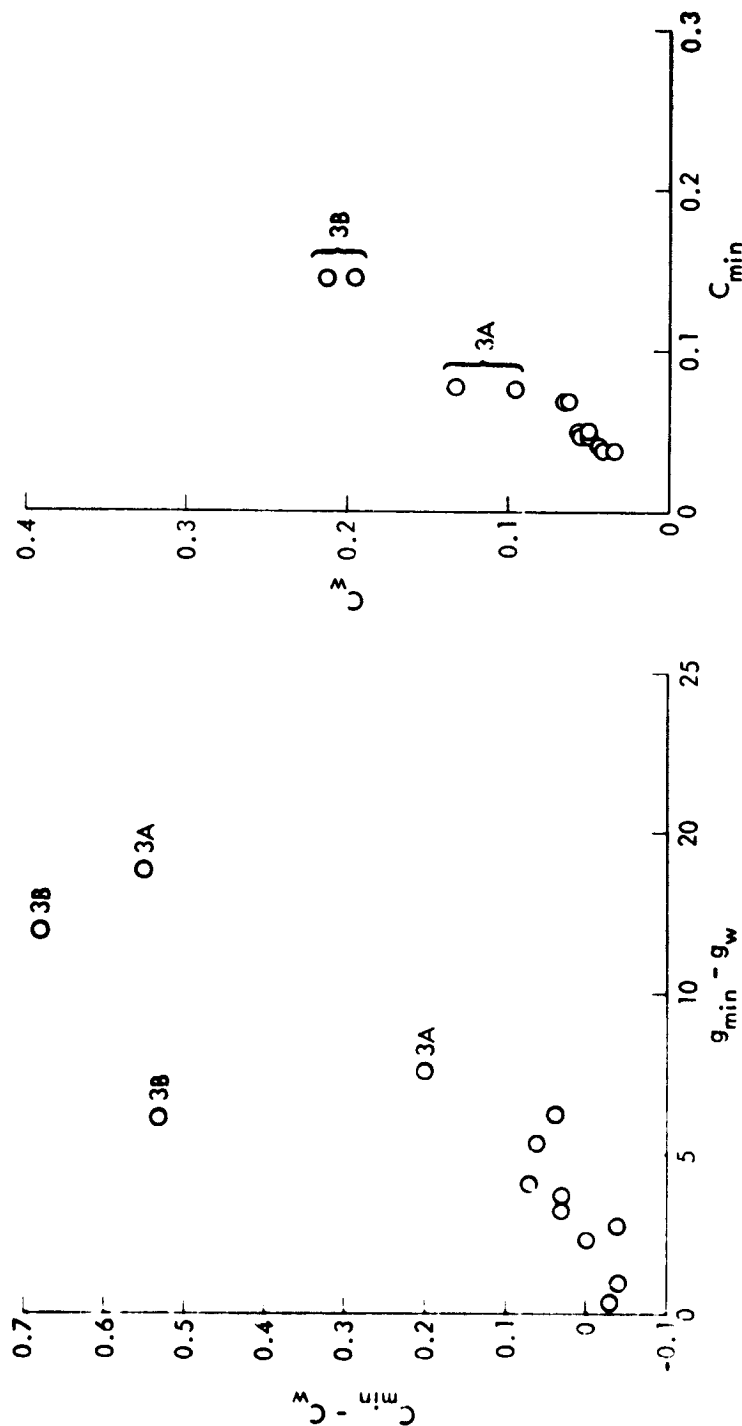


Figure 6-4a. Minimum Phase Contrast Minus Washout Contrast ($C_{min} - C_w$) Versus the Corresponding Minimum Phase and Washout Phase Angle Difference ($g_{min} - g_w$). Data indicate that as the Phase Angle Increases from Minimum Phase, Crater Contrast Increases from Minimum Phase Contrast.

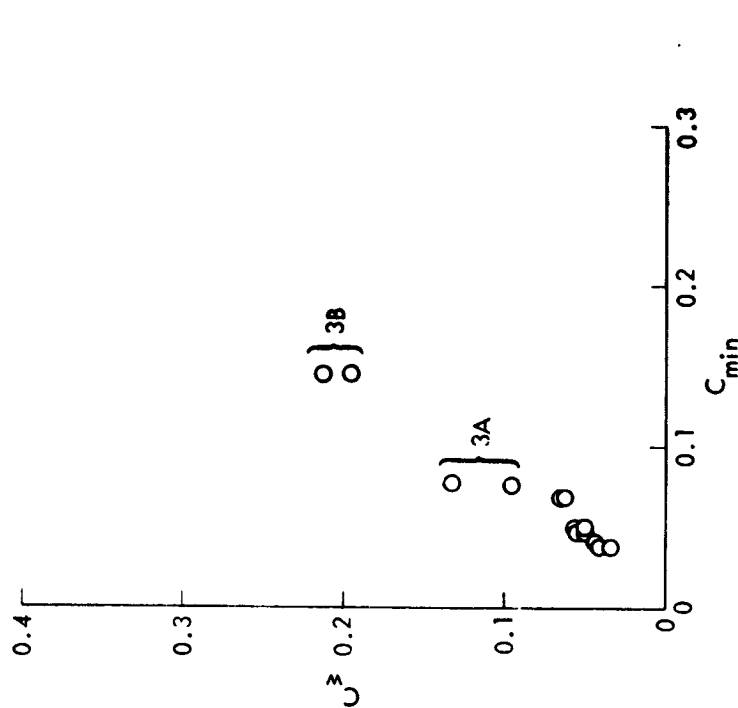


Figure 6-4b. Minimum Phase Contrast (C_{min}) Versus Washout Contrast (C_w). Data indicate that Washout Contrast is a Function of Albedo as Measured by C_{min} .

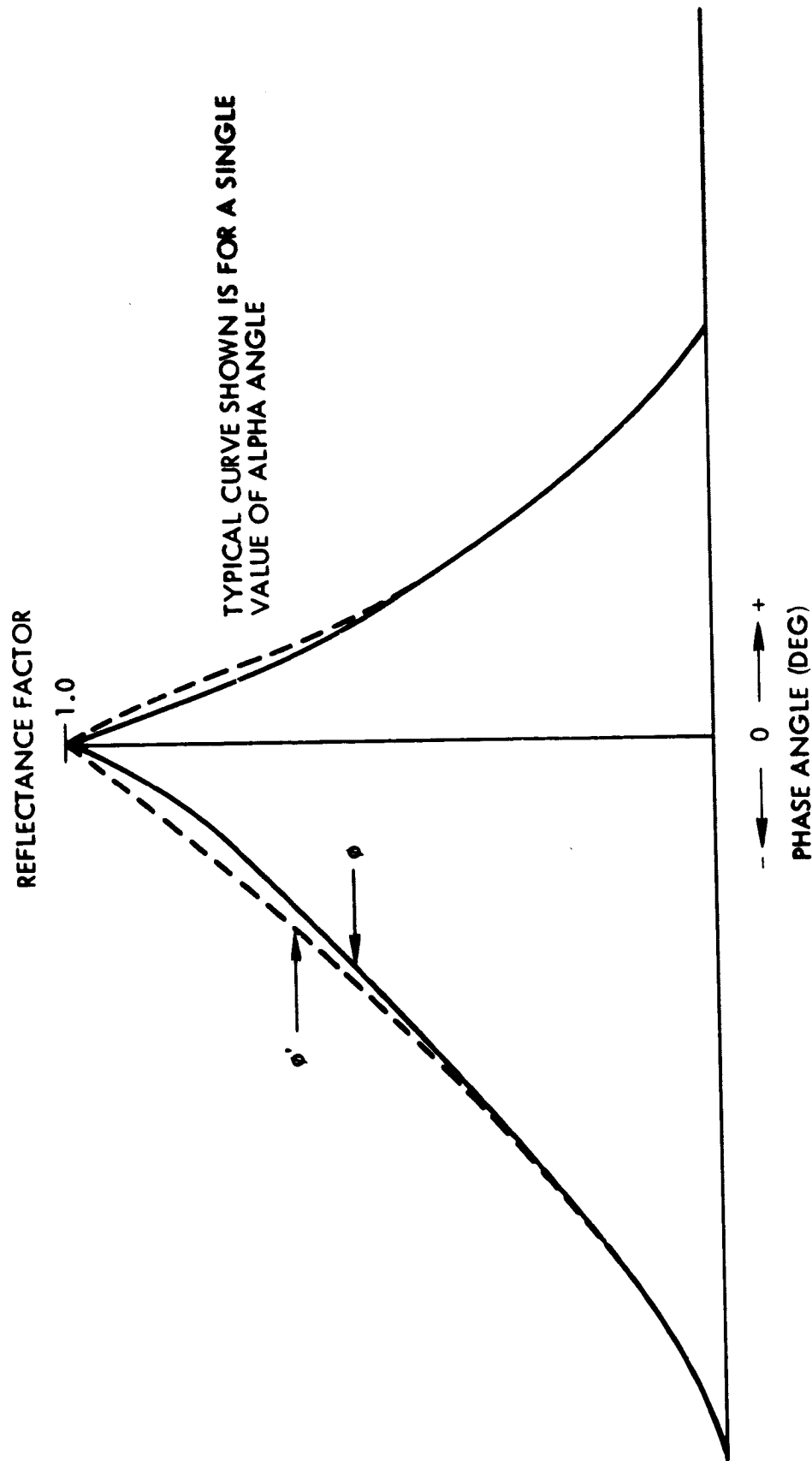


Figure 6-5. Graphical Illustration of Photometric Function Modification.
 ϕ' Describes Hypothetical Crater Reflectance, ϕ Describes Background Reflectance.

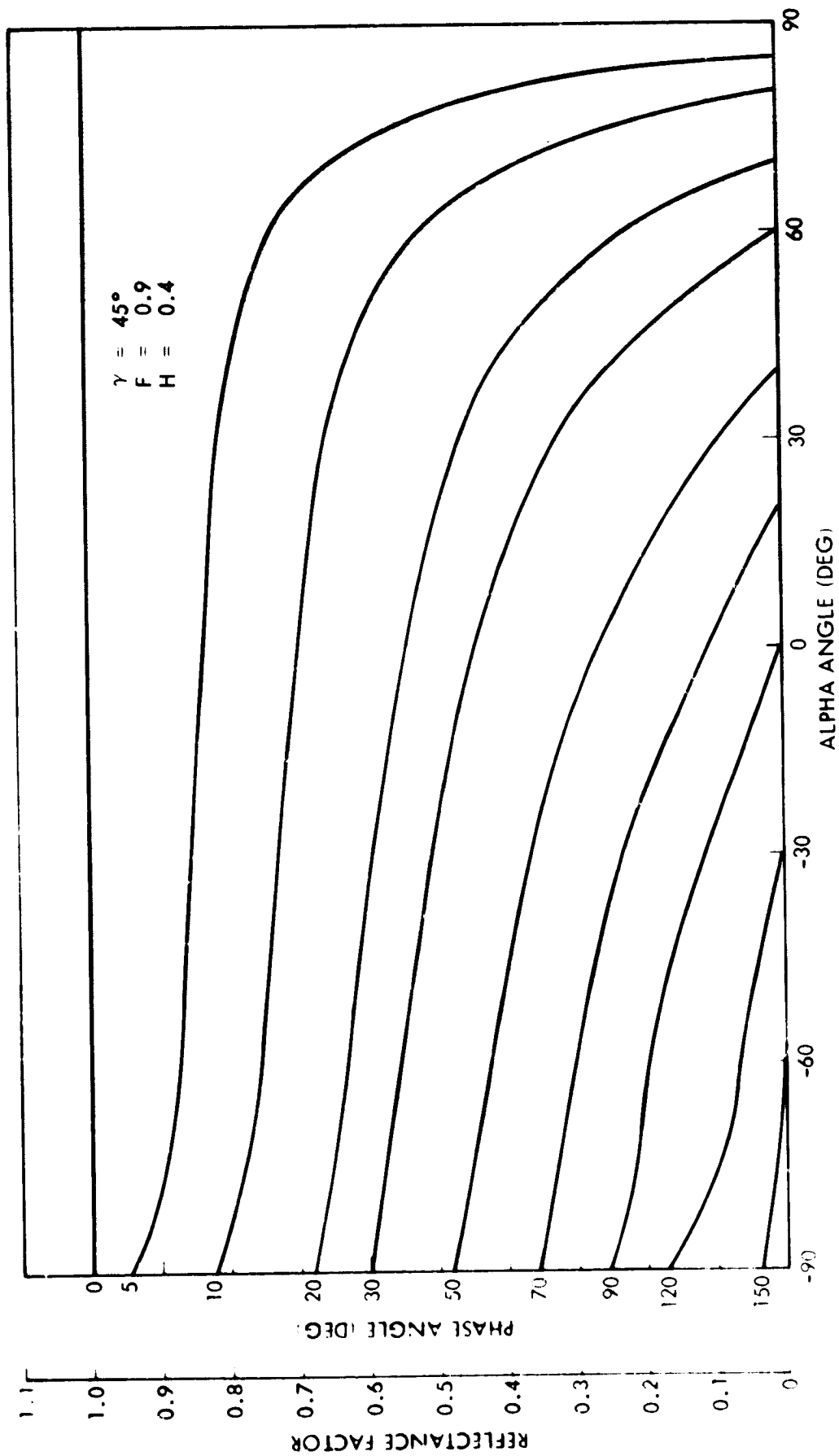


Figure 6-6. Hapke Photometric Function

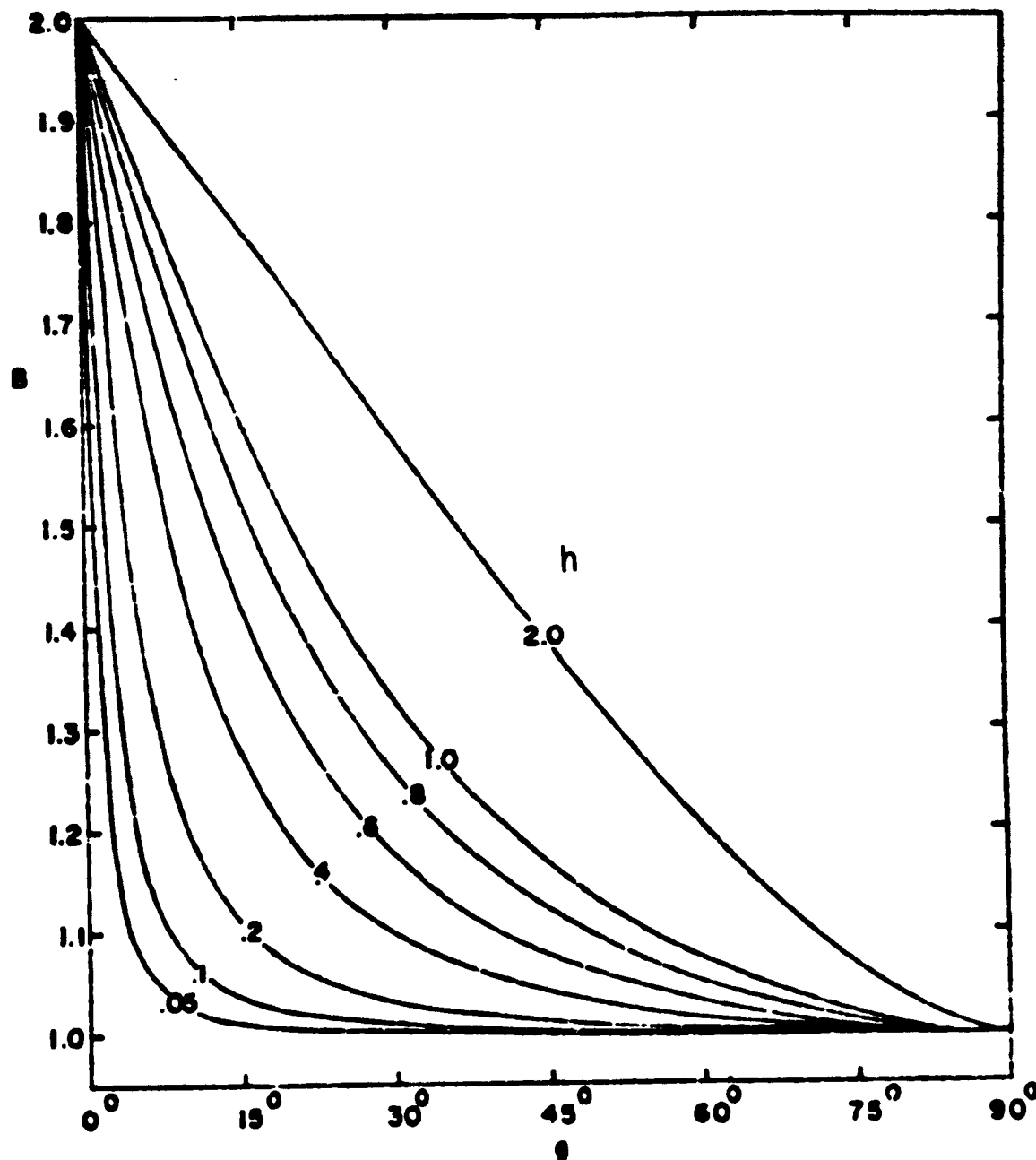


Figure 6-7. Retrodirective Function, B , versus phase angle, g , for various values of the parameter, h .
 $B(g) = 1$ for $90^\circ \leq g \leq 180^\circ$; $B(-g) = B(g)$.
(From Reference 10).

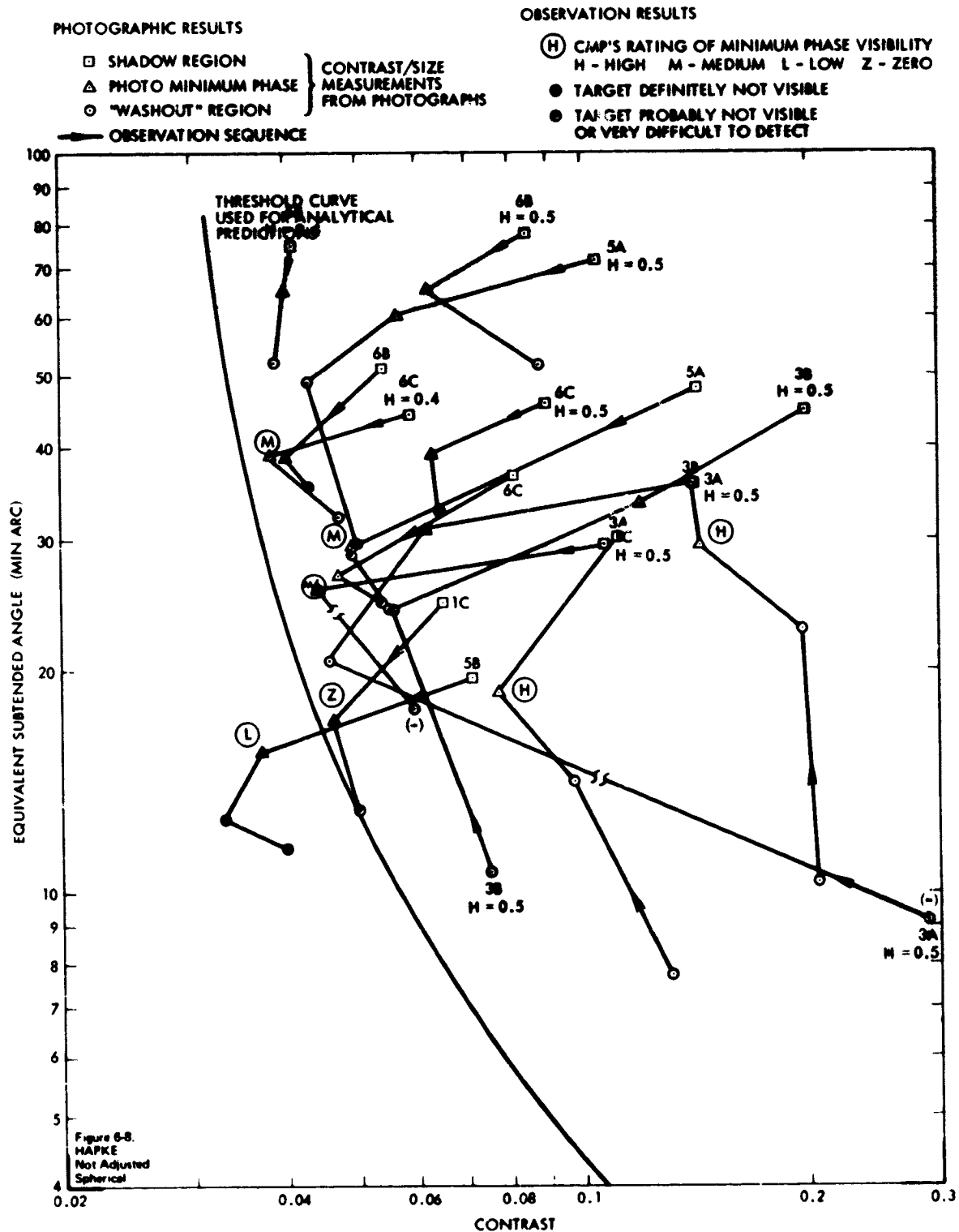


Figure 6-8. Overlay shows Crater Contrast Calculations for the Hapke Photometric Model with $H = 0.4$ for the Background Soil and $H = 0.5$ for the Crater Soil. For comparison equal albedo ($H = 0.4$) results are shown for two craters, 6A and 6B. Data unadjusted for subtended angle. Spherical section crater model was used. Printed page shows the Apollo 14 Visibility Test Results.

ORIGINAL PAGE IS
A PHOTOGRAPHY

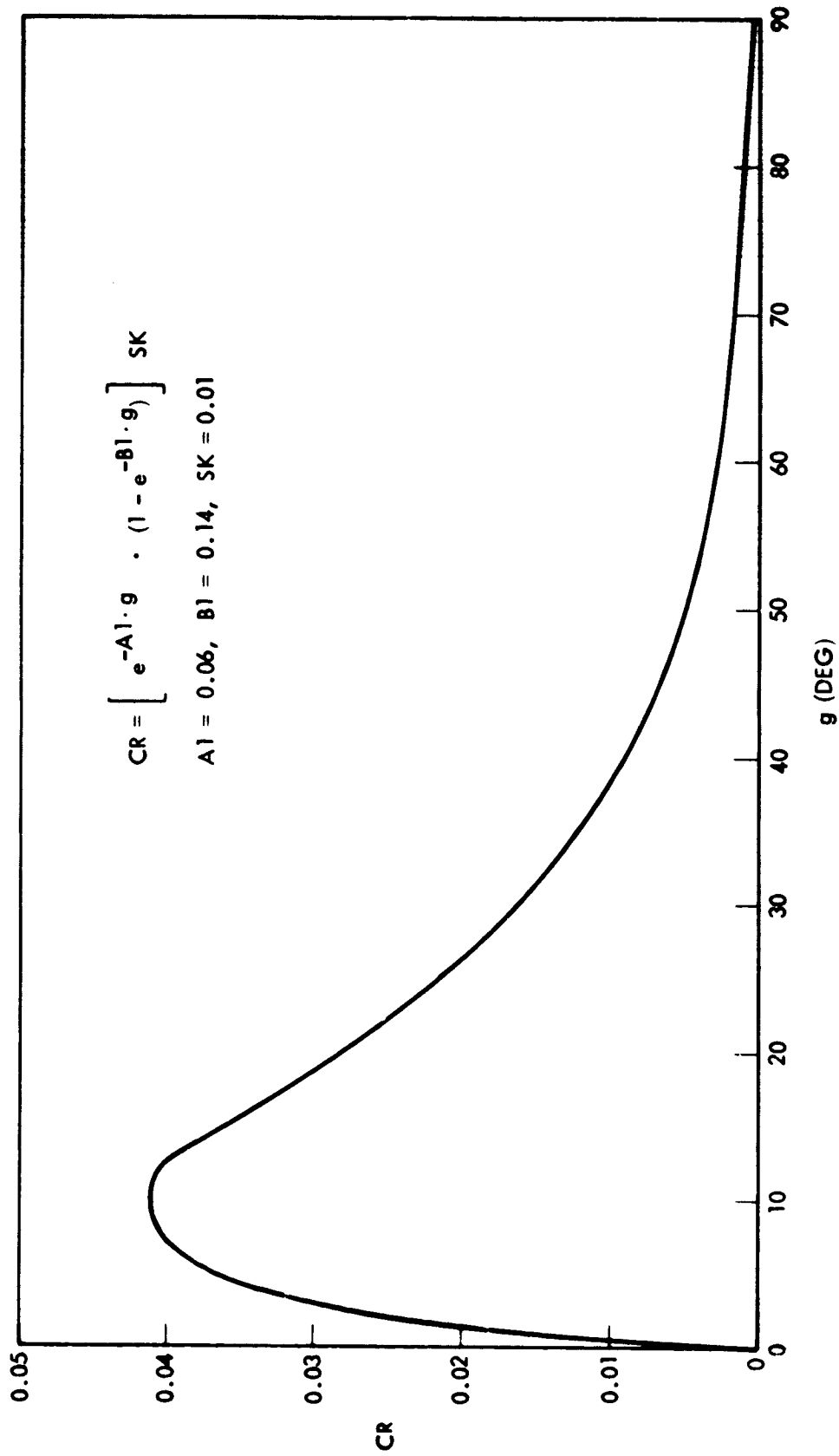


Figure 6-9. LRM Correction Term, CR, Versus Phase Angle, g.

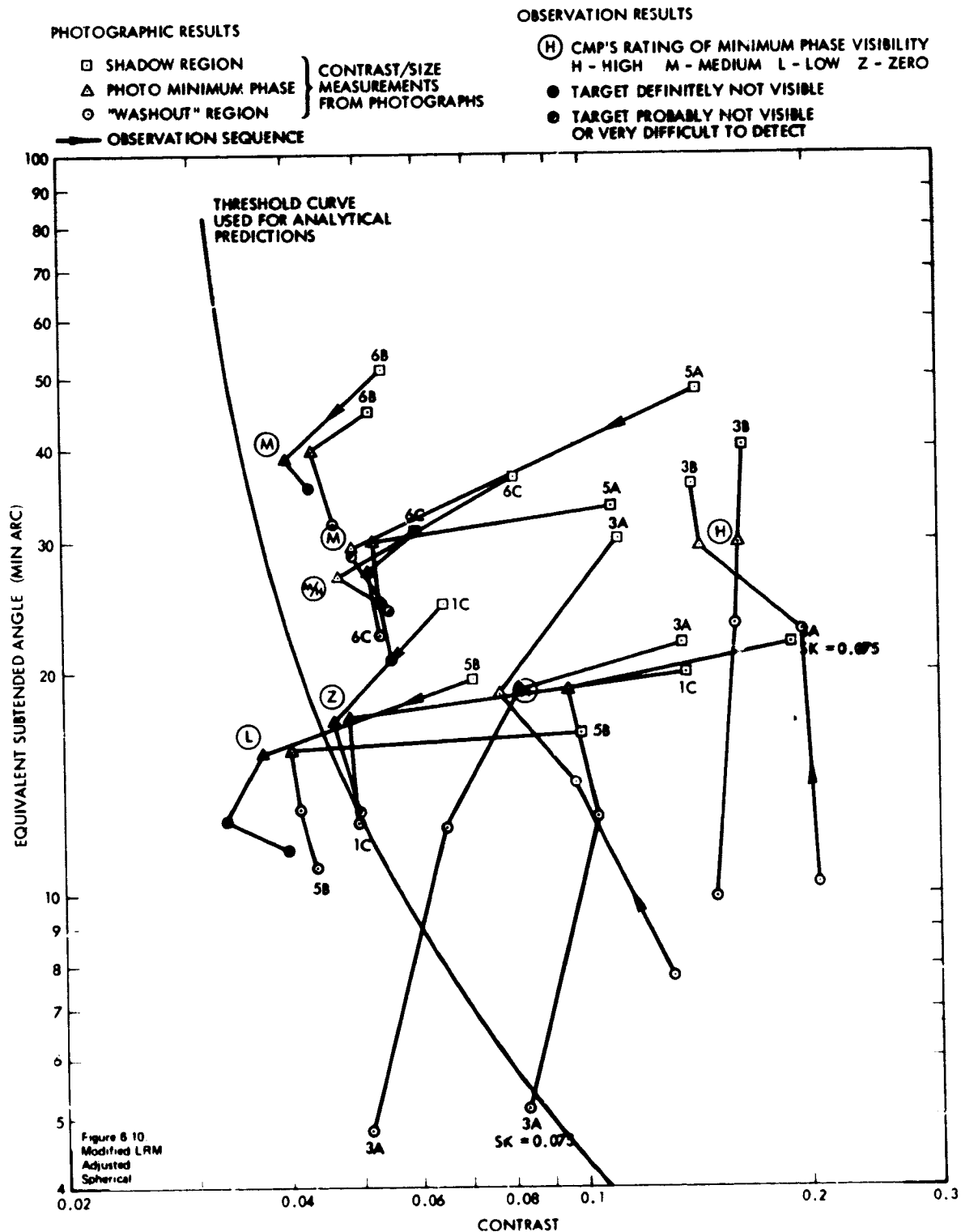


Figure 6-10. Overlay shows Crater Contrast Calculations for the Modified LRM Photometric Function with $SK = .01$, $A1 = 0.06$, $B1 = 0.14$ (see text). Data adjusted for subtended angle, spherical section crater model was used. A curve for $SK = 0.075$ is also shown for target 3A. Printed page shows the Apollo 14 Visibility Test Results. Compare to Figure 5-14.

7.0 DISCUSSION

The results of the Apollo 14 visibility test confirm the usefulness and validity of the techniques developed for analysis of lunar visibility problems. Additional information concerning lunar photometric functions, crater models, and interpretation of visibility estimates was gained. An overview of these results and how they relate to analyses of manned lunar operations is given in the present section.

7.1 Visibility Models and Mission Planning

As discussed at the end of Section 2, visibility analyses interact with many other considerations in the development of operational procedures, especially for a situation as complex as lunar landing. The techniques examined in this report, which are directed at visibility estimates for single craters, are only one element in a total study of visibility, although they comprise a basic starting point.

The most significant outcome of the Apollo 14 test is the increased confidence that can be placed in the method for visibility calculations and especially in the fact that one photometric function (LRM) was shown to be clearly superior to others which have been used. However, no matter how accurate, estimates which pertain to the visibility of single craters might be questioned in their applicability to detection and recognition performance in situations which involve patterns of landmarks, complex and varied backgrounds, boulders, and slopes, and crew tasks which vary from landing and surface exploration to landmark tracking from orbit. The value of the crater visibility analysis, as was touched on in Section 3.3, is that it provides a baseline specification of visibility conditions to which the specific characteristics of a given problem can be added to develop a complete analysis. Further, the analytical approach lends itself to parametric and trade-off studies. When combined with the other considerations that are specific to a given operational problem, it has been possible to generate guidelines that have been of substantial assistance for mission planning. Examples of such applications are given in References 34, 35, and 36 for descent visibility analyses; Reference 37 for Lunar Rover studies; Reference 38

for visibility through the LM engine induced dust plane; Reference 39 for a study of glare problems for an into-the-sun landing; and Reference 40 for an analysis of optimal look directions for surface photography.

However, this approach has limitations which follow from the difficulty of inferring astronaut performance in a complex control and perceptual task from performance estimates on isolated parts of that task. Obviously a "better" solution to descent visibility studies would have been the incorporation of a high fidelity model of the lunar surface into the LM simulator visual display system. Such an approach was impossible due to state-of-the-art limitations on simulator design, lack of high resolution terrain data for most sites, and lack of accurate photometric data for the sites.* Further, even laboratory experimental programs to investigate feature visibility would have been limited by the inability to accurately reproduce lunar terrain appearances at the landing sites in the laboratory. Thus, conclusions and recommendations regarding acceptable visibility conditions were rarely simple to arrive at; substantial considerations of past experience, trade-offs, site characteristics, etc., were always added to the basic results of visibility calculations.

7.2 Generality of Results

As explained in the introduction, the test was designed to study visibility under a fairly narrow range of conditions: in the washout area with sun elevation angles on the order of 20° to 30° . The washout region was of prime interest because this area posed the most unique and difficult visibility situation. The sun elevation angle range was based on the requirements of lunar landing, the most critical aspect of the mission with respect to visibility. Because the results confirmed the two most essential aspects of the analytical procedures, the photometric function and the threshold criterion, it seems reasonable to continue to apply these procedures to the entire range of viewing and illumination conditions.

* Visibility considerations were only one aspect of the Apollo program which had to proceed on limited information concerning the lunar environment. For instance, the LM footpad was designed before in-situ soil data were obtained. A remarkable feature of the Apollo program was the ability to design around unknown environments.

The most limiting aspect of the results is the narrow sun elevation angle range. Every Apollo crew has commented on the qualitative change of surface appearance that occurs with variations in sun elevation angle. Changes noted include hue variations (surface appears mostly black-gray-white at low SEAs to brownish-red at high SEAs), topographic changes (surface appears more flattened at high SEAs), and general comments about variation in overall appearance of features and patterns. It would have been of interest to obtain data under high sun elevation angle conditions, therefore, to determine if these effects are related to detection performance and if the photometric function at large phase angles also results in reasonable contrast predictions. Experience has been obtained on the lunar surface at sun elevation angles of about 45° for Lunar Rover Vehicle operations. Driving into the washout/zero phase regions was found to be a problem (as was driving into the sun) which is circumvented by slowing down and/or trying to keep at a non-zero sun relative azimuth angle (Ref. 41). Pre-mission traverse planning factors poor visibility regions into route determination in order to avoid or minimize disadvantageous conditions.

Another limitation to the results concerns the few data points taken. Typically, visibility experiments involve hundreds or thousands of trials to obtain data which can be statistically analyzed. In the present case, it was possible to draw conclusions from a handful of observations because of the goal of evaluating a well-developed model rather than from a necessity to obtain data from which to develop a model in the first place. Overall, this goal was met. However, the combination of few data points with the various unpredicted occurrences during the mission did result in somewhat less information being obtained than was possible. The most serious of the unexpected events were the very high albedos of the frontside targets, the loss of 25% of the data (pass 30F), and the lack of precise times at which visibility of the backside targets was lost. In spite of these problems, however, the data that were obtained were fairly clear in their relationships to the visibility models.

Although some modifications of the visibility model was indicated by the results, such changes are felt to be sufficiently marginal that their incorporation in the model does not seem worthwhile. Further, as the lunar

visibility model should not be used or interpreted in a "cookbook" fashion, the value of the Apollo 14 results lies more in the correct application and interpretation of visibility calculations than in second order corrections to the calculations themselves.

7.3 Lunar Surface Visibility and the Apollo Program

The visibility studies discussed in this report have had a unique and changing role in the Apollo program. In the period before the first manned lunar missions, the prime concern was with developing an understanding of an unusual lighting environment and of means for incorporating such understanding into mission planning. As with many other mission considerations, a conservative approach was taken to specification of acceptable lighting conditions in order to avoid even borderline situations. The extension of the acceptable lighting range for more recent Apollo missions was due to dual advances in operational capability (and confidence) and better knowledge of visual performance in the lunar environment. During this period, visibility studies and their interaction with mission planning advanced from a "special consideration" to a relatively routine aspect of mission analysis. The material in this report reflects the history of these studies and applications, as well as the results of the Apollo 14 tests themselves.

REFERENCES

- 1) H. E. Holt and J. J. Rennilson "Photometric and Polarimetric Properties of the Lunar Regolith" in Apollo 14 Preliminary Science Report, NASA SP-235, 1970. pp. 157 - 161.
- 2) P. Willingham "The Lunar Reflectivity Model for Ranger Block III Analysis," NASA/JPL TR32-664, Nov. 2, 1964.
- 3) N. N. Sytinskaya and V. V. Sharanov "Study of the Reflecting Power of the Moon's Surface," STL (now TRW)-TR-61-5110-23, May 1961 (translated).
- 4) D. L. Harris "Photometry and Colorimetry of Planets and Satellites" in The Solar System, Vol. III: Planets and Satellites, G. P. Kuiper and B. M. Middlehurst (eds.), University Chicago Press, 1961, pages 272 - 342.
- 5) V. A. Fedoritz "Photographic Photometry of the Lunar Surface," Reports of the Astronomical Observatory of the Charkow State University, Vol. 2, 1952.
- 6) A. G. Herriman, et al, "Ranger Pre-flight Science Analysis and the Lunar Photometric Model," NASA/JPL TR 32-384 (Revised), March 11, 1963.
- 7) M. Minnaert "Photometry of the Moon" in The Solar System, Vol. III: Planets and Satellites, G. P. Kuiper and B. M. Middlehurst (eds.), University Chicago Press, 1961, pages 213 - 248.
- 8) J. Gallagher and J. Hallock "A Lunar Photometric Function: Curves for Calculating the Differential Luminance of the Lunar Surface," MIT Inst. Lab. E-1819, July 1965.
- 9) B. W. Hapke "A Theoretical Photometric Function for the Lunar Surface," J. Geophysical Res., 1963, 68, 4571-4586.

REFERENCES (Continued)

- 10) B. W. Hapke "An Improved Theoretical Lunar Photometric Function,"
The Astronomical J., 1966, 71, 333-339.
- 11) B. W. Hapke "Photometric and Other Laboratory Studies Relating to the
Lunar Surface" in The Lunar Surface Layer, J. W. Salisbury and
P. E. Glaser (eds.), Academic Press, 1964, pp. 323 - 344.
- 12) R. W. Shorthill, et al, "Photometric Properties of the Lunar Surface,"
NASA CR-1429, Nov. 1969.
- 13) J. A. Swets and W. P. Tanner, Jr., "Decision Processes in Perception,"
Psychol. Rev. 1961, 68, 301 - 340.
- 14) Personnel Communication and Briefing Presentation to NASA by R. Troester,
Bellcomm, Inc.
- 15) S. Q. Duntley, et al, "Visibility," Applied Optics, 1964, 3, 549 - 598.
- 16) H. R. Blackwell "Contrast Thresholds of the Human Eye," J. Opt. Soc. Am.,
1946, 36, 624 - 643.
- 17) J. H. Taylor "Use of Visual Performance Data in Visibility Predictions,"
Applied Optics, 1964, 3, 562 - 569.
- 18) H. R. Blackwell "Specification of Interior Illumination Levels,"
Illum. Eng., 1959, 317 - 353.
- 19) K. Ziedman "Lunar Surface Visibility," TRW TR 05952-6011-R000, August 3,
1966.
- 20) R. R. Breshears and L. L. Lewyn "Visual Detection of Protuberance
Hazards on the Lunar Surface," NASA Study Report (OMSF), August 15,
1963.
- 21) T. Y. Feng "A Study to Determine Optimum Lunar Lighting Conditions for
Visual Selection of LEM Touchdown Point," Hughes Aircraft Co., Final
Report, NAS-9-5321, Jan. 1967.

REFERENCES (Continued)

- 22) I. Saulietis "Visibility of Lunar Craters During the LEM Final Approach Phase," MSC Internal Note No. 66-EG-4, Jan. 19, 1966.
- 23) J. L. Alward "Input Guide for Crater Contrast Program - ALTARG," TRW Systems Internal Memorandum 7538.2-020, May 26, 1972.
- 24) S. C. Wynn "TOPORAMA's Shading Program - SHADE, Case 310," Bellcom Memorandum Report, March 31, 1972.
- 25) J. L. Alward "Development of Conical Analytical Model for Moon Craters," TRW Systems Internal Memorandum 7538.2-019, May 24, 1972.
- 26) A. Morris "Pattern Target Analysis: Part I. A Theory; Part II. A Psychophysical Experiment," Visibility Laboratory, University of Calif., San Diego, SIO 59-62, Nov. 1959.
- 27) H. R. Blackwell and G. A. Bixel "The Visibility of Non-Uniform Target Background Complexes," Institute for Research in Vision, Ohio State Univ. Res. Found., Tech. Report No. 890-1, April 1960.
- 28) K. Ziedman "Visibility and Apollo 8 Photographic Results" in Apollo 8 Photography and Visual Observations, NASA SP-201, 1969, pp. 44 - 51.
- 29) E. S. Lamar, et al, "Size, Shape and Contrast in Detection of Targets by Daylight Vision. I. Data and Analytic Description," J. Opt. Soc. Am., 1947, 37, 531 - 543.
- 30) W. Moore "Timing Analysis for Apollo 14 Zero Phase Photographic Sequence," TRW Systems Internal Memorandum 7343.5-023, May 18, 1971.
- 31) Apollo 14, Photographic and Science Debriefing, 1971 (document not numbered).
- 32) K. Ziedman "Comments by Stu Roosa on Apollo 14 Zero Phase Photography," TRW Systems Internal Memorandum 7246.4-68, March 2, 1971. (The set of prints which Roosa examined were transmitted to NASA with the copies of this report.)

REFERENCES (Continued)

- 33) H. A. Pohn, R. L. Wildey, and T. W. Offield "Correlation of the Zero-Phase Brightness Surge (Heiligenschein) with Lunar-Surface Roughness" in Apollo 14 Preliminary Science Report, NASA SP-272, 1971, pp. 296 - 297. (See also H. A. Pohn, et al, "The Moon's Photometric Function Near Zero Phase Angle from Apollo 8 Photography," The Astrophysical J., 1969, 157, L193 - L195.
- 34) K. Ziedman "Visibility During Descent and Landing on Apollo 15 for a $T_0 + 24$ Launch," TRW Systems Internal Memorandum 7343.4-002, May 12, 1971.
- 35) K. Ziedman "Apollo 16 $T_0 + 24$ Descent Analysis: May 16 and June 15 Launch Dates," TRW Systems Internal Memorandum 7538.4-020, April 11, 1972.
- 36) K. Ziedman "Descent Visibility Analysis for Apollo 17: $T + 48$ Launch, Jan. 6, 1973, TRW Systems Internal Memorandum 7538.4-022, June 20, 1972.
- 37) R. E. Hutton "Lunar Roving Vehicle Operational Characteristics," TRW Technical Report 17618-6002-01, Feb. 1972 (see insert pages 3, 4 and report pages 83 - 97).
- 38) K. Ziedman "The Effects of Dust on Visibility During Lunar Landing," TRW Systems Internal Memorandum 7246.4-71, March 29, 1970.
- 39) R. Troester "Reduction in Lunar Surface Visibility Due to Glare During a Landing into the Sun," Bellcomm Tech. Memorandum 68-2013-5, Sept. 30, 1968.
- 40) H. W. Radin "Lunar Surface EVA Photography of Hadley Rille - Contrast as a Constraint," Bellcomm Tech. Memorandum 72-2015-2, Feb. 1972.
- 41) K. Ziedman "Crew Comments and Observations on Visibility Conditions During Apollo 16," TRW Systems Internal Memorandum 7538.4-024, July 19, 1972.

APPENDIX A. PHOTOGRAPHIC PROCESSING AND CALIBRATION

Type SO-349 70 mm film was used in Magazine R. Calibration plans for the film included pre- and post-flight exposure of 21 step gray scales on film samples stored on Earth as well as on the flight film to test for effects of time, space environment, and development uniformity. Only two gray scales were supplied, however, with the second generation positive prints used for the microdensitometry. Density measurements of these scales were averaged and used in the calculations of target contrasts. The exposure, processing and control methods employed by NASA/MSC are given in the Reference. Diffuse density-log E curves can also be obtained from NASA.

The two gray scales were scanned on two different occasions by Photometric Data Systems, Inc. using a different microdensitometer each time (the film scanning was done in two batches, the first being the minimum phase frames, the second being the remaining frames). In each case, the same circular aperture used to scan the targets was used to scan the gray scales (16 μ m diameter). Five scans were taken of each of the two gray scales (center and two on either side) and the results of all ten scans were averaged. The exposure levels (obtained from NASA/MSC) corresponding to each gray scale step are given in Table A-1. Plots of D-log E for the 10 scan averages obtained on each occasion are shown in Figure A-1. Exposure values corresponding to the original gray scale steps are indicated as is the curve which was fitted to the first set of data points. A similar curve was fitted to the second set of measurements. Note the vertical displacement of the two curves; according to the vendor, this effect was most likely due to a zero offset on the 1st set of measurements. As only the slope of the curve was essential to the present analysis, this discrepancy was not a problem (see error discussion in Appendix B).

Reference: "Apollo 14 Photographic Standards Document" TTR 7-1, Feb. 29, 1971, (NASA/MSC Photographic Technology Division).

TABLE A-1. EXPOSURE AND LOG EXPOSURE VALUES CORRESPONDING TO
ORIGINAL NEGATIVE GRAY SCALE STEPS, MAG R, APOLLO 14

GRAY SCALE STEP NO.	EXPOSURE (M-C-S)	LOG EXPOSURE
18	6.86	0.8364
17	4.85	0.6860
16	3.43	0.5356
15	2.42	0.3852
14	1.72	0.2348
13	1.21	0.0844
12	0.86	-0.066
11	0.61	-0.2164
10	0.43	-0.3668
9	0.30	-0.5172
8	0.22	-0.6676
7	0.15	-0.8180
6	0.11	-0.9684
5		-1.1188
4		

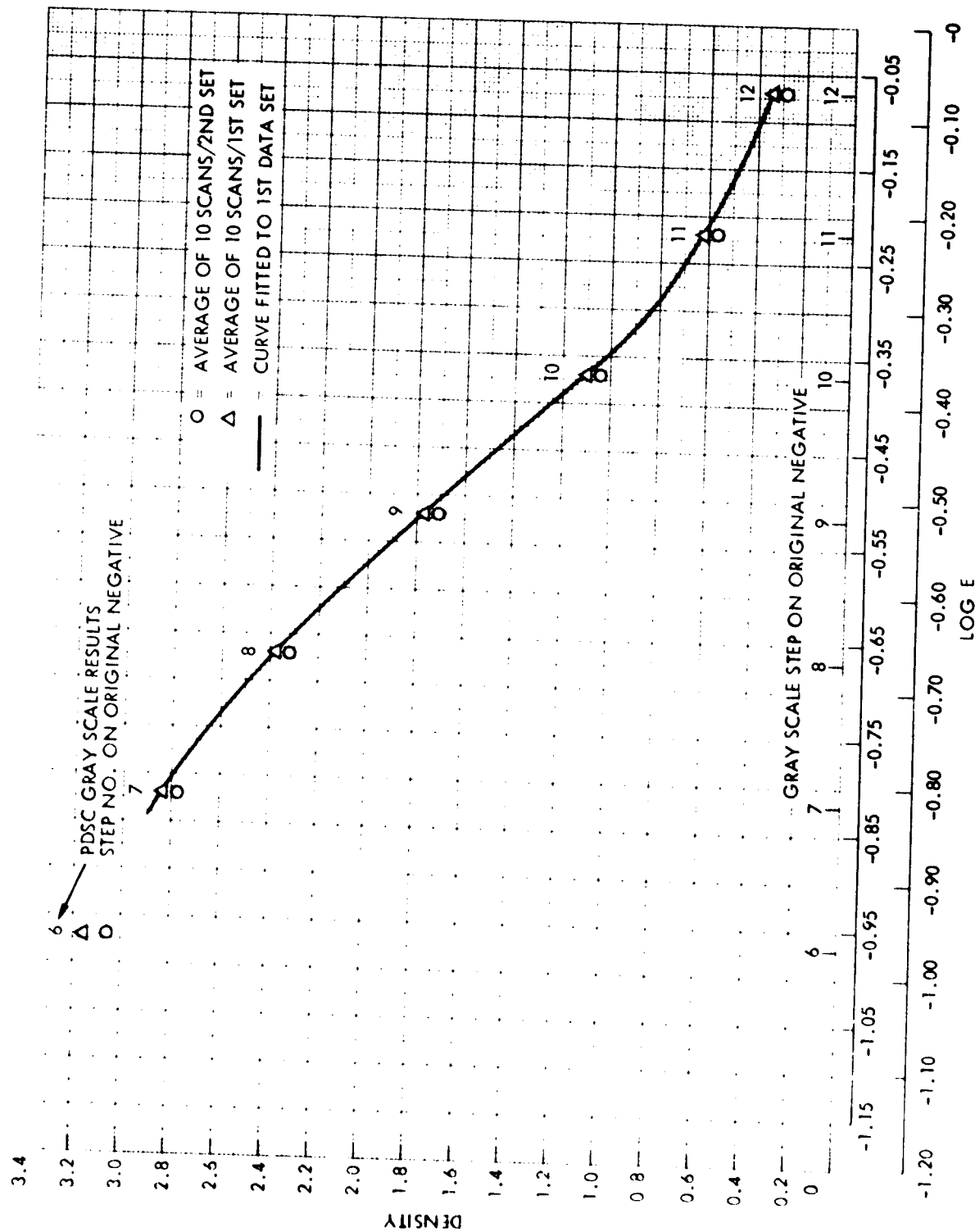


Figure A-1. D-Log E Calibration Curves Obtained from Micro-Densitometer Scans of Apollo 14 May 12 Gray Scales. Aperture Diameter = 16 μ m.

APPENDIX B. MICRODENSITOMETRY AND ERROR SOURCES

Estimation of errors in the determination of target contrast and subtended angle is extremely difficult due to the many different transformations applied to the data, as well as the judgmental aspects of determining target outlines that was discussed in Section 5. The purpose of this Appendix is to list the error sources and to provide quantitative estimates of errors where possible.

B.1 Error Sources

The main sources of error, listed in the temporal order of the processing steps, are:

- 1) Variations in film processing along the length and width of the film strip and accuracies of the gray scale exposure levels.
- 2) Electrical and mechanical noise in the microdensitometer.
- 3) Errors in reading density values in the strip chart records resulting from the scans of the gray scales.
- 4) Validity of the positions selected for the five gray scale scans (see Appendix A) of each gray scale.
- 5) Errors in the D-log E curve fitted to the resulting averages of density values.
- 6) Errors in selection of the crater outline.
- 7) Errors in selection of an appropriate background for each target.

B.2 Discussion

Variations in film processing were not analyzed. The individual gray scale scans did vary slightly from location to location; but the differences were less than 10% at most, and typically only a few percent. The strip chart record used to record the gray scale scans was "noisy" due to the small scanning aperture and, thus, some error was introduced in visually averaging the traces.

The overall microdensitometer noise level was analyzed, as a by-product of an image processing task undertaken with the Apollo 14 Descartes photography. A 1000 x 1000 point matrix was scanned twice without moving the film on the instrument on Apollo 14 Frame 10257 (targets 3A and 3B). These two scans were conducted by Photometric Data Systems at the time the second set of targets were scanned (see Appendix A). Using the image processing system at the Jet Propulsion Laboratory, a pixel by pixel difference record was made. If the results of the two scans were identical, then the difference record would be zero. The variance of the difference record is, thus, a measure of lack of repeatability. The results indicated a signal-to-noise ratio of about 140 or a 7 bit data range. As will be seen, the microdensitometer noise level is, thus, a negligible contributor to final uncertainty of contrast measurements.

The repeatability of contrast calculations was examined with the aid of the repeated scans on Frame 10257. Table B-1 presents the results of several cases examined. The first row compares contrast and average exposure calculations for 3B from the second 1000 x 1000 scan of Frame 10257 for the two different D-log E calibration curves corresponding to the two different batches of scans. The difference in contrast is small (about 3%) and the difference in mean exposure is as expected, as the first curve given higher exposure values than the second curve (Figure A-1). Note that the only difference between the two cases was the calibration curve; the same crater outline and exposure data set were used.

The second row gives results for the original scan of 3B (first batch of scans). In this case, the first calibration curve was used but a different type microdensitometer was used and a different crater outline placement was necessary (same size outline, but relocated with respect to scan corner). In this case, a contrast difference of about 9% exists, with a larger difference in absolute exposure. Finally, the last two rows compare repeated calculations for 3A using identical calibration curves and outlines, but with the first and second 1000 x 1000 scans of Frame 10257. In this case, the difference is only 1.3%, reflecting the high signal-to-noise ratio discussed above.

Table B-1. Comparison of Repeated Contrast (C) and Average Exposure (E) Calculations.

DATA FROM:		CALIBRATION FROM:			
		1st Set		2nd Set	
		C	E	C	E
Target 3B 10257	1000 x 1000 scan - Rep. 1	0.161	0.359	0.165	0.350
	Original Scan	0.148	0.380		
		<div> <div>2.5%</div> <div>8.8%</div> <div>11.5%</div> </div>			
Target 3A 10257	1000 x 1000 scan - Rep. 1			0.077	0.394
	1000 x 1000 scan - Rep. 2			0.078	0.394
		<div> <div>1.3%</div> </div>			

(Bright side contrasts shown, background was 10 scan lines larger than target outline)

It is concluded that differences in calibration data and repeated scans (at least with the second instrument, which was a better machine) are not major error sources for contrast calculations. Contrast differences arising between the two machines are apparently less than 10%, although this conclusion is based on limited data.

The most serious error sources, which are also the most difficult to quantify, are those involving the selection of the crater and background regions. In some cases, as for 3B, the boundary is distinct and can be easily specified (Figure 5-1); in other cases, the boundary was more diffuse or irregular and very difficult to specify (Figure 5-3). In general, it was necessary to iterate between the photographs and the computer plots illustrated by the above Figures to specify a boundary. After a crater outline was decided upon, the size of the background had to be determined. Only in a few cases was the background sufficiently homogeneous so that its size was unimportant.

This problem was approached, in part, by varying the size and position of the target outline and the size of the background. In this way, an estimate of error or variation could be obtained by examining background and target homogeneity, contrast variation, etc. In general, a criterion of 1.5 arc min. or 10 scan lines was used to define the width of the background region, unless a specific case indicated this should be larger or smaller. The 1.5 arc min. criterion is based on estimates of the critical width of boundaries for threshold detections. Typical results are shown in Tables B-2 and B-3. Table B-2 compares the effect of a size change of the target outline (keeping the background annuli a constant number of scans larger than the target) on bright side contrast for three typical cases. The largest difference shown is 9.1% for target 3B.

The effect of changing background size, keeping target outline constant for the same three targets given in B-2, is shown in Table B-3. Note the substantial difference between 1C, which had a fairly homogeneous background, and the other two targets whose background luminance changed as distance from the target increased. However, in either case reasonable size backgrounds (at least 5 scan lines larger than the target outline) do not result in more than a 10% variation in contrast.

Table B-2. Effect of Size Change of Target Crater Outlines on Bright Side Contrast Values.

<u>TARGET</u>	<u>FRAME</u>	<u>OUTLINE POSITION OR SIZE</u>	<u>BRIGHT SIDE CONTRAST</u>	<u>PERCENT DIFF.</u>
3B	10257	Nominal	0.143	
		2 scans smaller	0.130	9.1
		2 scans larger	0.146	2.1
1C	10225	Nominal	0.046	
		2 scans smaller	0.050	8.7
		2 scans larger	0.046	0
5A	10279	Nominal	0.055	
		2 scans smaller in minor axis	0.052	5.5
		2 scans larger in minor axis	0.058	5.5

Table B-3. Effect of Changing Background Size on Bright Side Contrast Values.

<u>TARGET</u>	<u>FRAME</u>	<u>BACKGROUND SIZE*</u>	<u>BRIGHT SIDE CONTRAST</u>	<u>PERCENT DIFF.**</u>
3B	10257	2	0.110	-23.0
		4	0.125	-12.6
		6	0.135	- 5.6
		8	0.143	0
		10	0.148	+ 3.5
1C	10225	2	0.049	+ 6.5
		4	0.049	+ 6.5
		6	0.049	+ 6.5
		8	0.046	0
		10	0.047	+ 2.2
5A	10279	2	0.049	-10.9
		4	0.048	-12.7
		6	0.053	- 3.6
		7	0.055	0

* Background size is number of scan lines greater than target boundary.

** Relative to background used for analysis (0%).

Thus, the largest single error of the contrast estimates is on the order of 10%. Derivation of a rule for combining the various error sources was not attempted; obviously, both systematic and random sources are effective but each target and each frame would have to be treated as a separate case, due to the differences in target and background specifications. An overall error of at least 10%, and certainly 20% at the outside, seems to be a reasonable estimate. Inspection of Figure 5-14 indicates that even a 20% error would not change the main conclusion (adequacy of model and threshold function), although certainly some of the lower order trends in the data could not be supported under a 20% assumed error.

APPENDIX C: OBSERVATIONAL RESULTS FOR EACH TARGET AREA

Because a small number of targets were used for the Apollo 14 tests, the test outcome could be biased by peculiarities of each target. Therefore, an area-by-area description of the CMP's observations are given to help evaluate the test results. The comparison of the CMP's observations with target detectability on the film record is also given, as are some comments on the misidentification of target 1A. A second generation positive transparency print of the flight film was used in the comparison (see Appendix A).

C.1 Observations

Area 1 - Targets 1A, 1B, 1C (SEA = 22°):

All three targets in this area (Figure 5-8) were acquired prior to minimum phase. Prior to minimum phase, all three targets exhibit shadowing and are located in well defined positions with respect to surrounding landmarks. Target 1C is seen at photographic minimum phase in Frame 10225; at this time it was completely lost by the CMP (rated zero) and, furthermore, it cannot be detected on the second generation transparencies of this frame at normal magnification, although it can be seen at 6X.* The albedo of this target is evidently nearly equal to that of its surroundings, a fairly smooth crater floor with many high albedo areas. In addition, 1C exhibits fairly uniform albedo over its surface. The crater is visible on the next frame (10226) (20 seconds later), but becomes undetectible under normal magnification at a VEA of 15° .

Target 1B, seen near its minimum phase point in Frame 10226, is a somewhat irregularly shaped, shallow crater which exhibits a non-uniform albedo distribution over its surface (see also Figure 5-8). It is located in fairly rugged terrain, but several distinctive features are available as lead-ins. This crater was visible on the film into the washout down to a VEA of 10° at normal magnification. Target 1A is not included in this discussion because of the anomalous observational results (see below).

* Normal magnification is that resulting in an image on the film which subtends the same angular dimension as did the actual target when seen from orbit. For the 70 mm format using an 80 mm lens, this is about 3X.

Area 2 - Targets 2A, 2B (SEA = 29°):

Target 2A is a steep, bright target located near the rim of Langemak (Figure 5-9). It was easily acquired and tracked through minimum phase (minimum phase visibility rated medium to low by the CMP), although the superimposed rays in the area make a very bright background which tends to obscure the target. Detailed inspection of the transparencies shows that with normal magnification it can be located as a bright "splotch" down to a 7° VEA by using two small, bright craters as lead-ins; however, it cannot be identified as a crater for values of VEA less than 15°.

Target 2B is a poorly defined depression in a very hummocky area (see also Figure 5-9). Although it could be identified from the photography, its similarity to adjacent features and the general nondescript character of this region apparently combined to make recognition very difficult under flight conditions (the CMP had very low confidence in his acquisition of 2B). It can be seen on the transparencies, with some difficulty, for values of VEA down to 20° for normal magnification.

Area 3 - Targets 3A, 3B (SEA = 26°):

Targets 3A and 3B are located in Ptolemaeus, a relatively dark, flat area with several features serving as good lead-ins. Both 3A and 3B were acquired at surprisingly low VEAs of about 3°. Target 3B was located first with Ptolemaeus as a reference, then by using Ptolemaeus D and the bright "beacon" crater to the NE of 3B. Target 3A could then be acquired by looking to the SE from 3B. The CMP's comments indicate that acquisition was initially uncertain but was confirmed by the time a VEA of 5° was reached. On the transparencies both craters show up as thin, bright lines against a dark background at the beginning of the pass.

Frame 10250 (Figure 5-10a) shows the craters about 140 seconds after the time of acquisition and Frame 10257 (Figure 5-10b) shows them at minimum phase. At minimum phase target 3B exhibits a fairly uniform high contrast, whereas 3A is a subdued crater of low apparent contrast except for its bright rim. Its rim undoubtedly accounts for the surprising results on 3A, as pre-mission photography indicated the entire crater was very subdued and acquisition at long ranges was not expected. Both targets were rated "high" for minimum phase visibility. Finally, Frame 10258 (Figure 5-10b) shows the targets after they moved uprange of zero phase.

Targets 3A and 3B cannot be definitely recognized in the second generation transparencies on frames prior to 10248 at normal magnification. Frame 10248 was taken about 40 seconds after the CMP reported detection and corresponds to a 4.82° VEA at 3A and 4.0° VEA at 3B. On Frame 10246, taken at about the same time the CMP reported acquisition, the rim of both targets can be recognized at 12 X magnification, but substantial examination time is required. Thus, the film seems to be slightly worse than the eye in this case, but not significantly so. The image of 3A on Frame 10246 covers an area of about $70 \times 10^{-4} \text{ mm}^2$ or about 10 resolution elements, assuming 40 lp/mm system resolution ($6.25 \times 10^{-4} \text{ mm}^2$ per resolution cell). Thus, recognition of these targets is made possible by utilizing near-maximum resolution capabilities of the camera/film system.

Area 4 - Targets 4A, 4B (SEA = 15°):

Both 4A and 4B were bright, easily locatable features (Parry M and Parry were used as lead-ins). They were seen almost immediately after the CMP switched his attention from area 3 to area 4 at a VEA of about 7° . Based on the area 3 results, 4A and 4B probably could have been detected prior to this time if the CMP had looked for them. As in the case of 3A and 3B, the area 4 targets had a relatively uniform, flat surround; both were rated high for minimum phase visibility (Figure 5-11). The low SEA at these targets coupled with their relatively high apparent contrast makes them of less interest than any of the other targets used.

Targets 4A and 4B can be detected on Frame 10257 at normal magnification, corresponding to a VEA of 1.99° and 2.11° , respectively. Thus, these targets are more easily detected on the film than are 3A or 3B - a result compatible with their greater apparent contrast.

Area 5 - Targets 5A, 5B, 5C (SEA = 23°):

These targets, grouped close together, are located in a hilly, generally featureless area near the rim of an old crater. Based on the photographic records, they were rated low in apparent contrast; the CMP rated them low (5B, 5C) and medium (5A) for minimum phase visibility. They are shown in Figures 5-12a,b. These targets tend to blend into their background and acquisition down-range of zero phase depends on the use of surrounding features to locate the targets. The difficulty of down-range acquisition is

illustrated in Figure 5-12b. Target 5A was lost at VEAs less than 16° on the transparencies at normal magnification.

Area 6 - Targets 6A, 6B, 6C (SEA = 31°):

Only two of these three targets, 6B and 6C, were acquired prior to minimum phase. Target 6A was a very flat, old crater (D/D = 47:1), which is not visible on the photography, although it was visible on the pre-mission photography used to select targets. The terrain in which the area 6 targets are located is in an old basin fill, somewhat like Ptolemaeus, but exhibiting a somewhat larger average luminance, a wider range of luminance variations and more craters. Targets 6B and 6C were tracked through minimum phase; minimum phase visibility of 6B was rated medium and that of 6C was rated high to medium. Target appearances prior to minimum phase and near minimum phase are shown in Figure 5-13. Even though the targets were tracked through minimum phase, they became difficult to locate down-range. On the transparencies, they were undetectable below VEAs of ~~15~~¹⁵ $^{\circ}$ at normal magnification.

C.2 Misidentifications

The three targets that were not seen or misidentified deserve individual comment. Target 6A, which was not seen at all, was an extremely shallow low contrast crater. This feature was quite subdued on the pre-flight photography used for target selection and only a suggestion of its outline could be seen on the Apollo 14 zero-phase frames. The combination of low contrast and relatively high sun angle (31°) was apparently effective in washing out 6A. Target 2B was a relatively obscure feature in a very hilly area which was nearly eliminated in pre-mission planning as being too difficult to identify. However, it was retained because no other feature in the area appeared any better and only one other target was available. The uncertainty encountered in its identification during the mission was, therefore, not unexpected.

The apparent misidentification of Target 1A is difficult to explain. Misidentification was inferred on the basis of the timing analysis (Reference 30), which showed a discrepancy of 35 seconds between the predicted minimum phase time and the time at which the CMP announced the target at zero phase. This is a very large discrepancy (for all the other targets, it was no larger than a few seconds), and implies the CMP was looking at the wrong target.

Further, the photography shows minimum phase at 1A at the predicted time. The one other explanation, that the time identification on the transcript is wrong, seems unlikely as all other time marks that can be independently checked are accurate. However, the conclusion that 1A was misidentified is rendered less certain by the fact that it was a fairly obvious target, it was acquired in good visibility conditions, and that the lead-ins for 1A identified post-mission by the CMP clearly lead to that feature. Therefore, some ambiguity remains concerning identification of this target.

APPENDIX D. CALCULATION OF EQUIVALENT SUBTENDED
ANGLES FROM NUMBER OF SCAN POINTS

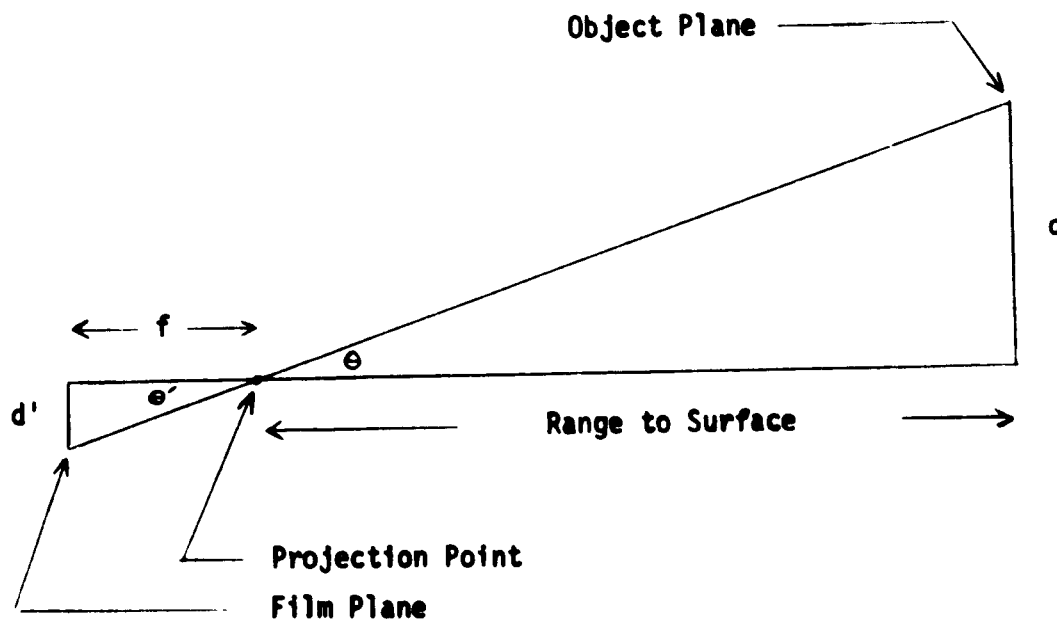


FIGURE D-1. CAMERA-FILM GEOMETRY (Not to Scale).

Camera-film geometry is shown in Figure D-1. The projection point of the camera lens is assumed to be located at the focal length, f , in front of the film plane. The area of a target image of arbitrary shape on the film is, with a small error, equal to the number of pixel elements comprising the image, N_T , multiplied by the square of the spacing of the pixels, $16\mu\text{m}$.

$$A_F = 2.56 \times 10^{-4} \times N_T \text{ mm}^2$$

The diameter of a circle of equivalent area to A_F is:

$$d' = 2 \frac{A_F}{\pi}^{1/2}$$

The distance d' subtends an angle θ' at the optical projection point:

$$\tan \theta' = \frac{d'}{f} = \frac{2}{f} \left(\frac{A_F}{\pi} \right)^{1/2}$$

If f is taken as the nominal value of 80 mm, and θ' is small so that $\tan \theta' = \theta'$:

$$\begin{aligned} \theta' &= 0.226 \times 10^{-3} (N_T)^{1/2} \text{ rad.} \\ &= 1.293 \times 10^{-2} (N_T)^{1/2} \text{ deg.} \\ &= 7.758 \times 10^{-1} (N_T)^{1/2} \text{ min. arc.} \end{aligned}$$

APPENDIX E. HAPKE MODEL

The equations for the Hapke model and the Fortran computer program (subroutine) used to evaluate them are given below. The equations were taken from a convenient summary in Reference 12 (but note that a sign error in the last term in the $L(\alpha, g)$ expression was corrected).

E.1 Hapke Equations

The amount of light received by a detector on the earth scattered from a region on the moon is given by:

$$E = E_0 \text{adv} \left(\frac{2}{3\pi} \right) A_p \phi(\alpha, \psi, g)$$

where: E = amount of light received by a detector of area, a , and solid angle of acceptance, dw .

E_0 = intensity of incident radiation

A_p = total reflectivity of a particle of lunar soil (Bond albedo).

ϕ = photometric function which is a function of:

α , luminance longitude,
 ψ , luminance latitude, and
 g , phase angle.

The photometric function may be written in the general form:

$$\phi(\alpha, \psi, g) = L(\alpha, g) \cdot \tau(g) B(g)$$

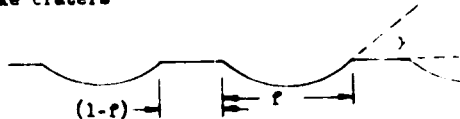
The three functions L , τ and B are given by:

$$L(\alpha, g) = \frac{K_1(1-f)\cos(\alpha+g)}{\cos(\alpha+g)+\cos\alpha} + \frac{K_2f}{2\cos\frac{1}{2}g\cos\frac{1}{2}\alpha\sin\gamma} \left[\cos(\alpha+g)\sin(\gamma+kg) - \frac{1}{2}\sin^2\frac{g}{2} \ln \left| \frac{\cos(\alpha+g)+\sin(\gamma+kg)}{\cos(\alpha+g)-\sin(\gamma+kg)} \right| \right]$$

$$\tau(g) = \frac{\sin|g| + \frac{1}{2}|g|\cos|g|}{\pi} + 0.1(1-\cos|g|)^2$$

$$B(g) = \begin{cases} 2 \frac{\tan|g|}{2h} \left[1 - \exp\left(-\frac{h}{\tan|g|}\right) \right] \left[3 - \exp\left(-\frac{h}{\tan|g|}\right) \right], & |g| \leq \frac{\pi}{2} \\ 1, & |g| > \frac{\pi}{2} \end{cases}$$

The first term in the L function is the Lommel-Seeliger law which describes the brightness of a surface which is porous on a microscopic scale but whose large scale topology is a flat horizontal plane. The second term describes the brightness of a wrinkled surface covered by cylindrical troughs whose axes are aligned with lines of longitude. The edge of the troughs have a slope γ and the troughs themselves cover a fraction of the surface f . The troughs behave like craters



when covered by a porous material and are mathematically more tractable. The constants for use in the equation are given below.

The first term of the B function is the Schoenberg function which describes the average scattering characteristics of particles of arbitrary shape having rough, diffuse surfaces oriented at random. The second term is an imperical forward scattering term describing light transmitted through the particles. If the surge effect near zero phase angle is taken into account, the B function takes the form:

$$\tau(g) = \frac{1}{2} [1 - \sin\frac{1}{2}g] \left[\frac{n(\cot\frac{1}{2}g)}{h} + 0.1(1-\cos|g|)^2 \right] B(g)$$

where $n = 1$ and $h = .05$ in the B function.

The B function describes the backscatter due to blocking and shadowing within the soil. The parameter h is related to the density of the porous surface layer by:

$$h = 2 \left(\frac{\rho}{\rho_0} \right)^{2/3}$$

REGION	DEFINITION	K_1	K_2	J	k
0	$\alpha \leq \frac{1}{2}\pi - \gamma$, $\frac{1}{2}\pi - \alpha \leq g \leq \frac{1}{2}\pi - \gamma$	1	0
1	$\alpha \leq \frac{1}{2}\pi - \gamma$, $\frac{1}{2}\pi - \alpha \leq g \leq \frac{1}{2}\pi - \gamma$	1	1	1	1/2
2	$\alpha \leq \frac{1}{2}\pi - \gamma$, $\frac{1}{2}\pi - \alpha \leq g \leq \frac{1}{2}\pi - \gamma$	1	1	1/2	0
3	$\alpha \leq \frac{1}{2}\pi - \gamma$, $\frac{1}{2}\pi - \alpha \leq g \leq \frac{1}{2}\pi - \gamma$	1	1	...	1/2
4	$\alpha \leq \frac{1}{2}\pi - \gamma$, $\frac{1}{2}\pi - \alpha \leq g \leq \frac{1}{2}\pi - \gamma$	1	1	1/2	1
5	$\alpha \leq \frac{1}{2}\pi - \gamma$, $\frac{1}{2}\pi - \alpha \leq g \leq \frac{1}{2}\pi - \gamma$	1	0

E.2 Program Listing

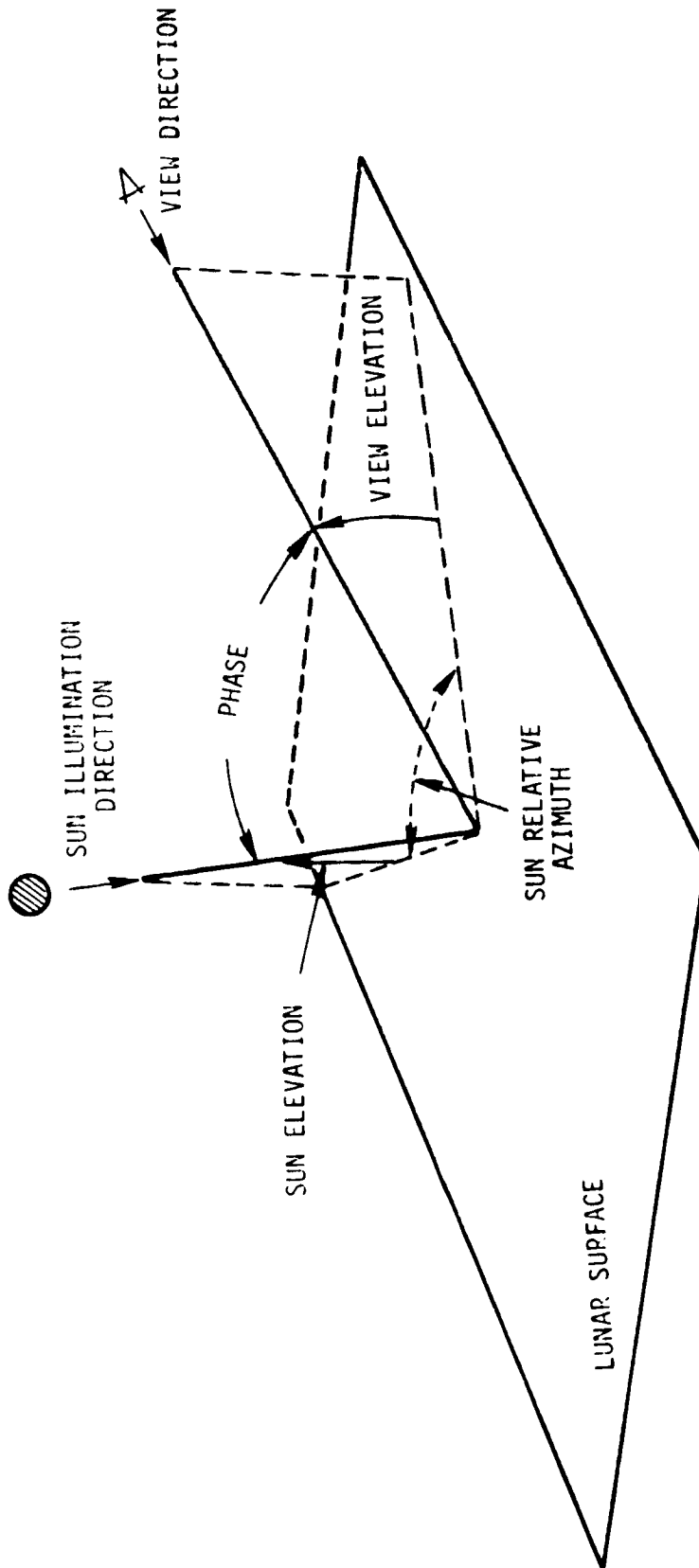
```

SUBROUTINE PHUTAB2(E,H,H1,A,G,PH)
P=3.1415926535897932
IF(A.GE.(-P/2).AND.A.LE.(P/2).AND.G.GE.(P/2-A).AND.G.LE.P)GOTO5
GO TO 10
5 K1=K2=0
HJ=HK=C
GO TO 100
10 IF(A.GE.(-P/2+H).AND.A.LE.(P/2).AND.G.GE.(P/2-H-A).AND.G.LE.
1(P/2-A)) GO TO 15
GO TO 20
15 K1=K2=1
HJ=1.

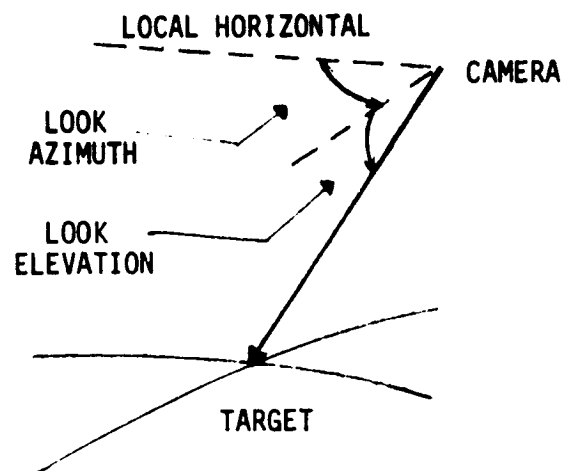
HK=.5
GO TO 100
20 IF(A.GE.(-P/2+H).AND.A.LE.(P/2-H).AND.G.GE.0..AND.G.LE.(P/2
1-H-A))GO TO 25
GO TO 30
25 K1=K2=1
HJ=.5
HK=0
GO TO 100
30 IF(A.GE.(-P/2).AND.A.LE.(-P/2+H).AND.G.GE.C..AND.G.LE.(P/2
1-H-A))GO TO 35
GO TO 40
35 K1=K2=1
HJ=0
HK=.5
GO TO 100
40 IF(A.GE.(-P/2).AND.A.LE.(-P/2+H).AND.G.GE.(P/2-H-A).AND.
1G.LE.(P-H))GO TO 45
GO TO 50
45 K1=K2=1
HJ=.5
HK=1.
GO TO 100
50 IF(A.GE.(-P/2).AND.A.LE.(-P/2+H).AND.G.GE.(P-H).AND.G.LE.
1(P/2-A))GO TO 55
DISPLAY*! REGIONAL CONDITION SATISFIED. HELLFIRE AND BRIMSTONE**
55 K1=1
K2=0
HJ=HK=C
100 W1=K1*(1-E)*COS(A+G)/(COS(A+G)+COS(A))
W2=K2*F/(2*COS(G/2)*COS(A)*SIN(H))
C=COS(A+HJ*G)
S=SIN(H+HK*G)
W3=C*S-(SIN(G/2))*2/2*ALOG(ABS((C+S)/(C-S)))
ELL=W1+W2+W3 ← L (α,g)
W4=(SIN(ABS(G))+(P-ABS(G))*COS(ABS(G)))/P
W5=0.1*(1-COS(ABS(G)))*2
SIGMA=W4+W5 ← Σ (g)
IF(ABS(C).LT.(P/2-.000000000000002))GO TO 110
HEE=1.
GO TO 120
110 W6=TAN(ABS(G))/(2*H1)
W7=EXP(-H1/TAN(ABS(G)))
W3=1-W7
W9=2-W7
HEE=2-W3-W7-W9 ← B(g)
120 PH=ELL+SIGMA*HEE
RETURN
END

```

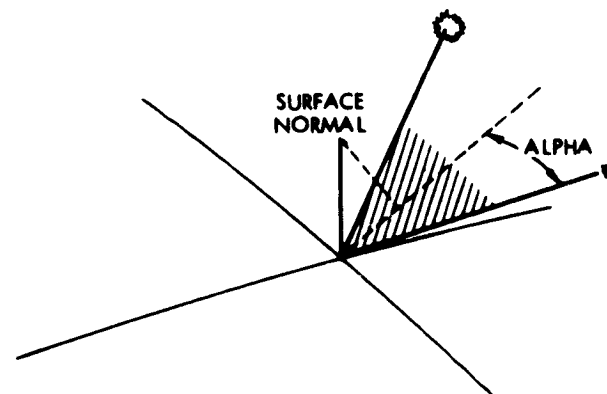
REGION
LOGIC

APPENDIX F. DEFINITION OF TERMS IN TABLES 5-1 THROUGH 5-3

I. Sun Elevation, Viewing Elevation, Relative Azimuth, and Phase Angle



II. Look Elevation and Look Azimuth



The dotted line is the projection of the surface normal onto the plane determined by the sun and viewing lines. If the viewing line lies between the sun line and the projection of the surface normal, then the alpha angle is positive; otherwise it is negative. In the drawing the alpha angle is negative.

III. Alpha Angle